Phase 2 Initial Borehole Drilling and Testing, Ignace Area

WP10 – Geological Integration Report for Borehole IG_BH02

APM-REP-01332-0265 December 2022

Nuclear Waste Management Organization

nwmo
NUCLEAR WASTE MANAGEMENT ORGANIZATION
SOCIÉTÉ DE GESTION DES DÉCHETS NUCLÉAIRES

Nuclear Waste Management Organization
22 St. Clair Avenue East, 6th Floor
Toronto, Ontario
M4T 2S3
Canada

Tel: 416-934-9814
Web: www.nwmo.ca

Phase 2 Initial Borehole Drilling and Testing, Ignace Area

WP10 – Geological Integration Report for Borehole IG_BH02

APM-REP-01332-0265

December 2022

Nuclear Waste Management Organization

All copyright and intellectual property rights belong to NWMO.

Document History

Title:	Phase 2 Initial Borehole Drilling and Testing, Ignace Area. WP10 – Geological Integration Report for Borehole IG_BH02		
Report Number:	APM-REP-01332-0265		
Revision:	R1	Date:	December 2022
Author Company(s): Nuclear Waste Management Organization			
Authored by:	Aaron DesRoches, Lindsay Waffle and Andrew Parmenter (NWMO)		
Verified by:	Eric Sykes, Mostafa Khorshidi and Raymond Munier		
Accepted by:	Sarah Hirschorn (Geoscience Director)		

Revision Summary		
Revision Number	**Date**	**Description of Changes/Improvements**
R0	2022-02	Initial issue
R1	2022-12	Minor editorial revisions

ABSTRACT

Title:	Phase 2 Initial Borehole Drilling and Testing, Ignace Area. WP10 – Geological Integration Report for Borehole IG_BH02
Report No.:	APM-REP-01332-0265
Author(s):	Aaron DesRoches, Lindsay Waffle and Andrew Parmenter
Company:	Nuclear Waste Management Organization
Date:	December 2022

The Initial Borehole Drilling and Testing project in the Ignace Area, Ontario is part of Phase 2 Geoscientific Preliminary Field Investigations of the Nuclear Waste Management Organization's (NWMO) Adaptive Phased Management (APM) Site Selection Phase. This project involves the drilling and testing of several deep boreholes within the northern portion of the Revell batholith. Borehole IG_BH02 is located approximately 35 km southeast of the Wabigoon Lake Ojibway Nation and 44 km northwest of the Town of Ignace. Access to the IG_BH02 drill site is via Highway 17 and a network of logging roads. This Geological Integration Report serves as the primary reference of the geological findings from the borehole drilling and testing activities at IG_BH02.

The objective of the Geological Integration Report is to summarize the main geological findings and provide an initial interpretation of the rock type and structural characteristics of the geosphere intersected by borehole IG_BH02, including delineation of rock unit and structural unit domains. In addition, distinct intervals of higher fracture frequency identified along the length of the borehole are documented. These components represent an initial geological model for IG_BH02 which can be further used in developing a site-scale 3D geological model.

Findings and uncertainties are summarized at the end of the report. One primary consideration is the understanding that the available information *is from a single borehole.* Whether or not the characteristics of the bedrock interpreted in this report will be representative of characteristics in other boreholes remains uncertain.

TABLE OF CONTENTS

ABSTRACT ..... **iii**

1 INTRODUCTION **1**

1.1 Technical Objectives and Scope of Report **1**

2 Background Information **2**

2.1 Geological Setting **2**

2.2 Background and Overview of Borehole Drilling and Testing **3**

2.2.1 Drilling Site Description 3

2.3 Borehole Construction Details for IG_BH02 ..... **5**

2.3.1 Borehole Deviation Analysis 6

3 Integrated Geological Interpretation **9**

3.1 Data Used for Geological Interpretation **9**

3.1.1 Terminology 10

3.2 Geological Results **11**

3.2.1 Lithological Interpretation 11

3.2.2 Alteration Interpretation 29

3.2.3 Rock Unit Classification 35

3.2.4 Structural Interpretation 38

3.2.4.1 Structures 41

3.2.4.2 Interpreted Fracture Sets 60

3.2.4.3 Fracture Infill Minerals 64

3.2.5 Structural Unit Classification 72

3.2.6 High Fracture Frequency Intervals (HFFIs) 74

4 Summary of Findings and Uncertainties **88**

4.1 Findings **88**

4.2 Uncertainties **92**

5 References **94**

Appendix A: Summary List of Work Packages Completed for IG_BH02 ..... **96**

Appendix B: Petrography and lithogeochemistry data **98**

Appendix C: Geophysical Near and Far Density Log Correction 104

Appendix D: Structure log integration methodology..... 106

Appendix E: Stereonets of Fractures by Structural Unit..... 110

Appendix F: Stereonets of IG_BH02 High Fracture Frequency Intervals (HFFI) 114

Appendix G: Summary of borehole logs at 1:1,000 scale..... 118

LIST OF TABLES

Table 1: Details of Borehole Diameter for IG_BH02 6

Table 2: Summary of Rock Types Encountered in IG_BH02 11

Table 3: Summary average of major oxides in the rock types of IG_BH02. Note that only 5 rock types were sampled for lithogeochemical analysis and there are no results for pegmatite, quartz, and biotite granodiorite-tonalite dykes. Aphanitic and Feldspar-phyric tonalite dykes are combined as they are compositionally the same. 15

Table 4: Mean geophysical response values for each logged rock type. 26

Table 5: Summary of alteration assemblages observed in IG_BH02 during geological core logging. Note that because multiple alteration assemblages could be logged in the same interval, the sum of total alteration logged is greater than the length of the borehole. 30

Table 6: Summary of Classified Rock Units 36

Table 7: Summary of structures observed in the borehole. 38

Table 8: Summary of interpreted fracture sets in the borehole. Presents the general description of the orientation with a mean dip and dip direction. 63

Table 9: Position ranges and standard statistics for fracture frequencies captured within the defined structural units (SU) within the borehole. 74

Table 10: High Fracture Frequency Intervals from IG_BH02 77

LIST OF FIGURES

Figure 1: Location and Geological setting of borehole IG_BH02 in the northern portion of the Revell batholith. 1

Figure 2: Location of the drilling site for borehole IG_BH02. 4

Figure 3: Aerial view of the drilling site for IG_BH02 – looking northeast. 5

Figure 4: Final casing and borehole construction schematic design for IG_BH02. The final average borehole path is 62.8° from the horizontal (Golder, 2020a). 6

Figure 5: Compilation of borehole IG_BH02 deviation measurements. Data sets include up- and down-hole televiewers surveys and gyro surveys. Average and standard deviation between the gyro and televiewer survey measurements are presented. Final borehole path (easting, northing, TVD) is defined based on final gyro measurements from the Sprint-IQ survey. 7

Figure 6: a) Borehole deviation presented as the total borehole closure versus true vertical depth; and b) bullseye plot showing the planned borehole trajectory (black) compared to the final SPRINT-IQ™ survey trajectory (red). 8

Figure 7: Input datasets used to derive a final lithology log. From left: optical televiewer log, four suites of continuous geophysical logs that aid in distinction of rock types, logged alteration (by type), and final lithology log. Due to the low spectral gamma counts, K, U and Th were evaluated using a 10 m window, resulting in a smoothing of their profiles. 13

Figure 8: Classification/nomenclature of felsic granitoid phases according to the normalized modal mineral content (Quartz + Alkali-feldspar + Plagioclase = 100 Vol%) as determined from investigation of 18 samples taken for lithogeochemical analysis. Average modal

mineralogy for each sample was determined semi-quantitatively using polished thin sections and plotted on a simplified ternary Streckeisen diagram after Le Bas and Streckeisen (1991)..... 14

Figure 9: Plutonic Rock Classification (Debon and Le Fort, 1983). Diagram axes correspond to proportions of K-feldspar and plagioclase to quartz. P is calculated from (K-(Na+Ca)) and Q is calculated from ((Si/3) – (K+Na+(2*Ca)/3)). Parameters calculated as oxide percentages converted to millications. Crosses show the mean composition for each rock type. 16

Figure 10: Representative example of biotite granodiorite-tonalite (sample IG_BH02_LG013). a) Core sample photograph. b) Billet photograph showing yellow staining of potassium feldspar (billet size is 25 x 40 mm). c) Thin section photomicrograph with rock-forming minerals plagioclase (pl) and quartz (qz). Sericite (white mica) alteration can be seen in plagioclase crystals; crossed polarizers transmitted light. 17

Figure 11: Representative example of biotite tonalite (sample IG_BH02_LG017). a) Core sample photograph. b) Billet photograph showing very minor yellow staining of potassium feldspar (billet size is 25 x 40 mm). c) Thin section photomicrograph with rock-forming minerals plagioclase (pl) and quartz (qz). Sericite (white mica) alteration can be seen in cores of plagioclase crystals; crossed polarizers transmitted light. 18

Figure 12: Representative examples of amphibolite (sample IG_BH02_LG021). a) Core sample photograph. b) Billet photograph (billet size is 25 x 40 mm) shows foliated and massive sections of sample. c) Thin section photomicrograph with main rock-forming minerals amphibole (am), plagioclase (pl), and quartz (qz); plane polarized transmitted light. 19

Figure 13: Representative examples of an aphanitic tonalite dyke (IG_BH02_LG001). a) Core sample photograph. b) Billet photograph showing very minor yellow staining of alkali feldspar and rare 1-2 mm phenocrysts (billet size is 25 x 40 mm). c) Thin section photomicrograph with rare 0.5-1mm plagioclase phenocrysts (pl). Plagioclase (pl) is also visible in the very fine-grained matrix, along with quartz (qz) and biotite (bt); crossed polarized transmitted light. 21

Figure 14: Representative examples of a feldspar-phyric tonalite dyke (IG_BH02_LG005). a) Core sample photograph. b) Billet photograph showing very minor yellow staining of alkali feldspar concentrated around plagioclase phenocrysts (billet size is 25 x 40 mm). c) Thin section photomicrograph with plagioclase (pl) phenocrysts in a very fine-grained matrix of plagioclase and quartz (pl + qz) and biotite (bt); crossed polarized transmitted light. 22

Figure 15: Representative examples of an aplite dyke (IG_BH02_LG014). a) Core sample photograph. b) Billet photograph yellow staining of alkali feldspar and increasing grain size toward contact with biotite granodiorite-tonalite (billet size is 25 x 40 mm). c) Thin section photomicrograph with major rock forming minerals alkali feldspar (af), plagioclase (pl), and quartz (qz). Note the relatively fresh look of the minerals compared to the host biotite granodiorite-tonalite, indicative of a later-stage intrusion; crossed polarized transmitted light..... 23

Figure 16: Chondrite-normalized rare-earth element (REE) plot (after Taylor and McLennan, 1985) of rock types from IG_BH02 and a representative average of 2.8 Ga low-heavy REE (HREE) tonalite-trondhjemite-granodiorite (TTG) from the Fennoscandian shield (black squares; Halla, 2018). Y-axis shows concentrations (expressed as logarithm to the base 10 of the value) of REE (x-axis, by atomic number) in IG_BH02 samples normalized to a reference Chondrite standard. REE patterns of biotite granodiorite-tonalite, aphanitic tonalite dykes, and feldspar-phyric tonalite dykes demonstrate steep fractionation and significant depletion of HREE. Aplite dykes demonstrate a less steep fractionation and

negative europium anomalies, suggesting they from are from a later stage, evolved granite source. The biotite granodiorite-tonalite sample represented by pink diamonds is an altered (albitized) sample. 25

Figure 17: Violin plots show the distribution of geophysical log responses associated with the logged rock types. Each violin shows the distribution of the data values with the median (thick dashed line), and quartiles (thin dashed lines) marked. Rock types are ordered based on total data counts from left to right in each graph. 28

Figure 18: Cross plots showing correlations between neutron, density, natural gamma and potassium count values of all rock types encountered in IG_BH02. Colored points represent mean values of the geophysical responses and the error bars represent standard deviation. 29

Figure 19: Alteration types and distribution along the borehole based on geological core logging and analysis of the optical televiewer log resulting in a final alteration log. A2 indicates intervals with slight alteration, A3 indicates intervals with moderate alteration, and A4 indicates intervals where alteration is pervasive along the borehole length..... 32

Figure 20: Common alteration assemblages logged in IG_BH02. a) Sample IG_BH02_LG009, biotite granodiorite-tonalite logged with potassic and hematite alteration. b) Photomicrograph of sample IG_BH02_LG009 showing plagioclase crystals (pl) heavily altered by white mica, biotite (bt) weakly altered by chlorite, alkali feldspar (af), and quartz. The inset shows a magnetite crystal replaced by hematite and rutile occurring within quartz; crossed-polarized transmitted light. c) Sample IG_BH02_LG013, biotite granodiorite-tonalite logged as silicified. d) Sample IG_BH02_LG013 showing quartz grains (qz), and plagioclase (pl) heavily altered by white mica; crossed-polarized transmitted light. e) Sample IG_BH02_LG018, biotite granodiorite-tonalite logged as potassic alteration. f) Sample IG_BH02_LG018 showing plagioclase (pl) moderately altered by clay and epidote, fresh alkali feldspar (af), and quartz (qz). Minor biotite that is strongly altered to chlorite is also visible. This thin section shows an irregular veinlet of quartz and alkali feldspar that is interpreted to have formed due to fluid overpressure at the end of magmatic crystallization (i.e., the alkali feldspar is primary and not a result of alteration); crossed-polarized transmitted light. g) Sample IG_BH02_LG023, albite-rich alteration zone (albitite). This is the strongest alteration observed in IG_BH02. h) Sample IG_BH02_LG023 showing plagioclase (pl), fine-grained Fe-chlorite (ch), and calcite occupying interstitial positions between the plagioclase grains. The abundance of plagioclase in association with typical alteration minerals (chlorite and calcite) is evidence that this sample is strongly altered; crossed-polarized transmitted light. i) Sample IG_BH02_LG025, chlorite-altered biotite granodiorite-tonalite. j) Sample IG_BH02_LG025 showing plagioclase weakly altered to white mica (pl), magmatic biotite intensely altered by Fe-chlorite (ch), and fresh alkali feldspar (af); crossed-polarized transmitted light..... 34

Figure 21: Summary of final logged lithology, alteration and key geophysical logs presented alongside interpreted rock units for IG_BH02. Due to the low spectral gamma counts, K, U and Th were evaluated using a 10 m window, resulting in a smoothing of their profiles. ... 37

Figure 22: Equal Area Lower Hemisphere Projections (stereonets) showing poles to planar structural measurements, unweighted (n = 2274). 39

Figure 23: Equal Area Lower Hemisphere Projections (stereonets) showing a summary of the poles for planar structural measurements. Top: all data – contours, unweighted (n = 2274). Bottom: all data – contours, Terzaghi-weighted (n = 4051). 40

Figure 24: Examples of primary igneous and ductile structure. a) Subtle variation in biotite content (from top left to bottom right) defining a primary igneous layering, in biotite granodiorite-tonalite (231 m along borehole). b) Foliation defined by biotite and quartz in cm-scale shear zone, in biotite granodiorite-tonalite (904 m along borehole). c) Cm-scale shear zone developed within amphibolite (659 m along borehole). d) Folded mylonite layer within a dm-scale shear zone, in amphibolite (673 m along borehole). 42

Figure 25: Stereonet showing poles and unweighted contours for Igneous Primary Structures (IPS; n = 36). 43

Figure 26: Stereonet showing poles and unweighted contours for all oriented geological contacts (n = 102). 44

Figure 27: Stereonet showing poles for amphibolite contacts (n = 9). Open symbols identify broken contacts (BR) and filled symbols identify intact contacts (IN). 45

Figure 28: Stereonet showing the distribution of poles to contacts for felsic dykes (n = 105), including, aphanitic/feldspar phyric tonalite dykes (n= 53), aplite dykes (n = 18), biotite granodiorite-tonalite dykes (n = 6), pegmatite dykes (n = 18), and quartz dykes (n = 10).. 46

Figure 29: Summary log showing the frequency per metre of brittle structures (left) in comparison to stick plots that show the distribution of all brittle structures (Joints – JN, Veins – VN and Faults - FLT) and all ductile structures (Shear Zones – SHR and Foliation – FO). 47

Figure 30: Stereonets showing orientation information for Foliation (FO). Top: All data – poles and contours, unweighted (n = 26). Bottom: All Foliation data, Terzaghi-weighted contours (n = 34). 48

Figure 31: Stereonets showing orientation information for Shear Zones (SHR-SHRD) and Mylonites (MYL). Top: All data – poles and contours, unweighted (n = 130). Bottom: All Shear Zone and Mylonite data, Terzaghi-weighted contours (n = 205). 50

Figure 32: Examples of brittle structure. a) Intact hairline joint with iron stain, in biotite granodiorite-tonalite (93 m). b) Broken joint with no surface alteration and no measurable geological aperture (688 m). c) Intact mm-scale quartz-filled vein, in biotite granodiorite tonalite (483 m). d) Intact hairline calcite-filled vein, in biotite granodiorite tonalite (222 m). e) Broken fault plane with quartz infill, in biotite granodiorite-tonalite (524 m). f) Lineation defined by aligned quartz on same fault plane as shown in (e). 51

Figure 33: Stereonets showing orientation information for Joints (JN). Top: All data – poles and contours, unweighted (n = 1474). Open symbols identify broken Joints (JN-BR) and filled symbols identify partially intact/intact Joints (JN-PIN/IN). Bottom: All Joint data, Terzaghi-weighted contours (n = 2746). 53

Figure 34: Stereonets showing orientation information for all Veins (VN). Top: All data – poles and contours, unweighted (n = 442). Open symbols identify broken Veins (VN-BR) and filled symbols identify partially intact/intact Veins (VN-PIN/IN). Bottom: All Vein data, Terzaghi-weighted contours (n = 753). 55

Figure 35: Stereonets showing orientation information for Faults (FLT). All data – poles (n = 163). Open symbols identify broken Faults (FLT-BR) and filled symbols identify partially intact/intact Faults (FLT-PIN/IN). Bottom: All Fault data, Terzaghi-weighted contours (n = 249). 56

Figure 36: Stereonet showing lineation orientation information for IG_BH02. Top: All lineations (n = 162) plotted by associated plane type (FLT – fault, FO – foliation, MYL – mylonite,

SHR – shear). Bottom: Poles to all oriented planes, by type, with identified lineations (n = 162). 58

Figure 37: Stereonet plot showing poles to all fracture planes logged as broken during geological core logging, with unweighted contours (n = 221). 59

Figure 38: Stereonet plot showing poles to all fracture planes logged as intact or partially intact, with unweighted contours (n = 1858). 60

Figure 39: Stereonets of all oriented fractures, including all joints, veins and faults. Top: All fractures – poles, unweighted (n = 2079). Identified pole clusters are colour-coded to highlight their distribution. Middle: All fractures – contours (n = 2079), unweighted. Bottom: All fractures – contours, Terzaghi-weighted (n = 3748). Middle and bottom stereonets are overlain by final fracture set interpretation. See text and Table 9 for additional summary. 62

Figure 40: Summary log showing the frequency per metre of all brittle structures (left) in comparison to stick plots that show the distribution of all fractures assigned to defined fracture sets 1, 2, 3, 4, 5, and 6, as well as unassigned random fractures. 64

Figure 41: Summary log showing the frequency per metre (Fracture Freq.) of all brittle structures (left) in comparison to stick plots that show the distribution of the most common infill mineral phases including quartz (Qz), chlorite (Chl), iron oxide stain (Fe), calcite (Ca), epidote (Ep), a granitic (Gt) assemblage that includes some combination of alkali-feldspar (Afs) with quartz, plagioclase and biotite, and, fractures that exhibit either clay (Cl), broken rock (Br), soft clay gouge (Go_So), or stiff clay gouge (Go_St). 65

Figure 42: Stereonet plot showing poles to all fracture planes logged with quartz +/- chlorite, biotite, phlogopite, muscovite, epidote, iron oxide staining, or calcite (n = 1069)..... 66

Figure 43: Stereonet plot showing poles to all fracture planes logged with chlorite (n = 448).... 67

Figure 44: Stereonet plot showing poles to all fracture planes logged with iron staining (n = 443). 67

Figure 45: Stereonet plot showing poles to all fracture planes logged with calcite (n = 488). 68

Figure 46: Stereonet plot showing poles to all fracture planes logged with epidote (n = 310). .. 69

Figure 47: Stereonet plot showing poles to all fracture planes logged with granitic infill, including alkali-feldspar +/- quartz, plagioclase and biotite (n = 189). 70

Figure 48: Stereonet plot showing poles to all fracture planes logged with clay, broken rock, or soft gouge..... 71

Figure 49: Stereonet showing poles to all fractures logged as having no identifiable mineral infill phase. Fractures logged in ‘televiewer’ (TV) datasets only, geological ‘core’ logging only (Core), or identified in ‘both’ datasets, are distinguished (n = 160). 72

Figure 50: Per metre fracture frequency (left) and cumulative fracture frequency curve (right) showing vertical distribution of all logged joints, faults, and veins along the borehole. The cumulative fracture frequency curve shows changes in slope where boundaries in structural units (SU) are defined. Structural unit boundaries are marked on the figure, and their positions are described in Table 9. 73

Figure 51: High fracture frequency intervals (HFFIs) interpreted based on fracture intensity from borehole fracture frequency log. Five high fracture frequency intervals are outlined by their yellow bands. The red dashed line represents the peak location. Stick plots indicate the distribution of each fracture type (joint, vein, fault) along the length of the borehole..... 76

Figure 52: Terzaghi-weighted stereonet plot of fractures (JN, VN, FLT) within high fracture frequency interval 1 (HFFI_1) from 19.11 – 34.38 m. Two peaks are defined, a major peak with a mean orientation of 045/85 (best fit plane shown as black dashed great circle) and a minor peak with a mean orientation of 108/77 (best fit plane shown as grey dashed great circle; DipDirection/Dip convention). 78

Figure 53: Core from a portion of HFFI_1 (24.71 – 36.28 m). Biotite granodiorite-tonalite above and below the feldspar-phyric tonalite dyke is characterized by well spaced, shallow and steeply dipping fractures. Pink coloured alteration halos (logged as potassic alteration and hematization) are visible around the dyke. Fracture intensity does not appear to significantly increase in association with the dyke (24.71-29.18 m)..... 79

Figure 54: Core from a portion of HFFI_2 (59.45 – 71.06 m). Biotite granodiorite-tonalite with visible pink and white alteration (logged as hematization, potassic alteration, bleaching, and silicification) surrounding feldspar-phyric felsic and quartz dykes. There is a slight visible increase in fracturing surrounding the dykes and six logged shear structures in and around the dykes. 80

Figure 55: Core from a portion of HFFI_3 (a: 272.35 – 284.21 m; b: 284.21 – 296.03 m). Biotite granodiorite-tonalite with an aphanitic tonalite dyke (a) and feldspar-phyric tonalite dykes (b). Pink coloured alteration is visible around the dykes (logged as potassic alteration and minor hematization). At the top of (b), silicification is logged between the two feldspar-phyric tonalite dykes. Fractures are well spaced in the biotite granodiorite-tonalite and more concentrated in the dykes. 81

Figure 56: Core from a portion of HFFI_4 (a: 367.44 – 379.39 m; b: 379.39 – 391.06 m). The interval starts in the aphanitic tonalite dyke at the top of (a) and continues to the third box of (b). Pink coloured alteration (logged as potassic and hematization) is visible around all the tonalite and pegmatite dykes. Visually, fracture intensity appears to increase around the dykes, especially the feldspar-phyric dyke from the bottom of (a) to the top of (b). There is an interval that is logged as shear but appears to be breccia filled with red (iron-oxide?) minerals around 380.25 m (top of b). The majority of the brittle and ductile structures cluster in a similar orientation, dipping shallowly toward the east (086/26). 83

Figure 57: Core from HFFI_5 (a: 663.29 – 674.92 m; b: 674.92 – 686.55 m). The interval starts in biotite granodiorite-tonalite in the box just above (a) and continues into the fourth box of (b). Pink coloured alteration (logged as potassic and hematization) is visible around all the tonalite and quartz dykes and amphibolite. The lighter grey alteration visible after the quartz dykes in (b) is the strongest alteration observed in IG_BH02; the biotite granodiorite-tonalite has been almost completely albitized. The brittle and ductile structures in this interval have a wide range of orientations, but the brittle structures do form two clusters, one steeply dipping to the east and the other steeply dipping to the southeast. Logged ductile structures are predominantly shallowly dipping to the north, northeast, and east. Despite this spread in structural orientation, the strong alteration and thick quartz veins (interpreted as hydrothermal veins) suggest that this interval was, or is, an important zone of fluid movement. 85

Figure 58: Lineament traces near IG_BH02 interpreted from LiDAR DEM and airborne geophysics data (DesRoches et al., 2018). Lineament traces are dominantly north-northeast and northwest trending. The approximate trace of IG_BH02 is shown as an orange dashed line. 87

Figure 59: Rose diagram of the lineaments (N = 40) around IG_BH02 (see Figure 58) interpreted from LiDAR DEM and airborne geophysics data (DesRoches et al., 2018). a)

Unweighted; b) Length-weighted to highlight more prominent lineaments. Lineament orientations are plotted using a bin size of 15 degrees. 88

Figure 60: Rose diagrams of the borehole logged fracture orientations using a minimum dip angle of 45 degrees, and bin size of 5 degrees. a) Unweighted (N = 1340 is the total number of fractures); b) Terzaghi-weighted to account for directional bias of the borehole path (weighted N = 2231 is the sum of the weightings). 88

Figure 61: Summary log of geological information, including (from left to right), final log of lithology, classification of rock units, per metre fracture frequency, and structural units, representing the 1-dimensional geological model for IG_BH02. 90

1 INTRODUCTION

Borehole Drilling and Testing project in the Ignace Area, Ontario is part of Phase 2 Geoscientific Preliminary Field Investigations of the Nuclear Waste Management Organization's (NWMO) Adaptive Phased Management (APM) Site Selection Phase.

Following the first stage of the Phase 2 Initial General Field Studies summarized by Golder (2015) and in collaboration with the community, an area located in the northern portion of the Revell batholith was selected by the NWMO for further investigation through an initial borehole drilling campaign which involves drilling and testing of several deep boreholes. The location of IG_BH02 is shown in Figure 1 and Figure 2. IG_BH02 had a planned inclination of -70° towards an azimuth of 225°. Further details on the final borehole path are presented in Section 2 of this report.

Borehole IG_BH02, is located approximately 35 km southeast of the Wabigoon Lake Ojibway Nation and 44 km northwest of the Town of Ignace. Access to the IG_BH02 drill site is via Highway 17 and a network of logging roads (Figure 2). This single borehole integration report serves as the primary reference of the geological findings from the borehole drilling and testing activities at IG_BH02.

The project fieldwork was carried out by a team led by Golder Associates Ltd. (Golder) on behalf of the NWMO. The overall program, described in the Initial Borehole Characterization Plan (Golder, 2017) includes activities related to: the mobilization and set up of the borehole drilling site, the recovery and logging of the bedrock core, drilling water management and groundwater sampling, borehole geophysical and hydraulic testing, laboratory testing, and on-going monitoring activities at the borehole. All activities are documented in work package (WP) data reports that describe test methods, collected data, and calculations, where applicable. The full list of work packages and associated data reports is included in Appendix A.

This report, which represents the tenth work package (WP10 Integration and Synthesis), presents an integrated summary of geological and geophysical information collected primarily during the completion of three work packages, including, WP02: Borehole Drilling and Coring (Golder, 2020a), WP03: Geological and Geotechnical Core Logging, Photography and Sampling (Golder, 2020b) and WP05: Geophysical Well Logging and Interpretation (Golder, 2020c).

1.1 Technical Objectives and Scope of Report

The objective of this Geological Integration report is to evaluate relevant data and provide an interpretation of the lithological and structural characteristics of the geosphere intersected by borehole IG_BH02. This initial interpretation will be revised as further boreholes are drilled to form a holistic interpretation for the geosphere.

Additional information related to developing an understanding of the petrophysical and transport properties of the bedrock of the Revell batholith, as well as the geomechanical, hydrogeological, litho- and hydrogeochemical, and thermal properties will be reported on separately and integrated into a Descriptive Geosphere Site Model (DGSM) report. The DGSM report will summarize the additional borehole- and laboratory-derived data related to these topics and will present this information including a geological model that integrates the WP10 results for each of the boreholes. The information presented in this report, which focuses on IG_BH02, represents the first step in this integration process.

The scope of this Single Borehole Data Integration report is summarized in the following sections:

- Section 1 provides the report introduction and includes the summary of technical objectives and scope of the sections in the report.

- Section 2 first briefly describes the geological setting for the area around the borehole location and then provides an overview of the borehole drilling and testing activity. This includes a brief site description, a summary of the borehole construction, and deviation surveys of the borehole.
- Section 3 presents the integrated summaries of the lithological, alteration and structural characteristics of the bedrock intersected by the borehole (Section 3.2). Then, using this information, an initial geological model, with interpretation of rock units, structural units, and high fracture frequency intervals for the borehole, is presented.
- Section 4 summarizes the findings and addresses uncertainties.
- Appendix A lists all Work Packages and Work Package report names produced as part of the full suite of activities associated with IG_BH02.
- Appendix B presents the petrographic, modal mineralogy, and lithogeochemical data, which are summarized in Section 3.
- Appendix C presents a table of values summarizing the correction applied to the geophysical near and far density log.
- Appendix D contains the methodology for integrating the un-oriented structural dataset generated during WP03 with the televiewer geophysical logs collected during WP05 to produce a final log of oriented structures. The integrated structural dataset is presented in Section 3.
- Appendix E presents lower hemisphere equal area projections (stereonets) summarizing the brittle fractures for each structural unit (SU) in the borehole, defined in Section 3.2.5.
- Appendix F presents lower hemisphere equal area projections (stereonets) summarizing the structural orientation information for all high fracture frequency intervals (HFFI) in the borehole, defined in Section 3.2.6.
- Appendix G presents a summary of the borehole logs for IG_BH02 at 1:1,000 scale.

2 BACKGROUND INFORMATION

2.1 Geological Setting

The approximately 2.7-billion-year-old Revell batholith is located in the western part of the Wabigoon Subprovince of the Archean Superior Province. The batholith is roughly elliptical in shape trending northwest, is approximately 40 km in length, 15 km in width, and covers an area of approximately 455 km^2. Based on recent geophysical modelling, the batholith has a relatively flat base that extends to depths of nearly 4 km in some regions (SGL, 2020). The batholith is surrounded by supracrustal rocks of the Raleigh Lake (to the north and east) and Bending Lake (to the southwest) greenstone belts (Figure 1).

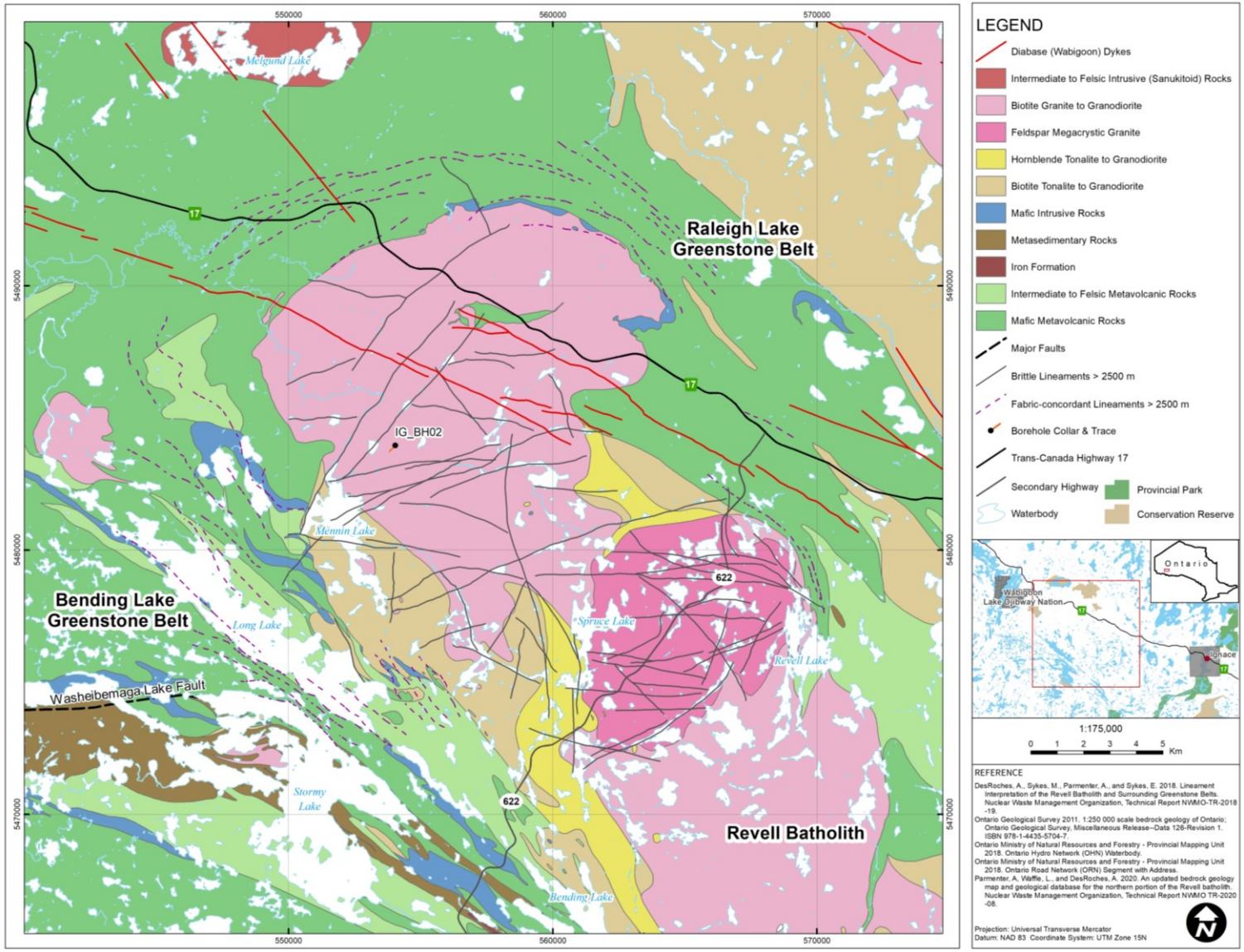


Figure 1: Location and Geological setting of borehole IG_BH02 in the northern portion of the Revell batholith.

Four main rock units are identified in the supracrustal rock group: mafic metavolcanic rocks, intermediate to felsic metavolcanic rocks, metasedimentary rocks, and mafic intrusive rocks (Figure 1). Sedimentation within the supracrustal rock assemblage was largely synvolcanic, although sediment deposition in the Bending Lake area may have continued past the volcanic period (Stone, 2009; Stone, 2010a; Stone, 2010b). All supracrustal rocks are affected, to varying degrees, by penetrative brittle-ductile to ductile deformation under greenschist- to amphibolite-facies metamorphic conditions (Blackburn and Hinz, 1996; Stone et al., 1998). In some locations, primary features, such as pillow basalt or bedding in sedimentary rock units is preserved, in other locations, primary relationships are completely masked by penetrative deformation. Uranium-lead (U-Pb) geochronological analysis of the supracrustal rocks produced ages that range between 2734.6 +/-1.1 Ma and 2725 +/-5 Ma (Stone et al. 2010).

Three main suites of plutonic rock are recognized in the Revell batholith (Figure 1), including, from oldest to youngest: a Biotite Tonalite to Granodiorite suite, a Hornblende Tonalite to Granodiorite suite, and a Biotite Granite to Granodiorite suite. Plutonic rocks of the Biotite Tonalite to Granodiorite suite occur along the southwestern and northeastern margins of the Revell batholith. The principal type of rock within this suite is a white to grey, medium-grained, variably massive to foliated or weakly gneissic, biotite tonalite to granodiorite. One sample of foliated and medium-grained biotite tonalite produced a U-Pb age of 2734.2+/-0.8 Ma (Stone et al., 2010). The Hornblende Tonalite to Granodiorite suite occurs in two irregularly shaped zones surrounding the central core of the Revell batholith. Rocks of the Hornblende Tonalite to Granodiorite suite range compositionally from tonalite through granodiorite to granite and also include significant proportions of quartz diorite and quartz monzodiorite. One sample of coarse-grained grey mesocratic hornblende tonalite produced a U-Pb age of 2732.3+/-0.8 Ma (Stone et al., 2010). Rocks of the Biotite Granite to Granodiorite suite underlie most of the northern, central and southern portions of the Revell batholith. Rocks of this suite are typically coarse-grained, massive to weakly foliated, and white to pink in colour. The Biotite Granite to Granodiorite suite ranges compositionally from granite through granodiorite to tonalite. This suite includes the oval-shaped potassium-feldspar megacrystic granite body in the central portion of the Revell batholith. One sample of coarse-grained, pink, massive potassium feldspar megacrystic biotite granite produced a U-Pb age of 2694.0+/-0.9 Ma (Stone et al., 2010).

Borehole IG_BH02 is located in the northern portion of the Revell batholith (Figure 1). Bedrock exposure in this part of the batholith is generally very good due to minimal overburden, few water bodies, and relatively recent forestry activities. The bedrock surrounding IG_BH02 is composed mainly of massive to weakly foliated felsic intrusive rocks that vary in composition between granodiorite and tonalite. Bedrock identified as tonalite transitions gradationally into granodiorite and no distinct contact relationships between these two rock types are typically observed (SRK and Golder, 2015; Golder and PGW, 2017). Massive to weakly foliated granite is identified at the ground surface to the southeast of the investigation area. The granite is observed to intrude into the granodiorite-tonalite bedrock, indicating that it is a distinct, younger intrusion (Golder and PGW, 2017).

A west-northwest trending mafic dyke interpreted from aeromagnetic data and observed during detailed mapping to be approximately 15-20 m wide, extends across the northern portion of the batholith (Figure 1; Golder and PGW, 2017). This dyke is associated with several other similarly-oriented mafic dykes that stretch across the northern portion of the Revell batholith and into the surrounding greenstone belts. All of these mafic dykes have a similar character and are interpreted to be part of the Wabigoon dyke swarm. One sample from the same Wabigoon swarm produced a U-Pb age of 1887+/-13 Ma (Stone et al., 2010), indicating that these mafic dykes are Proterozoic in age. It is assumed based on surface measurements that these mafic dykes are sub-vertical (Golder and PGW, 2017).

Long, narrow valleys are located northwest of IG_BH02 (Figure 2). These local valleys host creeks and small lakes that drain to the southwest and may represent the surface expression of structural features that extend into the bedrock. A broad valley east of IG_BH02 hosts a more continuous, un-named water body that flows to the south. The linear and segmented nature of this waterbody's shorelines may also represent the surface expression of structural features that extend into the bedrock (Figure 2; DesRoches et al., 2018).

Regional observations from mapping have indicated that structural features are widely spaced (typical 30 to 500 cm spacing range) and dominantly comprised of sub-vertical joints with two dominant orientations trending northeast and northwest (SRK and Golder, 2015; Golder and PGW, 2017). Interpreted bedrock lineaments generally follow these same dominant orientations in the northern portion of the Revell batholith (DesRoches et al., 2018). Minor subhorizontal joints have been observed with minimal alteration, suggesting they are younger and perhaps related to glacial unloading. One mapped regional-scale fault, the Washeibemaga Lake fault, trends east and is located to the west of the Revell batholith (Figure 1). Additional details of the lithological units and structures found at surface in the northern portion of the Revell batholith are provided in Golder and GW (2017).

2.2 Background and Overview of Borehole Drilling and Testing

2.2.1 Drilling Site Description

The drilling site for borehole IG_BH02 is located approximately 35 km southeast of the Wabigoon Lake Ojibway Nation and 44 km northwest of the Town of Ignace. Access to the IG_BH02 drilling site is via Highway 17 and a network of logging roads. Access to the site was established by clearing approximately 3.95 km of new road branching from Dyment road towards the south (Figure 2). The drilling site is approximately 70 m by 50 m and has an area of 3,500 m^2 (Figure 3). The borehole is located at the southern end of the drilling site. The drilling site was constructed to minimize the need for ground clearing and reduce the effects of erosion from water runoff. A large percentage of the site was rock outcrop, and a compacted aggregate pad was constructed to level off the area. An oblique aerial view of the site looking northeast is shown in Figure 3.

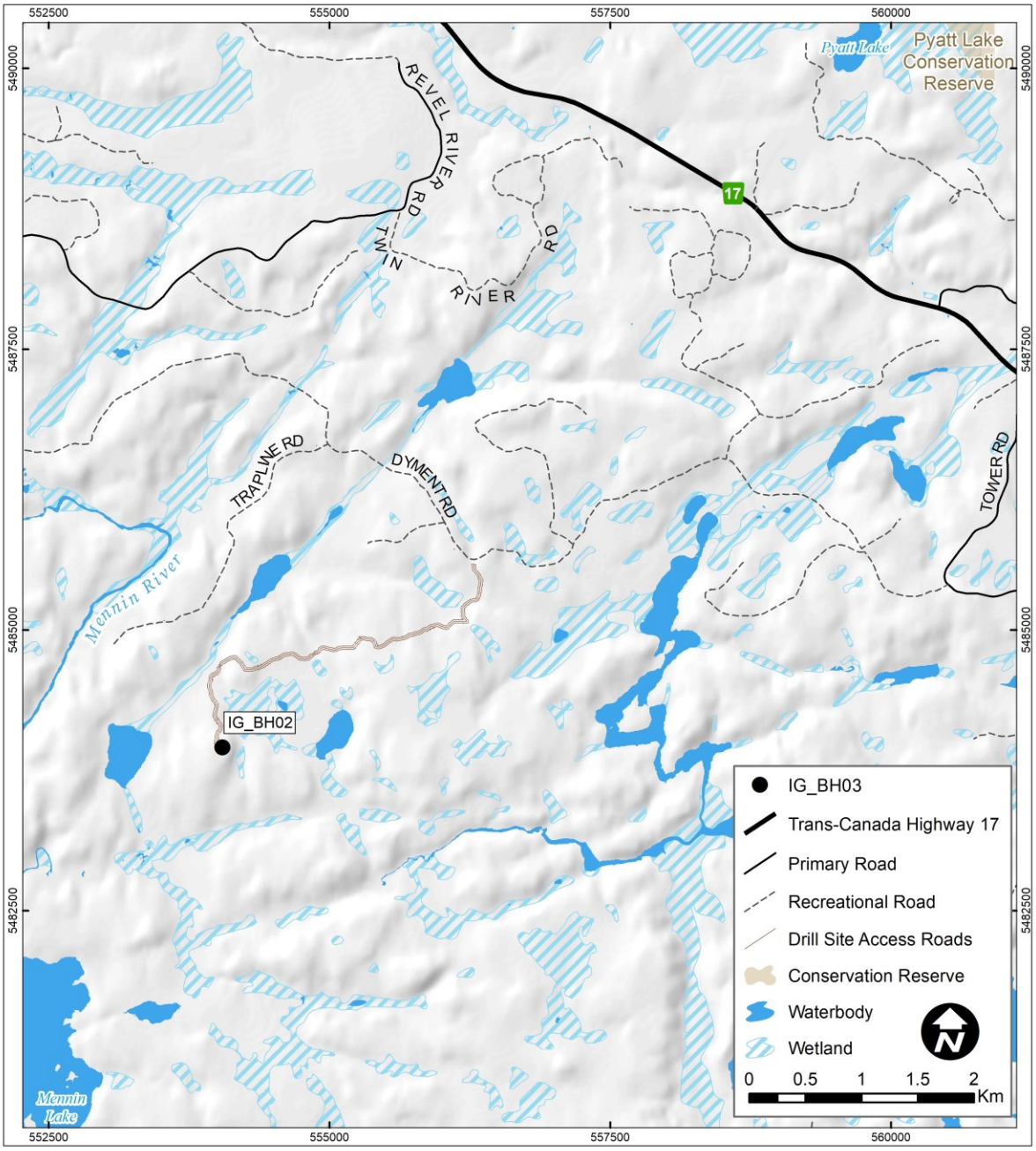


Figure 2: Location of the drilling site for borehole IG_BH02.



Figure 3: Aerial view of the drilling site for IG_BH02 – looking northeast.

2.3 Borehole Construction Details for IG_BH02

Borehole IG_BH02 was drilled at a planned inclination of -70° towards an azimuth of 225° using a diamond drill. Two sets of casing were installed in the upper parts of the borehole to ensure borehole stability and reduce mixing of shallow and deep groundwaters. A schematic of the final borehole construction is shown in Figure 4. The down-axis position along the borehole is measured in metres from surface.

As of January 2021, the borehole is sealed with five bridge plugs (BP) at various positions along the borehole to reduce the amount of water mixing between different intervals in the borehole. Bridge plug locations are shown in Figure 4.

PWT conductor casing was installed and cemented to a position along borehole of 9.75 m, to prevent drill fluid from escaping through the fractured upper bedrock. No overburden was encountered or recovered during drilling and casing installation. The borehole was drilled to 100.10 m along the borehole and evaluated to determine a position to install the PQ casing. The borehole was reamed, and PQ casing was installed to a desired position of 73.62 m.

The PQ casing was cemented in place using a high sulphate resistant cement (LaFarge) and the cement was left to cure for 30 hours. Drilling and coring activities resumed for the remainder of the borehole down to a drilled position along borehole of 1000.41 m. The final IG_BH02 casing diameters and positions, and borehole and core diameters, are shown in Figure 4 and Table 1.

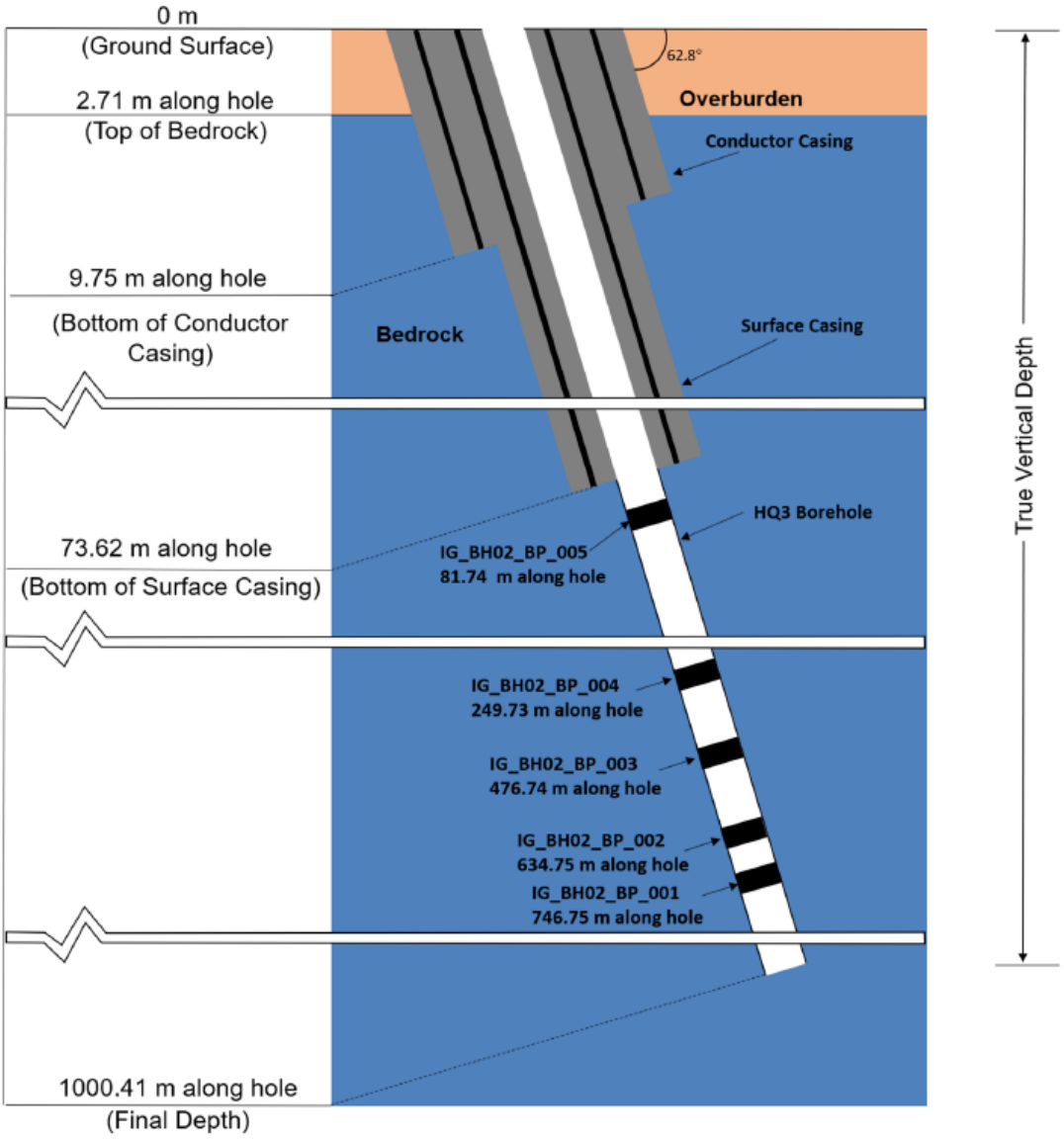


Figure 4: Final casing and borehole construction schematic design for IG_BH02. The final average borehole path is 62.8° from the horizontal (Golder, 2020a).

Table 1: Details of Borehole Diameter for IG_BH02

Position from (m)	Position to (m)	Diameter Type	Borehole Diameter (mm)
0	9.75	Conductor (PWT) Casing and Surface (PQ) Casing	143.76
9.75	73.62	Surface (PQ) Casing	121.0
73.62	1000.41	Open Borehole (HQ size)	96

2.3.1 Borehole Deviation Analysis

Borehole IG_BH02 was planned with an inclination of -70° (equivalent tilt is 70°) towards an azimuth of 225°. No deviation corrections were made during drilling. Two downhole deviation

surveys were conducted; one at 50 m intervals (downhole – multiple probe trips) to monitor deviation during drilling using the Reflex TrueShot probe, and the other at 10 m intervals at the end of drilling using the Reflex Sprint-IQ gyro (up hole – single trip; Golder, 2020a).

During the geophysical logging, four additional borehole deviation logs were continuously recorded using the onboard 3-axis magnetometer and accelerometers within the acoustic and optical televiewer probes (Figure 5). These surveys provided continuous inclination and declination data at ~2 mm intervals (Golder, 2020c). Due to the steel casing, the majority of the televiewer surveys were terminated at the base of the casing and are missing data from the first ~75 m. Therefore, a single televiewer survey conducted prior to installing the casing was used for this section of the borehole. Data from these surveys were mainly used to confirm and support the results of the final deviation survey using the Sprint-IQ probe. Figure 5 presents individual azimuth and tilt profiles plotted from each televiewer run and the Sprint-IQ gyro run. The standard deviation for the azimuth and tilt profiles is calculated to show the variability amongst the different profile runs. The mean profiles for the televiewer runs are calculated and compared to interpolated profiles derived from the Sprint-IQ gyro measurements at 10 metre increments. Although the gyro survey is used for the final borehole deviation, the televiewer surveys provided an estimate of the magnitude of variability between different runs, as well as an average for comparison with the gyro survey. Overall, the standard deviation for the azimuth and tilt is shown to be less than 2 degrees and 0.5 degrees, respectively.

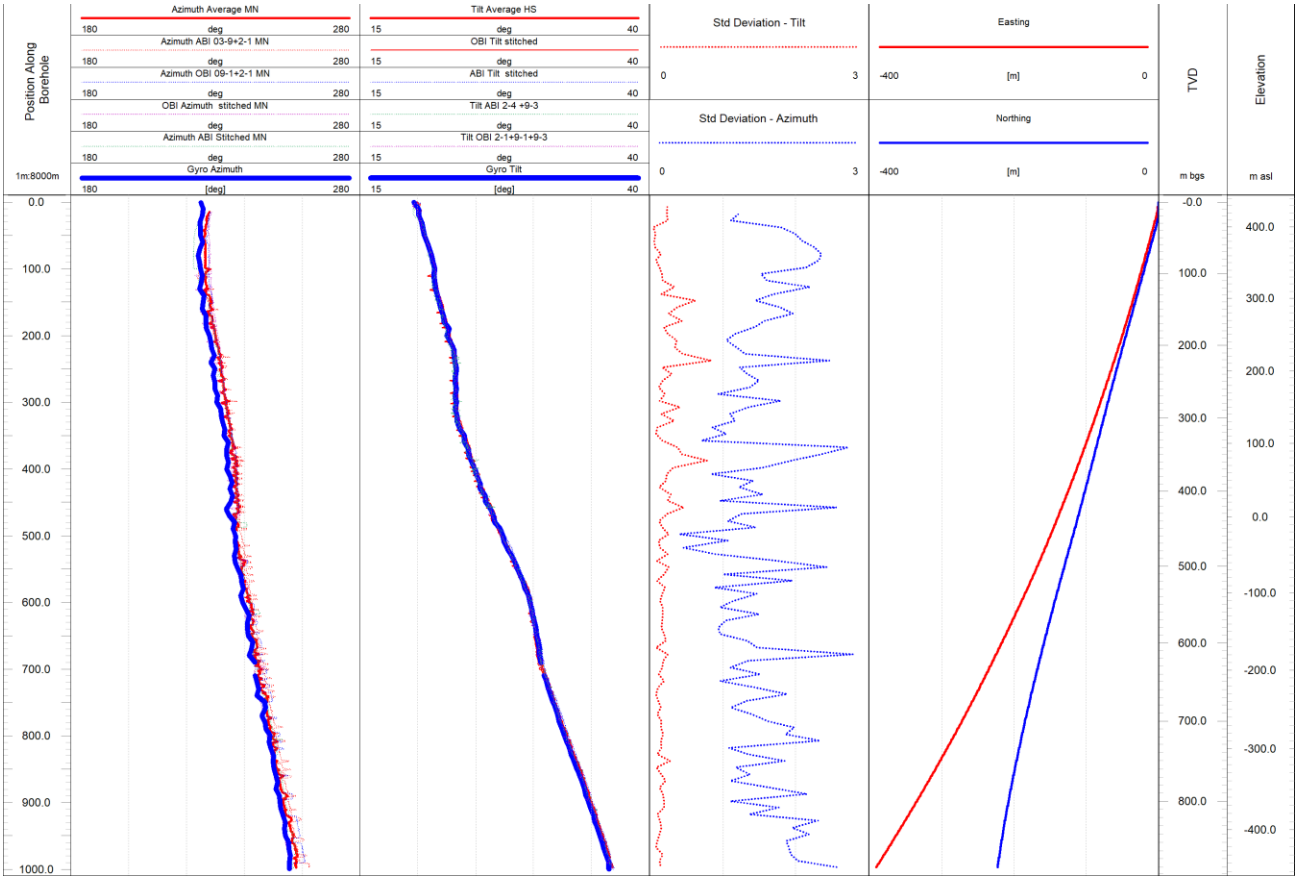


Figure 5: Compilation of borehole IG_BH02 deviation measurements. Data sets include up- and down-hole televiewers surveys and gyro surveys. Average and standard deviation between the gyro and televiewer survey measurements are presented. Final borehole path (easting, northing, TVD) is defined based on final gyro measurements from the Sprint-IQ survey.

By comparing manufacturer specifications between the Reflex Sprint-IQ Gyro and the two televiewer probes, the Sprint-IQ gyro is considered more accurate. Additionally, data recorded using the Sprint-IQ were performed in stationary mode, compared to the continuous mode of the televiewer probes. Despite the differences between the probes, the results indicated there is strong consistency between the average of the televiewers azimuth and tilt profiles and the Sprint-IQ survey data.

Borehole positioning was calculated using the Sprint-IQ gyro survey data based on the Minimum Curvature Method, which, based on API (1985), yields the most accurate location. The three components of the location along the borehole (easting, northing, and the true vertical depth (TVD)) were calculated for the Sprint-IQ survey (10 m stations) and presented in Figure 5 and Figure 6. The borehole collar is located at Easting and Northing coordinates of 554033.97 m and 5483950.29 m, respectively, using the local UTM coordinate system (NAD83 UTM Z15N). The elevation of 435.16 masl (metres above sea level) represents the ground surface based on the CGVD2013 vertical datum. The final true vertical depth of the borehole, calculated using the measured actual orientation of the borehole and the final depth based on the retrieved core, is 883.36 mbgs (Golder, 2020a). Figure 6 shows the borehole deviating 104.5 m to the West and 39.8 m to the South from the planned end location.

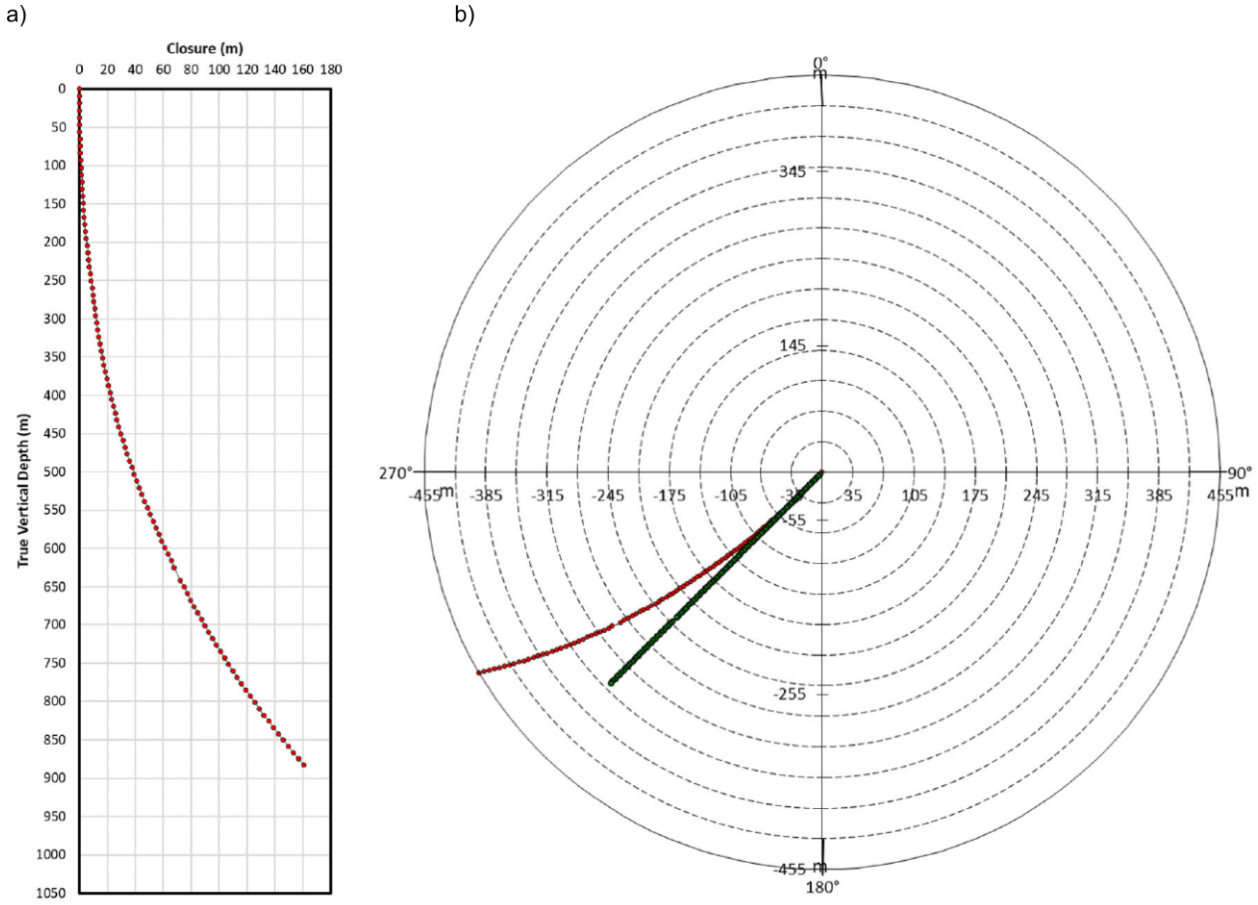


Figure 6: a) Borehole deviation presented as the total borehole closure versus true vertical depth; and b) bullseye plot showing the planned borehole trajectory (black) compared to the final SPRINT-IQ™ survey trajectory (red).

3 INTEGRATED GEOLOGICAL INTERPRETATION

The following section presents an integrated geological interpretation for IG_BH02 using the data collected during both geological core (WP03) and geophysical (WP05) logging activities, as well as relevant data from the laboratory analyses of core samples. The data sources and terminology used in order to develop the geological interpretation presented herein are described first in Section 3.1. The lithological interpretation, including final lithology and alteration logs is presented in Sections 3.2.1 and 3.2.2, respectively, resulting in the development of an integrated rock unit model described in Section 3.2.3. A structural interpretation is presented in Section 3.2.4, resulting in a structural unit model, described in Section 3.2.5, and a description of identified high fracture frequency intervals in Section 3.2.6.

3.1 Data Used for Geological Interpretation

The bedrock lithology, alteration, and structural features were logged continuously over a total borehole length of 1000.41 m (Golder, 2020b). This initial analysis was largely based on visual inspection of the core to describe the unique rock and alteration types, as well as associated characteristics including texture, fabric, and grain size. Variations in bedrock radiometric components were evaluated with the use of a handheld gamma-ray spectrometer, measured once per three metre core run, to help distinguish between the various granitoid phases encountered.

Structural features in the borehole were initially collected by geological core logging to evaluate unique structure types, mineral infillings, and other associated characteristics. Orientations of the logged structures were initially measured relative to an arbitrary reference line drawn along the length of the core axis.

Following completion of the drilling and logging activities, continuous borehole geophysical logs were acquired and the results from some of these logs were used to enhance the analysis of lithology, alteration, and structure (Golder, 2020b). The orientations of logged structures based on arbitrary references lines were corrected through analysis of the continuous downhole optical and acoustic televiewer surveys, following the method described in Appendix C.

Geological core logging data determined to be relevant to geological interpretation include the following, as presented in the geological and geotechnical core logging (WP03) report (Golder, 2020b):

- Lithology
    - Rock Class & Rock Type
    - Rock Fabric
    - Textures (Igneous, Metamorphic)
    - Grain Size (Ground Mass, Phenocryst/Porphyroblast)
    - Defining Minerals
    - Colours & Intensity
- Alteration
    - State
    - Mineral Assemblage
- Weathering
    - State
- Structure
    - Position Along Borehole
    - Type
    - Broken/Intact/Partially Intact
    - Sub-Type
    - Infilling or Defining Mineral Details
    - Rock Wall Strength

- Shape
- Roughness
- Dip and Dip Direction
- Alpha, Beta, Gamma, and Delta Angles
- Geological Aperture
- Width (where applicable)

Note that geological aperture is an estimated measurement of the open space between two adjacent fracture surfaces determined visually during geological core logging, during interpretation of downhole televiewer logs, or during the integration of data from these two sources. For our purposes, geological apertures are estimated values only because there are multiple possible sources of uncertainty in how a reported aperture value relates to the true aperture of a fracture identified as broken. There are uncertainties related to measurement inaccuracy, including where the opening is very small, where the opposing fracture planes are not parallel or fit poorly together, or due to limits in televiewer resolution. In addition, effects due to drilling or decompression may create or enhance the visible open space identified as aperture. Finally, aperture measured in core or on a borehole wall is only a local aperture that is not necessarily representative over the entire fracture.

To further enhance the bedrock lithology, alteration, and structure along the length of the borehole, the following geophysical log results were determined to be most relevant:

- Optical Televiewer
- Acoustic Televiewer
- Natural Gamma
- Spectral Gamma
- Gamma-Gamma Density
- Neutron

All geophysical logging results are summarized in a separate geophysical logging report (Golder, 2020c). Prior to interpreting the geophysical log responses associated with lithologies from the borehole, minor positional adjustments were made to the geophysical log data to match log responses to key lithological markers identified in geological core logging, such as amphibolites, which produce strong anomalies in density and neutron logs. Positional adjustments, when made, were typically less than 10 cm.

To further increase the lithological understanding of IG_BH02, 26 core samples were collected for whole-rock major and trace element lithogeochemistry; qualitative thin section analysis was also performed on 22 of the 26 samples. Core samples were crushed, sieved, and separated for three different analyses. A portion of each sample was subjected to a lithium metaborate/tetraborate fusion, with the resulting bead digested in a weak nitric acid solution. Analyses were carried out by inductively coupled plasma optical emission spectrometry (ICP-OES) and inductively coupled plasma mass spectrometry (ICP-MS). The second portion of each sample was subjected to multi-acid digestion and analysis by ICP-MS and the third portion was sent for Instrumental Neutron Activation Analysis (INAA). Results from these analyses are integrated below to present a final interpretation of the lithological and alteration characteristics of IG_BH02. The lithogeochemical data are included in Appendix B.

3.1.1 Terminology

Several terms are introduced throughout this section to aid in describing the integration process. This includes:

Rock Unit	-	A borehole length comprising a dominant rock type and/or a combination of rock types (and, if applicable, alteration and weathering types) that are considered distinct from adjacent parts of the borehole. A minimum unit thickness of five (5) m is used herein to define each rock unit. Each rock unit is uniquely labelled and can be repeated with a sub-label at different positions along borehole if appropriate.
Structural Unit	-	A borehole length comprising a relatively uniform per metre fracture frequency that is distinct from adjacent parts of the borehole. Each structural unit is uniquely labelled and can be repeated with a sublabel at different positions along borehole if appropriate.
Rock Type	-	A rock having a unique, identifiable set of characteristics.
High Fracture Frequency Interval	-	A cluster of fractures (i.e., faults, joints and or veins) that exceeds a minimum relative fracture frequency threshold along a distinct borehole length.

3.2 Geological Results

This section presents the results from the integration of the geological core logging (WP03) and geophysical logging (WP05) datasets along with integration of the results from an additional 26 samples selected for petrographic and lithogeochemical analysis. Through the process of data integration, a total of nine distinct rock types are identified for IG_BH02 (Table 2). A final log of lithology is presented which shows their distribution along the length of the borehole (Figure 7).

3.2.1 Lithological Interpretation

The main rock type intersected by borehole IG_BH02 is a biotite granodiorite-tonalite. Additional, subordinate, rock types identified in IG_BH02 include a tonalitic endmember of the main rock type (biotite tonalite), distinct metre-scale packages of amphibolite, and several suites of sub-metre thick dykes of varying felsic composition (Table 2). A total of 997.70 m of core was recovered, starting at 2.71 m along borehole (Golder, 2020b). This final interpretation of the rock types encountered in IG_BH02, shown in Figure 7, presents an updated understanding relative to the information that was initially reported in the WP03 data report (Golder, 2020b).

Table 2: Summary of Rock Types Encountered in IG_BH02

Rock Type	Texture	Fabric	Grain Size (mm)	Total Logged Length (m)	% of Recovered Core
Biotite granodiorite-tonalite	Equigranular	Massive to weakly foliated	0.1-5	954.42	95.7
Feldspar-phyric tonalite dyke	Porphyritic	Foliated to massive	<0.5* 1-3.5**	24.01	2.4
Amphibolite	Xenoblastic to inequigranular	Foliated	0.1-1	5.95	0.6
Aphanitic tonalite dyke	Equigranular	Foliated	<1	4.22	0.4
Aplite dyke	Equigranular	Massive	<1	3.01	0.3
Biotite granodiorite-tonalite dyke	Equigranular	Massive	0.1-5	2.42	0.2
Quartz dyke	Equigranular	Massive	<1	2.29	<0.2
Biotite tonalite	Equigranular	Massive	0.1-3	0.46	<0.1
Pegmatite dyke	Inequigranular	Massive	5-50	0.92	<0.1

**Groundmass **Phenocrysts*

A short summary of this evolution of understanding is included along with the lithological descriptions below that summarize the main characteristics of the rock types identified in IG_BH02.

Main Rock Type: Biotite granodiorite-tonalite

The bedrock intersected by IG_BH02 is dominated by a medium-grained granitoid rock with biotite as the primary mafic mineral. This granitoid rock represents a total of 95.7 % of the recovered core. The general consistency in character of the recovered core with the bedrock identified on the ground surface indicates that the biotite granodiorite-tonalite encountered in IG_BH02 is part of the same granodiorite-tonalite bedrock unit that was mapped at ground surface in the vicinity of the borehole (Golder and PGW, 2017). A total of 349 measurements were collected from a hand-held gamma ray spectrometer in the biotite granodiorite-tonalite during core logging, and the results are:

- Potassium content ranges from 0.2 – 1.0 % with an average of 0.71 %
- Uranium content ranges from 0 – 4.1 parts per million (ppm) with an average of 0.58 ppm
- Thorium content ranges from 0.3 – 29 ppm with an average of 3.49 ppm

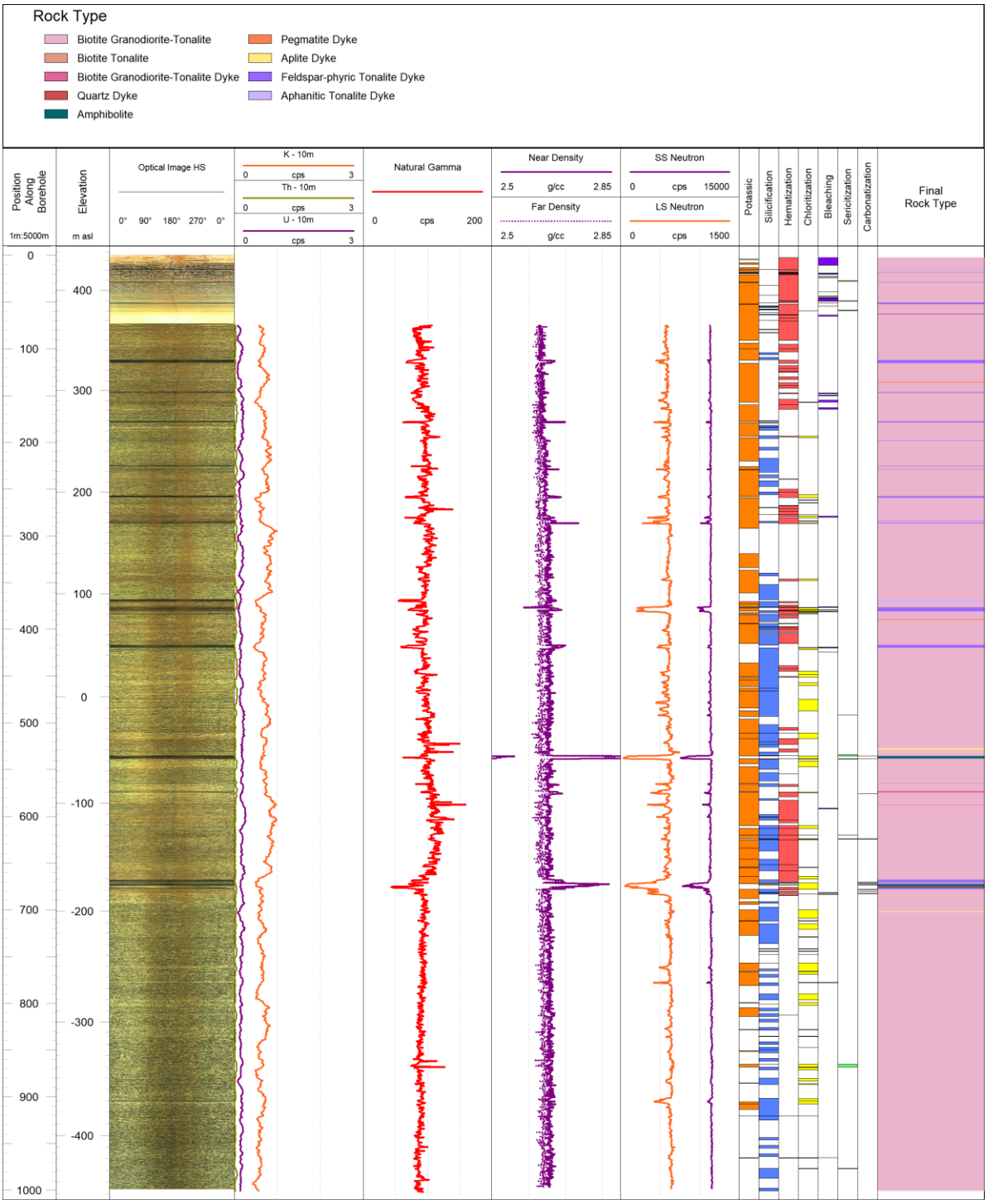


Figure 7: Input datasets used to derive a final lithology log. From left: optical televiewer log, four suites of continuous geophysical logs that aid in distinction of rock types, logged alteration (by type), and final lithology log. Due to the low spectral gamma counts, K, U and Th were evaluated using a 10 m window, resulting in a smoothing of their profiles.

Lithogeochemistry and petrography results from IG_BH02 indicate that the main rock type identified during geological core logging exhibits a range in composition that spreads across the tonalite to granodiorite boundary on a Quartz, Alkali feldspar, Plagioclase (QAP) ternary diagram (modal mineralogy) and plutonic rock classification diagram (lithogeochemistry). The lithogeochemistry data for samples from IG_BH02 support this interpretation (Figure 8 and Figure 9). The lithogeochemical data and modal mineral composition of the samples, determined semi-quantitatively using polished thin sections, is presented in Appendix B.

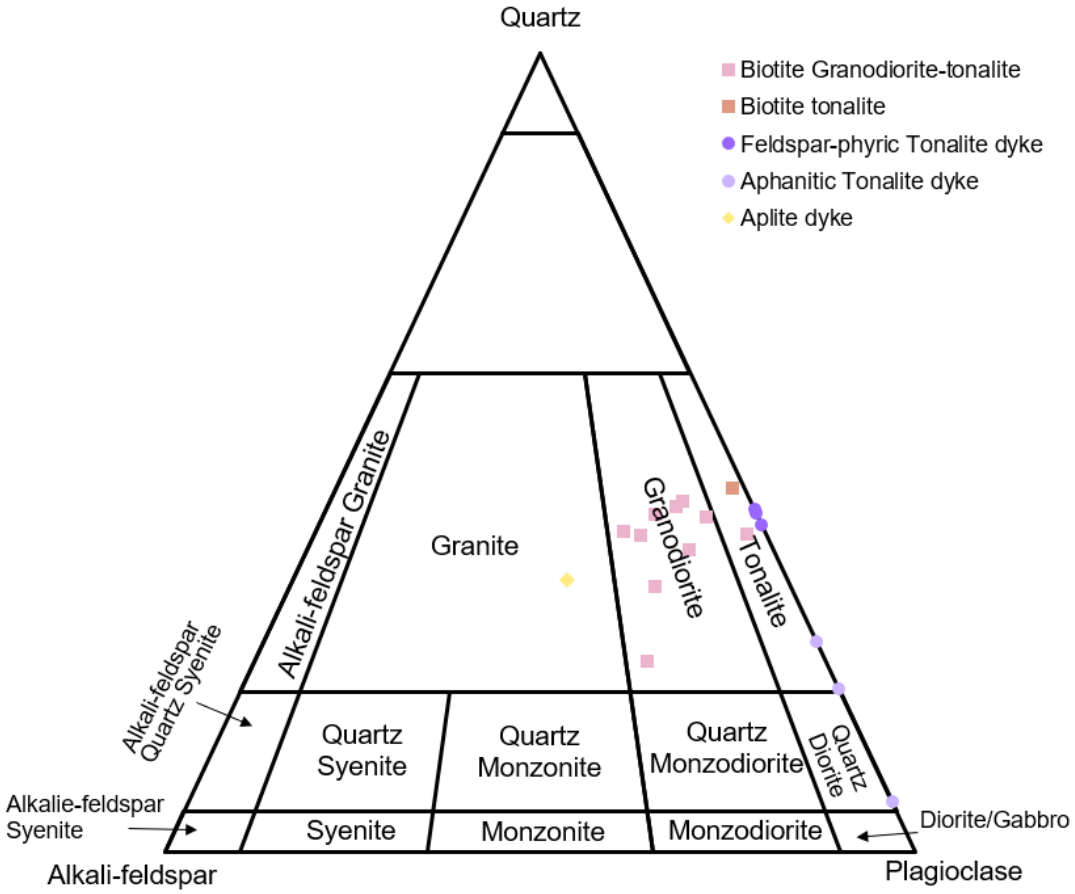


Figure 8: Classification/nomenclature of felsic granitoid phases according to the normalized modal mineral content (Quartz + Alkali-feldspar + Plagioclase = 100 Vol%) as determined from investigation of 18 samples taken for lithogeochemical analysis. Average modal mineralogy for each sample was determined semi-quantitatively using polished thin sections and plotted on a simplified ternary Streckeisen diagram after Le Bas and Streckeisen (1991).

The biotite granodiorite-tonalite unit is light to medium white-grey and mainly equigranular with mineral size tending towards the upper range of medium-grained (0.1-5.0 mm average) for all mineral phases (Figure 10). Its main mineral phases are quartz, plagioclase, potassium feldspar, and biotite, with the latter comprising 1-4.5 % of the matrix. This rock is predominantly massive although a weak biotite-defined foliation is locally apparent. There were 10 biotite granodiorite-tonalite samples from IG_BH02 sent for optical petrography, and they plot across the tonalite to granodiorite field on the QAP diagram (after Le Bas and Streckeisen, 1991; Figure 8) Modal mineralogy was determined using a known scale grid and visually determining area coverage of visible minerals in the polished thin section. Fifteen samples were sent for bulk lithogeochemical analysis and the major oxides demonstrate a felsic composition (Table 3) and plot across the

tonalite to granodiorite fields on the plutonic rock classification diagram (after Debon and Le Fort, 1983; Figure 9).

Table 3: Summary average of major oxides in the rock types of IG_BH02. Note that only 5 rock types were sampled for lithogeochemical analysis and there are no results for pegmatite, quartz, and biotite granodiorite-tonalite dykes. Aphanitic and Feldspar-phyric tonalite dykes are combined as they are compositionally the same.

Rock Type	Major Oxide Composition (average, %)									
	SiO_2	Al_2O_3	Fe_2O_3	MnO	MgO	CaO	Na_2O	K_2O	TiO_2	P_2O_5
Biotite granodiorite-tonalite	72.48	14.30	1.8	0.03	0.36	1.79	4.75	2.88	0.17	0.04
Biotite tonalite	72.59	14.75	2.59	0.05	0.55	2.63	4.68	1.75	0.25	0.06
Amphibolite	49.06	13.13	8.71	0.15	7.87	10.48	2.73	2.14	0.76	0.33
Aphanitic and Feldspar-phyric tonalite dykes	71.71	14.20	2.68	0.04	0.63	2.59	4.49	1.78	0.28	0.09
Aplite dyke	75.41	13.45	1.2	0.02	0.16	1.11	4.47	3.76	0.08	0.02

An endmember of the biotite granodiorite-tonalite unit was identified in IG_BH01 (NWMO and Golder, 2020) based on intervals of reduced grain size and increased biotite content. Petrographic and lithogeochemical analyses revealed these intervals were tonalitic in composition and this rock type was renamed *biotite tonalite*. One 0.46 m interval of biotite tonalite was logged in IG_BH02 and it plots in the tonalite field (Figure 8 and Figure 9). The biotite tonalite is medium to dark grey and equigranular with mineral size tending towards the lower range of medium grained (0.1-2.5 mm average; Figure 11). The biotite tonalite unit exhibits an equigranular and massive fabric. The main mineral phases are quartz, plagioclase, and biotite, with the latter comprising 4.5 % of the matrix.

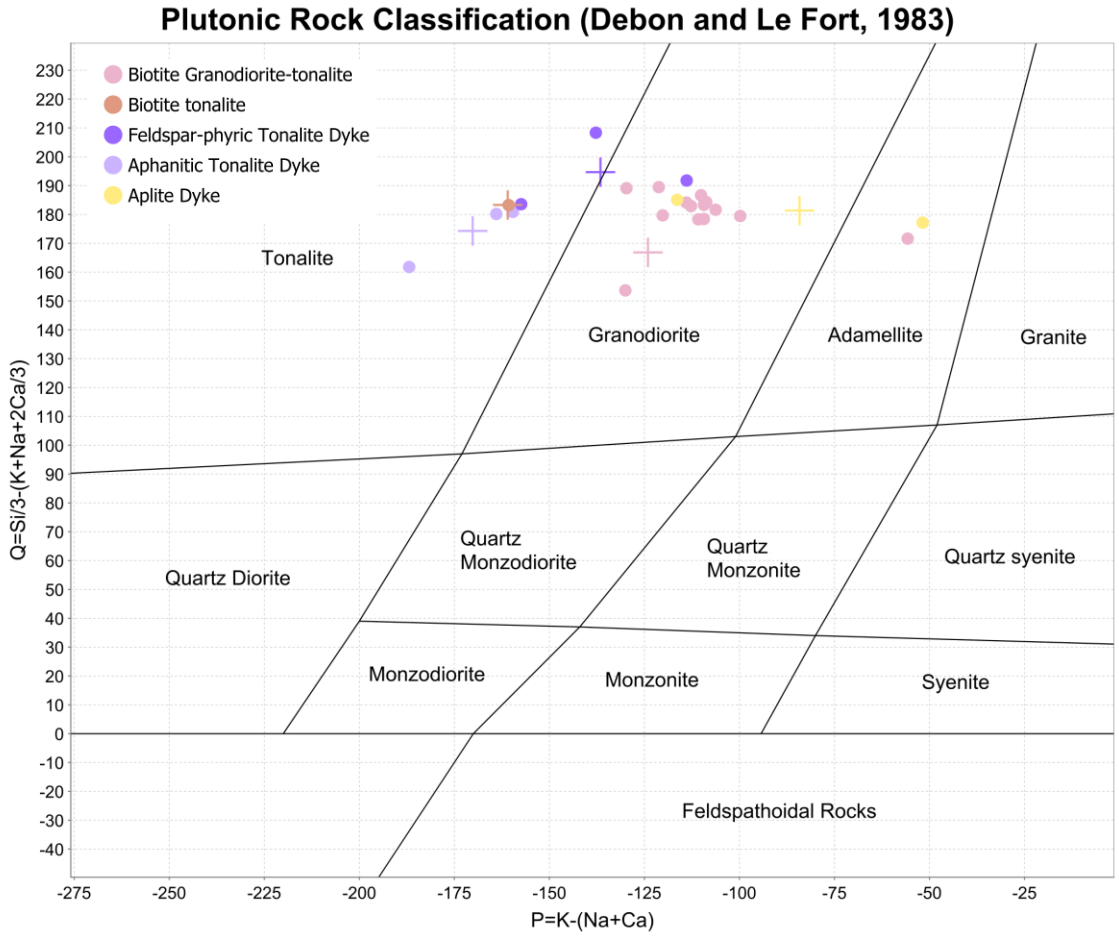


Figure 9: Plutonic Rock Classification (Debon and Le Fort, 1983). Diagram axes correspond to proportions of K-feldspar and plagioclase to quartz. P is calculated from (K-(Na+Ca)) and Q is calculated from ((Si/3) – (K+Na+(2*Ca)/3)). Parameters calculated as oxide percentages converted to millications. Crosses show the mean composition for each rock type.

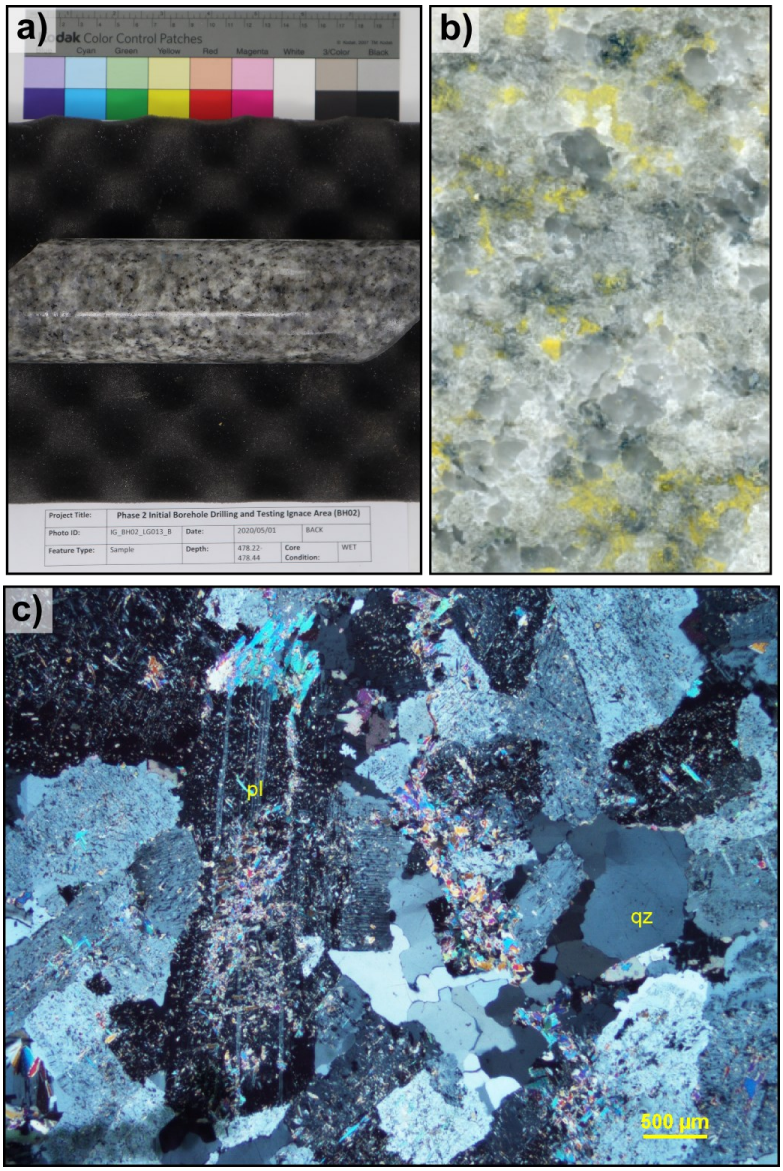


Figure 10: Representative example of biotite granodiorite-tonalite (sample IG_BH02_LG013). a) Core sample photograph. b) Billet photograph showing yellow staining of potassium feldspar (billet size is 25 x 40 mm). c) Thin section photomicrograph with rock-forming minerals plagioclase (pl) and quartz (qz). Sericite (white mica) alteration can be seen in plagioclase crystals; crossed polarizers transmitted light.

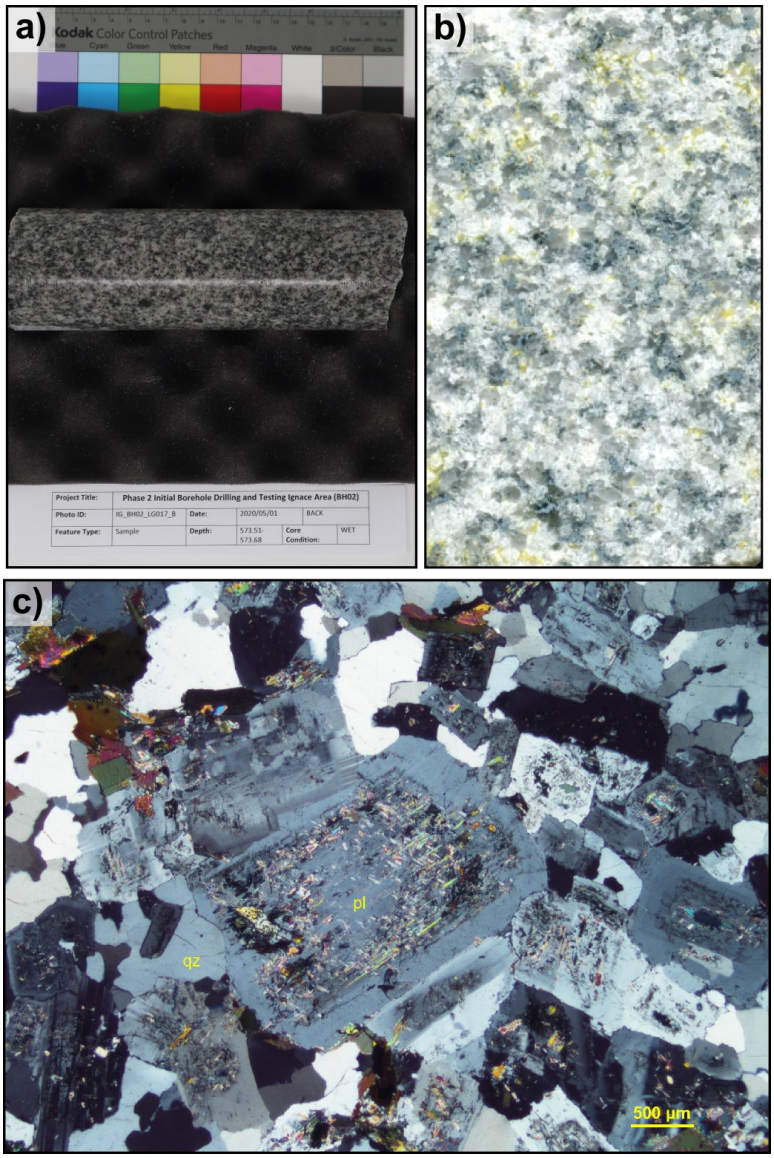


Figure 11: Representative example of biotite tonalite (sample IG_BH02_LG017). a) Core sample photograph. b) Billet photograph showing very minor yellow staining of potassium feldspar (billet size is 25 x 40 mm). c) Thin section photomicrograph with rock-forming minerals plagioclase (pl) and quartz (qz). Sericite (white mica) alteration can be seen in cores of plagioclase crystals; crossed polarizers transmitted light.

Subordinate Rock Types

In IG_BH02, the subordinate rock types encountered (amphibolite, aphanitic tonalite dykes, feldspar-phyric tonalite dykes, aplite dykes, quartz dykes, pegmatite dykes, and biotite granodiorite-tonalite dykes) represent a combined total of 4.3 % (43.28 m) of the recovered core (Table 2).

Amphibolite: Five occurrences of amphibolite were logged in IG_BH02, accounting for 5.95 m (0.6 %) of the total recovered core (Table 2). It is unclear whether the amphibolite units are dykes or xenoliths from the surrounding greenstone belts, or a combination, because primary contact relationships such as chilled margins are obscured by penetrative deformation localized along the amphibolite contacts. Based on the mineral assemblage and evidence of low-grade metamorphism, they will be referred to as *amphibolites* in this report and this term will be refined as more information is received from future boreholes and testing. The amphibolites range in width from 0.07 m to 2.83 m. All amphibolite occurrences were observed below 535 m along borehole (Figure

7). The identified amphibolites consistently exhibit sharp increases in density values and decreases in neutron values relative to the host biotite granodiorite-tonalite. Amphibolites are dark grey-green, equigranular, and usually fine-grained (<1 mm; Figure 12). The mineral assemblages include plagioclase (albite), tremolite/actinolite, biotite, chlorite, and epidote, +/- titanite, calcite, quartz, and iron oxides.

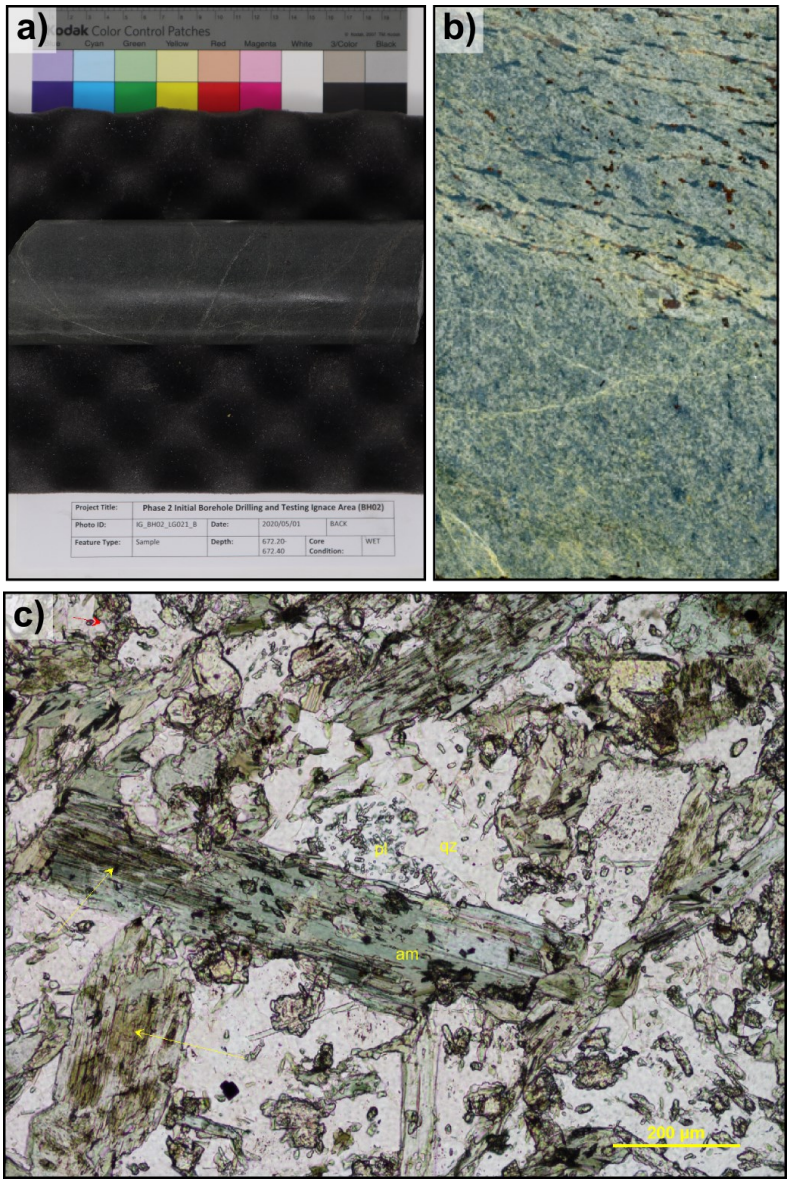


Figure 12: Representative examples of amphibolite (sample IG_BH02_LG021). a) Core sample photograph. b) Billet photograph (billet size is 25 x 40 mm) shows foliated and massive sections of sample. c) Thin section photomicrograph with main rock-forming minerals amphibole (am), plagioclase (pl), and quartz (qz); plane polarized transmitted light.

Lithogeochemistry shows an increase in iron and magnesium and a decrease in silica relative to the felsic units, which is expected in a mafic unit (Table 3). The amphibolites exhibit a well-defined foliation and sharp contacts; half of the contacts are broken (5/10; 50 %). As will be discussed later in the summary of structural information (Section 3.2.4 below), the contacts between individual amphibolite occurrences and the adjacent biotite granodiorite-tonalite primarily dip shallowly-moderately towards the north-northwest. A decimetre- to metre-scale pink coloured alteration halo

commonly envelops the amphibolite in the surrounding biotite granodiorite-tonalite. In addition, some fracture surfaces within the amphibolites are coated by chlorite.

Aphanitic and feldspar-phyric tonalite dykes: A suite of distinct felsic dykes was logged in 27 occurrences between 15 – 685 m along borehole (Figure 7). The dykes range in width from 0.09 m to 4.51 m and have a combined total length of 28.24 m, representing 2.8 % of the recovered core (Table 2). These dykes are characteristically dark grey-black with an aphanitic matrix (Figure 13). Petrographic analysis identified the mineral composition of the dykes as quartz, plagioclase, biotite, and major oxides suggesting a felsic composition (Table 3). 22 of the occurrences also exhibit distinct, medium-grained albite phenocrysts within a matrix that is otherwise compositionally and texturally similar to the other five occurrences (Figure 14). During visual core logging, these dykes were termed felsic or feldspar-phyric felsic dykes. Petrographic and lithogeochemical analyses of six samples from this suite of felsic dykes plot almost entirely within the tonalite field on the plutonic classification diagram, with the exception of one sample that had slightly higher potassium (either due to alteration or a slight increase in alkali feldspar content; Figure 9). Based on this additional information, the names have been refined to *aphanitic tonalite* and *feldspar-phyric tonalite* dykes.

All of the aphanitic tonalite and feldspar-phyric tonalite dykes exhibit sharp contacts with the adjacent biotite granodiorite-tonalite and, in some occurrences, a well-defined foliation is also present. In thin section, this foliation is defined by the alignment of biotite and quartz. Contacts were primarily intact with few occurrences (12/54; 22 %) identified as broken. Internally, these aphanitic tonalite and feldspar-phyric tonalite dykes vary between massive and foliated. The dyke contact orientations range from shallow (11°) to steep (79°) with an average dip of 35°. Their orientations will be discussed further in Section 3.2.4.1.

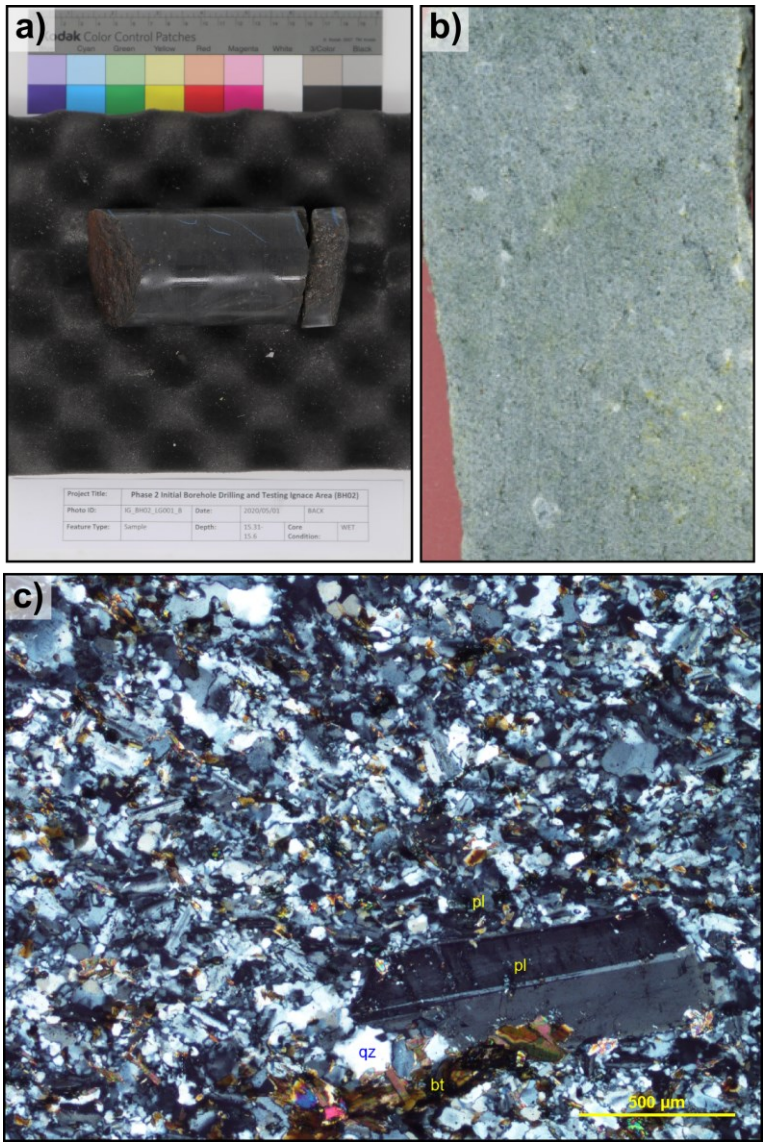


Figure 13: Representative examples of an aphanitic tonalite dyke (IG_BH02_LG001). a) Core sample photograph. b) Billet photograph showing very minor yellow staining of alkali feldspar and rare 1-2 mm phenocrysts (billet size is 25 x 40 mm). c) Thin section photomicrograph with rare 0.5-1mm plagioclase phenocrysts (pl). Plagioclase (pl) is also visible in the very fine-grained matrix, along with quartz (qz) and biotite (bt); crossed polarized transmitted light.

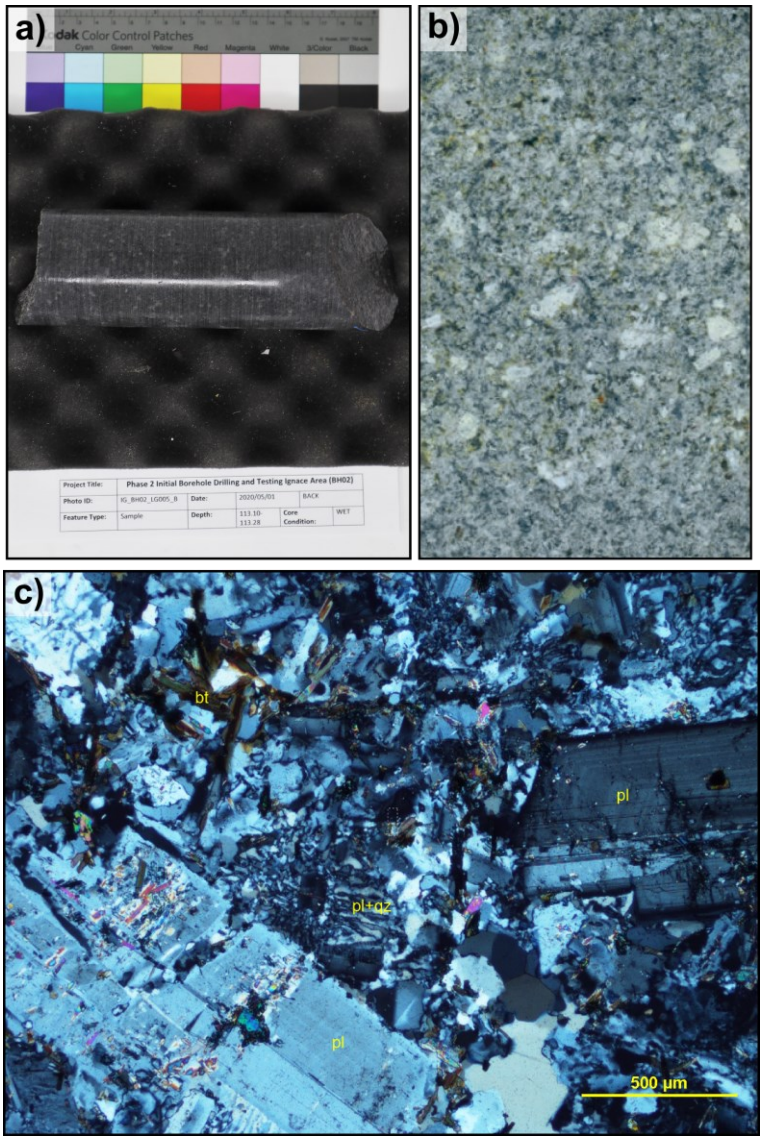


Figure 14: Representative examples of a feldspar-phyric tonalite dyke (IG_BH02_LG005). a) Core sample photograph. b) Billet photograph showing very minor yellow staining of alkali feldspar concentrated around plagioclase phenocrysts (billet size is 25 x 40 mm). c) Thin section photomicrograph with plagioclase (pl) phenocrysts in a very fine-grained matrix of plagioclase and quartz (pl + qz) and biotite (bt); crossed polarized transmitted light.

Aplite dykes: Aplite dykes, ranging in width between 0.05 m and 1.09 m, were observed in nine occurrences, and represent a combined total length of 3.01 m (0.3 %) of the recovered core (Table 2). The aplite dykes are light white-grey, equigranular and very fine-grained to aphanitic (<1 mm). The aplite dykes are granitic in composition (Figure 9 and Table 3) with main mineral phases of plagioclase, potassium feldspar, quartz and minor biotite (Figure 15). Contact between the aplite dykes and the adjacent biotite granodiorite-tonalite are consistently sharp and intact.

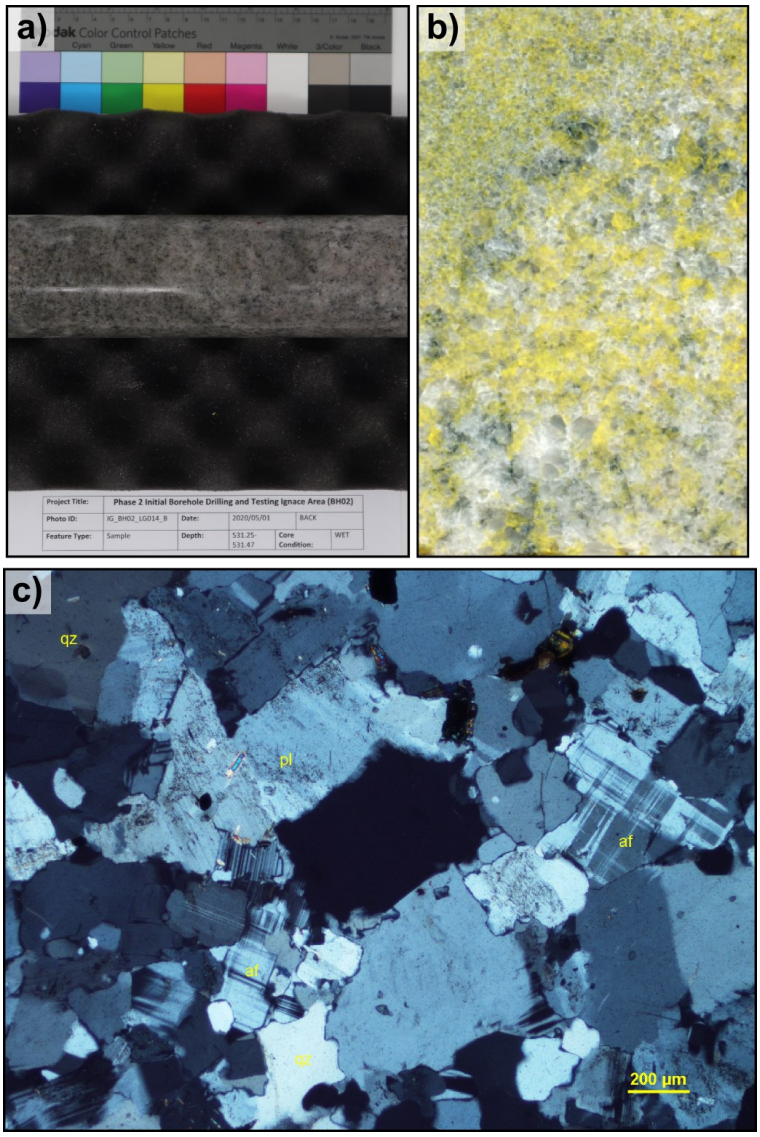


Figure 15: Representative examples of an aplite dyke (IG_BH02_LG014). a) Core sample photograph. b) Billet photograph yellow staining of alkali feldspar and increasing grain size toward contact with biotite granodiorite-tonalite (billet size is 25 x 40 mm). c) Thin section photomicrograph with major rock forming minerals alkali feldspar (af), plagioclase (pl), and quartz (qz). Note the relatively fresh look of the minerals compared to the host biotite granodiorite-tonalite, indicative of a later-stage intrusion; crossed polarized transmitted light.

Pegmatite Dykes: Pegmatite dykes, ranging in width from 0.05 m to 0.18 m, were observed in nine occurrences and represent a combined total length of 0.92 m (<0.1 %) of the recovered core (Table 2). Pegmatite dykes are mostly found in the upper 500 m of the borehole (Figure 7). These dykes are light grey-pink, massive, and inequigranular with distinct, very coarse-grained (5-10 mm), square-edged, K-feldspar crystals within a fine- to medium-grained (<1-5 mm) matrix of quartz and plagioclase. The pegmatite dykes exhibit sharp contacts with the adjacent granodiorite-tonalite, 17 of 18 contacts (94 %) were logged as intact.

Biotite granodiorite-tonalite dykes: Three biotite granodiorite-tonalite dykes, with widths between 0.1 m and 1.84 m and representing a total of 2.42 m (0.2 %) of total recovered core (Table 2), were observed in the recovered core at 413, 573, and 587 m along borehole (Figure 7). These

occurrences are identified as dykes herein as they appear to crosscut the main bedrock units. This interpretation will continue to be assessed as additional information becomes available. These dykes are light grey-off white, massive to weakly foliated, equigranular, and fine-grained (<1 mm), with a similar composition to the main biotite granodiorite-tonalite. The dykes exhibit sharp and consistently intact contacts with the adjacent biotite granodiorite-tonalite.

Quartz dykes: Five quartz dykes, with widths of 0.07 m and 1.19 m for a total of 2.29 m (representing 0.2 % of total recovered core; Table 2), were observed in the recovered core primarily clustered at 62 and 675 m along borehole (Figure 7). These dykes are white, massive and appear coarse-grained (> 5 mm) when individual quartz crystals can be discerned. The dykes are composed almost entirely of quartz with some minor occurrences of pyrite and are likely hydrothermal veins, but the current geological core logging procedure is to identify anything over 5 cm as a dyke or separate rock type and anything under 5 cm as a vein. This approach will be re-evaluated for future boreholes, but for consistency in this report these larger quartz bodies will be referred to as dykes.

Summary of rare-earth element data

Rare-earth element (REE) data, collected as part of the lithogeochemistry analysis, are plotted for all rock units with the exception of the pegmatite, quartz, and biotite granodiorite-tonalite dykes (Figure 16). Concentrations (expressed as logarithm to the base 10 of the value) of REE (shown on the x-axis, by atomic number) in these samples are normalized to a reference Chondrite standard. The chondrite-normalized pattern of the biotite granodiorite-tonalite, biotite tonalite, and feldspar-phyric and aphanitic tonalite dykes are steeply fractionated [average $(La/Yb)_{22}$ = 47.8] with significant depletion of heavy rare-earth elements [HREE; average $(Gd/Er)_{22}$ = 3.6]. IG_BH02 samples plot with other Neoarchean low-HREE granitoids of the tonalite-trondhjemite-granodiorite (TTG) suite, which carry a basaltic crust signature (Halla, 2018 and references therein). The origin of low-HREE TTGs is thought to be high-pressure melting of deep, thick oceanic crust during subduction. One reason for a depletion of HREE is residual garnets are retaining the HREE in the source basalt (Halla et al., 2009). The amphibolites are less steeply fractionated [average $(La/Yb)_2$ = 27.3] with significant depletion of HREE [average $(Gd/Er)_2$ = 3.1]. The aplite dykes demonstrate the least fractionation of the analyzed rock types [average $(La/Yb)_2$ = 24.7] and negative europium anomalies, suggesting they are from a later stage, evolved granite source. The similar pattern of all rock types (with the exception of the aplite dykes) indicates a common magmatic source. This suggests that the amphibolites may represent mafic dykes that intruded into the granodiorite-tonalite synchronous with either granitoid emplacement or regional deformation.

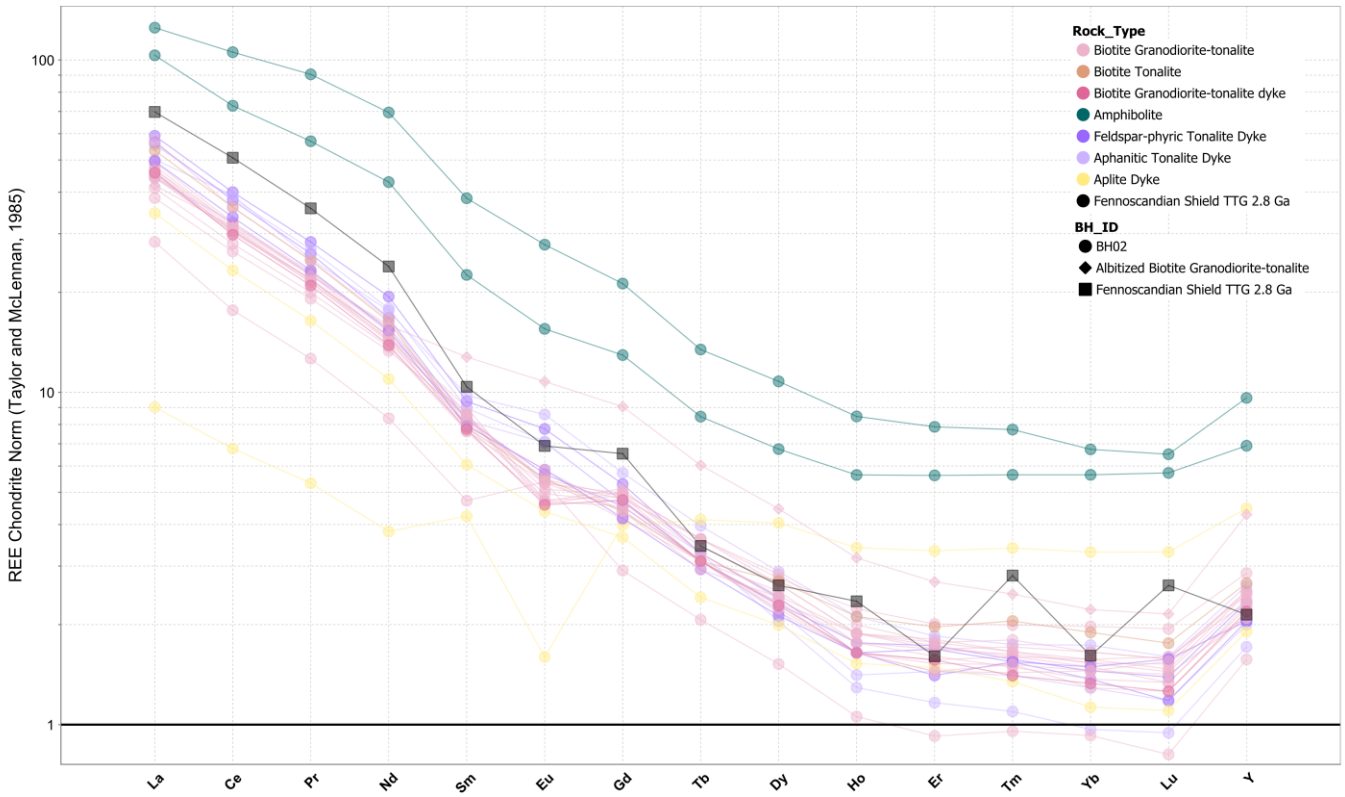


Figure 16: Chondrite-normalized rare-earth element (REE) plot (after Taylor and McLennan, 1985) of rock types from IG_BH02 and a representative average of 2.8 Ga low-heavy REE (HREE) tonalite-trondhjemite-granodiorite (TTG) from the Fennoscandian shield (black squares; Halla, 2018). Y-axis shows concentrations (expressed as logarithm to the base 10 of the value) of REE (x-axis, by atomic number) in IG_BH02 samples normalized to a reference Chondrite standard. REE patterns of biotite granodiorite-tonalite, aphanitic tonalite dykes, and feldspar-phyric tonalite dykes demonstrate steep fractionation and significant depletion of HREE. Aplite dykes demonstrate a less steep fractionation and negative europium anomalies, suggesting they from are from a later stage, evolved granite source. The biotite granodiorite-tonalite sample represented by pink diamonds is an altered (albitized) sample.

Summary of geophysical characteristics of the identified rock types

A suite of geophysical logs, including natural gamma, spectral gamma, gamma-gamma density and neutron are widely used both for identifying rock types and delineating contacts (e.g., Keys, 1997). Such subtle boundaries could reflect sharp or gradational changes in mineralogical composition, such that any variability not observed in the initial stage of geological core logging could be identified by assessment in comparison with these geophysical logs (Figure 17). The discussion below describes each of these geophysical logs to characterize the bedrock, in general, and applies this information to evaluate the specific rock types encountered in the borehole. A summary table of mean geophysical responses for each logged rock type is included in Table 4.

Table 4: Mean geophysical response values for each logged rock type.

Rock Type *(N=number of points)*	Natural Gamma (cps)	Neutron* (cps)	Density** (g/cm^3)	K (cps)	Th (cps)	U (cps)
Amphibolite (N=119)	79.77	72.34	2.80	0.59	0.03	0.17
Aphanitic tonalite dyke (N=71)	64.60	554.42	2.66	0.55	0.05	0.16
Aplite Dyke (N=59)	118.61	668.98	2.64	0.66	0.04	0.17
Biotite Granodiorite-Tonalite (N=17622)	95.34	605.90	2.64	0.69	0.04	0.17
Biotite Granodiorite-Tonalite Dyke (N=48)	108.23	452.86	2.66	0.79	0.05	0.20
Biotite Tonalite (N=9)	85.48	446.40	2.64	0.76	0.04	0.20
Feldspar-phyric Tonalite Dyke (N=415)	75.15	409.65	2.67	0.59	0.03	0.14
Pegmatite Dyke (N=17)	105.00	577.84	2.64	0.62	0.05	0.16
Quartz Dyke (N=41)	54.56	207.14	2.69	0.59	0.05	0.15

** long spacing neutron sensor values are presented.*
*** mean gamma-gamma density values, from near and far measurements, are presented.*

The natural gamma log quantifies the amount of radioactive isotopes occurring naturally within the bedrock. However, it does not identify the radioisotopes responsible. Results from the spectral gamma log can be useful to differentiate the relative amount of potassium, uranium and thorium (herein presented in counts per second, cps). Although data from natural gamma and spectral gamma logs do not correlate directly to specific rock types, their relative variabilities along the length of the borehole are used to assess mineralogical variation that indicate the change from one rock type to the next.

Data measured from both the gamma-gamma density and neutron logs were used to quantify petrophysical properties of the bedrock (e.g., bulk rock density), and were correlated to specific rock types. Measurement of these logs are, however, sensitive to variations in pore space in the bedrock. The gamma-gamma log measures the backscatter and attenuation of gamma photons emitted at a near and far sensors from the logging gamma source where the measured response is converted to bulk density through calibration prior to recording data.

The neutron log uses a neutron source and detector to measure the relative neutron counts in the bedrock along the borehole wall. Most neutron interactions can be inversely related to hydrogen ion concentrations in the bedrock, such that, responses can be generally related to water content or porosity of the bedrock (e.g., Daniels et al., 1984; Keys, 1997). In some instances, neutron counts can be influenced by relative changes in bedrock mineralogy, primarily the presence of hydrous minerals (e.g., biotite, amphiboles, and chlorite).

Electrical resistivity, single point resistance, and induction logs can be used as a diagnostic tool to interpret rock types and contacts; however, in this borehole there is no indication of changes associated with varying rock types. Evidence suggests that discrete variations in electrical resistivity or single point resistance may be largely correlated to the presence of fractures (e.g., fracture frequency) and particularly fractures with measured geological aperture or secondary porosity (e.g., fracture porosity).

Description of borehole geophysical data acquisition and processing are detailed in Golder (2020c). For this report, data underwent additional positional corrections, and for this analysis the data have been exported at a uniform spacing of 5 cm along the length of the borehole from bottom of casing to end of borehole. Continuously measured natural gamma, spectral gamma, neutron (long-spacing sensor), and density responses are presented in Figure 7 and were used to highlight variations in physical bedrock properties along the borehole. By comparing the laboratory reported wet density

values from 18 samples to the continuous geophysical density logs, it was determined that the geophysical logs, on average, overestimated the density values for the borehole by approximately 5 percent. A correction factor was determined by averaging the differences between each laboratory measurement and the field measurement at the corresponding position, for both the near and far density logs (see Appendix C). The geophysical density logs were corrected using the correction factor to reduce the geophysical log values by 5 percent (i.e., $DENSITY_{corrected} = DENSITY_{measured} / 1.05$), making the profile consistent with the measured laboratory values. A similar correction factor has been applied to the geophysical logs for boreholes IG_BH01 and IG_BH03, each of which required a correction factor of approximately 3 percent. For this analysis, a mean density profile was calculated based on the average of the corrected near and far density values along the length of the borehole.

The biotite granodiorite-tonalite phase represents the majority of the measured geophysical response values (see Figure 7 and Table 4) and can be attributed as the base-line values for the bedrock. Any deviations away from this response tend to be associated with various factors, including changes in rock type and associated mineralogy, presence of fractures and associated infillings, and/or presence of alteration types and associated intensities.

The distributions of natural gamma, density, and neutron responses present observable differences in the geophysical responses between each rock type. As shown in Figure 17, a suite of felsic dykes (aplite, biotite granodiorite-tonalite, and pegmatite dykes) present a subtle increase in natural gamma relative to the biotite granodiorite-tonalite. Conversely, the amphibolite, feldspar-phyric tonalite dykes, aphanitic tonalite dykes, and quartz dykes present a slight reduction in natural gamma response. Overall, natural gamma, neutron, and density distributions shown in Figure 17 display considerable similarities between all felsic rocks, with the exception of the quartz dykes. The quartz dykes show a slight reduction in measured natural gamma radiation and a significant reduction in neutron counts with respect to the other felsic rock types (Table 4 and Figure 17). The overall spectral gamma log response (potassium, uranium and thorium) for the entire borehole suggests that the rock types encountered are generally depleted in these radioactive isotopes and show a fairly consistent response for all rock types.

The amphibolite occurrences in the borehole present a characteristic reduction in neutron counts and an increase in bulk density relative to the biotite granodiorite-tonalite. The increased bulk density of amphibolites can be directly related to the presence of tremolite-actinolite which is a relatively dense mineral, especially in comparison to the main mineral phases comprising the felsic units (i.e., plagioclase, alkali feldspar, and quartz). The reduced neutron counts of the amphibolites can possibly be associated with an increase in apparent primary porosity. However, it is more likely related to secondary (e.g., fracture) porosity or the hydrous nature of their mineral assemblage (e.g., chlorite, amphibole).

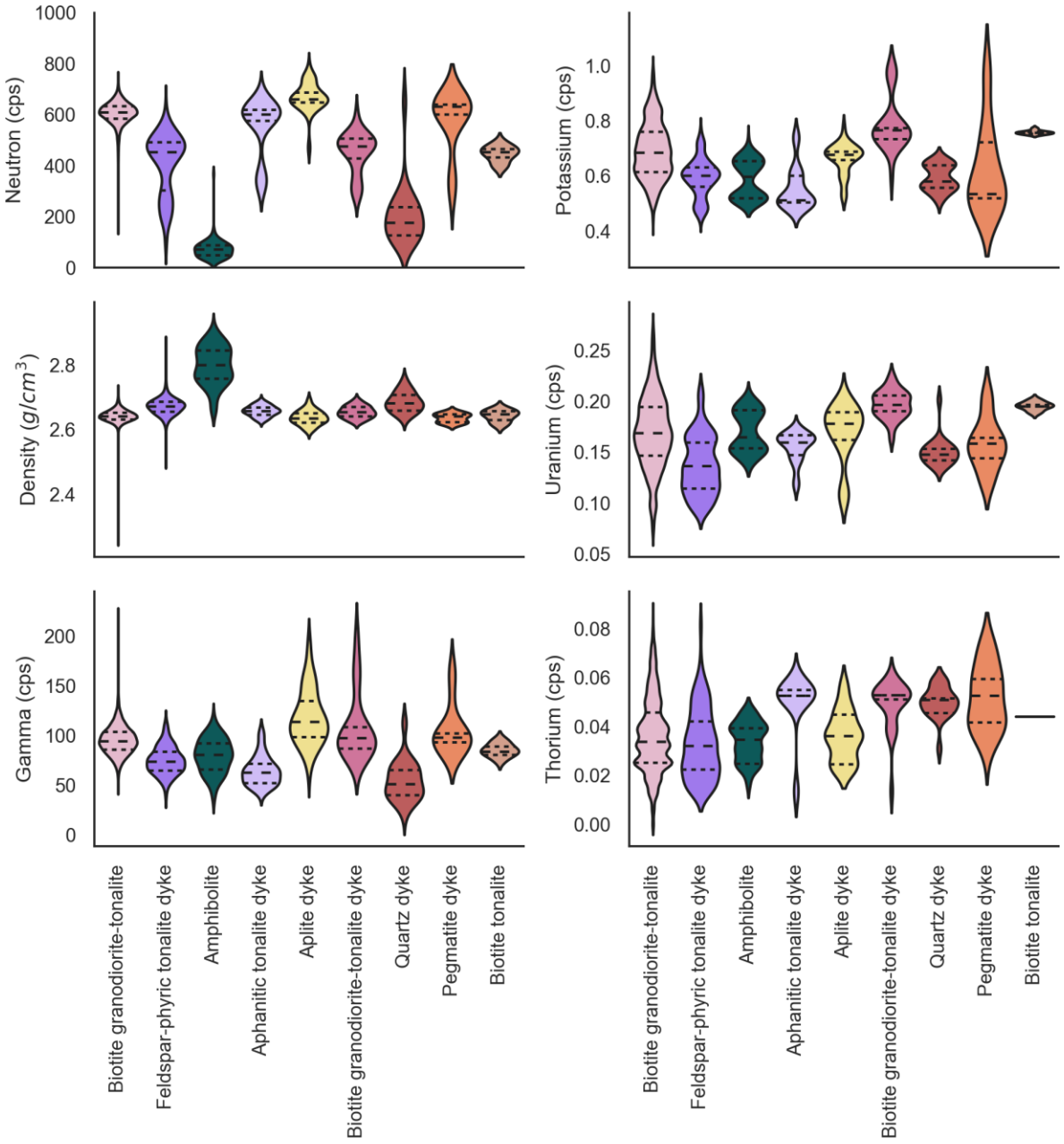


Figure 17: Violin plots show the distribution of geophysical log responses associated with the logged rock types. Each violin shows the distribution of the data values with the median (thick dashed line), and quartiles (thin dashed lines) marked. Rock types are ordered based on total data counts from left to right in each graph.

The distribution of Neutron, Density, Natural Gamma and Potassium values are presented in Figure 18 showing the cross-correlation between the selected geophysical log data and corresponding rock types. Scattered data points are plotted for the entire length of the borehole at 5 cm intervals. The larger data points represent mean centroid values of the geophysical responses and the error bars represent the standard deviation.

Overall, the distributions of biotite granodiorite-tonalite, biotite tonalite, pegmatite, feldspar-phyric tonalite dykes, and aphanitic tonalite dykes largely overlap making distinguishing between them using geophysical comparison plots alone difficult. However, the quartz dykes are characterized by a reduced neutron count and a slight increase in bulk density values which is apparent in Figure 18. In addition, the amphibolites are uniquely characterized by low neutron counts, and high bulk densities and can be distinguished from the other felsic units in all cross-plots (Figure 18). Density values for the amphibolites consistently exceed 2.75 g/cm^3.

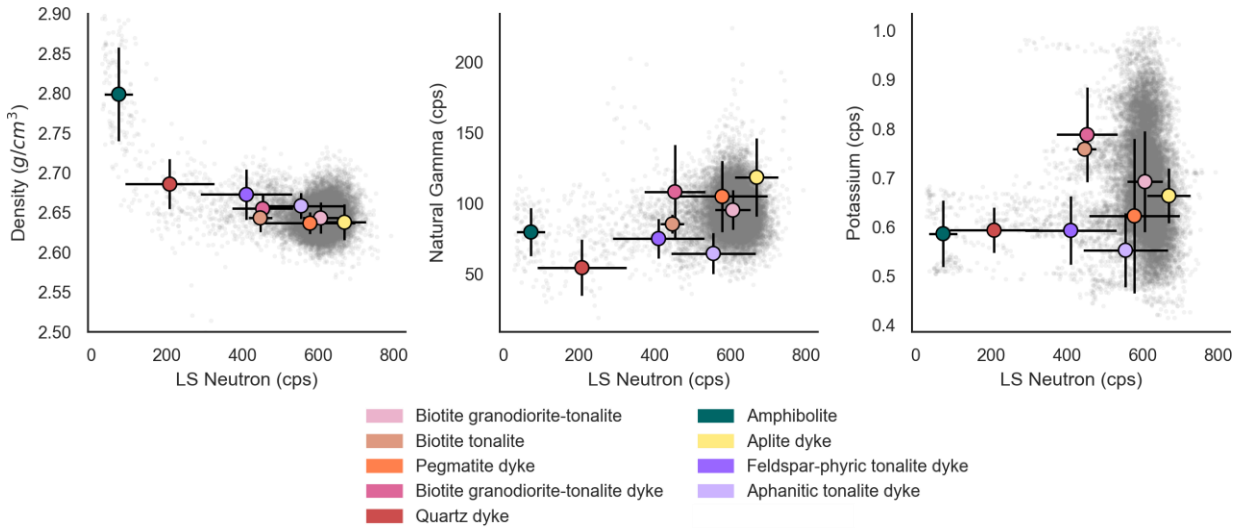


Figure 18: Cross plots showing correlations between neutron, density, natural gamma and potassium count values of all rock types encountered in IG_BH02. Colored points represent mean values of the geophysical responses and the error bars represent standard deviation.

3.2.2 Alteration Interpretation

Seven alteration types were logged in IG_BH02 with a combined total length of 1523.9 m. Because multiple alteration assemblages could be logged in the same interval, the sum of total logged alteration is greater than the length of the borehole. The alteration types logged, in order of prevalence, were: potassic alteration, silicification, hematization, chloritization, bleaching, carbonatization, and sericitization. The distribution of each alteration type is shown in the final alteration log (Figure 19). Descriptions of each alteration type are included in Table 5, and hand sample and thin section examples are shown in Figure 20. Detailed descriptions of alteration types observed during geological core logging are also included in the IG_BH02 WP03 report (Golder, 2020b).

During geological core logging, 748.5 m of the recovered core was assigned as slightly altered (A2), where the alteration is generally confined to fractures with little or no penetration beyond the fracture plane. 326.2 m was assigned as moderately altered (A3), where alteration may penetrate into the wall rock and create an envelope or halo of alteration around a fracture plane. 18.77 m was assigned as highly altered (A4), where alteration is pervasive along the borehole length.

Table 5: Summary of alteration assemblages observed in IG_BH02 during geological core logging. Note that because multiple alteration assemblages could be logged in the same interval, the sum of total alteration logged is greater than the length of the borehole.

Alteration Type	Total length (m) of logged core	Position along Borehole Association	Hand Sample Description	Associated secondary alterations
Potassic	639.2 m	Throughout borehole, limited below 800 m	Pink colour; individual occurrences range from hairline to tens of metres	All
Silicification	417.6 m	Spread throughout borehole, increase below 350 m	Grey discolouration and reduction in clarity of grain boundaries (esp. quartz); occurrences range from hairline to tens of metres	All but sericitization
Hematization	303.3 m	Predominantly above 700 m	Red, brown, or rusty staining of rock or coating around mineral grains; occurrences range from hairline to tens of metres	Bleaching, chloritization, potassic, silicification
Chloritization	123.0 m	Spread throughout borehole; increase below 350 m	Appearance of green chlorite; occurrences range from hairline to 12 m. Associated with dykes and amphibolite.	Potassic, carbonatization, sericitization, silicification, hematization
Bleaching	21.6 m	Predominantly above 200 m	Whitening of the altered rock mass; occurrences range from hairline to 7.3 m	Chloritization, hematization
Carbonatization	12.0 m	Between 530 – 685 m	Off-white colour, formation of carbonate minerals (calcite), mainly associated with amphibolite; occurrences range from hairline to 5.9 m	Chloritization (as primary alteration type)
Sericitization	7.2 m	Clusters between 27 – 60 m, 491 – 625 m, and 865 – 978 m	White to grey colour; occurrences range from hairline to 3.1 m	Potassic, carbonatization, hematization

Eleven samples sent for optical petrography and lithogeochemical analysis from IG_BH02 specifically targeted logged alteration assemblages. Ten of the samples exhibited weak alteration of the rock mass with moderate alteration to some individual minerals. One sample (IG_BH02_LG023) was identified as strongly albitized. The section of IG_BH02 where this sample comes from, 679 – 683.25 m, is the locus of strongest alteration observed in the borehole. The interval of strongly-albitized biotite granodiorite-tonalite indicates alkali metasomatism occurred, but sodium was more mobile than potassium.

In some intervals of biotite granodiorite-tonalite, hematite was found to partially replace magnetite grains (Figure 20b). These intervals were originally identified as potassic alteration during geological core logging; none of the intervals logged with potassic alteration show evidence of true hydrothermal potassic alteration (secondary alkali feldspar, biotite, sulphides) when examined petrographically. The pink colour is a product of magmatic (primary) alkali feldspar or replacement of very fine-grained sulphides or magnetite by iron oxides. These iron oxides (e.g., hematite) stain the surrounding crystals red, causing the entire interval to look pink.

Two intervals with alteration logged as bleaching showed weak to moderate alteration of plagioclase by white mica with some associated chlorite and epidote (Figure 20i-j). This suggests that what is being called bleaching during geological core logging is actually the alteration of plagioclase feldspar to white mica (sericite) causing a whitening of the grains and, therefore, the overall rock. Based on petrographic analysis, all plagioclase feldspar grains record some degree of sericitization (white mica), often associated with chloritization of biotite +/- epidote. This white mica

alteration was present in the aphanitic and feldspar-phyric tonalite dykes as well as the biotite 0granodiorite-tonalite rock mass, suggesting it is a result of hydrothermal alteration that took place after, or contemporaneous to, emplacement of all rock types (with the exception of the later-stage aplite dykes).

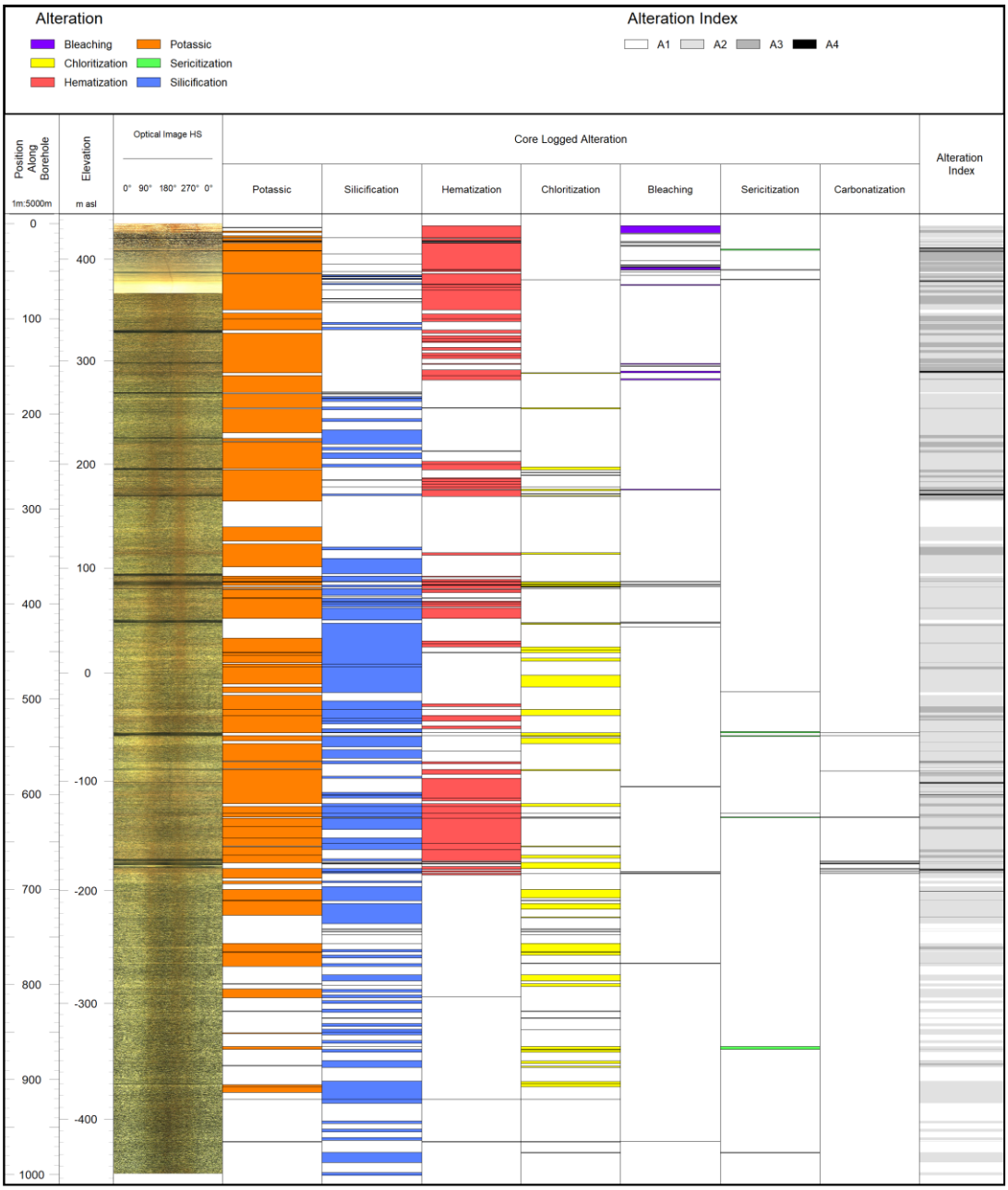


Figure 19: Alteration types and distribution along the borehole based on geological core logging and analysis of the optical televiewer log resulting in a final alteration log. A2 indicates intervals with slight alteration, A3 indicates intervals with moderate alteration, and A4 indicates intervals where alteration is pervasive along the borehole length.

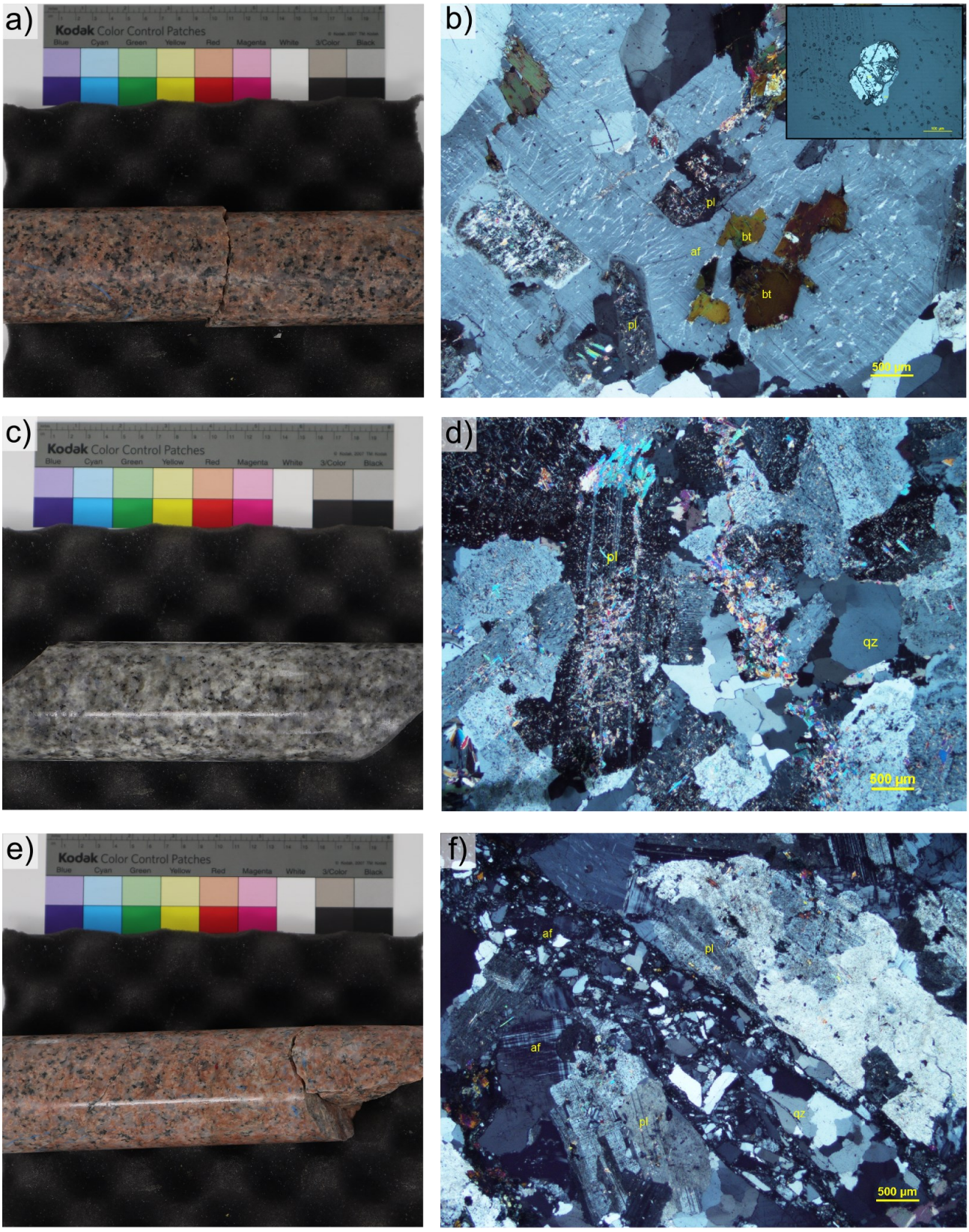


Figure continued on next page…

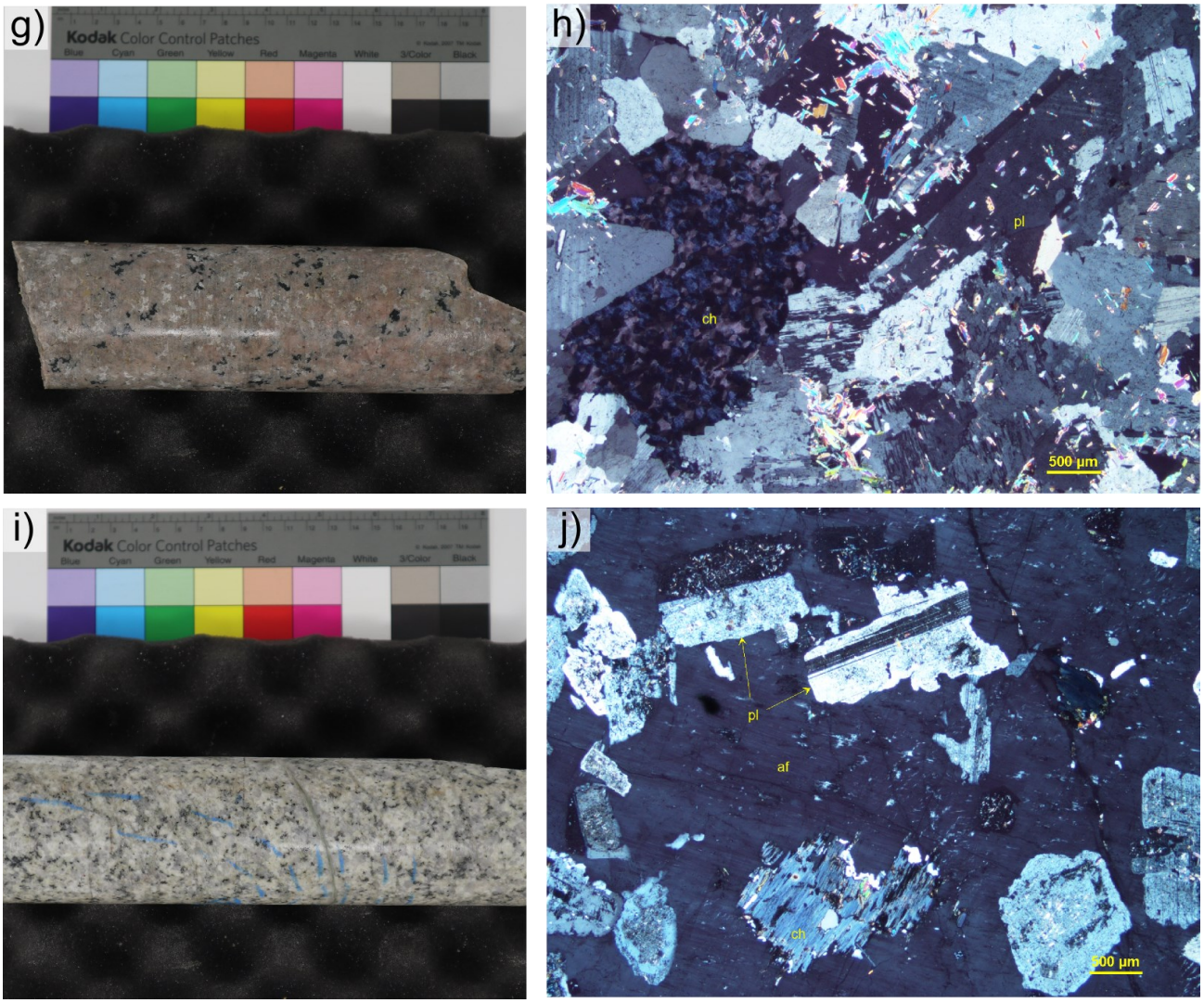


Figure 20: Common alteration assemblages logged in IG_BH02. a) Sample IG_BH02_LG009, biotite granodiorite-tonalite logged with potassic and hematite alteration. b) Photomicrograph of sample IG_BH02_LG009 showing plagioclase crystals (pl) heavily altered by white mica, biotite (bt) weakly altered by chlorite, alkali feldspar (af), and quartz. The inset shows a magnetite crystal replaced by hematite and rutile occurring within quartz; crossed-polarized transmitted light. c) Sample IG_BH02_LG013, biotite granodiorite-tonalite logged as silicified. d) Sample IG_BH02_LG013 showing quartz grains (qz), and plagioclase (pl) heavily altered by white mica; crossed-polarized transmitted light. e) Sample IG_BH02_LG018, biotite granodiorite-tonalite logged as potassic alteration. f) Sample IG_BH02_LG018 showing plagioclase (pl) moderately altered by clay and epidote, fresh alkali feldspar (af), and quartz (qz). Minor biotite that is strongly altered to chlorite is also visible. This thin section shows an irregular veinlet of quartz and alkali feldspar that is interpreted to have formed due to fluid overpressure at the end of magmatic crystallization (i.e., the alkali feldspar is primary and not a result of alteration); crossed-polarized transmitted light. g) Sample IG_BH02_LG023, albite-rich alteration zone (albitite). This is the strongest alteration observed in IG_BH02. h) Sample IG_BH02_LG023 showing plagioclase (pl), fine-grained Fe-chlorite (ch), and calcite occupying interstitial positions between the plagioclase grains. The abundance of plagioclase in association with typical alteration minerals (chlorite and calcite) is evidence that this sample is strongly altered; crossed-polarized transmitted light. i) Sample IG_BH02_LG025, chlorite-altered biotite granodiorite-tonalite. j) Sample IG_BH02_LG025 showing plagioclase weakly altered to white mica (pl), magmatic biotite intensely altered by Fe-chlorite (ch), and fresh alkali feldspar (af); crossed-polarized transmitted light.

3.2.3 Rock Unit Classification

Rock units (RU) are defined primarily on the dominant rock type encountered within the borehole and the degree of subordinate rock types encountered in the interval. The core logged rock types, combined with key continuous geophysical datasets, were used to distinguish distinct rock types within each RU and define the top and bottom interval positions. Using the available datasets, three RUs are defined within the borehole (Figure 21).

Rock Unit 1 (RU1) extends from the ground surface (0 m) to a position along borehole of 535.14 m. This interval predominantly consists of biotite granodiorite-tonalite (505.28 m, 94.5 % of the interval), with aphanitic and feldspar-phyric tonalite, quartz, pegmatite, and aplite dykes making up the remaining 5.5%. The majority of the subordinate rock type in this RU consists of feldspar-phyric and aphanitic tonalite dykes, which accounts for 16.94 m of logged core as 22 individual dyke occurrences. Twelve of the 22 occurrences are not associated with any visible alteration or structure and have clean, sharp contacts with the biotite granodiorite-tonalite. The other ten occurrences are associated with pink alteration (logged as potassic but likely hematite, see section 3.2.2) and three dykes are also associated with silicification. One dyke at 62.89 m is associated with quartz dykes and one at 371.18 m is associated with pegmatite dykes; the other 20 dykes contact the biotite granodiorite-tonalite directly. One dyke at 376.34 m is overprinted by brittle deformation (breccia, hematite infill, and logged faults). The orientation of the aphanitic and feldspar-phyric dyke contacts in RU1 are inconsistent, ranging from gently to steeply-inclined and dipping broadly towards the north-northeast to the south-southeast (41/44 contacts have dip azimuths between 0 – 180°). By comparison to rock units in other boreholes, RU1 has the highest amount of logged feldspar-phyric tonalite dykes. Throughout RU1 the biotite granodiorite-tonalite is massive, light grey to white in colour, and predominantly medium-grained. The majority of the hematite alteration and bleaching is recorded in this interval, in addition to well-distributed “potassic” (potentially sericitization + weak hematization) alteration and silicification. With the exception of the upper ~80 m of the borehole, where casing is installed, the density, gamma and neutron logs exhibit relatively uniform profiles through this unit.

Rock Unit 2 (RU2) is 143.14 m long extending from 535.14 m to 678.28 m along borehole and was primarily defined based on the presence of amphibolite units. This RU is composed primarily of medium-grained, massive, biotite granodiorite-tonalite and biotite tonalite phase making up 89.87 % of the interval (128.55 m). The subordinate rock types make up the remaining 10.13 % of the interval comprising five amphibolites, feldspar-phyric, pegmatite, aplite, and biotite granodiorite-tonalite dykes. The differentiating feature of this RU is the increased presence of the discrete amphibolite units, consisting of 4.41 % (6.31 m) of the rock unit. The amphibolites are dark green to grey in colour, fine-grained, and massive to strongly foliated. The alteration in this unit is still dominated by well-distributed “potassic” alteration, silicification, and hematite alteration. In contrast to RU1, there is a slight increase in logged chloritization and a decrease in logged bleaching. The amphibolites cluster at 535 – 575 m (two occurrences) and 671 – 676 m (three occurrences). These two zones show distinct peaks in the density log that are coincident with the logged amphibolites, and a sharp reduction in the neutron counts. Overall, the amphibolite contacts show similar geometry: gently to moderately inclined and dipping north-northwest, with logged foliation in the same orientation.

Rock Unit 3 (RU3) is 322.93 m long and extends from 678.28 m to 1000.41 m along borehole. RU3 is extremely homogeneous; ~99.5 % consists of biotite granodiorite-tonalite with a measured length of 321.04 m. The remaining ~0.5 % (1.5 m) of this rock unit is composed of a few thin occurrences of feldspar-phyric, quartz, pegmatite, and aplite dykes. Similar to the other defined rock units, the main biotite granodiorite-tonalite is predominantly medium-grained and massive. This unit has well-distributed silicification and an increase in well-distributed logged chloritization. In contrast to RU1 and RU2, logged “potassic” alteration is minor and hematization is very minor and concentrated

around the top of the interval. Dyke contacts in this interval predominantly dip to the northeast (10/14, 71 %) and range from gently to steeply inclined; the exceptions are a moderately inclined aplite dyke at 702 m that dips west and a moderately inclined pegmatite dyke at 986 m that dips south-southeast. As with RU1, the density, gamma, and neutron logs exhibit relatively uniform profiles through this unit.

Table 6 presents a summary of the final RU interpretations, classified according to the dominant rock type encountered therein. The final classification based both on the distribution of the dominant rock types identified and catalogued in the final lithology log, and summarized in the RU descriptions above, suggest that the RUs can be classified in two dominant domains, including: (1) biotite granodiorite-tonalite, and (2) biotite granodiorite-tonalite with amphibolite. Similarities observed between each of the RU descriptions, mainly dominant rock type, allow the RU intervals to be classified into common rock units. Rock units RU1 and RU3, are dominated by biotite granodiorite-tonalite, exhibit similar geophysical signatures, and are devoid of amphibolites. These two rock units are reclassified as RU1a and RU1b. RU2 represents the only interval dominated by biotite granodiorite-tonalite with the presence of amphibolite units, allowing for a singular classification as RU2.

Table 6: Summary of Classified Rock Units

Positional Range (m)	RU#	Dominant Rock Type	Classified RU
0 – 535.14 m	RU1	Biotite granodiorite-tonalite	RU1a
535.14 m to 678.28 m	RU2	Biotite granodiorite-tonalite, with amphibolite	RU2
678.28 m – 1000.41 m	RU3	Biotite granodiorite-tonalite	RU1b

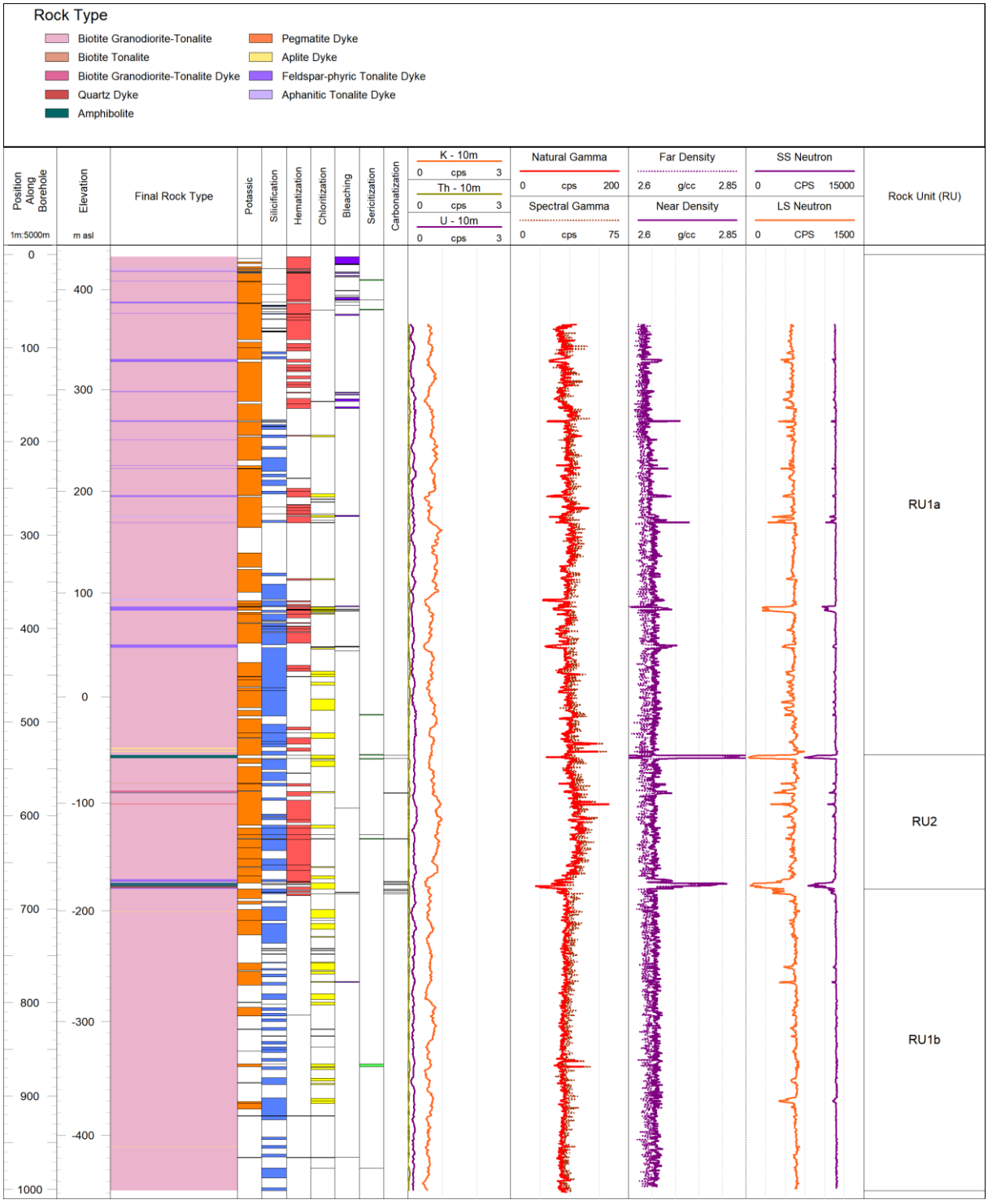


Figure 21: Summary of final logged lithology, alteration and key geophysical logs presented alongside interpreted rock units for IG_BH02. Due to the low spectral gamma counts, K, U and Th were evaluated using a 10 m window, resulting in a smoothing of their profiles.

One uncertainty associated with this initial rock unit model is the location of interpreted rock unit boundaries along the borehole. All three of the rock units are predominantly composed of biotite granodiorite-tonalite, consequently, there is no hard physical boundary that can be used to

differentiate the rock units. As described above, the boundaries are largely based on clustering of amphibolites along the length of the borehole. As a result, these rock unit boundaries have a fair amount of subjectivity embedded in their locations. Despite this uncertainty, it is likely that these rock unit subdivisions adequately parse the borehole into domains that capture the general changes in the rock types that may be important in characterizing the geosphere. It will be important to evaluate whether additional geoscientific information from the other boreholes will fit within this rock unit framework or if a different picture will emerge.

3.2.4 Structural Interpretation

A description and interpretation of bedrock structural features measured along the borehole are presented in this section. Structural measurements include both geological and geotechnical characteristics captured during geological core logging and geophysical televiewer logging, integrated together into a final structure log. The final integrated structure log contains 2570 natural features (Table 7). This total includes 103 geological contacts, 2305 planar structures, and 162 linear structures. Of the total number of natural planar features, 1294 were logged and observed only during geological core logging, 957 structures were logged both in geological core logging and televiewer logging, and 125 structures were logged and observed only by televiewer. All 162 linear structures were identified only during geological core logging when the planar surface hosting the lineation could be directly observed. An additional 578 non-natural mechanical breaks were recorded during geological core logging which have already been separated from the dataset presented below.

Table 7: Summary of structures observed in the borehole.

Structure Type	Number of Oriented Structure				Un-oriented Occurrences (Core Logged Only)	Total Structures Logged
	Core Logged Only	Both (Core and Televiewer)	Televiewer Logged Only	Total		
Joint (JN)	951	462	61	1474	20	1494
Vein (VN)	153	226	63	442	5	447
Fault (FLT)	51	112	0	163	2	165
Lineation (LIN)	162	0	0	162	0	162
Shear Zones (SHR/SHRD)	74	54	0	128	1	129
Contact (CO)	10	92	0	102	1	103
Igneous Primary Structure (IPS)	29	7	0	36	0	36
Foliation (FO)	24	1	1	26	0	26
Broken Core Zone (BCZ)	0	2 (4*)	0	2	2	4
Mylonite (Myl)	1	1	0	2	0	2
Fold Axial Surface (FAX)	1	0	0	1	0	1
Lost Core Zone (LCZ)	0	0	0	0	1	1
Total	1456	957	125	2538	32	2570

** True orientations were not assigned to two out of four broken core zones identified in both core and televiewer logging due to low confidence in tracing a single defining plane for these occurrences.*

During geological core logging, structures were oriented relative to an arbitrary reference line drawn along the length of the axis of each core run. The methodology for assigning true dip and dip direction to each logged structure, integrating the geological core logging information with the orientation information extracted from the televiewer log datasets, is presented in Appendix D.

During this process of structure integration, 2376 (99 %) of the planar features (102 lithological contacts and 2274 other planar structures) were oriented and assigned true dip and dip direction. The remaining 32 un-oriented structures could not be assigned a true dip or dip direction as a result of being located within sections of the core that could not be corrected with the televiewer information. Oriented structural data are plotted by structure type and shown on equal area, lower-hemisphere stereographic projections (stereonets) throughout this section. Table 7 provides a summary of the results from the integration, presented by unique structure type.

Borehole trajectory will directly influence the under-representation of certain orientations of planar structures (e.g., Terzaghi, 1965). IG_BH02, which was drilled at an inclination of -70° towards an azimuth of 225°, will mostly under-represent vertical structures that strike SW-NE and structures that strike NW-SE and dip parallel to the borehole plunge. To acknowledge this bias and begin to explore the implications of it, the presentation below includes Terzaghi-weighted contoured pole densities along with the unweighted data for all planar structures except for oriented lithological contacts. The legend associated with each of the weighted stereonets indicates the number of features expected based on the Terzaghi weighting. The minimum bias angle applied for this analysis, using the software DIPS© (Version 7) by Rocscience, is 15°, giving a maximum weight of 3.86. A summary of orientation information for all 2274 naturally occurring, oriented, planar structures (excluding lithological contacts) is presented in Figure 22. In comparing the unweighted and Terzaghi-weighted contours (Figure 23), it is clear that the latter emphasizes the pole clusters of steeper dipping structures oriented at a low angle to the core axis, and de-emphasizes the gently dipping structures oriented at a high angle to the core axis.

More recently, advanced procedures for addressing orientation bias have been reported in the literature (e.g., Davy et al., 2006). However, such alternative approaches require not yet available information such as fracture size-distribution for each orientation set. The use of such methods will be made possible, and justified, as additional borehole and surface structural information become available.

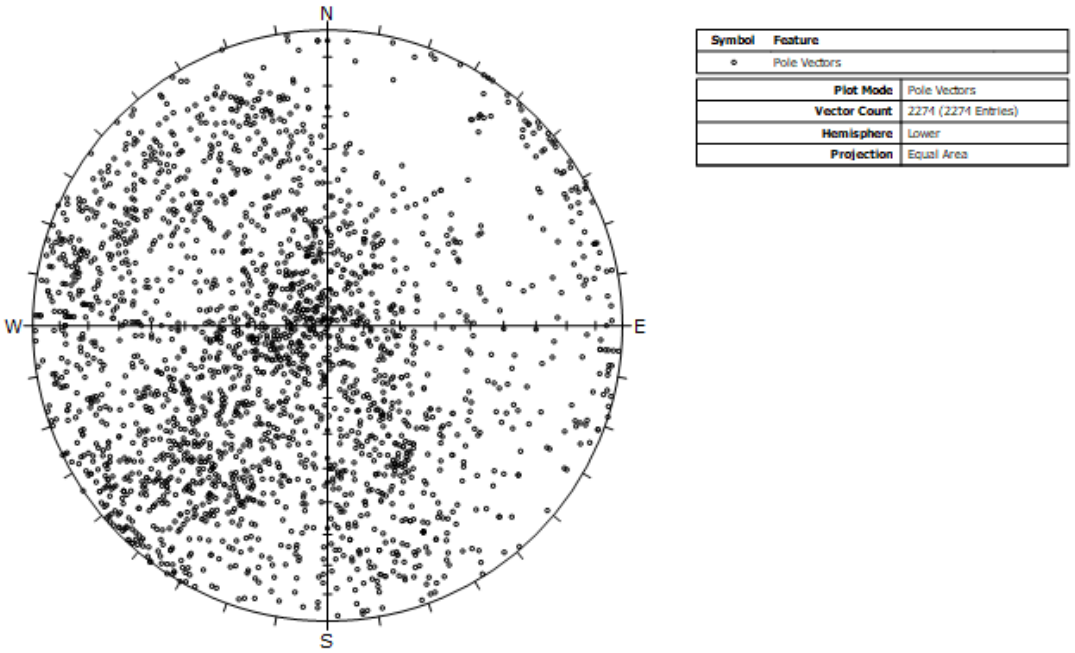


Figure 22: Equal Area Lower Hemisphere Projections (stereonets) showing poles to planar structural measurements, unweighted (n = 2274).

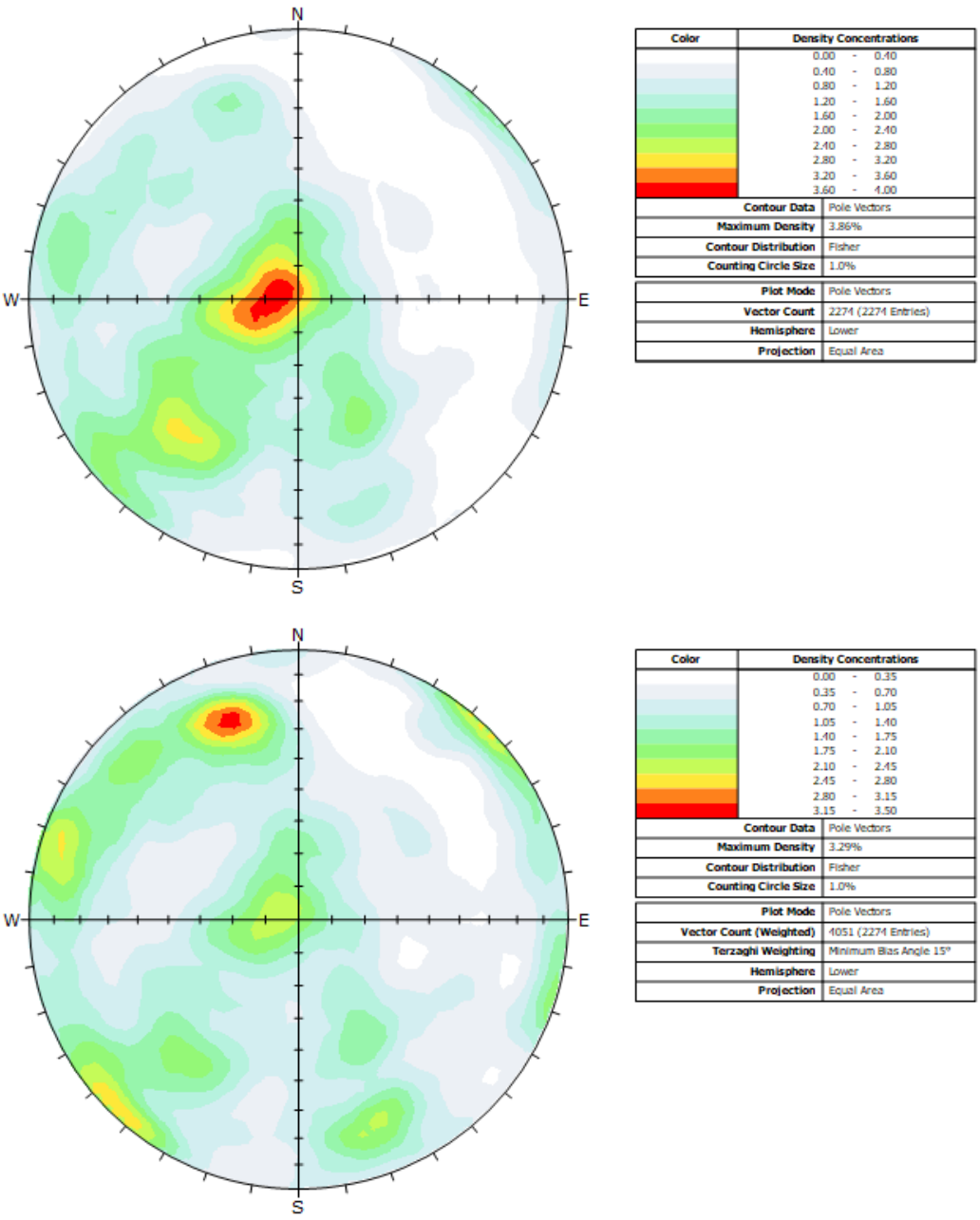


Figure 23: Equal Area Lower Hemisphere Projections (stereonets) showing a summary of the poles for planar structural measurements. Top: all data – contours, unweighted (n = 2274). Bottom: all data – contours, Terzaghi-weighted (n = 4051).

3.2.4.1 Structures

The structural information presented below includes discussion of features logged as igneous primary structures, contacts, ductile structures, brittle structures (including joints, veins and faults), and linear structures.

Igneous Primary Structures

Igneous primary structures (IPS) include features interpreted to have originated with the formation or emplacement of the igneous rock, including igneous flow foliation and igneous layering. For IG_BH02, a total of 36 igneous primary structures were identified. These features are generally characterized by sharp to gradational changes in grain size or concentration of the main rock-forming minerals in the granodiorite-tonalite bedrock, including biotite, quartz, or plagioclase. All occurrences were intact in the core and all occurrences were successfully oriented. The thicknesses of the igneous primary structures range from sub-mm-scale to a maximum of 8 mm. One example of igneous primary layering, identified by a subtle variation in biotite content, is shown in Figure 24a. Some of the igneous primary structures identified may instead be mafic schlieren. The true nature of all features logged as igneous primary structures will continue to be assessed as additional information becomes available. Figure 25 presents the stereographic projection of all igneous primary structures. The majority of poles define planes that dip moderately towards the southeast and moderately to gently towards the south.

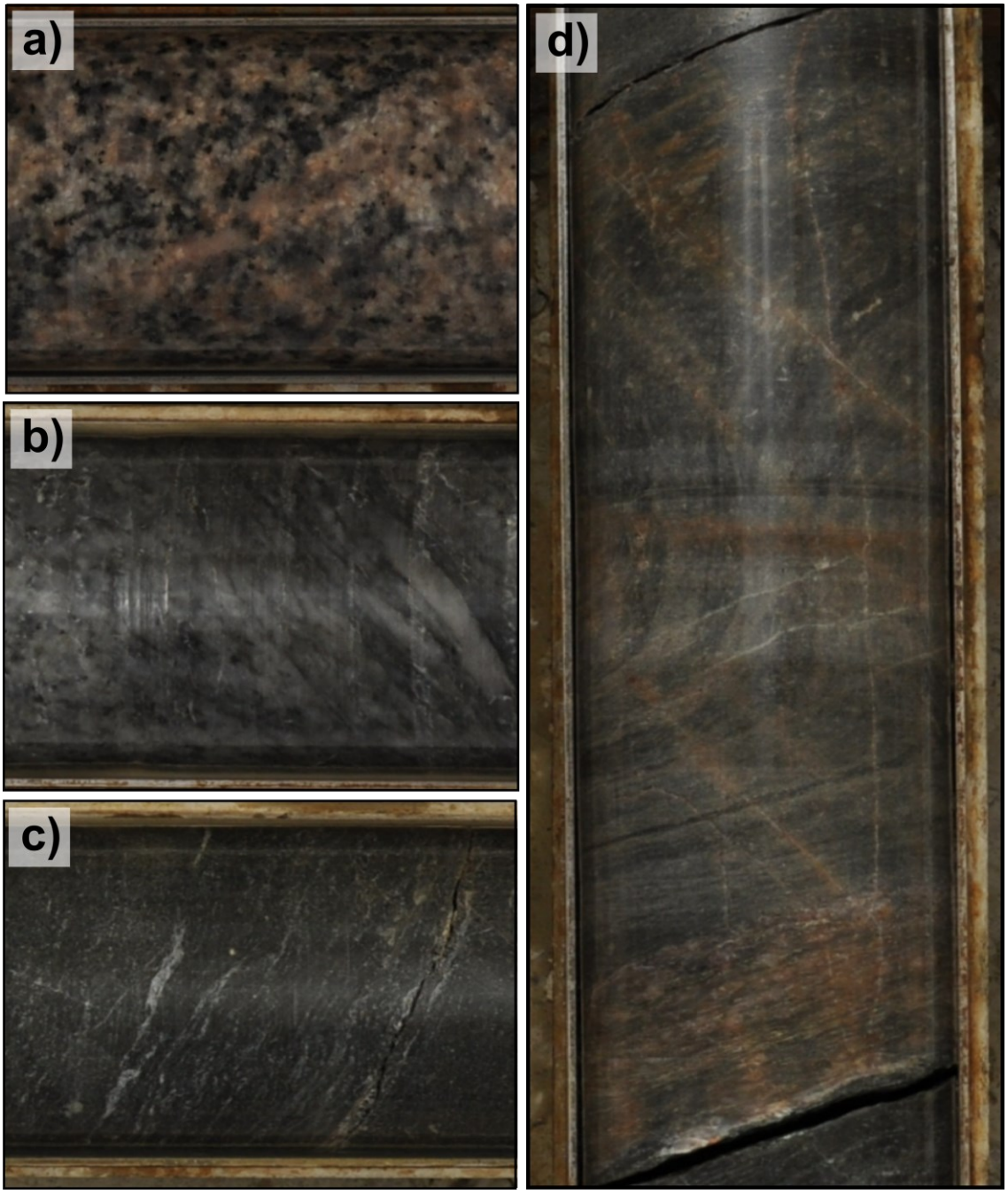


Figure 24: Examples of primary igneous and ductile structure. a) Subtle variation in biotite content (from top left to bottom right) defining a primary igneous layering, in biotite granodiorite-tonalite (231 m along borehole). b) Foliation defined by biotite and quartz in cm-scale shear zone, in biotite granodiorite-tonalite (904 m along borehole). c) Cm-scale shear zone developed within amphibolite (659 m along borehole). d) Folded mylonite layer within a dm-scale shear zone, in amphibolite (673 m along borehole).

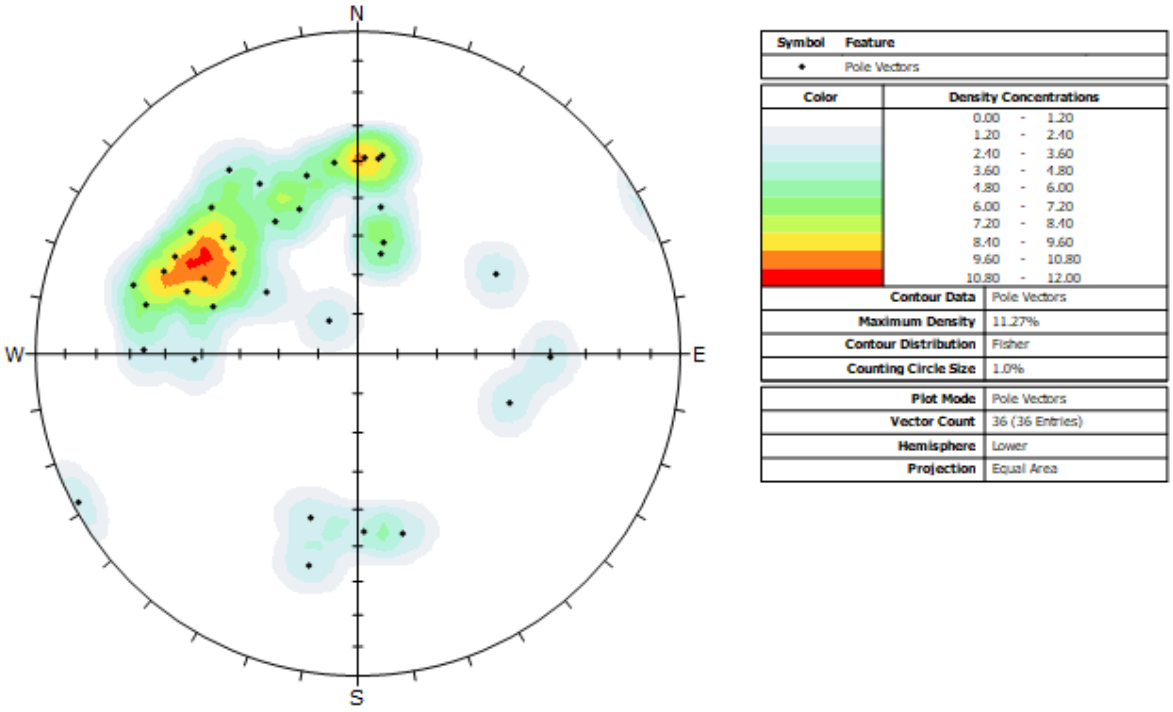


Figure 25: Stereonet showing poles and unweighted contours for Igneous Primary Structures (IPS; n = 36).

Contacts

Top and bottom contact (CO) orientations were logged for each change in rock type wherever the boundary was sharp enough to confidently identify a contact plane. The majority of the logged contacts represent boundaries between occurrences of biotite granodiorite-tonalite and subordinate rock types. Ninety-seven of the logged contacts were identified as sharp, three were identified as gradational, and three were identified as chilled margins. The later occurrences were all identified at aphanitic/feldspar-phyric tonalite dyke contacts.

Out of a total of 103 logged contacts, 102 of these could be confidently oriented using the televiewer data. In the other occurrence, a single plane could not be defined with confidence during the geological core logging due to the gradational nature of the amphibolite contact. The poles to the planes defining all oriented geological contacts are shown in Figure 26. One prominent pole cluster defines moderately to gently inclined east-dipping geological contacts. The remainder of the geological contacts dip steeply to moderately towards the northeast.

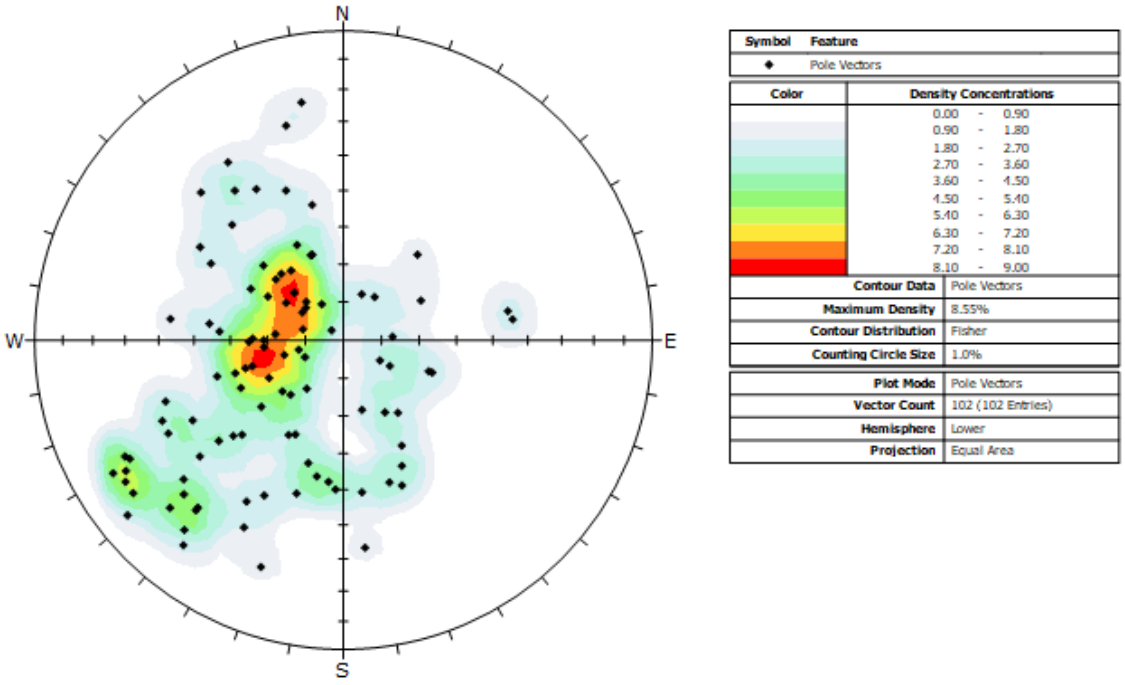


Figure 26: Stereonet showing poles and unweighted contours for all oriented geological contacts (n = 102).

A total of two biotite tonalite contacts (one occurrence) with the adjacent biotite granodiorite-tonalite were oriented, both of which were logged as intact. The contacts are nearly parallel and dip gently towards the southeast (DipDirection/Dip = 133/29 and 130/04).

Nine amphibolite contacts were successfully oriented (Figure 27), including four instances logged as broken. The majority of the poles to amphibolite contacts plot in the southeast quadrant of the stereonet indicating gently to moderately inclined contacts that dip northwest to north-northwest. The amphibolite occurrences generally exhibit evidence of penetrative ductile to brittle-ductile deformation obscuring any indication of their primary relationship with the surrounding bedrock. The deformation manifests as cm- to dm-scale localized shear zones (Figure 24c) that are developed within the amphibolite occurrences as well as along, and sub-parallel to, their contacts.

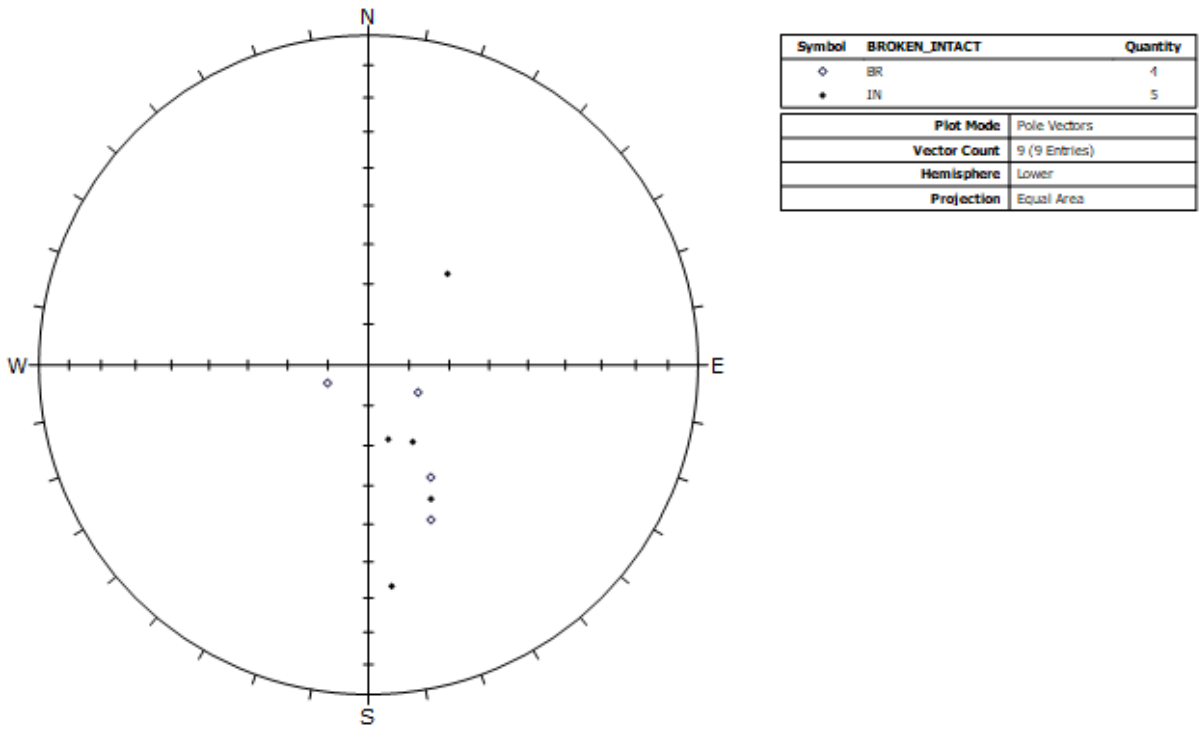


Figure 27: Stereonet showing poles for amphibolite contacts (n = 9). Open symbols identify broken contacts (BR) and filled symbols identify intact contacts (IN).

The poles to the contact orientations for five distinct felsic phases interpreted as dykes are shown in Figure 28. This includes occurrences of aphanitic/felspar-phyric tonalite dykes, aplite dykes, pegmatite dykes, biotite granodiorite-tonalite dykes, and quartz dykes. The aphanitic/feldspar-phyric tonalite dykes are the most commonly occurring felsic dyke phase in IG_BH02. Poles to the aphanitic/feldspar-phyric tonalite dyke contacts (n = 53), identified by open black triangles, define occurrences that are moderately to gently inclined and dip northeast. The majority of aphanitic/feldspar-phyric tonalite dyke contacts were logged as sharp, and 12 were identified as broken. Poles to aplite dyke contacts (n = 18), identified by purple diamonds, define occurrences that are steeply inclined and dip northeast, and occurrences that are moderately to gently inclined and dip north or west. All aplite dyke contacts were logged as sharp, and none were identified as broken. Poles to pegmatite dyke contacts (n = 18), identified by red diamonds, mostly define occurrences that are moderately or gently inclined and dip southeast, with few additional occurrences of steeply inclined contacts that dip northeast. Most pegmatite dyke contacts were logged as sharp, and one was identified as broken. Poles to quartz dykes contacts (n = 10), identified by blue diamonds, define occurrences that are mostly gently inclined and dip west. Most quartz dyke contacts were logged as sharp, and three were identified as broken. Poles to biotite granodiorite-tonalite dykes (n = 6), identified by green triangles, define occurrences that are gently inclined and dip east. All biotite granodiorite-tonalite dyke contacts were logged as sharp, and one was identified as broken.

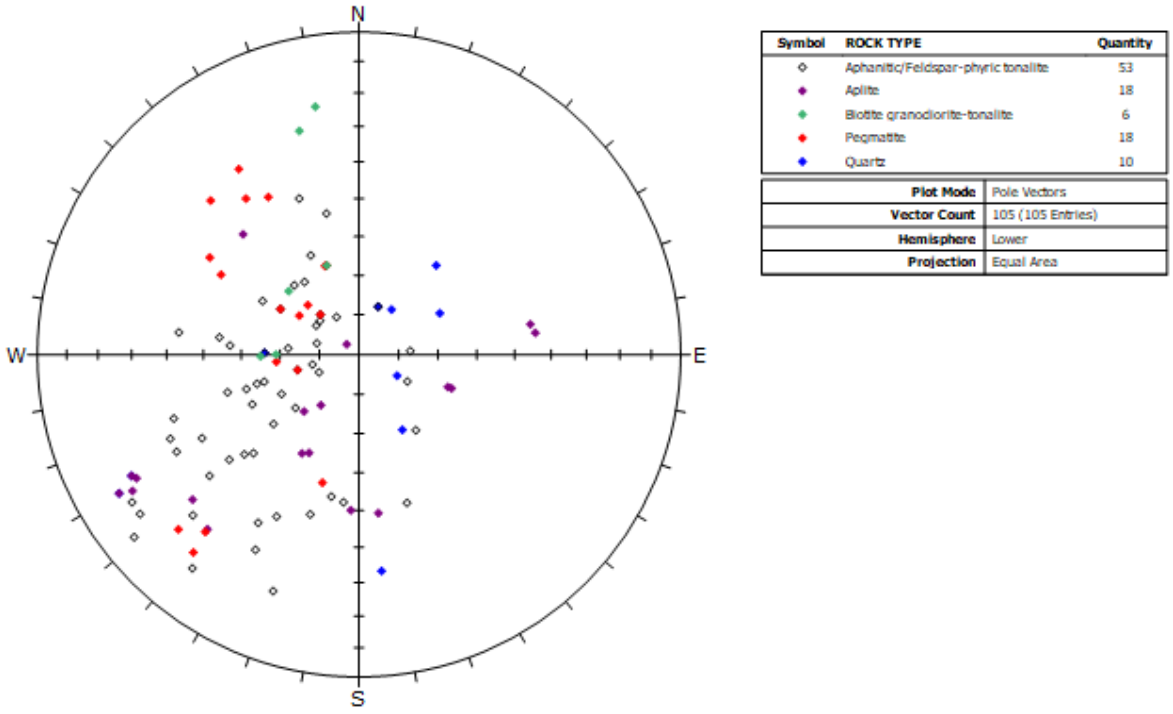


Figure 28: Stereonet showing the distribution of poles to contacts for felsic dykes (n = 105), including, aphanitic/feldspar phyric tonalite dykes (n= 53), aplite dykes (n = 18), biotite granodiorite-tonalite dykes (n = 6), pegmatite dykes (n = 18), and quartz dykes (n = 10).

Ductile Structures

Ductile structures identified in IG_BH02 include foliation (FO) and both ductile shear zones (SHR) and brittle-ductile shear zones (SHRD). In addition, a single fold axis (FAX) was identified, which will be discussed below along with the foliation description, and two occurrences of mylonite (MYL) were identified, one of which is associated with the recognized fold structure. The mylonite occurrences will be discussed below along with the shear zone description. Some examples of ductile structures encountered in the borehole are shown in Figure 24b-d. Stick plots indicating the distribution of the ductile structures are included in Figure 29. Figure 29 also includes the overall per metre fracture frequency and stick plots for all brittle structures logged in the borehole. The brittle structures will be described in detail after presentation of the ductile structures.

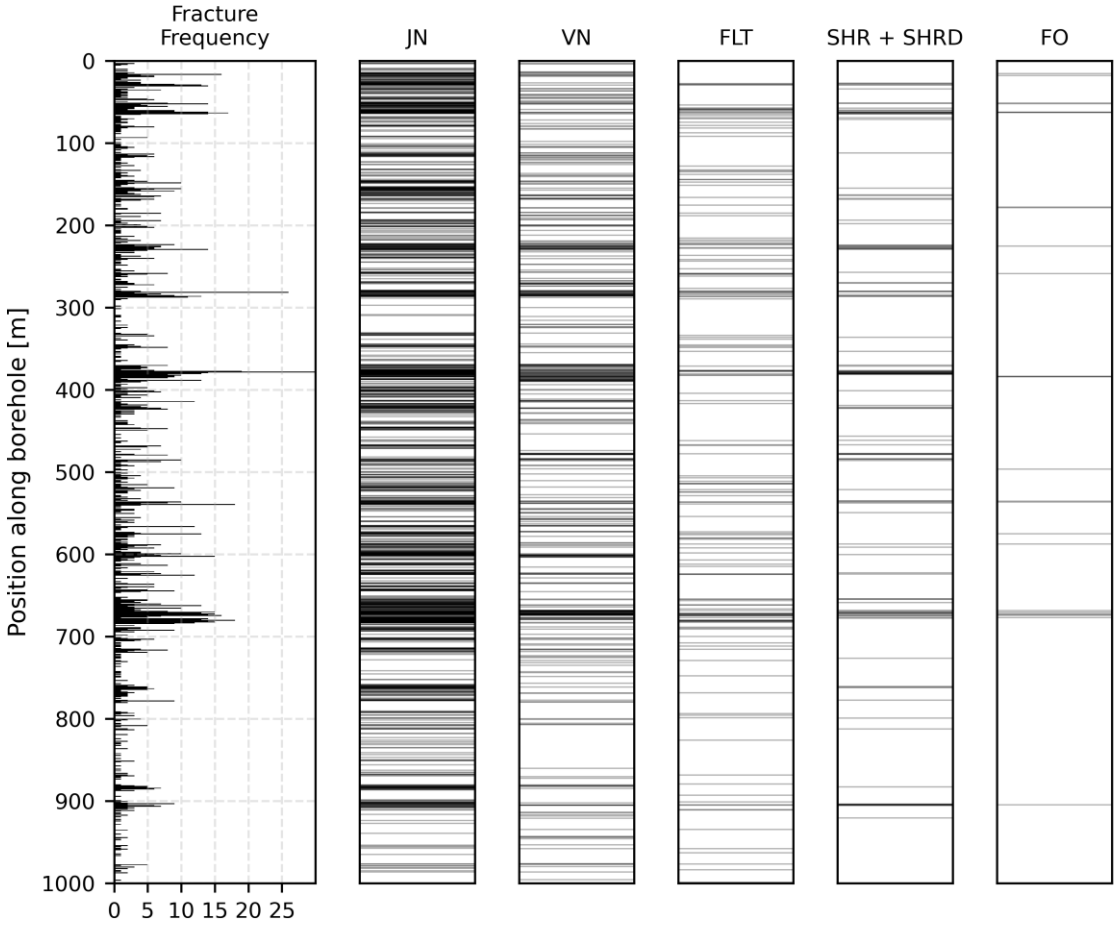


Figure 29: Summary log showing the frequency per metre of brittle structures (left) in comparison to stick plots that show the distribution of all brittle structures (Joints – JN, Veins – VN and Faults - FLT) and all ductile structures (Shear Zones – SHR and Foliation – FO).

Foliation was logged where preferential orientation of mineral grains was observed. A total of 26 foliation occurrences were recorded. These occurrences are mostly broadly distributed within the upper 700 m along the length of the borehole, with evidence of a slightly denser cluster of measured foliation planes at approximately 675 m (Figure 29). Where a foliation is identified within granodiorite-tonalite it is primarily described as weak and defined by the alignment of biotite. Locally, a well-developed foliation is identified in felspar-phyric felsic dyke occurrences, where it is defined by aligned feldspar phenocrysts +/- biotite, and also in amphibolite occurrences, where it is defined by aligned amphibole minerals. An example of well-developed foliation, from a shear zone in biotite granodiorite-tonalite, is shown in Figure 24b. The single logged fold structure was identified within an amphibolite, defined by folded light and dark banding. The fold axial surface dips gently towards the northeast (14° towards 032°; Figure 24d).

Figure 30 presents the stereonet of foliation orientations. All foliation occurrences were successfully oriented. The majority of the poles define foliation planes that are subhorizontal or dip gently south or west. Overall, the poles to the foliation are also broadly distributed along the north-south axis of the stereonet. There is very little difference in the pattern of contours in the Terzaghi-weighted dataset relative to the unweighted dataset.

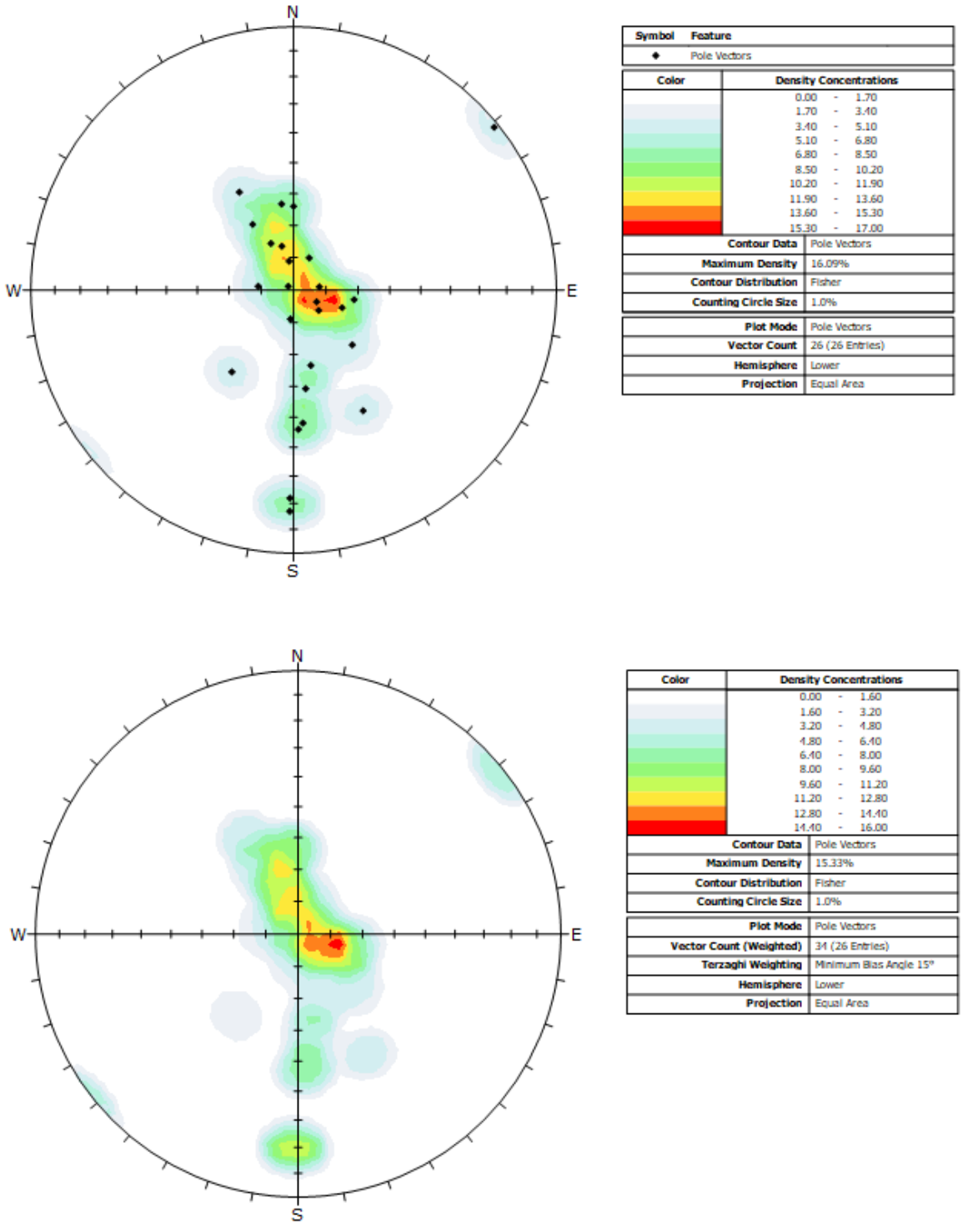


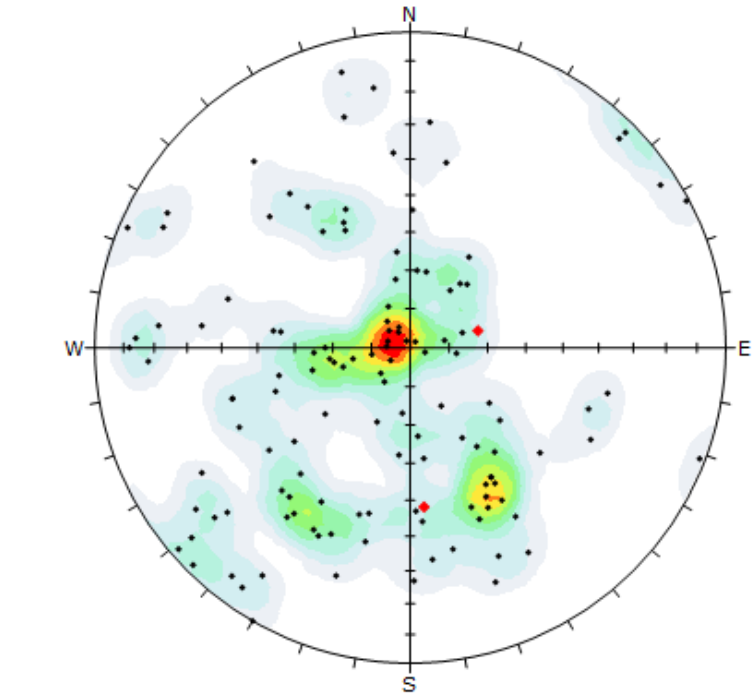
Figure 30: Stereonets showing orientation information for Foliation (FO). Top: All data – poles and contours, unweighted (n = 26). Bottom: All Foliation data, Terzaghi-weighted contours (n = 34).

A total of 129 shear zones were logged in IG_BH02. These structures were initially identified during geological core logging as either ductile shear zones (SHR) or brittle-ductile shear zones (SHRD). In the assessment of the entire shear zone dataset, it was determined that all occurrences more

likely represent a continuum of ductile to brittle deformation. Therefore, the presentation herein integrates all occurrences simply as a single ductile shear zone dataset (SHR + SHRD). In addition, two mylonite (MYL) occurrences were identified in IG_BH02. These structures are also considered to be a part of the same ductile to brittle continuum and are therefore also described below. Shear zone examples are shown in Figure 24b, Figure 24c, and Figure 24d.

Seventy-five (58 %) of the shear zones, and one mylonite (50 %), were identified in geological core logging only. The remaining 54 shear zones, and one mylonite, were identified in both geological core logging and televiewer logs. One hundred and twenty-eight (>99 %) of the shear zones, and both mylonite occurrences, were successfully oriented. Shear zones range in width (length along borehole) from hairline to 100 cm. The two mylonite occurrences are 34 and 52 cm in width, respectively. The most common mineral phase associated with shear zones is quartz, with lesser associations of chlorite, epidote, hematite, muscovite, and amphibole. The most common mineral phase associated with mylonite are quartz and plagioclase, with minor chlorite.

The shear zones are commonly observed along the contacts of amphibolite occurrences and, in some cases, feldspar-phyric felsic dykes. Some occurrences are also identified within the biotite granodiorite-tonalite. Both mylonite occurrences were identified within amphibolite. The stick plot of shear zone occurrences highlights the observation that they are identified along the entire length of the borehole (Figure 29). Peaks in the fracture frequency are coincident with slight increases in the density of shear zone occurrences. In addition, the distribution of shear zones is sparsest below approximately 675 m which is also coincident with an overall decrease in fracture frequency. The two mylonite occurrences were identified at 538 m and 673 m, coincident with local peaks in the fracture frequency, and also situated close to the top and bottom boundaries of rock unit RU2 (Figure 29). Figure 31 presents the unweighted and weighted stereonets for all oriented shear zones and mylonites. There is one prominent pole cluster in the unweighted dataset that defines subhorizontal to gently inclined shear zones that dip east. Another pole cluster defines moderately inclined shear zones that dip northwest. A third, less prominent, pole cluster defines moderately inclined shear zones that dip northeast. The Terzaghi weighted dataset emphasizes a cluster of subvertical shear zones that strike northwest. One of the mylonite occurrences dips gently west, the other dips moderately north.

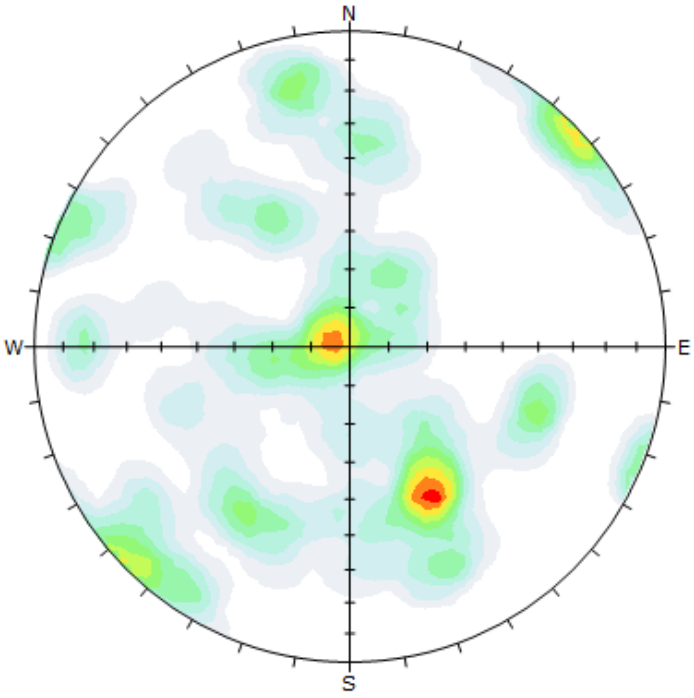


Symbol	SHR_MYL	Quantity
◆	MYL	2
•	SHR	128

Color	Density Concentrations
	0.00 - 0.80
	0.80 - 1.60
	1.60 - 2.40
	2.40 - 3.20
	3.20 - 4.00
	4.00 - 4.80
	4.80 - 5.60
	5.60 - 6.40
	6.40 - 7.20
	7.20 - 8.00

Contour Data	Pole Vectors
Maximum Density	7.97%
Contour Distribution	Fisher
Counting Circle Size	1.0%

Plot Mode	Pole Vectors
Vector Count	130 (130 Entries)
Hemisphere	Lower
Projection	Equal Area



Color	Density Concentrations
	0.00 - 0.65
	0.65 - 1.30
	1.30 - 1.95
	1.95 - 2.60
	2.60 - 3.25
	3.25 - 3.90
	3.90 - 4.55
	4.55 - 5.20
	5.20 - 5.85
	5.85 - 6.50

Contour Data	Pole Vectors
Maximum Density	6.16%
Contour Distribution	Fisher
Counting Circle Size	1.0%

Plot Mode	Pole Vectors
Vector Count (Weighted)	205 (130 Entries)
Terzaghi Weighting	Minimum Bias Angle 15°
Hemisphere	Lower
Projection	Equal Area

Figure 31: Stereonets showing orientation information for Shear Zones (SHR-SHRD) and Mylonites (MYL). Top: All data – poles and contours, unweighted (n = 130). Bottom: All Shear Zone and Mylonite data, Terzaghi-weighted contours (n = 205).

Brittle Structures

This section describes the brittle structures, including all joints (JN), veins (VN), and faults (FLT), representing the group of features collectively identified as fractures. A summary of the per metre fracture frequency for all brittle structures, as well as stick plots detailing their distribution in the borehole, is included in Figure 29. Typical examples of brittle structures identified in the borehole are included in Figure 32.

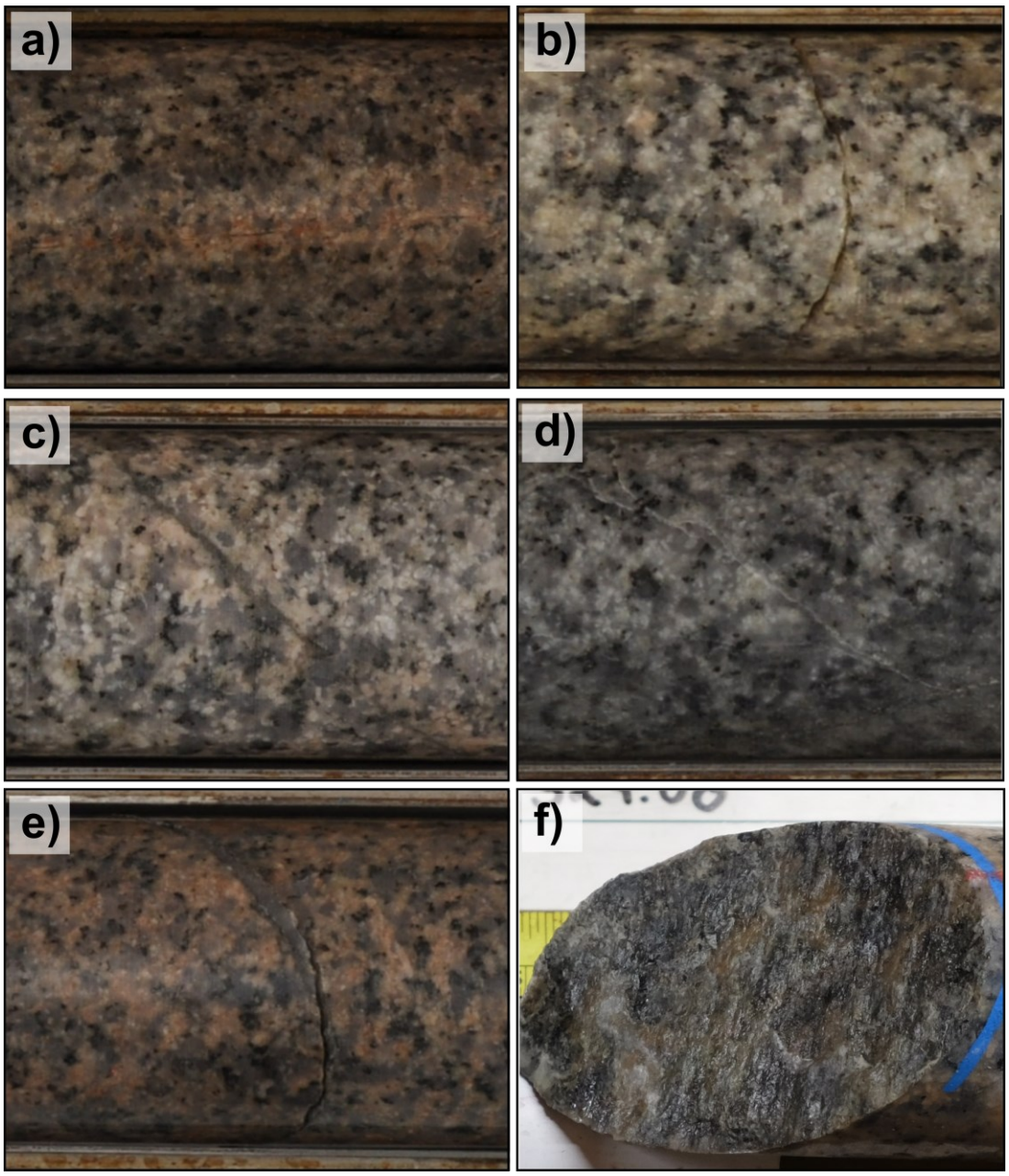
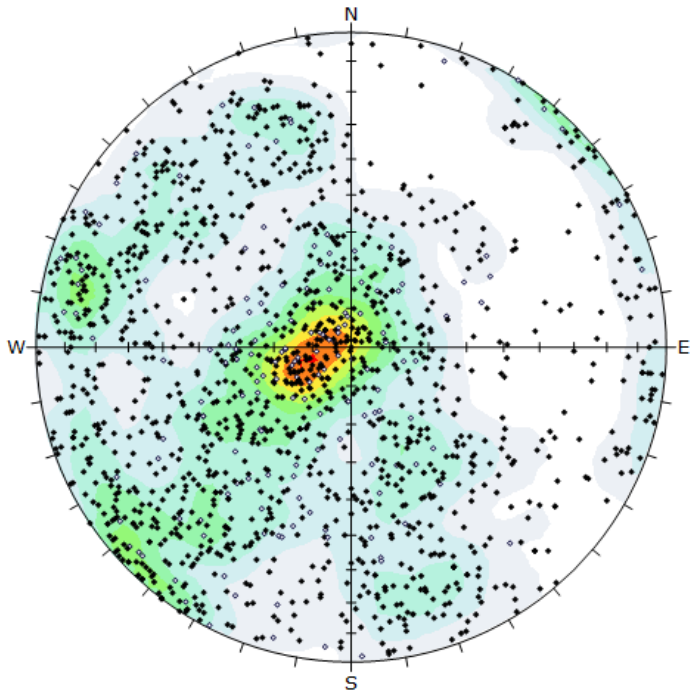


Figure 32: Examples of brittle structure. a) Intact hairline joint with iron stain, in biotite granodiorite-tonalite (93 m). b) Broken joint with no surface alteration and no measurable geological aperture (688 m). c) Intact mm-scale quartz-filled vein, in biotite granodiorite tonalite (483 m). d) Intact hairline calcite-filled vein, in biotite granodiorite tonalite (222 m). e) Broken fault plane with quartz infill, in biotite granodiorite-tonalite (524 m). f) Lineation defined by aligned quartz on same fault plane as shown in (e).

A total of 1494 joints were logged in IG_BH02. They are distributed along the entire length of the borehole and since they dominate the total brittle structure dataset the peaks in the per metre fracture frequency correlate well with the clusters evident in the stick plot of all joints (Figure 29). A total of 170 of the 1494 joints (11 %), were logged as broken, while the remaining 1324 (89 %) were logged as intact or partially intact. The majority of the joints (1454/1494; 97 %) exhibit no measurable geological aperture, meaning that any natural aperture, if present, was too small to identify visually. In the remaining 40 occurrences, mm to cm-scale geological apertures (maximum of 14 mm) were identified through analysis of the televiewer data. Where joints were logged as broken during geological core logging, and did not exhibit any geological aperture, the adjacent broken core pieces were able to be fit back together without any visual evidence of an opening along the fracture plane. In these instances, it is possible that the break was mechanically induced as a result of the drilling process along a joint that was otherwise intact in situ.

Joint surfaces were logged as clean, with no associated mineral infill, in 92 occurrences (6 %), while the remaining 1402 (94 %) included observation of staining, slight alteration, or coating with a hairline (<1 mm width) infill. The most common secondary mineral phases associated with the joints were quartz, chlorite, iron oxide (hematite), calcite, and epidote.

Typical examples of joints are shown in Figure 32, including, a hairline intact joint with iron stain (Figure 32a) and a hairline broken joint with no discernible surface alteration (Figure 32b). The majority of identified joints were logged in both geological and televiewer logs (462; 31 %) or geological core logging only (951; 64 %), with the remaining joints identified in televiewer logs only (61; 4 %). Through the integration process, 1474 of 1494 (>99 %) joints were successfully oriented. Figure 33 presents the unweighted and weighted stereonets for all oriented joints. The unweighted stereonet emphasizes one prominent pole cluster of subhorizontal joints. Much less prominent pole clusters also define steeply inclined to vertical, northwest- and north-northeast-trending, joints. These latter, less prominent pole clusters are emphasized in the Terzaghi-weighted joint dataset suggesting that they may represent subsets of vertical, northwest- and north-northeast-striking, joint sets. Additional pole clusters in the weighted dataset emphasize two steeply inclined joint sets, one trending east-northeast and the other trending west-southwest.

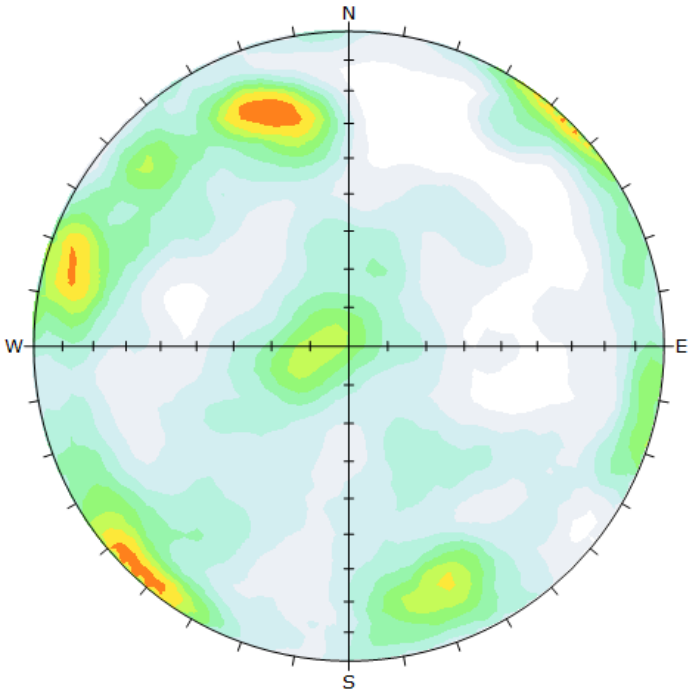


Symbol	STRUCT-BR_IN	Quantity
◇	JN-BR	164
◆	JN-PIN/IN	1310

Color	Density Concentrations
	0.00 - 0.45
	0.45 - 0.90
	0.90 - 1.35
	1.35 - 1.80
	1.80 - 2.25
	2.25 - 2.70
	2.70 - 3.15
	3.15 - 3.60
	3.60 - 4.05
	4.05 - 4.50

Contour Data	Pole Vectors
Maximum Density	4.12%
Contour Distribution	Fisher
Counting Circle Size	1.0%

Plot Mode	Pole Vectors
Vector Count	1474 (1474 Entries)
Hemisphere	Lower
Projection	Equal Area



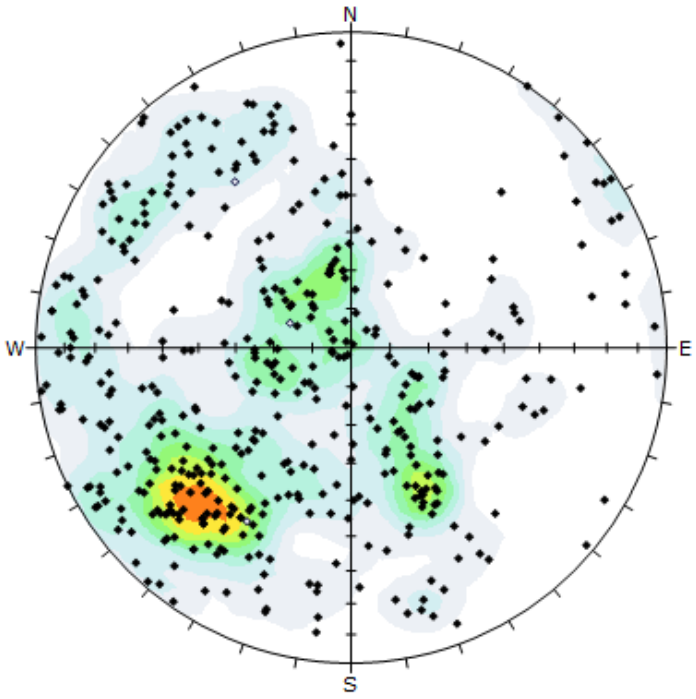
Color	Density Concentrations
	0.00 - 0.35
	0.35 - 0.70
	0.70 - 1.05
	1.05 - 1.40
	1.40 - 1.75
	1.75 - 2.10
	2.10 - 2.45
	2.45 - 2.80
	2.80 - 3.15
	3.15 - 3.50

Contour Data	Pole Vectors
Maximum Density	3.13%
Contour Distribution	Fisher
Counting Circle Size	1.0%

Plot Mode	Pole Vectors
Vector Count (Weighted)	2746 (1474 Entries)
Terzaghi Weighting	Minimum Bias Angle 15°
Hemisphere	Lower
Projection	Equal Area

Figure 33: Stereonets showing orientation information for Joints (JN). Top: All data – poles and contours, unweighted (n = 1474). Open symbols identify broken Joints (JN-BR) and filled symbols identify partially intact/intact Joints (JN-PIN/IN). Bottom: All Joint data, Terzaghi-weighted contours (n = 2746).

A total of 447 veins were logged in IG_BH02, distributed along the entire length of the borehole. The majority of the veins (444; 99 %) were logged as intact or partially intact and the remaining three vein occurrences were logged as broken. The stick plot of vein occurrences highlights the observation that veins are identified along the majority of the borehole, including distinct higher density intervals around 400 m and 675 m along the length of the borehole. In addition, veins are relatively sparse between 800 and 900 m along the length of the borehole (Figure 29). A total of 384 veins (86 %) were identified in geological core logging and therefore confidently associated with mineral phases. A total of 63 veins (14 %) were identified only in the televiewer dataset. In the latter occurrences, the infilling mineral could not be determined with certainty. The main mineral infilling phases identified include, quartz in 196 veins (44 %; Figure 32c), followed by a 'granitic' assemblage of alkali feldspar +/- plagioclase +/- quartz with lesser muscovite in 126 occurrences (28 %), calcite in 88 veins (20 %; Figure 32d), iron oxide stain in 74 veins (16 %), chlorite in 67 veins (15 %), and epidote in 50 veins (11 %). Logged vein thicknesses range between hairline (sub-mm) and 5 cm. A total of 442 of the 447 veins (99 %) were successfully oriented. Figure 34 presents the unweighted and weighted stereonets for all oriented veins. The poles scatter broadly across the southwestern and northwestern quadrants of the stereonet and are markedly less prominent in the northeastern and southeastern quadrants. One main pole cluster corresponds to veins that are moderately to steeply inclined and dip to the northeast. Lesser pole clusters indicate gently to moderately inclined veins that dip north-northwest and subhorizontal to gently inclined veins that dip broadly east to southeast. Steeply inclined veins that dip east-southeast to south-southeast are identified by four distinct adjacent pole clusters in the Terzaghi-weighted dataset.



Symbol	STRUCT-BR_IN	Quantity
◇	VN-BR	3
◆	VN-PIN/IN	439

Color	Density Concentrations
	0.00 - 0.60
	0.60 - 1.20
	1.20 - 1.80
	1.80 - 2.40
	2.40 - 3.00
	3.00 - 3.60
	3.60 - 4.20
	4.20 - 4.80
	4.80 - 5.40
	5.40 - 6.00

Contour Data	Pole Vectors
Maximum Density	5.36%
Contour Distribution	Fisher
Counting Circle Size	1.0%

Plot Mode	Pole Vectors
Vector Count	442 (442 Entries)
Hemisphere	Lower
Projection	Equal Area

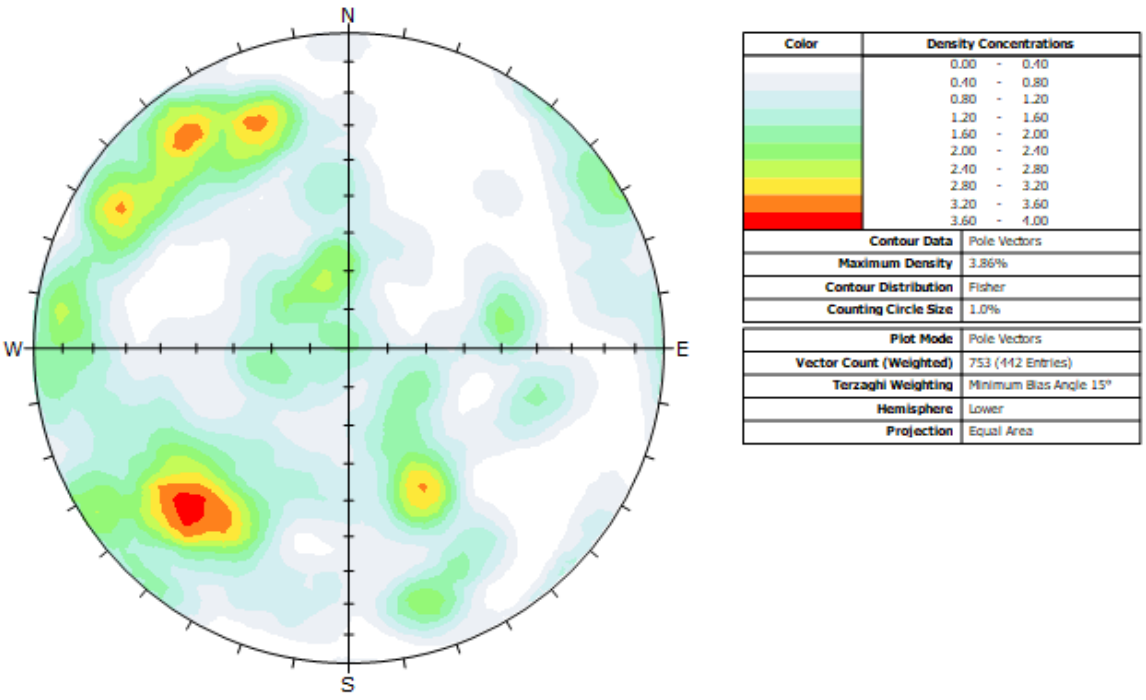


Figure 34: Stereonets showing orientation information for all Veins (VN). Top: All data – poles and contours, unweighted (n = 442). Open symbols identify broken Veins (VN-BR) and filled symbols identify partially intact/intact Veins (VN-PIN/IN). Bottom: All Vein data, Terzaghi-weighted contours (n = 753).

Faults include features interpreted to have resulted from brittle deformation and exhibit some evidence of displacement. A total of 165 faults were logged in IG_BH02. The stick plot highlights the observation that faults are distributed along the entire length of the borehole, with a subtle cluster evident at approximately 675 m (Figure 29). The main diagnostic criterion used to identify a fault in the recovered core is the presence of slickenlines on the fault surfaces. In 152 (92 %) of the logged faults, the surface was recorded as a hairline structure with geological aperture less than one mm. The geological apertures of the remaining 13 faults range between one and five mm. The most common secondary mineral phases identified were chlorite in 98 faults (59 %), epidote in 71 faults (43 %), quartz in 60 faults (37 %), iron oxide stain in 52 faults (32 %), and calcite in 49 faults (30 %). In addition, a clay infill was identified to infill seven faults (4 %) and broken rock or, soft or hard, gouge was identified in six faults (4 %). A typical example of a fault is shown in Figure 32e, highlighting the observation that faults in IG_BH02 are very narrow and discrete structures with only slight evidence of damage in the rock surrounding the fault plane in Figure 32e. However, the rock mass surrounding the fault plane has experienced a low degree of alteration, evidenced by its continuous reddish colour. Figure 32f shows the same fault plane as shown in Figure 32e but with the plane exposed to highlight the associated slickenlines, defined by quartz.

One hundred and twelve of the faults were identified in both geological and televiewer logging (68 %), with the remaining 53 faults observed in geological core logging only (32 %). One hundred and sixty-three faults (99 %) were successfully oriented. Figure 35 presents the unweighted and weighted stereonets for all oriented faults. In the unweighted dataset, one broad pole cluster defines moderately inclined northeast-dipping faults. Less prominent pole clusters define moderately to gently inclined and east-dipping faults, and steeply inclined and south-southeast-dipping faults. Vertical, north-northeast-striking, faults become more evident in the Terzaghi-weighted dataset.

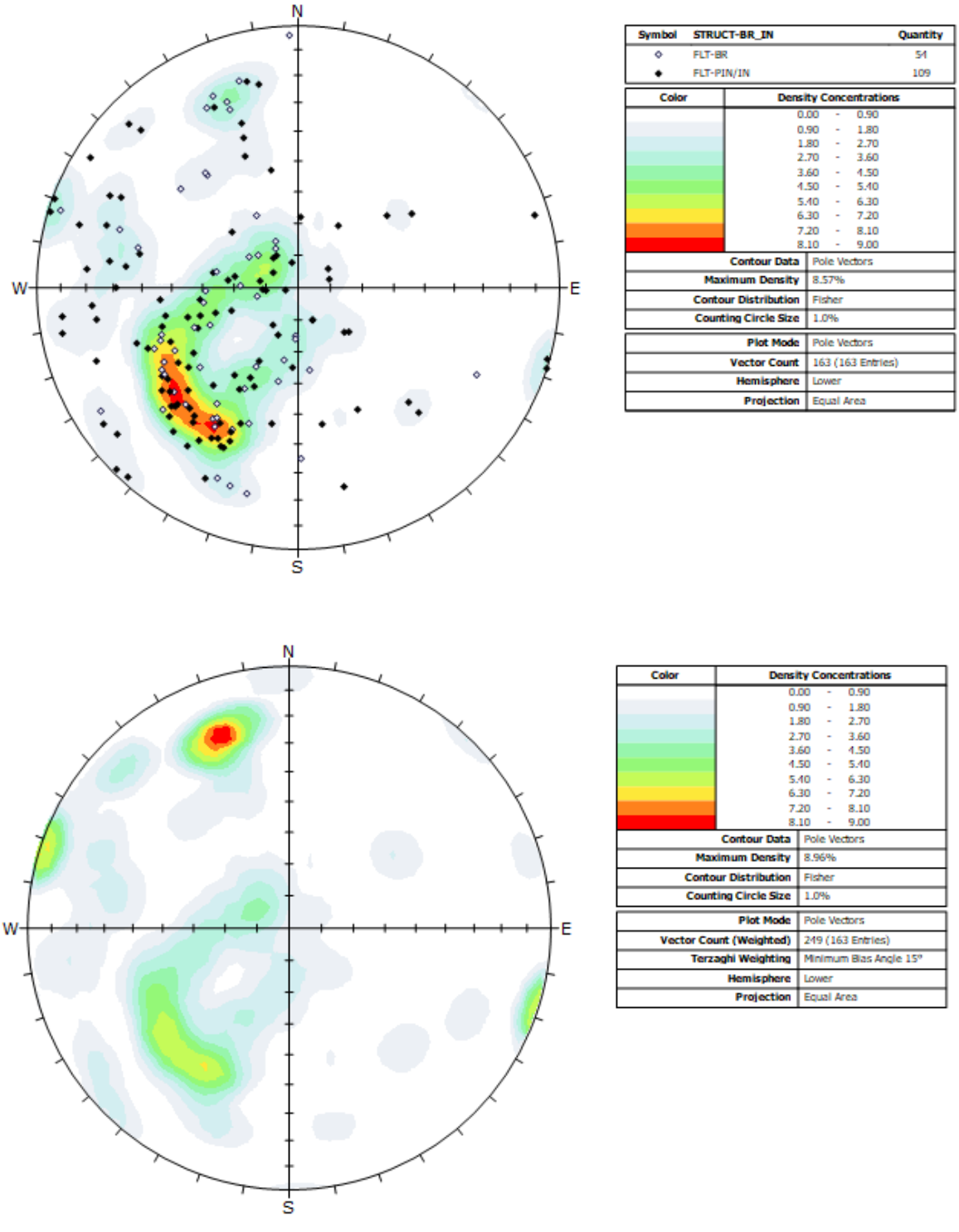
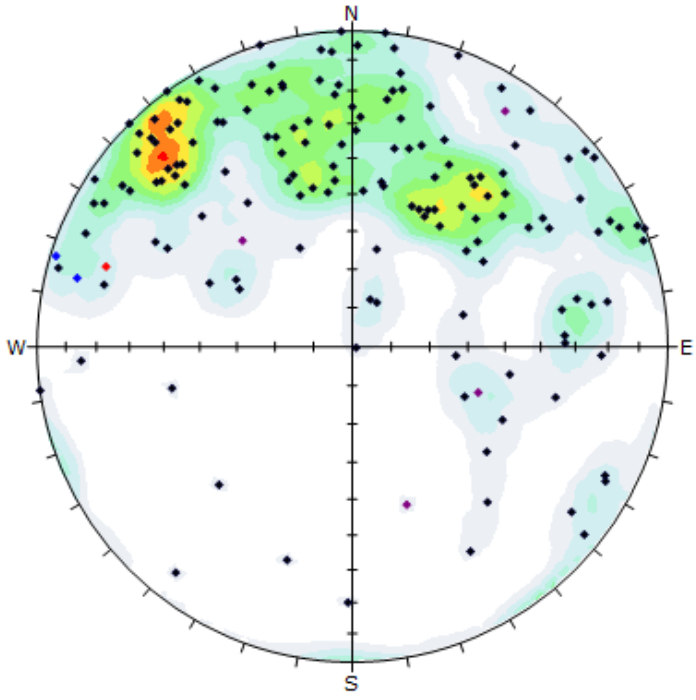


Figure 35: Stereonets showing orientation information for Faults (FLT). All data – poles (n = 163). Open symbols identify broken Faults (FLT-BR) and filled symbols identify partially intact/intact Faults (FLT-PIN/IN). Bottom: All Fault data, Terzaghi-weighted contours (n = 249).

Lineations

A total of 162 lineations were identified during geological core logging, including 155 occurrences identified on fault planes, four occurrences on shear planes, one in a mylonite occurrence, and two additional occurrences identified on foliation planes. Most lineations identified during visual core logging are characterized as slickenlines on fault planes. The most common minerals identified as defining these lineations are chlorite and epidote, with lesser occurrences defined by alignment of quartz, muscovite, iron staining, and calcite. The mineral lineations associated with the shear zones and mylonite occurrences are defined by a similar assemblage of quartz, chlorite, epidote, and calcite. The mineral lineations identified on the foliation planes are defined by quartz.

The majority of lineations, which are predominantly identified on fault planes, plunge gently northwest. To a lesser extent lineations also plunge moderately north to northeast. Few lineations plunge at greater than 50° in any direction (Figure 36). The single prominent cluster of poles to lineated planes (Figure 36), all of which are faults, defines an average surface that dips moderately towards the northeast. The overall pattern of lineations suggests, therefore, strike-slip motion on the majority of fault surfaces, with lesser occurrences of oblique-slip, or dip-slip motion. The few occurrences of lineations identified on foliation planes and within logged mylonites are nearly horizontal and trend west-northwest. There is a higher degree of variability in trend and plunge of the few lineations identified on shear planes.



Symbol	TYPE	Quantity
◆	FLT	155
◆	FO	2
◆	MYL	1
◆	SHR	4

Color	Density Concentrations
	0.00 - 0.60
	0.60 - 1.20
	1.20 - 1.80
	1.80 - 2.40
	2.40 - 3.00
	3.00 - 3.60
	3.60 - 4.20
	4.20 - 4.80
	4.80 - 5.40
	5.40 - 6.00

Contour Data	Pole Vectors
Maximum Density	5.64%
Contour Distribution	Fisher
Counting Circle Size	1.0%

Plot Mode	Pole Vectors
Vector Count	162 (162 Entries)
Hemisphere	Lower
Projection	Equal Area

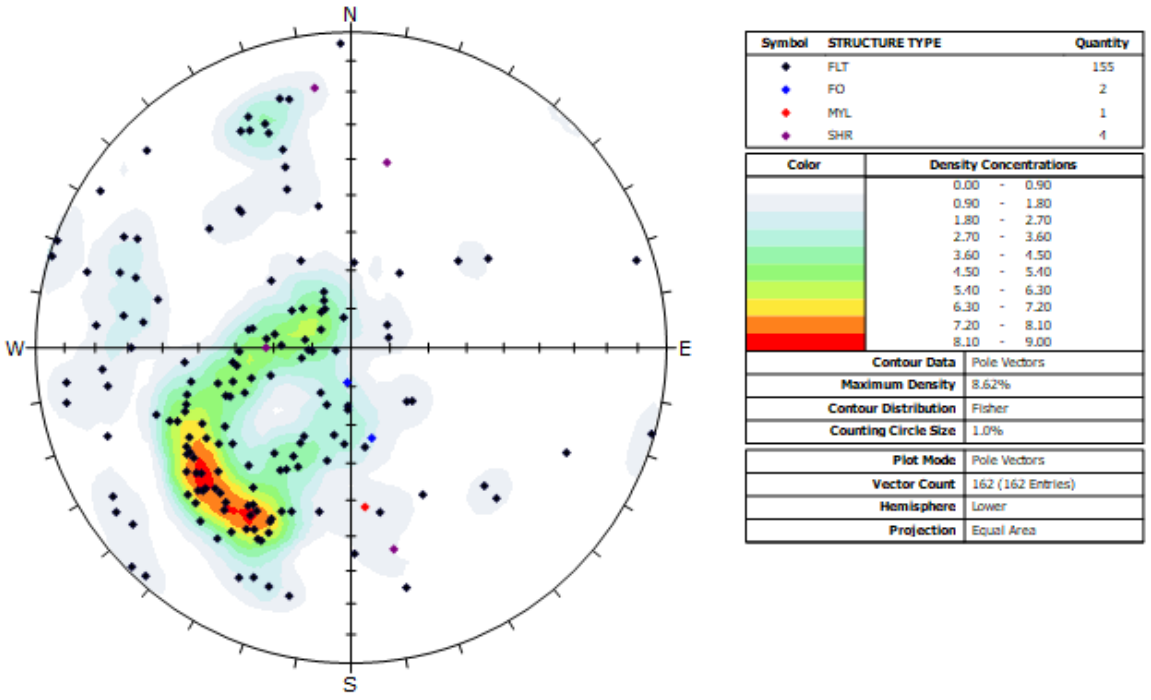


Figure 36: Stereonet showing lineation orientation information for IG_BH02. Top: All lineations (n = 162) plotted by associated plane type (FLT – fault, FO – foliation, MYL – mylonite, SHR – shear). Bottom: Poles to all oriented planes, by type, with identified lineations (n = 162).

Broken vs Intact or Partially Intact Structures

During the geological core logging, naturally occurring fractures were categorized as being broken (BR) when the core was physically broken into separate pieces at the location of the logged structure. Otherwise, they were categorized as intact (IN) or partially intact (PIN) where complete or partial cohesion was maintained along the logged structure. Of the 2079 oriented fractures, 221 (11 %) were logged as broken (Figure 37) and 1858 (89 %) were logged as intact or partially intact (Figure 38). This categorization is based on a visual assessment of core condition when the core is removed from the barrel and initially examined. As mentioned earlier in the discussion of joints, which includes the majority of broken fractures, most of the adjacent broken fracture planes could be physically fit back together with no visible geological aperture. Therefore, the broken characteristic alone does not imply any direct relationship to the potential for a fracture to be hydraulically conductive. This categorization also does not include any judgement on whether or not the drilling activity itself may have induced the break. The primary difference between the distribution of poles to fractures logged as broken versus intact (or partially intact), comparing Figure 37 with Figure 38, is that broken structures tend to have gentler dips.

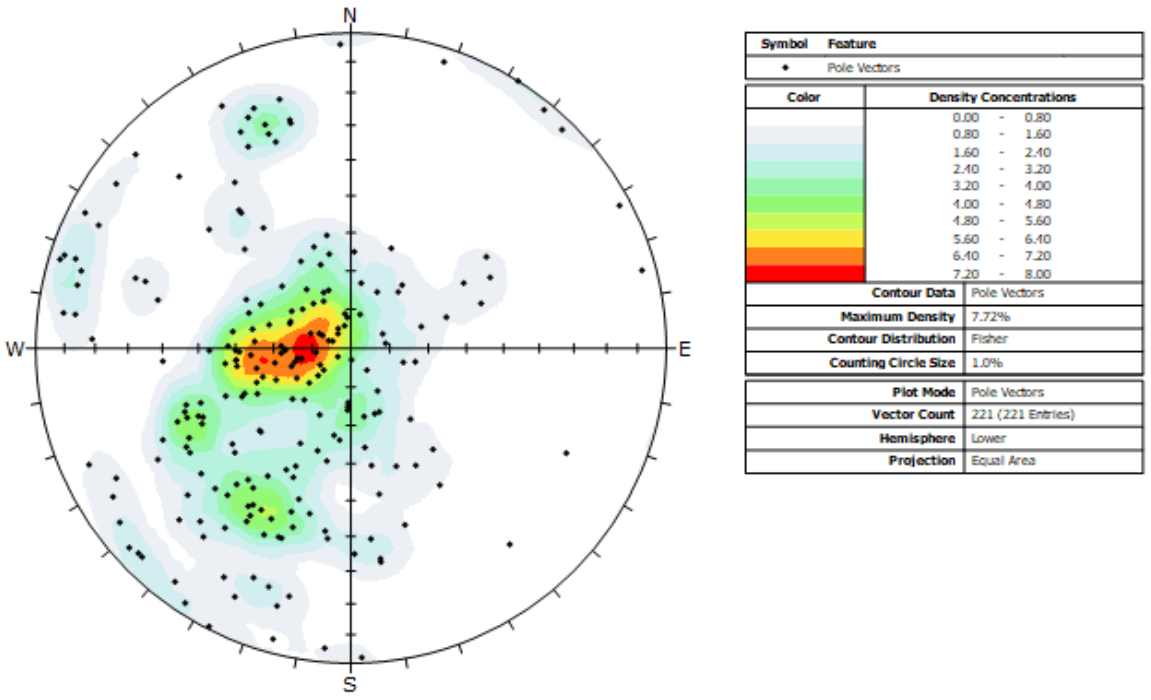


Figure 37: Stereonet plot showing poles to all fracture planes logged as broken during geological core logging, with unweighted contours (n = 221).

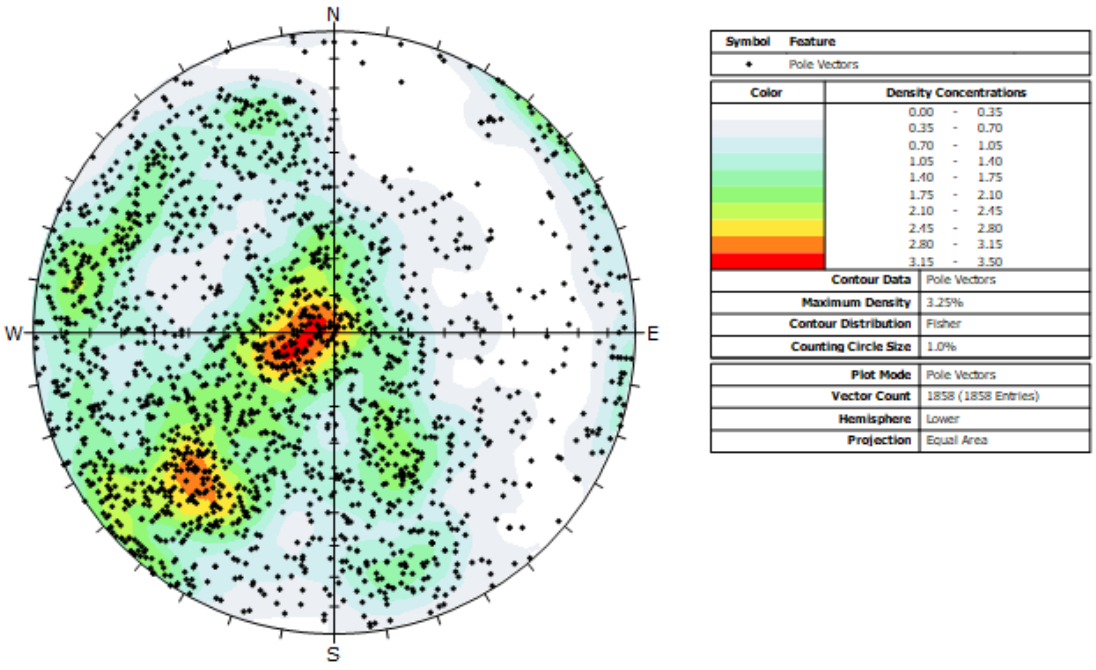


Figure 38: Stereonet plot showing poles to all fracture planes logged as intact or partially intact, with unweighted contours (n = 1858).

3.2.4.2 Interpreted Fracture Sets

Figure 39 presents the distribution of fracture poles and contoured stereographic distribution of poles to all logged fractures (joints, veins, faults, n = 2079) in order to assess for the presence of visible pole clusters that may define fracture sets in IG_BH02. These identified fracture sets can be compared with fracture sets identified in other boreholes, and also with surface mapped fracture and interpreted fracture (lineament) orientations, to provide guidance in developing three-dimensional fracture network models. Shear zones have not been included in this assessment.

Based on visual assessment of pole clusters and using a contour density cut-off of 1 % from the Terzaghi-weighted dataset as a guide, eight clusters labelled (i) to (viii) were initially identified in IG_BH02. Expert judgement was also employed to refine boundaries between pole clusters. These clusters are outlined on the stereonet of unweighted poles to all fractures (upper stereonet plot in Figure 39), and include:

- a large pole cluster that overlaps the centre of the stereonet to define a subhorizontally-oriented to moderately inclined, east-dipping fracture set (Cluster i - red symbols in Figure 39, top stereonet);
- a pole cluster that defines a moderately to steeply inclined fracture set dipping south- to south-southeast (Cluster ii - green symbols in Figure 39, top stereonet);
- a pole cluster that defines a steeply inclined fracture set dipping east-southeast (Cluster iii - orange symbols in Figure 39, top stereonet);
- a pole cluster that defines a steeply inclined fracture set dipping west-northwest (Cluster iv - blue symbols in Figure 39, top stereonet);
- a pole cluster that defines a steeply inclined fracture set dipping northeast (Cluster v - yellow symbols in Figure 39, top stereonet);

- a pole cluster that defines a steeply inclined fracture set dipping southwest (Cluster vi – grey symbols in Figure 39, top stereonet;
- a pole cluster that defines a moderately inclined fracture set dipping northeast (Cluster vii – light blue symbols in Figure 39, top stereonet; and
- a pole cluster that defines a steeply inclined fracture set dipping north-northwest (Cluster viii – purple symbols in Figure 39, top stereonet.

The remaining unclustered poles are not assigned to any particular possible fracture set and are therefore assigned to an additional random set.

The same eight pole clusters are also outlined on the unweighted and Terzaghi-weighted contour plots (middle and bottom images in Figure 39, respectively). The Terzaghi-weighted plot de-emphasizes the shallower-dipping pole clusters and emphasizes the steeply inclined pole clusters (Figure 39). Notably, the Terzaghi-weighted contours, relative to the unweighted contours, also extend closer to the perimeter of the stereonet than the unweighted contours, providing some indication that the steeply inclined and oppositely-dipping pole clusters, (iii and iv) and (v and vi), potentially represent members of the same near-vertical to vertically-oriented fracture sets.

Given that IG_BH02 plunges southwest at an approximate 70° inclination, near vertical to vertical fractures, especially those that strike or dip in the same direction as the borehole plunge, were relatively poorly sampled during drilling. Therefore, there remains some uncertainty as to whether or not pole clusters (ii) and (viii) also represent a single, vertical, west-southwest striking fracture set. However, even with Terzaghi weighting applied these two pole clusters do not extend to the perimeter of the stereonet and so in the current interpretation they are considered to represent two separate fracture sets. There also remains some uncertainty in the overall assignment of fracture sets because a large number of poles remain outside of any assigned fracture set regions.

As a final interpretation of fracture sets for IG_BH02, pole cluster (i) is assigned to Fracture Set 1 defined by subhorizontally-oriented to moderately inclined, east-dipping fractures, pole cluster (ii) is assigned to Fracture Set 2 defined by moderately to steeply inclined, south- to south-southeast-dipping fractures, pole clusters (iii) and (iv) are combined and assigned to Fracture Set 3 defined by vertical north-northeast-striking fractures, pole clusters (v) and (vii) are combined and assigned to Fracture Set 4 defined by vertical northwest-striking fractures, pole cluster (vii) is assigned to Fracture Set 5 defined by moderately inclined fractures dipping northeast, and pole cluster (viii) is assigned to Fracture Set 6 defined by steeply inclined fractures dipping north-northwest. These final Fracture Set IDs are labelled on the unweighted and Terzaghi-weighted contour plots in Figure 39 and summarized in Table 9.

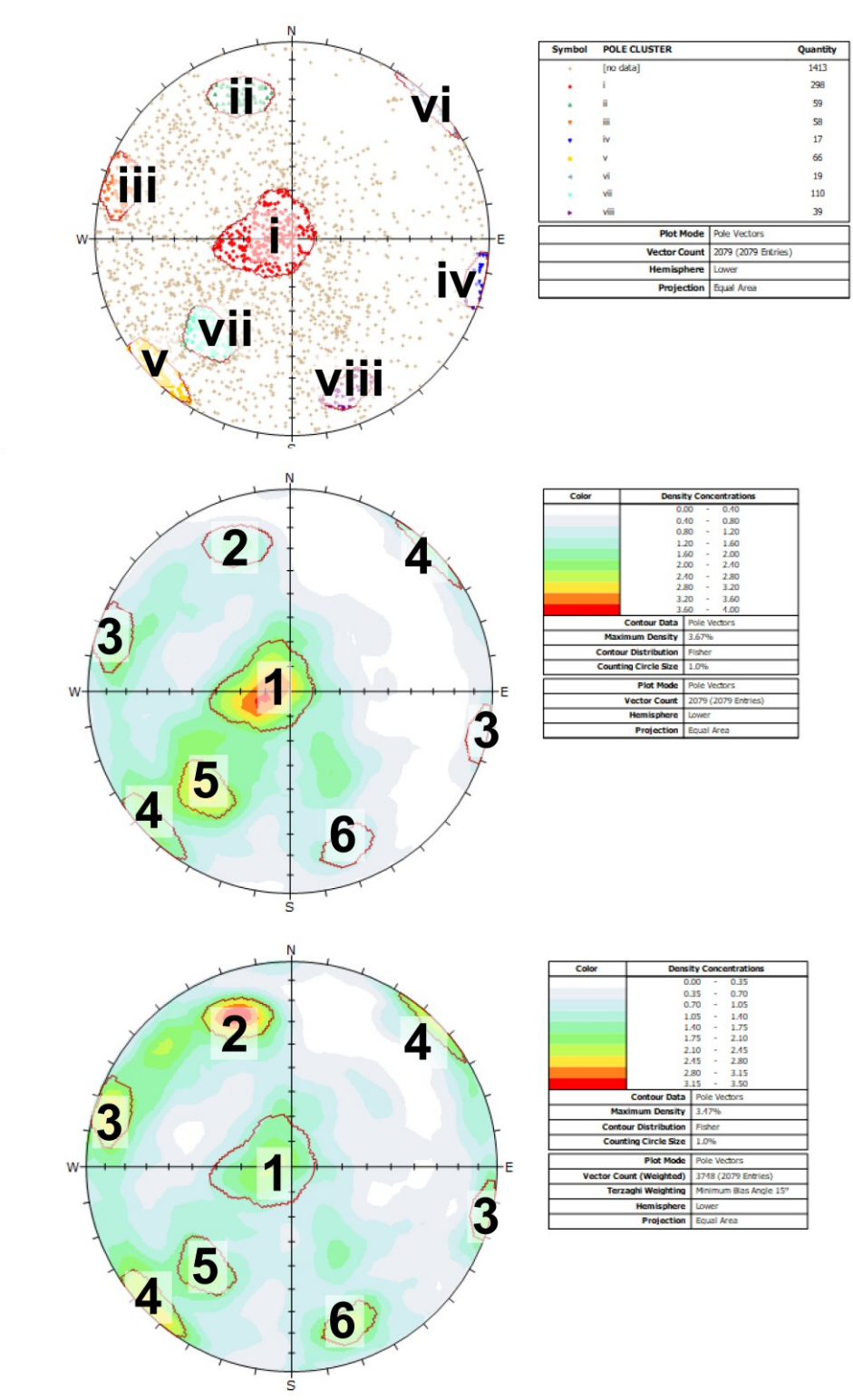


Figure 39: Stereonets of all oriented fractures, including all joints, veins and faults. Top: All fractures – poles, unweighted (n = 2079). Identified pole clusters are colour-coded to highlight their distribution. Middle: All fractures – contours (n = 2079), unweighted. Bottom: All fractures – contours, Terzaghi-weighted (n = 3748). Middle and bottom stereonets are overlain by final fracture set interpretation. See text and Table 9 for additional summary.

Table 8: Summary of interpreted fracture sets in the borehole. Presents the general description of the orientation with a mean dip and dip direction.

Fracture Set ID	Orientation	Mean Dip / Dip Direction	Fracture Count
1	Subhorizontal to moderately inclined set, dipping east	10 / 096	298
2	Moderately to steeply inclined set, dipping south-southeast	67 /160	59
3	Vertical set, striking north-northeast	90 / 102	75
4	Vertical set, striking northwest	90 / 045	85
5	Moderately inclined set, dipping northeast	55 / 041	110
6	Steeply inclined set, dipping north-northwest	71 / 340	39

Regarding the relationship between fracture sets and ductile structures, foliation is predominantly subhorizontal and poles to foliation overlap with Fracture Set 1. The majority of shear zones are subhorizontal to gently inclined and east-dipping (Figure 31), which also overlap with Fracture Set 1. Importantly, poles to steeper inclined shear zones overlap with the defined poles cluster regions of all of the additional fracture sets (Figure 31). The similarity of orientation between the brittle fracture sets and the ductile structures suggests that pre-existing ductile fabrics exerted some control on the development of brittle structures in the rock mass, in particular Fracture Set 1.

Regarding the relationship between fracture sets and types of brittle structures, the large number of joints relative to veins and faults is consistent with the presence of joints in all identified fracture sets except for the Fracture Set 5 (Figure 33). Poles to veins cluster prominently in the Fracture Set 5, and less so in the Fracture Set 1. In the Terzaghi-weighted vein dataset there is also some overlap with the Fracture Sets 2 and 3 (Figure 34). Poles to faults cluster prominently in the Fracture Set 5 and less so in Fracture Set 1. In the Terzaghi-weighted fault dataset, there is overlap with the Fracture Sets 2 and 3.

Stick plots of the distribution of each fracture assigned to a fracture set, as well as unassigned random fractures, are plotted adjacent to the per metre fracture frequency of IG_BH02 (Figure 40). This presentation aids in assessing the degree of clustering evident by fracture set. Set 1 fractures are unevenly distributed along the length of the borehole with clustering evident in the same locations as prominent peaks in the fracture frequency. There is a noticeable decrease in number of set 1 fractures below the fracture frequency peak at around 675 m, including almost 200 m without any occurrences between approximately 675 and 875 m. Set 2 fractures are sparsely distributed along the majority of the borehole, with the exception of an interval of slightly higher frequency from approximately 575 to 675 m, followed immediately by an interval of very low set 2 fracture frequency down to approximately 875 m. Set 3 fractures are irregularly distributed along the length of the borehole with slightly increased frequency intervals alternating with slightly decreased frequency intervals. Set 4 fractures are most frequent in the upper approximately 50 m of the borehole. At deeper positions along borehole the set 4 fractures are irregularly distributed with slightly increased frequency intervals alternating with slightly decreased frequency intervals. Set 5 fractures exhibit a remarkably consistent, moderate, frequency along the entire length of the borehole. Fractures assigned to set 6 are the most sparsely distributed fractures in IG_BH02. They are broadly distributed to non-existent along the majority of the borehole length, except for a peak in occurrences at around 900 m. The unassigned random fractures (1413/2079; 68%) are present along the entire length of the borehole.

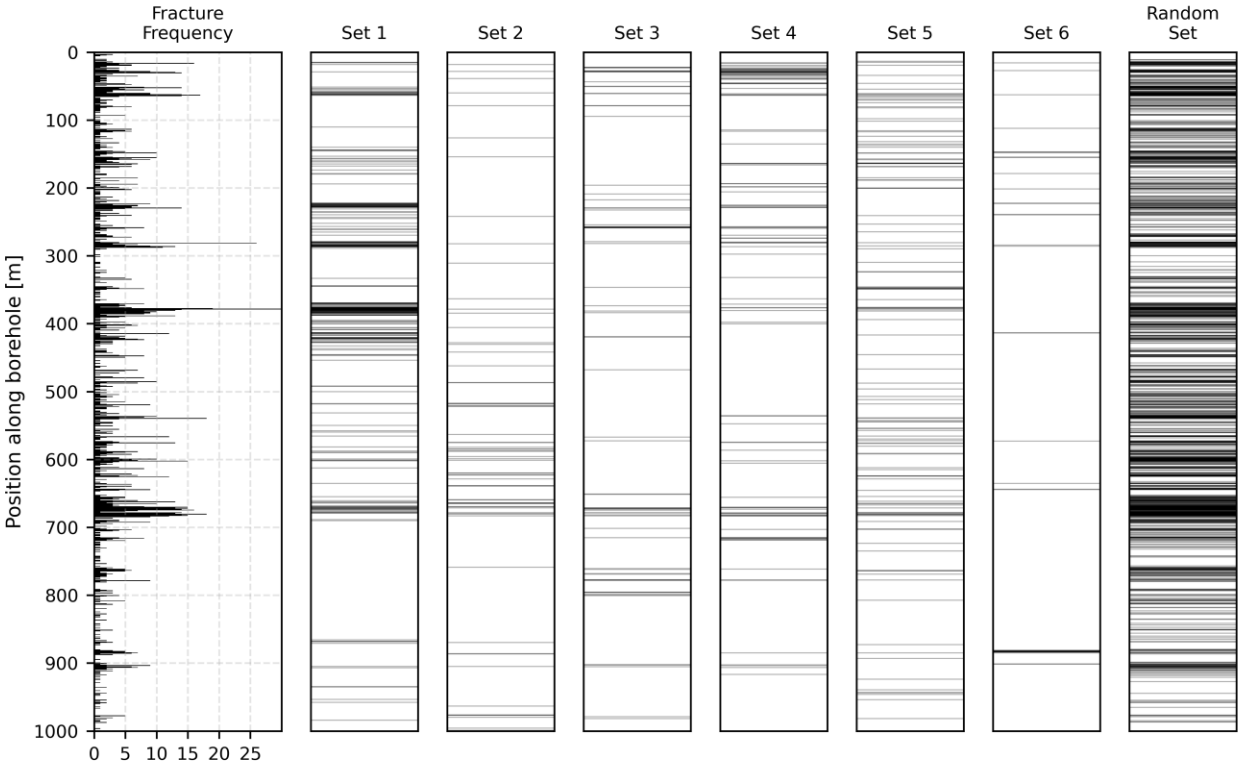


Figure 40: Summary log showing the frequency per metre of all brittle structures (left) in comparison to stick plots that show the distribution of all fractures assigned to defined fracture sets 1, 2, 3, 4, 5, and 6, as well as unassigned random fractures.

It is understood that there is some uncertainty in the present assessment, including based on the relatively large number of fractures remaining unassigned. The fracture set interpretation will continue to be refined as other boreholes are drilled in different directions.

3.2.4.3 Fracture Infill Minerals

Fracture infill, or secondary, minerals are observed in association with all fracture types in IG_BH02, and include surface staining or hairline infilling in joints, mineral lineations on fault surfaces, and vein infilling. Of the 2079 oriented planar fractures, 1919 (92 %) were identified during geological core logging to host infilling minerals. The most prominent infill mineral phase identified in IG_BH02 is quartz, which occurs both as the sole mineral phase and in association with some occurrences of chlorite, iron oxide stain, calcite, and epidote. The discussion below focuses on the orientation and distribution of these mineral phases. Stick plots of the distribution of each of these infill mineral types are plotted adjacent to the per metre fracture frequency of IG_BH02 in Figure 41.

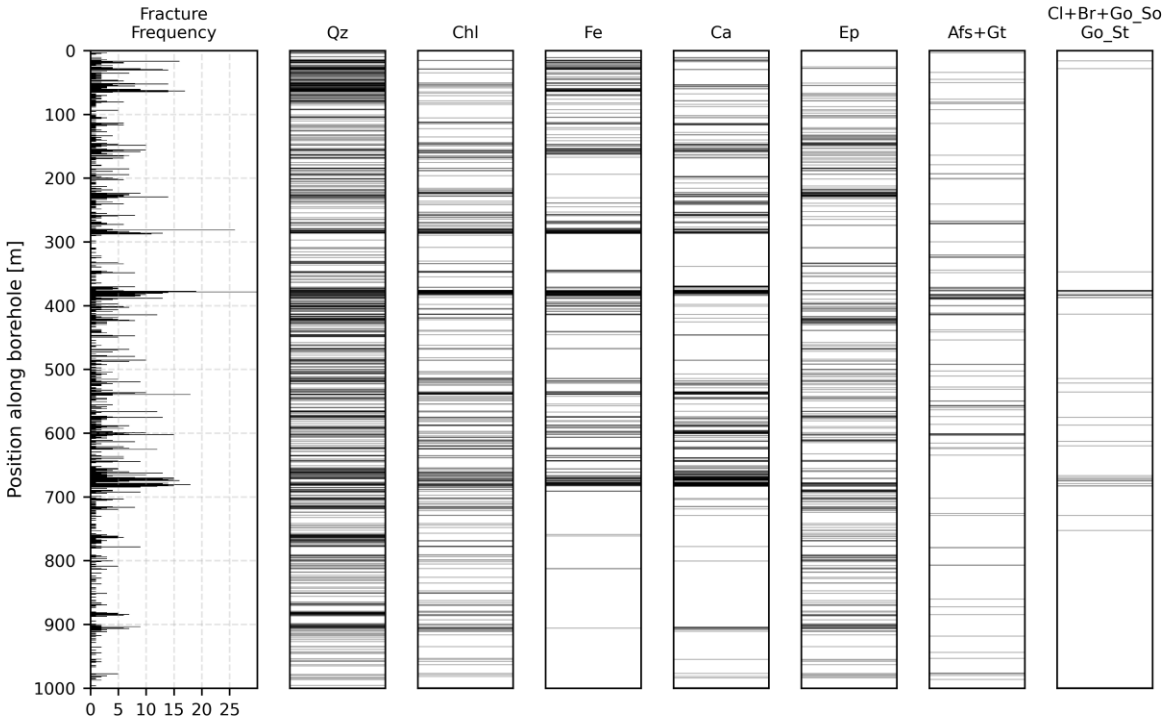


Figure 41: Summary log showing the frequency per metre (Fracture Freq.) of all brittle structures (left) in comparison to stick plots that show the distribution of the most common infill mineral phases including quartz (Qz), chlorite (Chl), iron oxide stain (Fe), calcite (Ca), epidote (Ep), a granitic (Gt) assemblage that includes some combination of alkali-feldspar (Afs) with quartz, plagioclase and biotite, and, fractures that exhibit either clay (Cl), broken rock (Br), soft clay gouge (Go_So), or stiff clay gouge (Go_St).

Quartz +/- chlorite, biotite, muscovite, epidote, iron oxide stain, or calcite was logged in 1069 of the 2079 (51 %) oriented fractures. Two prominent pole clusters of quartz +/- accessory mineral-filled fractures fall within fracture set 1 and fracture set 5 (Figure 42). To a lesser extent, fracture sets 3 and 4, and lesser so, fracture sets 2 and 6, are also evident in the quartz-filled fracture data set. Fractures with quartz +/- accessory mineral infill are distributed along the entire length of the borehole. The frequency of quartz infill is slightly increased in the upper 100 m, around 400 m, and around 675 m (Figure 41).

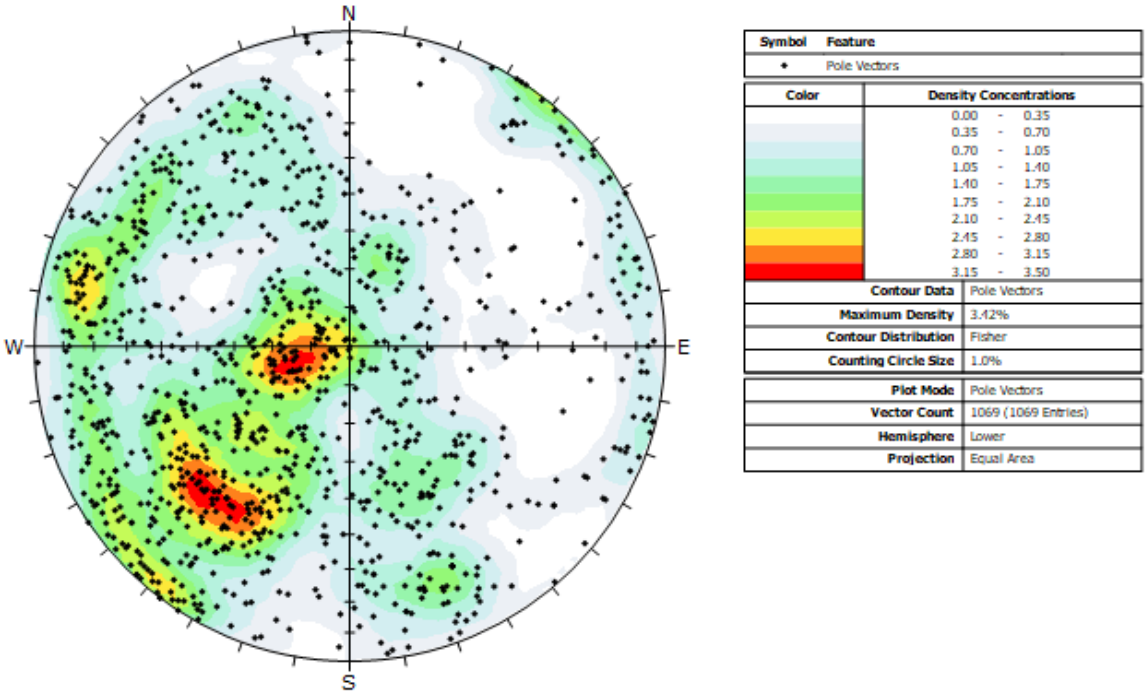


Figure 42: Stereonet plot showing poles to all fracture planes logged with quartz +/- chlorite, biotite, phlogopite, muscovite, epidote, iron oxide staining, or calcite (n = 1069).

Chlorite is identified as an infill mineral phase in 448 of the 2079 (22 %) oriented fractures and the distribution of the poles to these fractures exhibit one prominent cluster that can be attributed to fracture set 1 (Figure 43). Poles to chlorite-filled fractures also overlap fracture sets 2 and 5. The distribution of chlorite-filled fractures is relatively consistent along the length of the borehole with slight increases in concentration at around 300 m and 400 m (Figure 41).

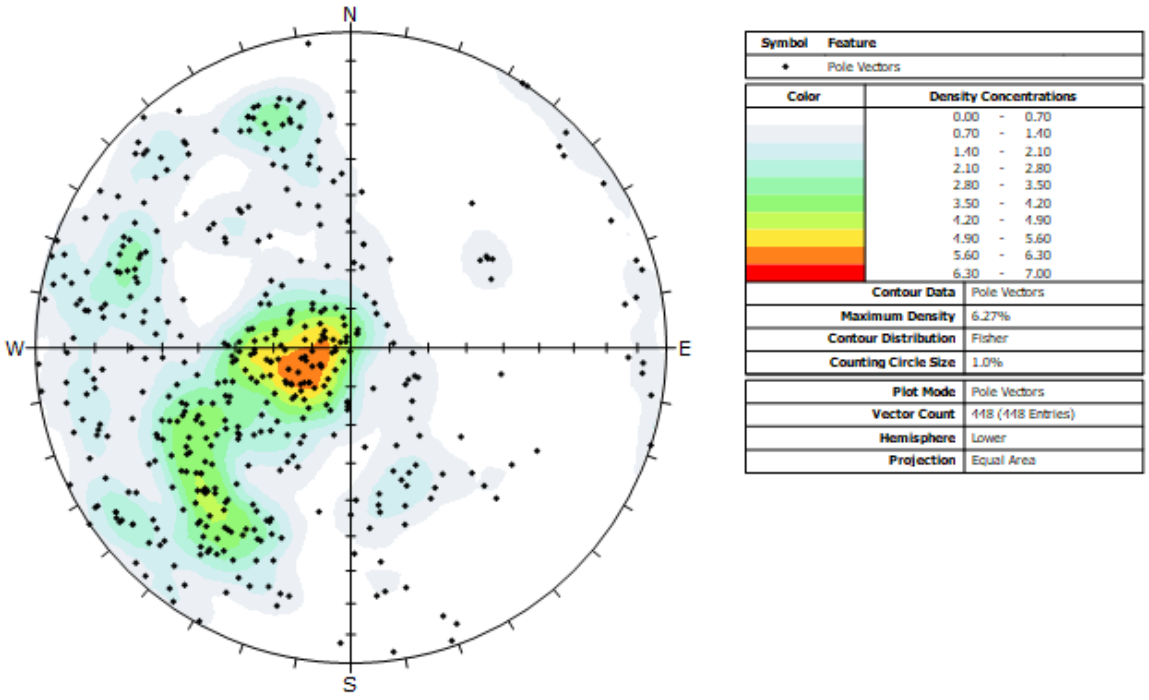


Figure 43: Stereonet plot showing poles to all fracture planes logged with chlorite (n = 448).

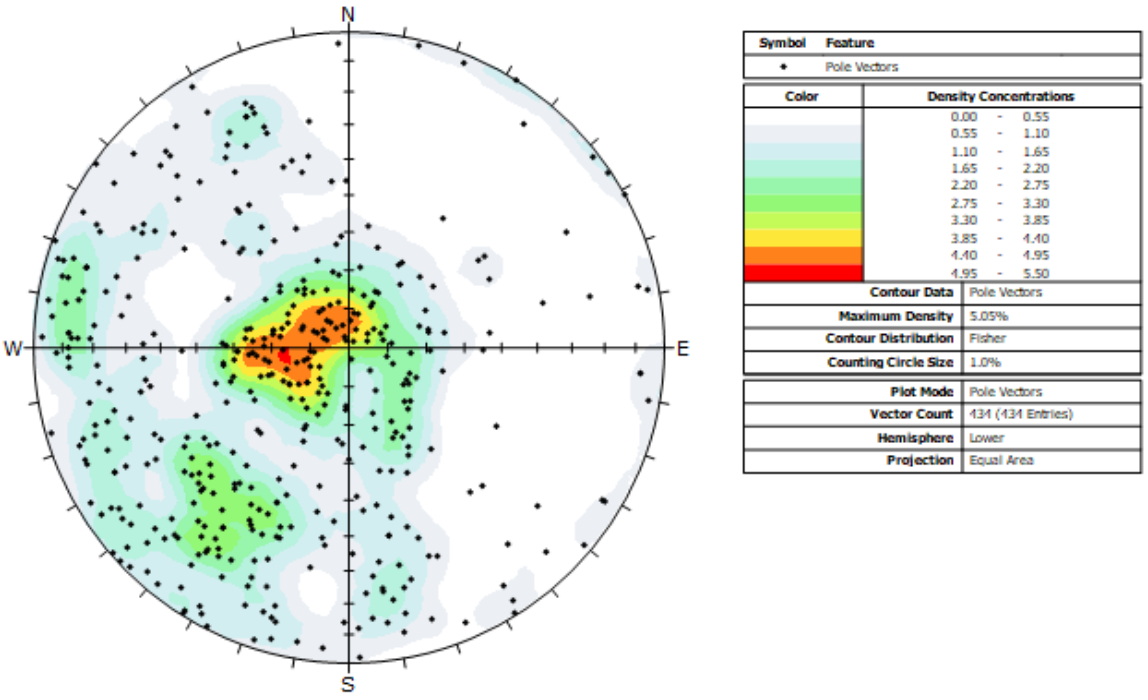


Figure 44: Stereonet plot showing poles to all fracture planes logged with iron staining (n = 443).

An iron oxide mineral, potentially hematite, is present primarily as a stain (but locally as a much thicker fill, on 434 of the 2079 (21 %) oriented fractures (Figure 44). One prominent pole cluster of

iron oxide-filled fractures fall within fracture set 1 and a less prominent pole cluster overlaps with the region of fracture set 5. The distribution of iron oxide-stained fractures is heterogeneous along the borehole with a varying frequency in the upper 675 m and a marked decrease with increasing position down to the bottom of the borehole (Figure 41).

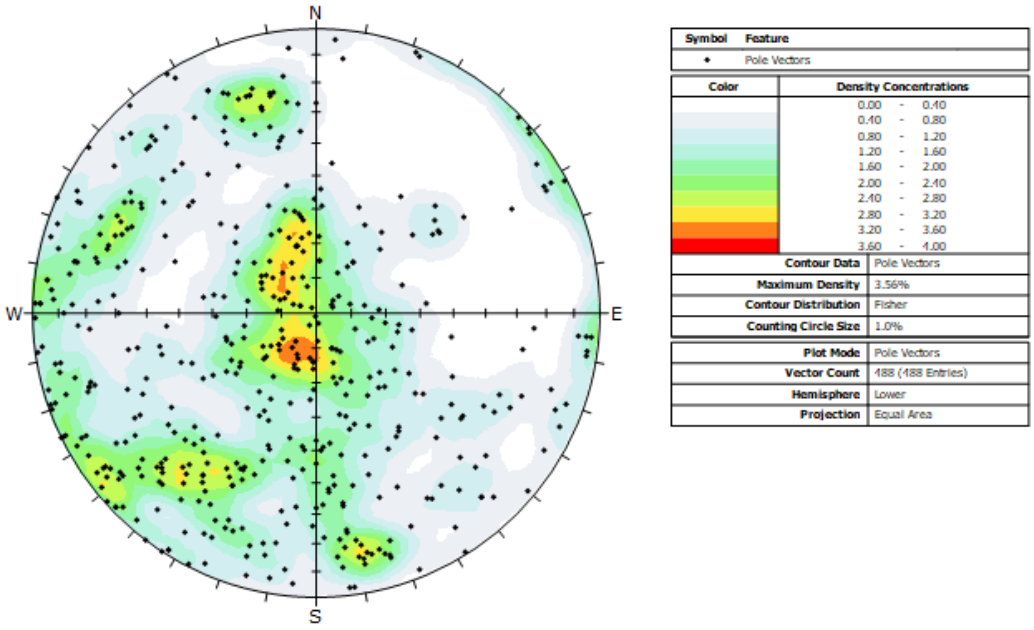


Figure 45: Stereonet plot showing poles to all fracture planes logged with calcite (n = 488).

Calcite is identified as a mineral infill phase on 488 of the 2079 (23 %) oriented fractures. The distribution of the poles to calcite-filled fractures exhibits several small but relatively prominent clusters that overlap with fracture sets 1, 2, 4, 5, and 6 (Figure 45). The distribution of calcite-filled fractures is heterogeneous along the borehole with a varying frequency in the upper 675 m and a marked decrease with increasing position down to the bottom of the borehole (Figure 41).

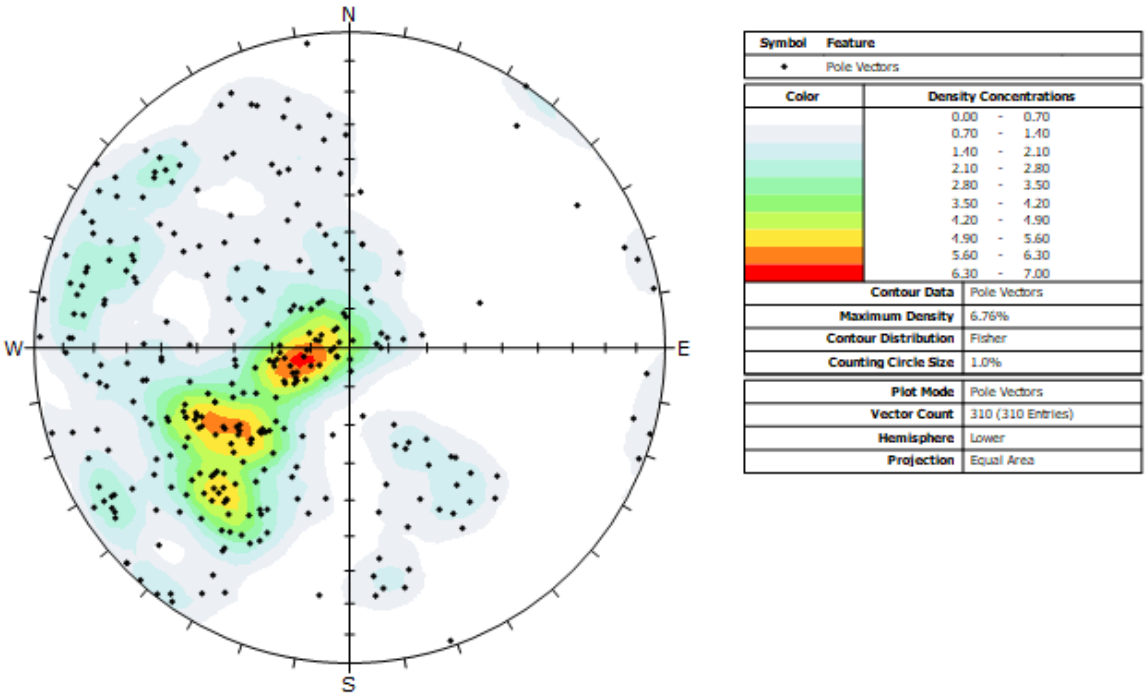


Figure 46: Stereonet plot showing poles to all fracture planes logged with epidote (n = 310).

Epidote is identified as a mineral infill phase on 310 of the 2079 (15 %) oriented fractures. The distribution of poles to epidote-filled fractures exhibits prominent pole clusters that coincides with fracture sets 1 and 5 (Figure 46). Epidote-filled fractures are relatively uniformly distributed along the entire length of the borehole (Figure 41).

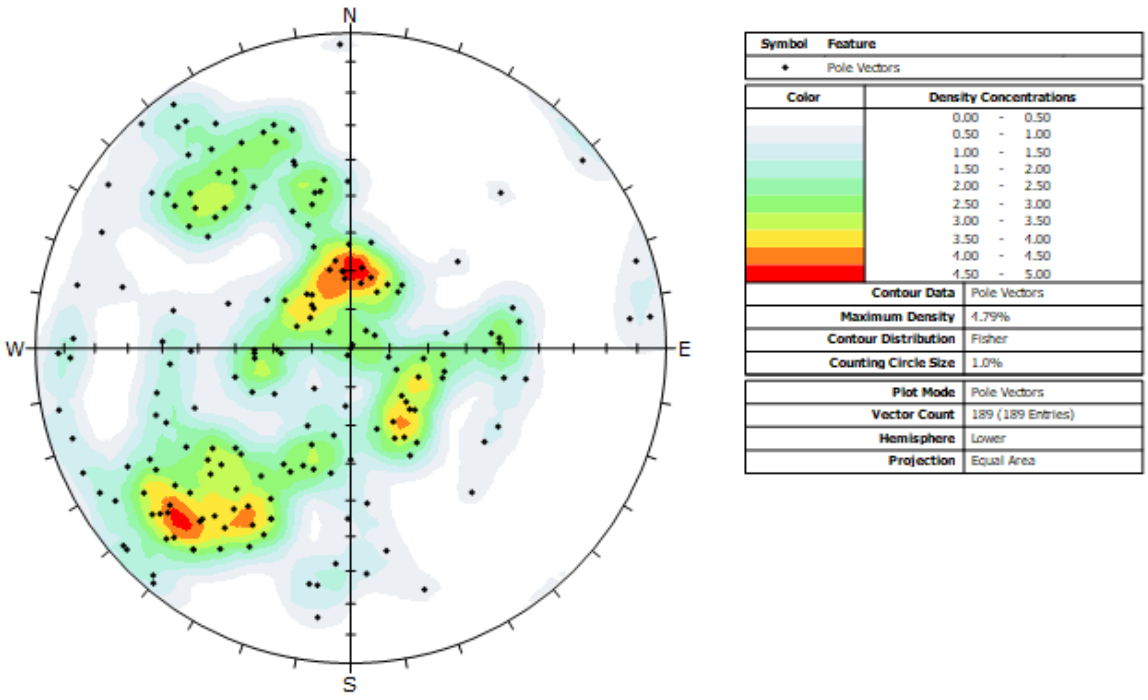


Figure 47: Stereonet plot showing poles to all fracture planes logged with granitic infill, including alkali-feldspar +/- quartz, plagioclase and biotite (n = 189).

A granitic infill assemblage characterized by alkali-feldspar +/- quartz, plagioclase and biotite, and lesser muscovite, including some coarser-grained pegmatitic occurrences, is identified in 189 of the 2079 (9 %) oriented fractures. One prominent cluster of poles to granitic-filled fractures overlaps with fracture set 1, while another overlaps with fracture set 5. A third pole cluster, defining gently inclined northwest-dipping granitic-filled fractures falls outside of any defined fracture set region (Figure 47). Granitic-filled fractures are relatively sparsely distributed along the entire length of the borehole with a slightly increased frequency around 400 m (Figure 41).

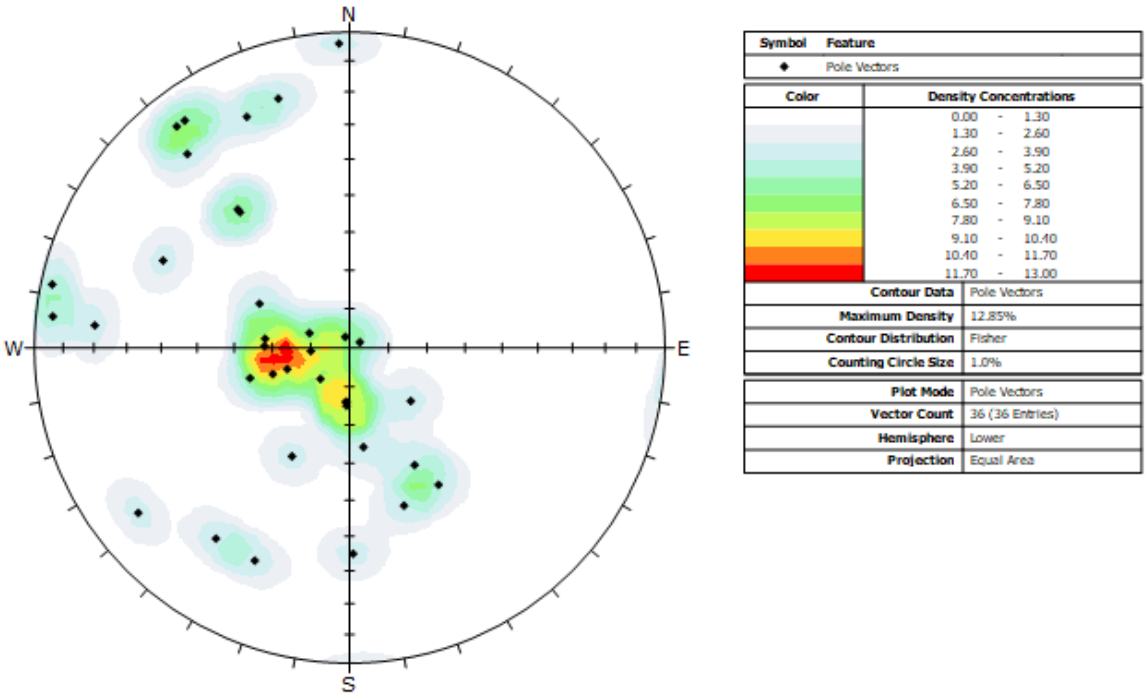


Figure 48: Stereonet plot showing poles to all fracture planes logged with clay, broken rock, or soft gouge.

Fractures infilled with clay, soft or stiff clay gouge, or broken rock, were logged in 36 of 2079 (2 %) oriented fractures. One prominent pole cluster defines gently inclined fracture planes that dip east or north (Figure 48), overlapping fracture set 1. The distribution of these clay or broken rock-filled fractures is limited to a few occurrences near the top of the borehole and with the remainder identified between approximately 350 m and 750 m (Figure 41).

A total of 160 fractures (8 %) have no associated infill mineral phase assigned to them. This includes 124 fractures that were only identified in the televiewer datasets and could not confidently be assessed for infill mineral type, even if present (Figure 49). The poles to fractures with no assigned infill minerals exhibit one prominent cluster in the southwest quadrant of the stereonet defining moderately inclined northwest-dipping fractures that were only identified in the televiewer dataset.

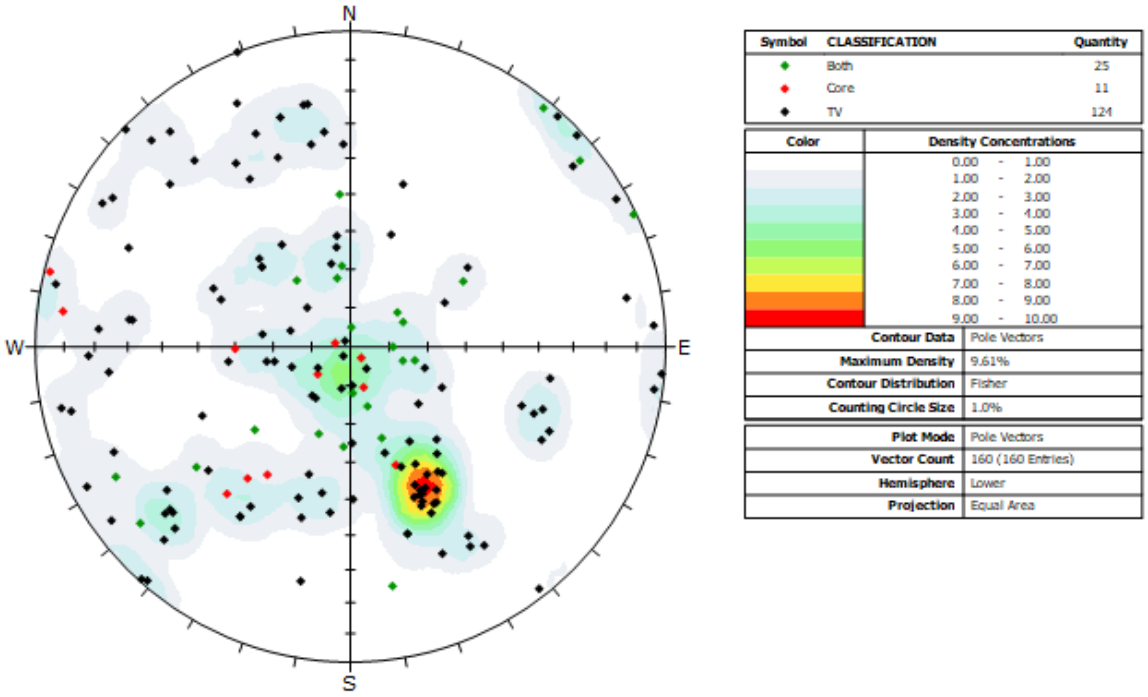


Figure 49: Stereonet showing poles to all fractures logged as having no identifiable mineral infill phase. Fractures logged in 'televiewer' (TV) datasets only, geological 'core' logging only (Core), or identified in 'both' datasets, are distinguished (n = 160).

3.2.5 Structural Unit Classification

Structural units (SU) have been defined to capture the general variation in fracture frequency along the length of the borehole. Boundaries between structural units were defined primarily on the basis of broad changes in slope visible in the cumulative fracture frequency curve. This curve was derived using the fracture dataset (i.e., joints, veins, and faults, including broken and intact/partially intact structures) and is presented in Figure 50. The per metre mean fracture frequency, derived using the same dataset, is also reported as an additional indicator of these same general trends. A total of five SUs are defined for IG_BH02 (Figure 50). Stereonets of fracture orientation data for each defined SU are included in Appendix E:.

Structural unit 1 (SU1) extends from the ground surface (0 m) to 65.50 along borehole m (Figure 50). This unit exhibits a relatively shallow slope in the cumulative fracture frequency curve and corresponds to a high degree of fracturing than the adjacent, deeper, SU2. The average fractures per metre in this unit is 4.05, however, fracture frequency is not consistent throughout the unit, and ranges from metre-long intervals completely devoid of fractures and intervals up to 18 fractures per metre. There are 246 oriented fractures in SU1, including 201 joints, 31 veins, and 14 faults (Appendix E:). Poles to these fractures overlap with Fracture Sets 3 and 4, and to a lesser extent Fracture Sets 1 and 5.

Structural unit 2 (SU2) is a 225.50 m interval that extends from 65.50 m to 291.00 m along borehole. SU2 is defined by a relatively shallow slope (though steeper than SU1) in the cumulative fracture frequency curve, corresponding to a moderate degree of fracturing of the bedrock compared to the adjacent SU's above and below (Figure 50). SU2 has an average fracture frequency of 2.10 fractures per metre and exhibits high local variability in counts ranging between 0 and 27 fractures per metre. There are 470 oriented fractures in SU2, including 296 joints, 126

veins, and 48 faults (Appendix E:). Poles to these fractures overlap with all defined Fracture Sets except for Fracture Set 2.

Structural unit 3 (SU3) is 81.50 m in length and extends from 291.00 m to 370.50 m along borehole (Figure 50). This unit shows a steep slope in the cumulative fracture frequency curve corresponding to an overall low fracture frequency with an average of 0.81 fractures per metre. Within the interval the fracture frequency shows local variability ranging between 0 and 9 fractures per metre. There are 65 oriented fractures in SU3, including 38 joints, 20 veins, and 7 faults (Appendix E:). Poles to these fractures overlap with Fracture Set 1 and another pole cluster falls between the regions defining Fracture Sets 4 and 5.

Structural unit 4 (SU4) extends from 370.50 m to 683.00 m along borehole (Figure 50), with a length of 312.50 m. Over this interval, both the fracture frequency and cumulative frequency curves show a moderate amount of fracturing compared to neighbouring intervals in the borehole, with an average frequency of 3.12 fractures per metre and ranging between 0 and 27 fractures per metre. There are 974 oriented fractures in SU4, including 709 joints, 199 veins, and 66 faults (Appendix E:). Poles to these fractures overlap with Fracture Sets 1, 2 and 5, and to a lesser extent Fracture Set 3. An additional pole cluster falls between the regions defining Fracture Sets 1 and 6.

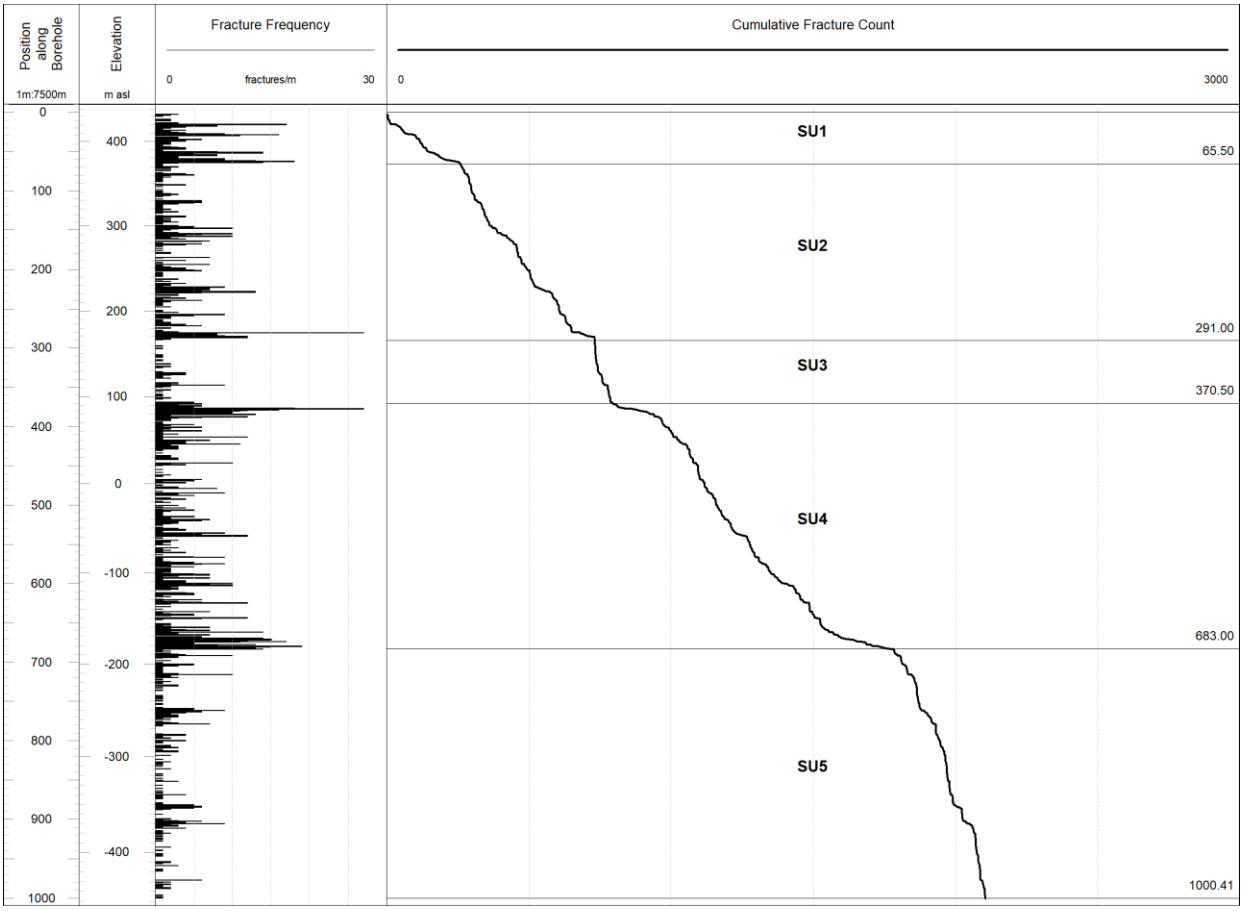


Figure 50: Per metre fracture frequency (left) and cumulative fracture frequency curve (right) showing vertical distribution of all logged joints, faults, and veins along the borehole. The cumulative fracture frequency curve shows changes in slope where boundaries in structural units (SU) are defined. Structural unit boundaries are marked on the figure, and their positions are described in Table 9.

The lower portion of the borehole is defined as Structural unit 5 (SU5), from 683.00 m to the bottom of the hole (1000.41 m along borehole). It represents a 317.41 m length along the borehole with a relatively low fracture intensity. The change in the slope of the cumulative fracture frequency curve is well defined at 683 m transitioning from SU4 to structural unit 5 (SU5). The cumulative fracture frequency curve for SU5 is characterized by a steep slope reflecting a lower degree of fracturing of the bedrock. Overall, the fractures recorded appear to be uniformly distributed and the interval is characterized by an average frequency of 1.06 fractures per metre, ranging from 0 up to 14 fractures per metre. There are 324 oriented fractures in SU5, including 230 joints, 66 veins, and 28 faults (Appendix E:). Poles to these fractures overlap with Fracture Sets 2, 3,4, 5 and 6. In addition, a small number of the fracture poles in SU5 overlap with Fracture Set 1.

As with the rock units defined previously, the criteria for defining the interpreted structural units may be modified once additional fracture data is collected in future boreholes. The framework presented here represents an interpretation based on general broad trends in the available data.

Table 9: Position ranges and standard statistics for fracture frequencies captured within the defined structural units (SU) within the borehole.

	SU1	***SU2***	***SU3***	***SU4***	***SU5***
Position Range (m)	0 – 65.50	65.50-291.00	291.00-370.50	370.50-683.00	683.00-1000.41
Thickness (m)	65.50	225.50	79.50	312.50	318.21
Min (/m)	0.00	0.00	0.00	0.00	0.00
Max (/m)	18.00	27.00	9.00	27.00	14.00
Average (/m)	4.05	2.10	0.81	3.12	1.06
Standard Deviation (/m)	4.46	3.05	1.53	4.11	1.82

3.2.6 High Fracture Frequency Intervals (HFFIs)

Along with the broad changes in fracture frequency that are used to define the SUs described above, additional more discrete intervals of increased fracture frequency were also identified in IG_BH02. These occurrences are referred to as high fracture frequency intervals (HFFIs) and are defined as a cluster of fractures (i.e., faults, joints and or veins) that exceeds a minimum relative fracture intensity threshold along a distinct borehole length (see below for details of IG_BH02). The spatial distribution of fractures and their intensity over the length of the borehole provide meaningful justification for defining HFFIs within the subsurface. Within the boreholes, the HFFIs are primarily dominated by fractures that share similar orientations within a single fracture set (i.e., fracture corridor) or by fractures in a range of orientations (i.e., fracture swarm), and locally may also comprise few minor ductile shear zones. Fracture summaries presented in the previous sections provide details on fracture sets, fracture types, and fracture mineral infilling which may contribute to the characterization of the HFFIs. At the end of this section, an attempt is made to broadly correlate the identified HFFIs with lineaments trends that were interpreted based on remote sensing data on the ground surface in proximity to IG_BH02.

HFFIs were defined using a semi-automated approach applied to the borehole fracture frequency per metre log. To visualize contiguous zones of increased fracture intensity, the fracture frequency distribution was smoothed with a uniformly weighted moving average filter using the “uniform_filter1d” function from the SciPy processing package in Python (Virtanen et al. 2020). This filter is equivalent to a moving mean and is commonly applied to time-series data to smooth high-frequency data and enable detection of broader responses. This filter preserves the low-frequency components of the input data while high-frequency components are attenuated. The magnitude of the filter is defined by the uniform window size (w), which controls the degree of

smoothing applied. In this study, a step size and window size of 1 m and 15 m, respectively, were defined.

The HFFIs are defined using the smoothed fracture frequency curve using two peak detection algorithms, “find_peaks” and “peak_widths” from the SciPy processing package (Virtanen et al. 2020). The peak detection algorithm finds all local maxima by simple comparison of neighboring values. A peak is defined as a local maximum where any sample whose two direct neighbours have a smaller amplitude. The difference in magnitude with the neighbouring values is defined by a threshold value in the algorithm, such as the peak prominence. The prominence of a peak measures the magnitude of the peak relative to the neighbouring values and is defined as the vertical distance between the peak and its lowest neighbouring value. Using the smoothed fracture frequency curve as input data, the peak prominence threshold was set at four for this study.

Once peaks are defined, the peak widths are based on the anomaly width at a specified distance between the peak maxima and the lowest neighbouring value (i.e., along the prominence height). In this study, a relative height of 0.5 is used at a threshold to extract the width of the peak.

Figure 51 presents the HFFI results from the fracture frequency data in IG_BH02. Based on the smoothed fracture frequency data and the peak detection analysis, from and to position along borehole (in metres) and overall width (in metres along borehole axis) of five HFFIs have been defined. Figure 51 shows the cumulative counts of fractures along the length of the borehole and displays the fracture frequency per metre and the filtered fracture frequency. The cumulative curve, along with these data plots show evidence of discrete intervals of increased fracture intensity. Stick plots of joints, veins and faults display the location of each individual fracture type along the borehole length. A summary of the HFFIs for IG_BH02 are presented in Table 10, including dominant fracture orientation(s), rock type(s) present, fracture set association, alteration, and fracture infill characteristics.

Although the results presented in Figure 51 are visually verified to be ideal candidates for HFFI interpretation, changing the peak detection algorithm input parameters can result in other possible HFFI outcomes. For example, reducing the peak prominence threshold or the applied window size in the smoothing function results in an increase in the number of peaks identified from the data. Conversely, increase these parameters reduces the number of peaks identified. Similarly, adjusting the peak height parameter used in the peak width algorithm works to either increase or decrease the width of the identified interval, however the peak location remains the same. Despite these possible uncertainties, the approach used here attempted to optimize the peak picking parameters through trial and error in order to visually match the identified peaks to the obvious increases in fracture frequency observed in the data. The application of this approach can then be applied to other boreholes, therefore reducing interpreter bias and subjectivity in the identification of HFFI in the boreholes.

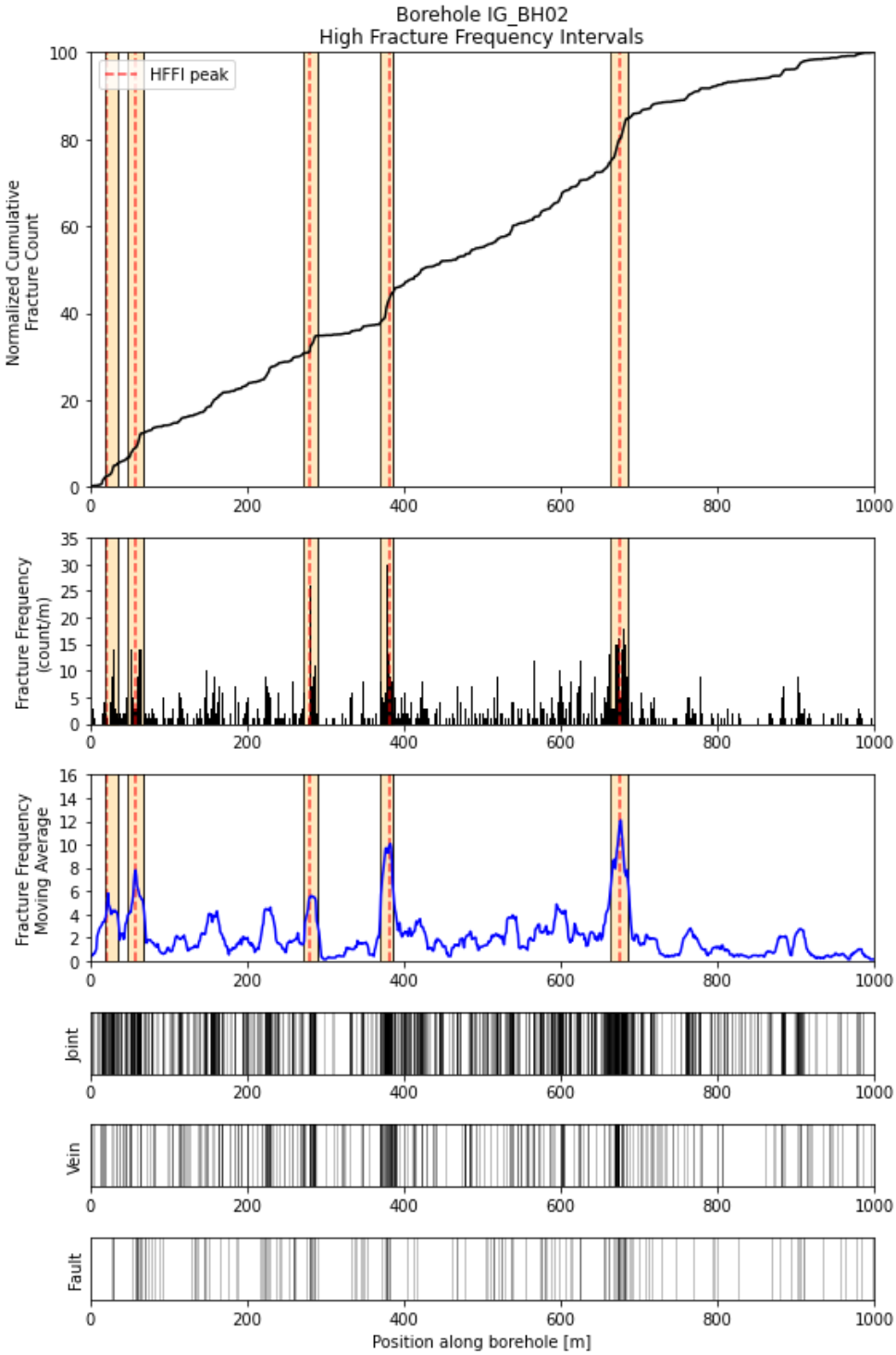


Figure 51: High fracture frequency intervals (HFFIs) interpreted based on fracture intensity from borehole fracture frequency log. Five high fracture frequency intervals are outlined by their yellow bands. The red dashed line represents the peak location. Stick plots indicate the distribution of each fracture type (joint, vein, fault) along the length of the borehole.

Table 10: High Fracture Frequency Intervals from IG_BH02

High Fracture Frequency Interval (HFFI)	Top Position (m)	Bottom Position (m)	Width (m)	Dominant Fracture Set Orientations* (**major;** minor *(STR TYPE)*)	Rock Type, Alteration, Infill
IG_BH02_HFFI_1	19.11	34.38	15.27	**045/85** *(JN, FLT)*; 108/77 *(JN)*	Biotite granodiorite-tonalite with one feldspar-phyric tonalite dyke. Hematization, bleaching, potassic alteration, minor sericitization and silicification. Quartz, muscovite, and minor chlorite infill associated with the 045/85 peak. Quartz, muscovite, and iron oxide infill associated with the 108/77 peak. Quartz and iron oxides are most common infill types.
IG_BH02_HFFI_2	47.50	68.27	20.77	028/51 *(JN, VN, FLT)*, 115/77 *(JN, VN)*, 167/44 *(JN)*	Biotite granodiorite-tonalite, two feldspar-phyric tonalite dykes, and two quartz dykes. Bleaching, hematization, potassic alteration, minor silicification and sericitization, and one occurrence of chloritization. No specific infill type associated with each of the fracture sets; dominant infill type in interval is quartz.
IG_BH02_HFFI_3	272.84	289.33	16.49	**086/26** *(JN, VN, FLT)*	Biotite granodiorite-tonalite, one aphanitic tonalite dyke, and two feldspar-phyric tonalite dykes. Hematization, potassic alteration, minor chloritization and silicification, and one interval of bleaching. Chlorite and iron oxide infill associated with main fracture set. Quartz infill is common in the interval.
IG_BH02_HFFI_4	369.78	386.62	16.84	**061/18** *(JN, VN, FLT)*; 125/05 *(JN, VN)*	Biotite granodiorite-tonalite, three aphanitic tonalite dykes, four pegmatite dykes, and one feldspar-phyric tonalite dyke. Chloritization, hematization, potassic alteration, silicification, and minor bleaching. Calcite infill dominantly associated with the fracture set oriented 061/18. Many infill types logged in this interval: iron oxide, quartz, muscovite, granite (alkali feldspar, quartz, and plagioclase), muscovite, chlorite, and minor chlorite, soft gouge, and epidote.
IG_BH02_HFFI_5	662.81	686.19	23.38	097/86 *(JN, VN)*, 162/68 *(JN, VN)*	Biotite granodiorite-tonalite with four feldspar-phyric tonalite dykes, three amphibolites, and two quartz dykes. Potassic alteration, carbonatization, minor bleaching, hematization, silicification, and chloritization. Calcite, chlorite, and clay infill associated with 097/86 fracture set. Calcite and quartz infill associated with the 162/68 fracture set. Other common infill types logged in interval are epidote, iron oxide, soft gouge, and talc.

**DipDirection/Dip convention*

For each HFFI, fracture (including joints, veins, and faults) orientations are plotted on stereonets to further evaluate the orientation distributions and define one or more orientations that are characteristic of the interval (e.g. HFFI_1 in Figure 52, see Appendix F: for stereonets of all defined HFFIs). Figure 52 presents a Terzaghi-weighted stereonet for HFFI_1 containing 64 fractures (faults, veins, and joints). Dominant orientations in Table 10 are interpreted manually as the peaks defined by the Terzaghi-weighted pole density maxima. The resulting fracture orientations from within the HFFIs can provide input into modelling such zones as surfaces in deterministic fracture network models.

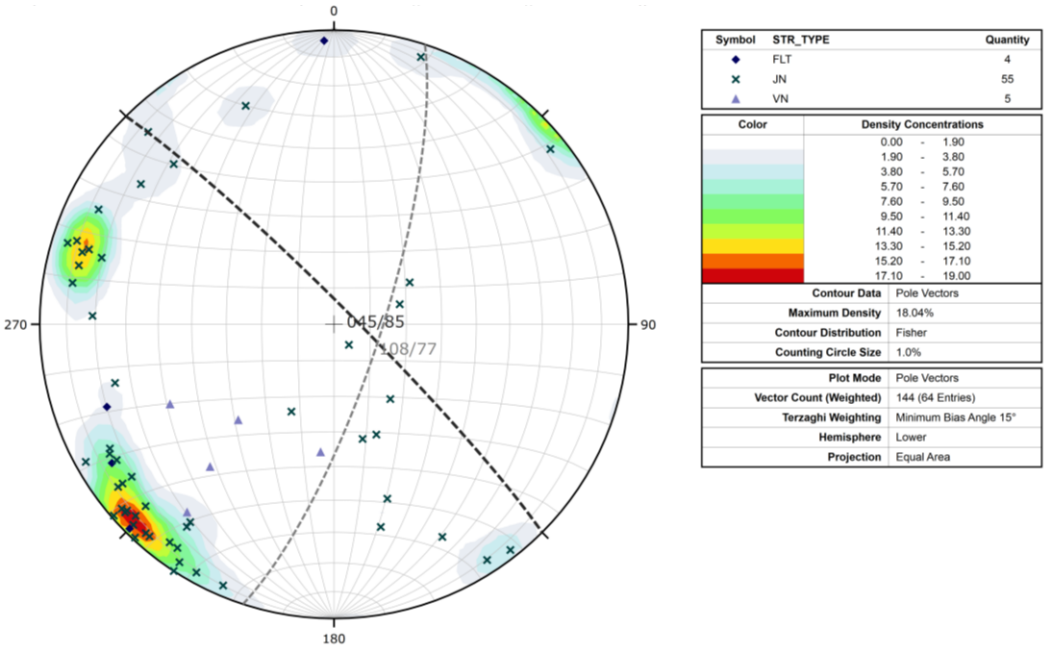


Figure 52: Terzaghi-weighted stereonet plot of fractures (JN, VN, FLT) within high fracture frequency interval 1 (HFFI_1) from 19.11 – 34.38 m. Two peaks are defined, a major peak with a mean orientation of 045/85 (best fit plane shown as black dashed great circle) and a minor peak with a mean orientation of 108/77 (best fit plane shown as grey dashed great circle; DipDirection/Dip convention).

HFFI_1 (19.11 – 34.38 m)

HFFI_1 is dominantly biotite granodiorite-tonalite with a 0.53 m feldspar-phyric tonalite dyke from 28.65 – 29.18 m (Figure 53). There are visible, pink-coloured alteration halos (logged as potassic alteration and hematization) around the feldspar-phyric tonalite dyke. The contacts of the dyke cluster with the major peak that dips 85° toward the northeast. The fractures in this interval are mainly joints with four logged faults and five logged veins. Fractures are well-spaced, and most are at a relatively low angle to the core-axis, indicating a steep dip. The intersection of these steep fractures and minor shallow dipping fractures creates intervals of broken core, especially visible around the upper and lower contacts of the dyke (Figure 53). There are three shear zones associated with the major fracture peak (045/85) and one associated with the minor peak at 108/77. All shear zones are minor, discrete structures and are in the biotite granodiorite-tonalite with the exception of one logged at 28.91 m in the tonalite dyke. The increase in fracture frequency is almost certainly related to the tonalite dyke, as evidenced by the similar orientation of the contacts to the main fracture orientation peak. The lack of notable faults or shear structures suggests it is not a structurally significant interval.



Figure 53: Core from a portion of HFFI_1 (24.71 – 36.28 m). Biotite granodiorite-tonalite above and below the feldspar-phyric tonalite dyke is characterized by well spaced, shallow and steeply dipping fractures. Pink coloured alteration halos (logged as potassic alteration and hematization) are visible around the dyke. Fracture intensity does not appear to significantly increase in association with the dyke (24.71-29.18 m).

HFFI_2 (47.50 – 68.27 m)

HFFI_2 is dominantly biotite granodiorite-tonalite with two feldspar-phyric tonalite dykes and two quartz dykes. The feldspar-phyric tonalite dykes are from 50.74 – 52.39 m (1.65 m) and 62.89 – 63.47 m (0.58 m). The quartz dykes are around the deeper feldspar-phyric tonalite dyke, from 62.59 – 62.8 m (0.21 m) and 63.47 – 63.59 m (0.12 m). Pink and white coloured alteration (logged as hematization, potassic alteration, bleaching, and silicification) is visible at the upper and lower contacts of the feldspar-phyric tonalite and quartz dykes (Figure 54). The orientations of the fractures in this interval are well dispersed with three minor clusters identified: one dipping steeply to the southeast, one dipping moderately to the south-southeast, and one dipping moderately to the northeast. Some of the dyke contacts cluster with the minor fracture peaks identified (2/7 contacts cluster with the 167/44 peak; 2/7 contacts cluster with the 028/51 peak) and the rest (3/7) are randomly oriented. There appears to be an increase in fracture frequency associated with the dykes, especially the deeper feldspar-phyric tonalite and quartz dykes (Figure 54). There are six discreet shear structures logged between and within the feldspar-phyric tonalite and quartz dykes. The shear structures do not cluster with any of the minor fracture peaks. The most common infill minerals logged are quartz and iron oxide with minor logged muscovite, plagioclase, calcite, chlorite, biotite, and epidote. There is no correlation between any of the logged mineral infills and the minor fracture orientation clusters. The increase in fracture frequency appears to be associated with the feldspar-phyric tonalite and quartz dykes, but the fractures in the surrounding biotite granodiorite-tonalite are otherwise well-spaced and not associated with any significant infill or alteration. One source of uncertainty in this interval is the quartz dykes, which are interpreted as hydrothermal veins. Their presence suggests fluid flow either during or after emplacement of the feldspar-phyric tonalite dyke.



Figure 54: Core from a portion of HFFI_2 (59.45 – 71.06 m). Biotite granodiorite-tonalite with visible pink and white alteration (logged as hematization, potassic alteration, bleaching, and silicification) surrounding feldspar-phyric felsic and quartz dykes. There is a slight visible increase in fracturing surrounding the dykes and six logged shear structures in and around the dykes.

HFFI_3 (272.84 – 289.33 m)

HFFI_3 is mainly biotite granodiorite-tonalite with one 0.72 m aphanitic tonalite dyke from 280.09 – 280.81 m and two feldspar-phyric tonalite dykes from 284.21 – 284.39 m (0.18 m) and 286.21 – 286.84 m (0.63 m). Pink coloured alteration (logged as potassic with minor hematization) and silicification is visible around the two feldspar-phyric tonalite dykes (Figure 55). Fractures in this interval are dominantly clustered dipping shallowly toward the east (086/26). The four contacts of the feldspar-phyric tonalite dykes are oriented with the main cluster of fractures (shallowly dipping toward the east) whereas the contacts of the aphanitic tonalite dyke are steeply dipping toward the north. There are seven shear structures logged, all associated with the aphanitic or feldspar-phyric tonalite dykes, but almost all of them fall outside the orientation of the main cluster of fractures. The mineral infill logged is dominantly chlorite and quartz; chlorite infill is logged in fractures that cluster with the main peak while the quartz infill is predominantly in randomly oriented structures. Iron oxide and calcite infill are also logged in fractures that cluster with the main peak. The increase in fracture frequency and alteration is associated with the three dykes, and fractures in the surrounding biotite granodiorite-tonalite are well spaced.

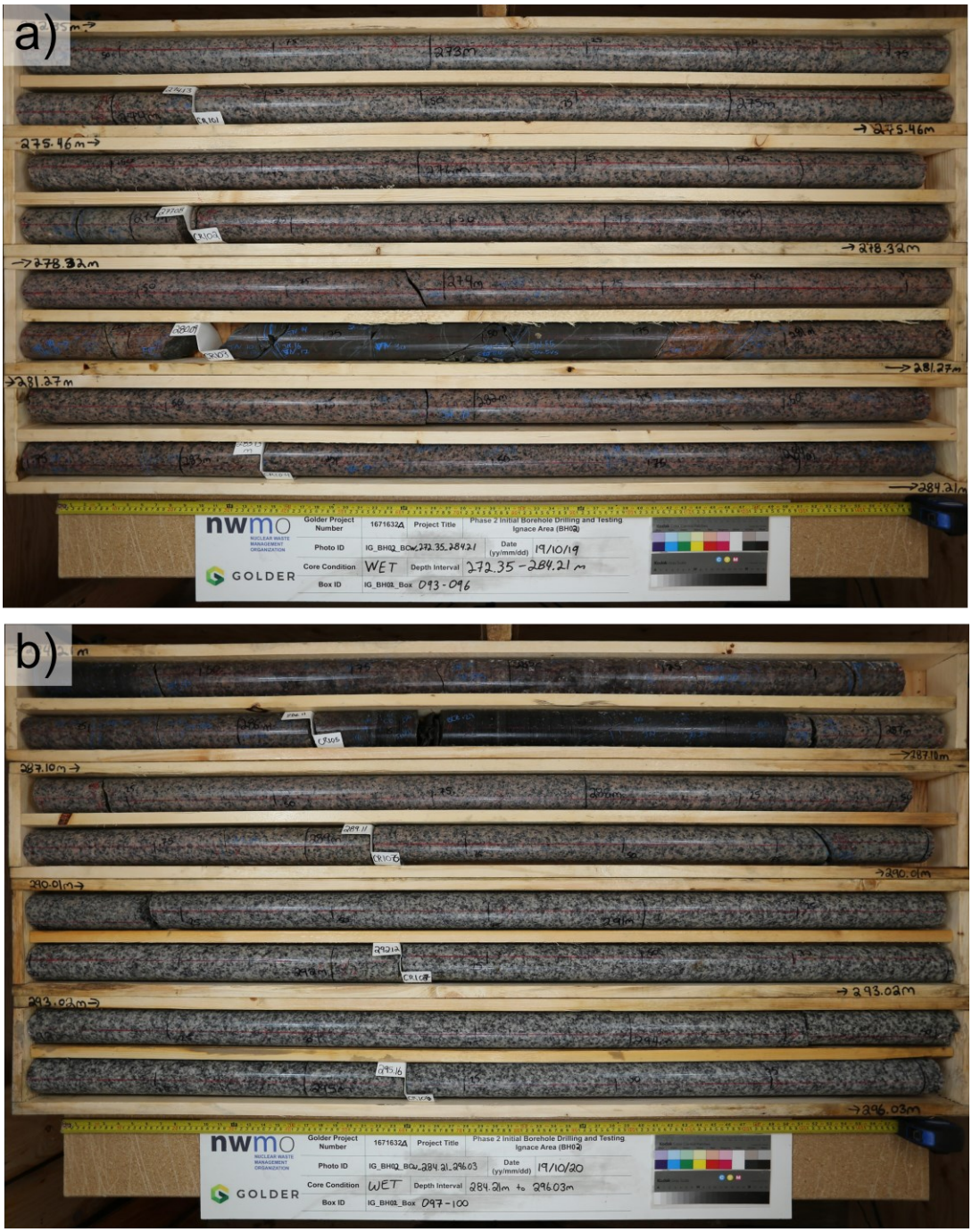


Figure 55: Core from a portion of HFFI_3 (a: 272.35 – 284.21 m; b: 284.21 – 296.03 m). Biotite granodiorite-tonalite with an aphanitic tonalite dyke (a) and feldspar-phyric tonalite dykes (b). Pink coloured alteration is visible around the dykes (logged as potassic alteration and minor hematization). At the top of (b), silicification is logged between the two feldspar-phyric tonalite dykes. Fractures are well spaced in the biotite granodiorite-tonalite and more concentrated in the dykes.

HFFI_4 (369.78 – 386.62 m)

HFFI_4 starts in an aphanitic tonalite dyke (0.57 m width) with a 0.18 m thick pegmatite dyke at the lower contact. This is followed by 0.55 m of biotite granodiorite-tonalite, a 0.1 m pegmatite dyke,

another 0.22 m thick aphanitic tonalite dyke, and a 0.06 m pegmatite dyke at the lower contact. Then there is 1.48 m of biotite granodiorite-tonalite, a 0.12 m pegmatite dyke at 371.4 m, and then 3.28 m of biotite granodiorite-tonalite. From 376.34 – 380.85 m there is a feldspar-phyric tonalite dyke (4.51 m total) and then the interval ends with 7.31 m of biotite granodiorite-tonalite (Figure 56).

There is visible pink coloured alteration associated with the dykes, which is logged as hematization and potassic alteration (Figure 56). Significant silicification is also logged in association with the dykes, as well as minor chloritization and bleaching. HFFI_4 has a broad cluster of fractures that dip shallowly toward the east. Eight of the 12 dyke contacts are oriented with the fracture peak, three are steeply dipping toward the northeast, and one is moderately dipping toward the east. There are 19 shear structures logged in this interval, and 17 of them cluster with the main fracture peak. Fracture intensity and alteration visually increases around the dykes, in particular the thick feldspar-phyric tonalite dyke at 376.34 m.

There are several shear zones and one interval that is logged as sheared but appears to be infilled breccia in the middle of the feldspar-phyric tonalite dyke, around 380.25 m (Figure 56b). The infill material is red, potentially iron-oxide, suggesting a later-stage brittle overprint of the initially ductile deformation that involved iron-rich fluids. Eight faults and one broken core zone are logged in this interval, mainly associated with the dykes (Figure 56); seven of the eight faults and the broken core zone all cluster with the main orientation peak (061/18). The most common infill mineral logged is calcite, with iron oxide and quartz the next most common. As there is such a strong cluster of structures in this interval, all of the logged infill is associated with the main cluster. Muscovite infill shows the greatest spread in logged orientation, some instances cluster with the main peak while more than half (9/16) are randomly oriented. This interval has 5 occurrences of clay infill and 2 occurrences of soft gouge, which is significant as the entire borehole only has 12 logged occurrences of these infill types. The presence of these infill types suggests geologically younger displacement and their orientation mirrors that of the interval, dipping shallowly toward the east.

Overall, HFFI_4 is characterized by a strong cluster of brittle structures, the association of ductile structures that are similarly oriented, the presence of alteration around the dykes, the brittle overprinting of ductile structures with iron-oxide infill minerals and clay and soft gouge infill suggests geologically younger displacement at this interval.

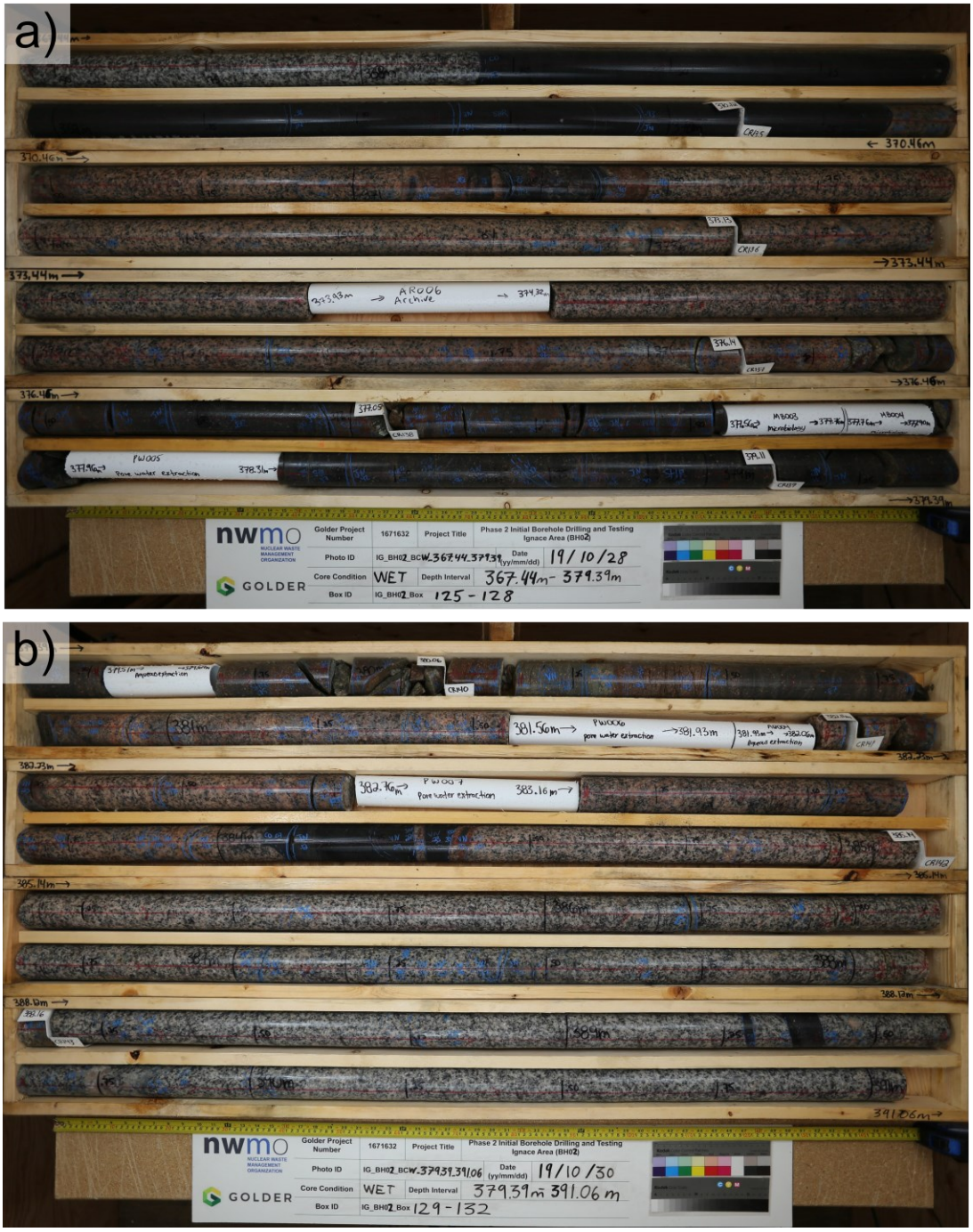


Figure 56: Core from a portion of HFFI_4 (a: 367.44 – 379.39 m; b: 379.39 – 391.06 m). The interval starts in the aphanitic tonalite dyke at the top of (a) and continues to the third box of (b). Pink coloured alteration (logged as potassic and hematization) is visible around all the tonalite and pegmatite dykes. Visually, fracture intensity appears to increase around the dykes, especially the feldspar-phyric dyke from the bottom of (a) to the top of (b). There is an interval that is logged as shear but appears to be breccia filled with red (iron-oxide?) minerals around 380.25 m (top of b). The majority of the brittle and ductile structures cluster in a similar orientation, dipping shallowly toward the east (086/26).

HFFI_5 (662.81 – 686.19 m)

HFFI_5 straddles the bottom of RU2 and the top of RU1b and starts in biotite granodiorite-tonalite. At 668.18 m there is a 2.58 m thick feldspar-phyric tonalite dyke, followed by 1.06 m of biotite granodiorite-tonalite. Beginning at 671.82 m there is an interval of amphibolite, two feldspar-phyric felsic dykes, and two quartz dykes that ends at 677.92 m. Following this there is 5.12 m of biotite granodiorite-tonalite, a small 0.115 m feldspar-phyric felsic dyke, and then the interval ends in biotite granodiorite-tonalite.

There is pinkish alteration visible around the dykes and the amphibolite, logged as potassic alteration and some minor hematization (Figure 57) and a light grey alteration that was logged as silicification and bleaching is visible at the bottom of the interval (Figure 57b). A sample of this grey alteration was sent for lithogeochemical and petrographic analysis and it was found to be almost 100% secondary albite, making this albitized interval the strongest alteration observed in IG_BH02 (see section 3.2.2 for more information). Minor chloritization is logged in association with the amphibolite.

The structures (faults, joints, and veins) in HFFI_5 show a wide range in orientations. Two peaks are defined, both steeply dipping, one toward the southeast and the other toward the east. Compared to the other HFFIs, the peaks are defined by relatively low-density concentrations. None of the contacts are associated with these peaks, and only two of 12 logged faults are associated. Of the ductile structures logged, one of 19 structures (a shear zone) is associated with one of the fracture peaks. The other 11 shear zones, single logged mylonite, and six foliation measurements are all clustered around the centre of the stereonet, dipping shallowly toward the north, northeast, and east, respectively. The most common infill mineral in HFFI_5 is calcite, followed by quartz, epidote, and chlorite. As with all structures in the interval, there is a significant spread in orientations with all of these infill types. The cluster defining planes that dip moderately toward the southeast does seem to have dominantly quartz infill logged, but otherwise there are no strong associations between orientation and mineral infill. HFFI_5 has two occurrences of clay and two of soft gouge, which is significant considering the entire borehole has these two infill types logged only 12 times total. The presence of these infill types may indicate geologically younger displacement in this interval. Despite the broad spread in structural orientations, the presence of highly altered host rock (albitized biotite granodiorite-tonalite), the amphibolite, the quartz dykes (hydrothermal veins), and the clay and soft gouge infill suggest that this potentially is, or was in the past, an important zone of fluid movement and may have experienced geologically younger displacement than other HFFIs.

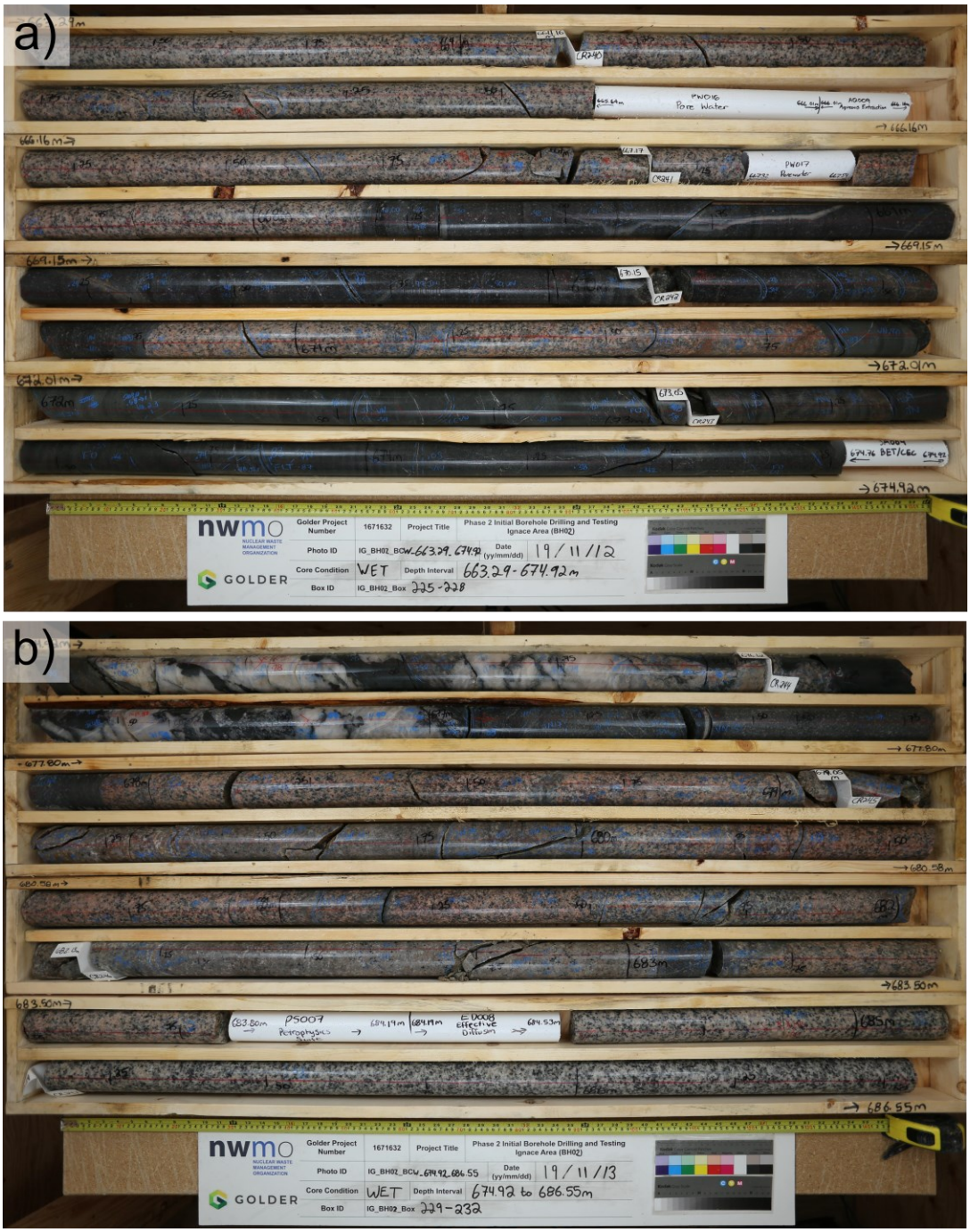


Figure 57: Core from HFFI_5 (a: 663.29 – 674.92 m; b: 674.92 – 686.55 m). The interval starts in biotite granodiorite-tonalite in the box just above (a) and continues into the fourth box of (b). Pink coloured alteration (logged as potassic and hematization) is visible around all the tonalite and quartz dykes and amphibolite. The lighter grey alteration visible after the quartz dykes in (b) is the strongest alteration observed in IG_BH02; the biotite granodiorite-tonalite has been almost completely albitized. The brittle and ductile structures in this interval have a wide range of orientations, but the brittle structures do form two clusters, one steeply dipping to the east and the other steeply dipping to the southeast. Logged ductile structures are predominantly shallowly dipping to the north, northeast, and east. Despite this spread in structural orientation, the strong alteration and thick quartz veins (interpreted as hydrothermal veins) suggest that this interval was, or is, an important zone of fluid movement.

Comparison of Fracture Orientations to Local Lineament Network

Fracture orientations in the borehole display some correlation to the dominant lineament trends that were interpreted using remote sensing data (DesRoches et al., 2018). Figure 58 displays the interpreted structural lineaments in proximity to IG_BH02. West-northwest trends are the most prominent lineament azimuth in the unweighted rose diagram (Figure 59a). However, by weighting the lineaments by length (Figure 59b), there is a dominant north-northeast trend based on the presence of a single long lineament located in the western part of Figure 58. Three northwest trending lineaments cross the path of IG_BH02 (Figure 58).

Rose diagrams for both unweighted and Terzaghi-weighted borehole-logged fractures, with a minimum dip angle of 45°, are shown in Figure 60. Notwithstanding the broad spread in orientations, general northwest and northeast peaks are evident in the weighted and unweighted borehole dataset.

Comparing the interpreted lineament trends with those of the interpreted fracture sets highlights some similarities in orientations. The north northeast-trending lineaments are consistent with the strike of fracture set 3 and some of the peaks in HFFI_1, 2, and 5. The northwest-trending lineaments are consistent with the strike of fracture sets 4 and 5, and one cluster of shear zones. The northwest-trending lineaments are also consistent with the major fracture peak in HFFI_1.

It is worth noting that the northeast-trending lineaments parallel the dominant direction of glacial advance and retreat across the region. It is uncertain therefore whether all northeast trending interpreted lineaments reflect structurally significant features of the bedrock or if some are instead a product of glacial erosion. However, the understanding that the steeply inclined and northeast-striking fracture set 3 is present along the length of the borehole suggests that at least some of these lineaments do represent real bedrock structures. It is therefore a working hypothesis that the same orientations clear at surface lineament scale are also present at borehole scale.

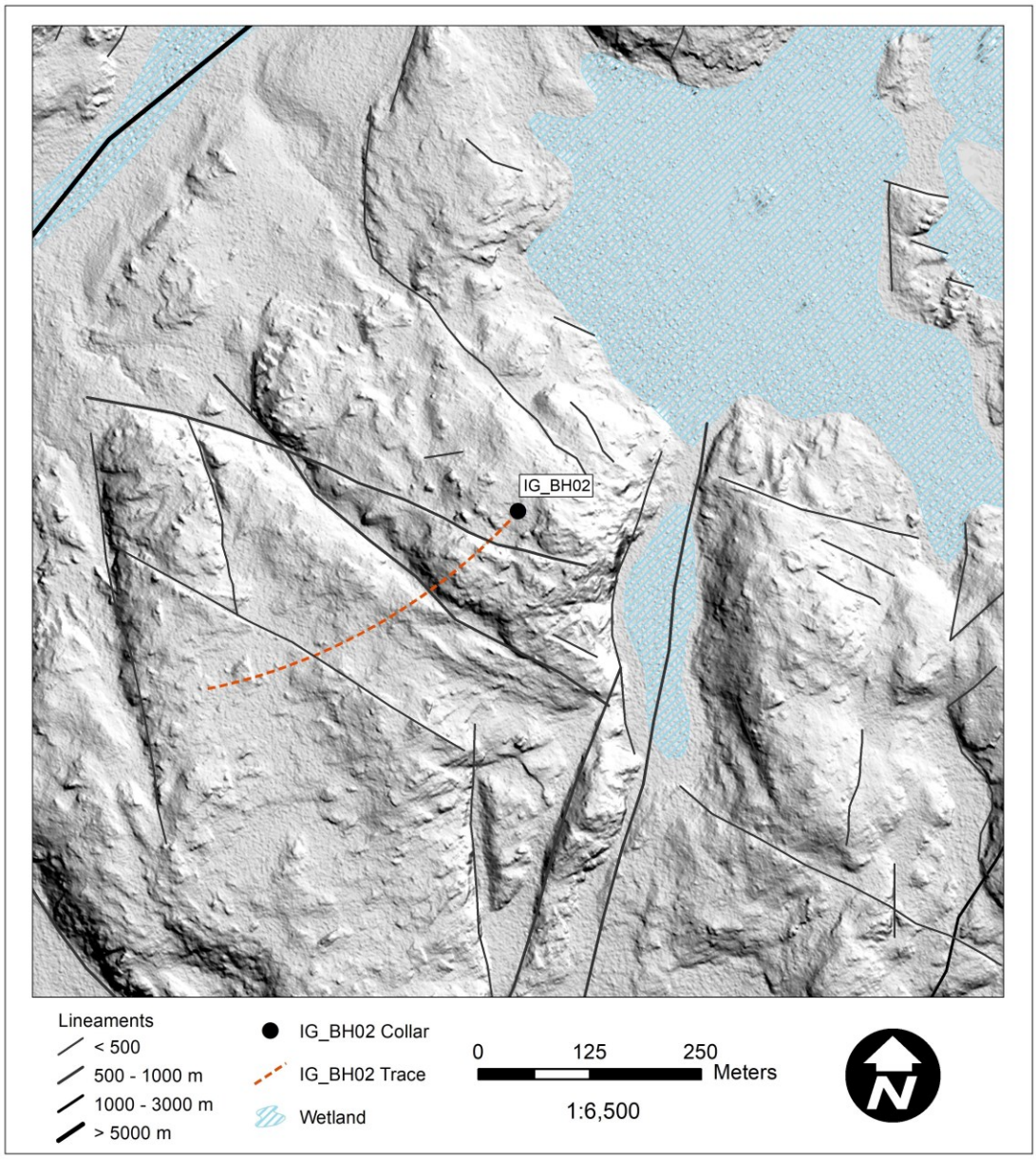


Figure 58: Lineament traces near IG_BH02 interpreted from LiDAR DEM and airborne geophysics data (DesRoches et al., 2018). Lineament traces are dominantly north-northeast and northwest trending. The approximate trace of IG_BH02 is shown as an orange dashed line.

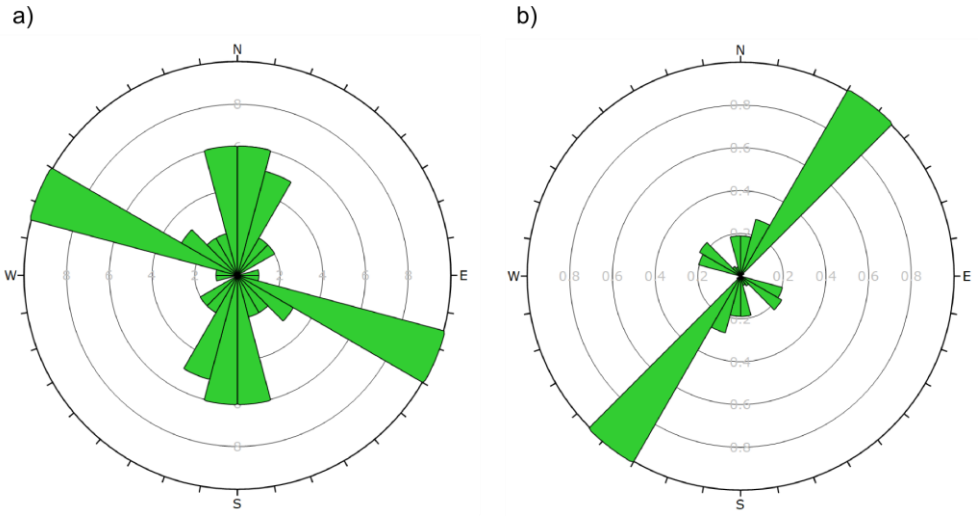


Figure 59: Rose diagram of the lineaments (N = 40) around IG_BH02 (see Figure 58) interpreted from LiDAR DEM and airborne geophysics data (DesRoches et al., 2018). a) Unweighted; b) Length-weighted to highlight more prominent lineaments. Lineament orientations are plotted using a bin size of 15 degrees.

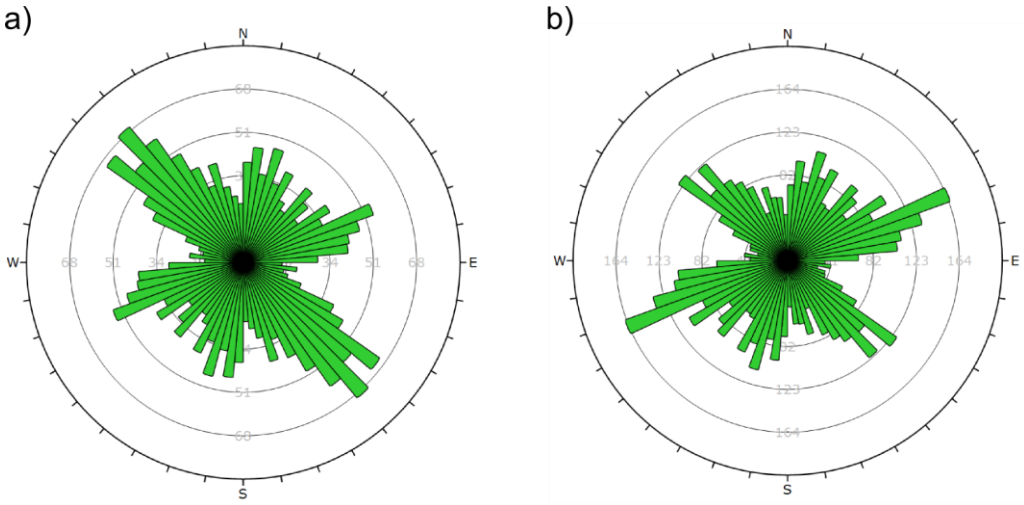


Figure 60: Rose diagrams of the borehole logged fracture orientations using a minimum dip angle of 45 degrees, and bin size of 5 degrees. a) Unweighted (N = 1340 is the total number of fractures); b) Terzaghi-weighted to account for directional bias of the borehole path (weighted N = 2231 is the sum of the weightings).

4 SUMMARY OF FINDINGS AND UNCERTAINTIES

4.1 Findings

The geological findings are based on the geological information available to date, which are summarized in this report. One primary consideration is the understanding that the available information *is from a single borehole.* Whether or not the characteristics of the bedrock described throughout this report will transfer to other boreholes remains uncertain. However, the level of uncertainty related to the overall understanding of the bedrock across the study area is expected to decrease as information from multiple boreholes is acquired and integrated together. A simplified

summary of the geological model for IG_BH02 is presented in Figure 61, showing the final lithology log, rock units, per metre fracture frequency, structural units, and high fracture frequency intervals.

The bedrock intersected by IG_BH02 is homogeneous. IG_BH02 is dominated by a medium-grained rock of tonalitic to granodioritic composition, representing a total of 95.7 % of the recovered core. Optical and acoustic televiewer, natural and spectral gamma, gamma-gamma density and neutron geophysical logs provided additional evidence to distinguish subordinate rock types from the main rock types in this crystalline rock environment. The integration of visual geological core logging and geophysical logging was useful for developing the final interpretation of logged rock types and alteration and was critical for assigning true orientations to the logged structures.

The lithogeochemical and petrographic datasets provided mineral and rock chemistry information used to distinguish subtle variations between the felsic igneous rocks encountered in the borehole. Some of these distinctions were not evident based on the geological and geophysical core logging alone. The majority of the felsic igneous rocks encountered share a similar mineralogy, ranging in composition between tonalite and granodiorite, except for a suite of aplitic dykes of more granitic composition and some quartz dykes.

Aphanitic and feldspar-phyric tonalite dykes represent the most common subordinate rock type identified during borehole drilling, followed by amphibolite. These tonalite dyke occurrences were predominantly observed within the upper half of the borehole as narrow (cm- to m-scale) units. The amphibolites were observed in the middle of the borehole, also as narrow (cm- to m-scale) units. Contact orientations for the tonalite dykes are predominantly moderately to gently inclined and northeast dipping. The contact orientations for the amphibolites are gently to moderately inclined and northwest to north-northwest dipping. Rare earth element (REE) data exhibit a similar pattern for all rock types (with the exception of the aplite dykes), which may indicate a common magmatic source. This provides some evidence that the amphibolites may represent metamorphosed mafic dykes that intruded into the granodiorite-tonalite synchronous with either granitoid emplacement or regional deformation.

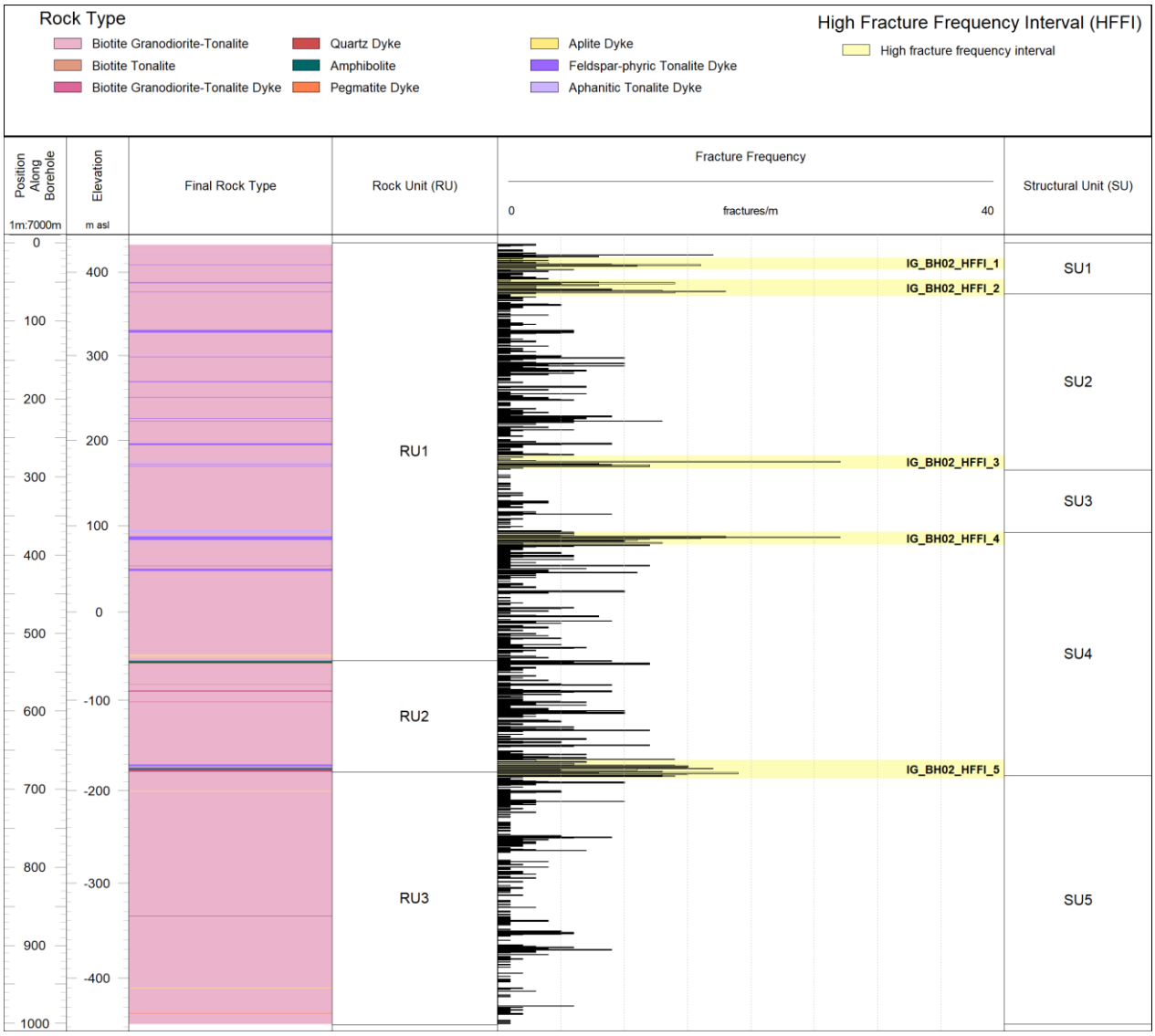


Figure 61: Summary log of geological information, including (from left to right), final log of lithology, classification of rock units, per metre fracture frequency, and structural units, representing the 1-dimensional geological model for IG_BH02.

Overall, the degree of alteration of the bedrock intersected by IG_BH02 appears to be relatively low even though alteration products are found along a large proportion of the borehole length. Seven alteration types (potassic, silicification, hematization, chloritization, bleaching, sericitization, and carbonatization) were identified during geological and geophysical logging. The majority of logged alteration was identified above 700 m along borehole, dominated by the distribution of logged potassic alteration and hematization, and slightly lesser silicification. It should be noted that, based on optical petrographic analysis, none of the intervals logged with potassic alteration show evidence of true hydrothermal potassic alteration (secondary alkali feldspar, biotite, sulphides) when examined petrographically. The pink colour of the recovered core is a product of magmatic (primary) alkali feldspar or replacement of very fine-grained sulphides with iron oxide minerals.

Based on broad changes in rock type along the borehole, three rock units were defined. The distribution of alteration was not considered to be a useful characteristic for distinguishing the rock units. The majority of the borehole has a massive texture, with some subordinate rock types dominantly hosting ductile or brittle-ductile structure (foliation and shear zones). The presence or absence of ductile or brittle-ductile fabric was not considered to be a useful characteristic for defining rock units.

The structures identified in the borehole included features associated with ductile, brittle-ductile, and brittle deformation processes. Ductile structures are distributed irregularly along the entire length of the borehole, though with a slightly decreased intensity below approximately 700 m. A foliation is predominantly weak, subhorizontal or gently inclined, and south or west dipping. Poles to the foliation are nearly coincident with the main pole cluster in the shear zone data set. Shear zones exhibit characteristics of both brittle and ductile deformation processes, including rare mylonite occurrences and fractures. Shear zones are commonly identified in association with aphanitic and feldspar-phyric tonalite dykes, or amphibolite, occurrences. The deformation manifests as cm- to dm-scale localized shear zones that are developed along, and sub-parallel to, the contacts of these subordinate rock types. Overall an increased degree of ductile to brittle structural complexity is commonly associated with aphanitic and feldspar-phyric tonalite dyke, and amphibolite, occurrences suggesting that the presence of these subordinate rock types has served to focus fluid flow at some point in the geological past.

Joints are overwhelmingly the most common fracture type identified in the borehole, followed by veins and faults. Faults are consistently very narrow, identified mainly by the presence of slickenlines, and exhibit only slight evidence of damage in the rock surrounding the fault plane.

The complete fracture dataset appears to indicate the presence of six fracture sets:

- a subhorizontal to moderately inclined set, dipping east (Set 1),
- a moderately to steeply inclined set, dipping south-southeast (Set 2),
- a vertical set, striking north-northeast (Set 3),
- a vertical set, striking northwest (Set 4),
- a moderately inclined set, dipping northeast (Set 5), and
- a steeply inclined set, dipping north-northwest (Set 6).

Overall, the lineation dataset provides good indication that motion throughout the history of ductile to brittle deformation was most prominently directed northwest-southeast. Strike-slip motion appears to predominate on moderately to steeply inclined planes, primarily faults, that dip towards the northeast. It is unknown at this point what the shortening and extension directions were, and whether the observed planes and lineations formed contemporaneously under the same paleostress regime or at different times under different orientations of applied stress. Information from other boreholes and surface mapping campaigns will attempt to clarify these outstanding questions.

The borehole was subdivided into five structural units based on variation in fracture frequency log and slope of the cumulative fracture frequency curve. The subdivision resulted in average fracture frequencies for the structural units ranging between 0.81 and 4.05 fractures per metre.

Five high fracture frequency intervals (HFFIs) were defined along the borehole using a semi-automated approach applied to the borehole fracture frequency per metre log. The intervals range in width from just over 15 m to almost 24 m. Two HFFIs were identified in the upper 50 m of the borehole, with additional occurrences around 280 m, 375 m, and 675 m. All HFFIs include at least one subordinate rock type occurrence. The most common subordinate rock types represented are the aphanitic or feldspar-phyric tonalite dykes which are present (at least one of these two end members) in all HFFIs.

Logged structures, defined fracture sets, and HFFIs, in the borehole display some correlation to the dominant lineament trends in proximity to the borehole. The north northeast-trending lineaments are consistent with the strike of fracture set 3, and some of the peaks in HFFI_1, 2, and 5. The northwest-trending lineaments are consistent with the strike of fracture sets 4 and 5, and one cluster of shear zones. The northwest-trending lineaments are also consistent with the major fracture peak in HFFI_1. These correlative borehole-interpreted fracture sets, and peak HFFI orientations, are subvertical to moderately inclined. Therefore, it is possible that some interpreted lineaments, currently interpreted to represent vertically oriented fracture zones, could instead have steep to moderate dips.

Considering all of the geological observations described throughout the report, several key summary points are highlighted below. These observations align with a developing understanding that, while the rock is homogeneous overall, there are distinct regions along the borehole that have relatively distinct character, including that:

- aphanitic and feldspar-phyric tonalite dykes cluster in the upper half of the borehole within RU1,
- amphibolite occurrences cluster between 500 and 700 m within RU2,
- both aphanitic and feldspar-phyric tonalite dykes, and amphibolite, shows evidence of ductile strain and brittle deformation internally and along their contacts, as well as evidence of hematization and chloritization, and
- there is a marked decrease in fracture frequency below 700 m.

The significance of the geological relationships identified here, will continue to be explored as additional information is gathered from future surface and subsurface investigations, including the drilling of additional boreholes and two-dimensional and vertical seismic profiling.

4.2 Uncertainties

With subsurface information available from only one borehole, many geological uncertainties remain. With respect to the distribution of subordinate rock types, a key uncertainty relates to the nature of the aphanitic and feldspar-phyric tonalite dyke and amphibolite occurrences. With respect to the amphibolite occurrences, it remains uncertain whether they represent deformed mafic dykes or vestiges of greenstone belt material. However, the lithogeochemical data presented above does suggest a common magmatic source for all rock types except the aplite dykes. This association does allow that the amphibolites may represent mafic dykes that intruded into the granodiorite-tonalite synchronous during either granitoid emplacement or regional deformation. The distribution of the amphibolite and the other subordinate rock types in three-dimensions is also a remaining uncertainty. Regarding the significance of the logged alteration, it is acknowledged that some uncertainty remains regarding the significance of the few intervals of higher intensity alteration to the overall character of the bedrock.

With respect to structure, there is uncertainty in the true density and mean orientation of steeply dipping structures. Although a Terzaghi-weighting was applied to correct for borehole orientation bias, it is understood that there are other techniques available. Further exploration of the best approach to account for the borehole orientation bias will be investigated as additional data becomes available, including data from differently oriented angled boreholes. Whether or not the drilling activity itself, or stress relief, may have induced the broken character of logged fractures also remains an uncertainty. The true nature of logged televiewer-only and core-only structures also remains uncertain. In addition, the timing and number of stages of fracture development (and re-activation), mineral infilling and alteration, and the resulting implications for the geological history of the area remain uncertain.

The subset of identified fractures that are likely to be hydraulically conductive also remains uncertain. This is especially important in understanding the significance of logged geological apertures. As mentioned above, geological apertures are estimated values only because there are multiple possible sources of uncertainty in how a reported aperture value relates to the true aperture of a fracture identified as broken. There are uncertainties related to measurement inaccuracy, including where the opening is very small, where the opposing fracture planes are not parallel or fit poorly together, or due to limits in televiewer resolution. In addition, effects due to drilling or decompression may create or enhance the visible open space identified as aperture. Finally, aperture measured in core or on a borehole wall is only a local aperture that is not necessarily representative over the entire fracture. There are also cases where fractures are logged as broken but exhibit no measurable geological aperture. Additional analysis of the observed structures in the acoustic and optical televiewer datasets, including fractures and their characteristics (e.g., broken vs intact nature, mineral infilling, orientation), will aim to reduce these uncertainties.

The absolute dimensions of the rock units (RU) and structural units (SU) presented above were defined based on a subjective and non-unique approach. With the same data inputs, alternative approaches may have defined more or less units and ultimately produced a different geological model for the borehole. Finally, a statistically robust method was used to define high fracture frequency intervals (HFFI) along the borehole. However, the approach is still non-unique. Different analytical approaches may produce a different result. Furthermore, the broader geological significance of these intervals, identified along a single borehole, remains uncertain.

5 REFERENCES

American Petroleum Institute (API), 1985. Directional Drilling Survey Calculation Methods and Terminology (Bulletin No. D20). Dallas, TX.

Blackburn, C.E., Hinz, P., 1996. Gold and base metal potential of the northwest part of the Raleigh Lake greenstone belt, northwestern Ontario-Kenora Resident Geologist's District; in Summary of Field Work and Other Activities 1996, Ontario Geological Survey, Miscellaneous Paper 166, p.113-115.

Daniels, J.J., Olhoeft, G.R., Scott, J.H., 1984. Interpretation of core and well log physical property data from drill hole UPH-3, Stephenson County, Illinois (USGS Numbered Series No. 82–941). United States Geological Survey.

Davy, P., Darcel, C., Bour, O., Munier, R., De Dreuzy, J.-R., 2006. A note on the angular correction applied to fracture intensity profiles along drill core. Journal of Geophysical Research: Solid Earth 111, B11408. https://doi.org/10.1029/2005JB004121

DesRoches, A., Sykes, M., Parmenter, A., Sykes, E., 2018. Lineament Interpretation of the Revell Batholith and Surrounding Greenstone Belts (No. NWMO-TR-2018-19). Nuclear Waste Management Organization.

Debon, F., Le Fort, P., 1983. A chemical and mineralogical classification of common plutonic rocks and associations. Earth and Environmental Science Transactions of the Royal Society of Edinburgh 73, 135–149.

Golder Associates Ltd., 2015. Phase 2 Geoscientific Preliminary Assessment, Findings from Initial Field Studies: Township of Ignace, Ontario (No. APM-REP-06145-0001). Nuclear Waste Management Organization.

Golder Associates Ltd., 2017. Phase 2 Initial Borehole Drilling and Testing, Ignace Area: Initial Borehole Characterization Plan for IG_BH01 (No. APM-PLAN-01332-0242). Nuclear Waste Management Organization.

Golder Associates Ltd., 2020a. Phase 2 Initial Borehole Drilling and Testing, Ignace Area. WP02 Data Report – Borehole Drilling and Coring for IG_BH02 (No. APM-REP-01332-0240). Nuclear Waste Management Organization.

Golder Associates Ltd., 2020b. Phase 2 Initial Borehole Drilling and Testing, Ignace Area. WP03 Data Report – Geological and Geotechnical Core Logging, Photography and Sampling for IG_BH02 (No. APM-REP-01332-0249). Nuclear Waste Management Organization.

Golder Associates Ltd., 2020c. Phase 2 Initial Borehole Drilling and Testing, Ignace Area. WP05 Data Report – Geophysical Well Logging for IG_BH02 (No. APM-REP-01332-0269). Nuclear Waste Management Organization.

Golder Associates Ltd., 2021a. Phase 2 Initial Borehole Drilling and Testing, Ignace Area. WP04b Data Report - Geomechanical Testing of Core for IG_BH02 (No. APM-REP-01332-0251). Nuclear Waste Management Organization.

Golder Associates Ltd., 2021b. Phase 2 Initial Borehole Drilling and Testing, Ignace Area. WP06 Data Report – Hydraulic Testing for IG_BH02. (No. APM-REP-01332-0256). Nuclear Waste Management Organization.

Golder Associates Ltd., 2021c. Phase 2 Initial Borehole Drilling and Testing, Ignace Area. WP7 Data Report – Opportunistic Groundwater Sampling for IG_BH02 (No. APM-REP-01332-0254). Nuclear Waste Management Organization.

Golder Associates Ltd., 2022. Phase 2 Initial Borehole Drilling and Testing, Ignace Area. WP4C Data Report – Porewater Extraction and Analysis and Petrographic Analysis for IG_BH02 (No. APM-REP-01332-0245). Nuclear Waste Management Organization.

Golder Associates Ltd., Paterson Grant and Watson, Ltd., 2017. Phase 2 Geoscientific Preliminary Assessment: Geological Mapping, Township of Ignace and Area, Ontario (No. APM-REP-01332-0225). Nuclear Waste Management Organization.

Halla, J., 2018. Highlights on Geochemical Changes in Archaean Granitoids and Their Implications for Early Earth Geodynamics. Geosciences 8, 353. https://doi.org/10.3390/geosciences8090353

Halla, J., van Hunen, J., Heilimo, E., Hölttä, P., 2009. Geochemical and numerical constraints on Neoarchean plate tectonics. Precambrian Research 174, 155–162. https://doi.org/10.1016/j.precamres.2009.07.008

Keys, W.S., 1997. A Practical Guide to Borehole Geophysics in Environmental Investigations. CRC Press.

Le Bas, M.J., Streckeisen, A.L., 1991. The IUGS systematics of igneous rocks. Journal of the Geological Society 148, 825–833. https://doi.org/10.1144/gsjgs.148.5.0825

OGS (Ontario Geological Survey), 2011. 1:250 000 scale bedrock geology of Ontario, Ontario Geological Survey, Miscellaneous Release Data 126 - Revision 1.

Parmenter, A., Waffle, L., DesRoches, A. 2020. Bedrock geology of the Revell batholith and surrounding greenstone belts (No. NWMO-TR-2020-08). Nuclear Waste Management Organization.

Sander Geophysics Limited (SGL), 2020. 3D Geophysical Forward and Inversion Modelling of the Revell Batholith and Surrounding Greenstone Belt. (No. APM-REP-01332-0270). Nuclear Waste Management Organization.

SRK Consulting, Inc., Golder Associates Ltd., 2015. Phase 2 Geoscientific Preliminary Assessment, Observation of General Geological Features, Township of Ignace, Ontario (No. APM-REP-06145-0004). Nuclear Waste Management Organization.

Stone, D., 2009. Geology of the Bending Lake Area, Northwestern Ontario (Open File Report No. 6240), Summary of Field Work and Other Activities 2009. Ontario Geological Survey, Sudbury, Canada.

Stone, D., 2010a. Geology of the Stormy Lake Area, Northwestern Ontario, Project Unit 09-003 (Open File Report No. 6260), Summary of Field Work and Other Activities 2010. Ontario Geological Survey, Sudbury, Canada.

Stone, D., 2010b. Precambrian geology of the central Wabigoon Subprovince area, northwestern Ontario (Open File Report No. 5422). Ontario Geological Survey.

Stone, D., Davis, D.W., Hamilton, M.A., Falcon, A., 2010. Interpretation of 2009 Geochronology in the Central Wabigoon Subprovince and Bending Lake Areas, Northwestern Ontario, Project Unit 09-003 (Open File Report No. 6260), Summary of Field Work and Other Activities 2010. Ontario Geological Survey.

Stone, D., Halle, J., Chaloux, E., 1998. Geology of the Ignace and Pekagoning Lake Areas, Central Wabigoon Subprovince (Misc. Paper No. 169), Summary of Field Work and Other Activities 1998. Ontario Geological Survey.

Taylor, S.R., McLennan, S.M., 1985. The continental crust: Its composition and evolution. United States.

Terzaghi, R.D., 1965. Sources of Error in Joint Surveys. Géotechnique 15, 287–304. https://doi.org/10.1680/geot.1965.15.3.287

Virtanen, P. et al. 2020. SciPy 1.0--Fundamental Algorithms for Scientific Computing in Python. Nature Methods, 17, 261–272.

Appendix A: Summary List of Work Packages Completed for IG_BH02

WP Number	WP Name	Report Reference
WP01	Site Infrastructure and Access Road Construction	No report
WP02	Borehole Drilling and Coring	Golder, 2020a
WP03	Geological and Geotechnical Core Logging, Photography and Sampling	Golder, 2020b
WP04a2	Effective Diffusion Coefficients – Crystalline Rock	Golder, in prep.
WP04b	Geomechanical Testing of Core	Golder, 2021a
WP04c	Porewater Extraction and Analysis and Petrographic Analysis	Golder, 2022
WP05	Geophysical Well Logging and Interpretation	Golder, 2020c
WP06	Hydraulic Testing	Golder, 2021b
WP07	Opportunistic Groundwater Sampling and Testing	Golder, 2021c
WP08	Temporary Well Sealing	No report

Appendix B: Petrography and lithogeochemistry data

Petrography

Semi-quantitative optical petrography was completed by Activation Laboratories in Thunder Bay, Ontario (LGXXX). Modal mineralogy was determined using a known scale grid and visually determining area coverage of minerals in the sample. Note that only rock types plotted on the QAP diagram (Figure 8) are listed. PLA = plagioclase feldspar; QTZ = quartz; AFS = alkali feldspar.

Modal mineralogy (original and normalized) presented as percentages, determined semi-quantitatively using polished thin sections.

Sample ID	From (position along borehole; m)	To (position along borehole; m)	Mineral %			Total	Mineral %			Total	Final Rock Type
			PLA	QTZ	AFS		PLA	QTZ	AFS		
IG_BH02_LG001	15.29	15.41	83.0	5.5	0.0	88.5	93.8	6.2	0.0	100.0	Aphanitic tonalite dyke
IG_BH02_LG002	15.75	15.90	13.0	9.0	0.0	22.0	59.1	40.9	0.0	100.0	Feldspar-phyric tonalite dyke
IG_BH02_LG003	60.05	60.20	44.0	42.0	13.5	99.5	44.2	42.2	13.6	100.0	Biotite granodiorite-tonalite
IG_BH02_LG005	113.10	113.28	49.0	36.0	0.0	85.0	57.6	42.4	0.0	100.0	Feldspar-phyric tonalite dyke
IG_BH02_LG007	280.60	280.80	78.0	20.0	0.0	98.0	79.6	20.4	0.0	100.0	Aphanitic tonalite dyke
IG_BH02_LG008	284.50	284.70	46.5	43.5	9.0	99.0	47.0	43.9	9.1	100.0	Biotite granodiorite-tonalite
IG_BH02_LG009	346.75	347.00	41.0	38.0	9.0	88.0	46.6	43.2	10.2	100.0	Biotite granodiorite-tonalite
IG_BH02_LG010	368.50	368.65	56.0	20.0	0.0	76.0	73.7	26.3	0.0	100.0	Aphanitic tonalite dyke
IG_BH02_LG011	372.24	372.44	43.0	39.0	16.5	98.5	43.7	39.6	16.7	100.0	Biotite granodiorite-tonalite
IG_BH02_LG012	381.03	381.20	50.0	37.0	11.0	98.0	51.0	37.8	11.2	100.0	Biotite granodiorite-tonalite
IG_BH02_LG013	478.22	478.44	52.0	42.5	7.0	101.5	51.2	41.9	6.9	100.0	Biotite granodiorite-tonalite
IG_BH02_LG014	531.25	531.47	31.0	29.0	25.0	85.0	36.5	34.1	29.4	100.0	Aplite dyke
IG_BH02_LG017	573.51	573.68	51.0	44.0	1.5	96.5	52.9	45.6	1.6	100.0	Biotite tonalite
IG_BH02_LG018	600.43	600.62	47.0	32.0	17.5	96.5	48.7	33.2	18.1	100.0	Biotite granodiorite-tonalite
IG_BH02_LG020	668.29	668.44	52.0	39.0	0.0	91.0	57.1	42.9	0.0	100.0	Feldspar-phyric tonalite dyke
IG_BH02_LG022	680.74	680.91	40.5	39.5	18.5	98.5	41.1	40.1	18.8	100.0	Biotite granodiorite-tonalite
IG_BH02_LG025	777.49	777.75	51.5	23.5	23.5	98.5	52.2	23.9	23.9	100.0	Biotite granodiorite-tonalite
IG_BH02_LG026	904.5	904.74	56.5	39.0	2.5	98.0	57.6	39.8	2.6	100.0	Biotite granodiorite-tonalite

Lithogeochemistry

All analyses performed by Activation Laboratories Ltd. in Thunder Bay or Ancaster, Ontario. In addition to the results included below, 63 certified reference materials (to measure accuracy), 7 duplicates (to measure precision), and 18 method blanks (to monitor contamination) were analysed by Actlabs to ensure overall quality control in the lithogeochemical analyses. Certified reference material (CRM) measurements averaged within 0.1 % of certified values (>99 % accuracy). There were a few CRM samples that were >10% off their certified values in one element, but other elements in the material were within an acceptable range of > 90% accuracy so these discrepancies were deemed insignificant. Duplicate sample measurements averaged within 7 % of original measured values (>93% precision), and the method blanks all returned measurements below, or within an acceptable range of, detection limit (no discernable contamination).

Lithogeochemical results of various tests carried out by Activation Laboratories. For details on each analysis performed, see section 3.2.1.

Report Number: A20-05149																							
Report Date: 18/6/2020																							
Analyte Symbol	From (position along borehole; m)	To (position along borehole; m)	Au	As	Br	Cr	Ir	Sc	Se	Sb	Mass	SiO2	Al2O3	Fe2O3(T)	MnO	MgO	CaO	Na2O	K2O	TiO2	P2O5	LOI	Total
Unit Symbol			ppb	ppm	ppm	ppm	ppb	ppm	ppm	ppm	g	%	%	%	%	%	%	%	%	%	%	%	%
Detection Limit			2	0.5	0.5	5	5	0.1	3	0.2		0.01	0.01	0.01	0.001	0.01	0.01	0.01	0.01	0.001	0.01		0.01
Analysis Method			INAA	INAA	INAA	INAA	INAA	INAA	INAA	INAA	INAA	FUS-ICP	FUS-ICP	FUS-ICP	FUS-ICP	FUS-ICP	FUS-ICP	FUS-ICP	FUS-ICP	FUS-ICP	FUS-ICP	GRAV	FUS-ICP
IG_BH02_LG001	15.29	15.41	< 2	< 0.5	< 0.5	17	< 5	2.7	< 3	< 0.2	32.3	70.95	14.65	2.7	0.035	0.68	2.93	4.42	1.66	0.296	0.09	0.48	98.89
IG_BH02_LG002	15.75	15.9	< 2	< 0.5	< 0.5	28	< 5	1.9	< 3	1	31.2	72.86	13.56	2.11	0.036	0.33	1.86	4.2	2.58	0.22	0.07	0.58	98.41
IG_BH02_LG003	60.05	60.2	< 2	< 0.5	< 0.5	17	< 5	2	< 3	< 0.2	30.8	72.33	14.43	1.91	0.025	0.34	1.24	4.5	2.73	0.175	0.05	0.8	98.54
IG_BH02_LG004	73.47	73.68	< 2	< 0.5	< 0.5	19	< 5	1.9	< 3	< 0.2	1.07	74.01	14.09	1.73	0.033	0.32	1.74	4.39	3.01	0.16	0.03	0.45	99.96
IG_BH02_LG005	113.1	113.28	< 2	< 0.5	< 0.5	22	< 5	2.8	< 3	7.1	31.1	71.59	14.6	2.96	0.039	0.71	3.06	4.34	1.75	0.308	0.1	0.5	99.95
IG_BH02_LG006	132.25	132.4	< 2	0.5	< 0.5	22	< 5	2	< 3	< 0.2	1.03	74.22	14.18	1.86	0.036	0.37	2.02	4.53	2.47	0.174	0.04	0.68	100.6
IG_BH02_LG007	280.6	280.8	< 2	< 0.5	18.1	14	< 5	2.9	< 3	< 0.2	32.3	70.15	14.51	2.92	0.049	0.75	1.91	5.54	1.22	0.315	0.09	1.39	98.85
IG_BH02_LG008	284.5	284.7	< 2	< 0.5	1.2	20	< 5	1.8	< 3	< 0.2	29.6	72.63	14.02	1.7	0.028	0.32	1.58	4.47	2.9	0.154	0.04	1.65	99.49
IG_BH02_LG009	346.75	347	< 2	< 0.5	11.7	35	< 5	2.1	< 3	< 0.2	28.1	72.64	13.75	1.81	0.034	0.38	1.42	4.52	2.91	0.164	0.05	0.93	98.61
IG_BH02_LG010	368.5	368.65	< 2	0.5	< 0.5	23	< 5	2.9	< 3	< 0.2	31.1	71.82	14.62	2.74	0.032	0.65	3.09	4.5	1.71	0.306	0.1	0.37	99.92
IG_BH02_LG011	372.24	372.44	< 2	< 0.5	< 0.5	29	< 5	1.8	< 3	0.4	30.7	73.51	13.5	1.55	0.031	0.27	1.53	4.38	3.24	0.131	0.04	0.48	98.66
IG_BH02_LG012	381.03	381.2	< 2	< 0.5	1.1	30	< 5	2.2	< 3	< 0.2	30.4	73.34	13.55	1.88	0.037	0.42	1.56	4.4	2.81	0.16	0.05	0.87	99.06
IG_BH02_LG013	478.22	478.44	< 2	< 0.5	< 0.5	22	< 5	2.2	< 3	< 0.2	30.5	73.13	13.74	1.84	0.033	0.31	1.78	4.38	2.84	0.167	0.04	1.92	100.2
IG_BH02_LG014	531.25	531.47	< 2	< 0.5	< 0.5	22	< 5	1	< 3	< 0.2	32.5	75.78	13.04	0.78	0.015	0.06	0.59	4.3	4.59	0.038	0.01	0.19	99.41

IG_BH02_LG015	536.48	536.82	< 2	< 0.5	< 0.5	668	< 5	34.5	< 3	< 0.2	30.2	42.77	12	10.3	0.159	10.24	11.38	1.99	3.26	0.94	0.47	5.72	99.24
IG_BH02_LG016	567.26	567.44	< 2	< 0.5	11.2	13	< 5	2.1	< 3	< 0.2	1.04	74.5	14.07	1.88	0.034	0.34	1.84	4.47	2.97	0.165	0.04	0.46	100.8
IG_BH02_LG017	573.51	573.68	< 2	< 0.5	18.5	21	< 5	2.9	< 3	0.3	31.7	72.59	14.75	2.59	0.045	0.55	2.63	4.68	1.75	0.25	0.06	0.56	100.5
IG_BH02_LG018	600.43	600.62	< 2	< 0.5	4	24	< 5	1.6	< 3	< 0.2	30.5	74.38	13.74	1.43	0.026	0.32	1.06	4.11	4.51	0.13	0.04	0.68	100.4
IG_BH02_LG019	632.98	633.26	< 2	< 0.5	< 0.5	23	< 5	1.9	< 3	< 0.2	1.05	73.68	14.16	1.8	0.033	0.33	1.75	4.36	3.09	0.163	0.05	0.43	99.85
IG_BH02_LG020	668.29	668.44	2	< 0.5	1.7	23	< 5	3.8	< 3	< 0.2	30	72.9	13.25	2.65	0.037	0.68	2.7	3.93	1.75	0.26	0.07	1.13	99.37
IG_BH02_LG021	672.2	672.4	< 2	1	1.4	376	< 5	19	< 3	0.4	33.1	55.35	14.26	7.12	0.133	5.49	9.57	3.46	1.02	0.574	0.18	3.11	100.3
IG_BH02_LG022	680.74	680.91	3	1.7	6.8	22	< 5	2	< 3	< 0.2	30.3	74.15	13.99	1.82	0.033	0.36	1.86	4.46	2.63	0.167	0.04	0.66	100.2
IG_BH02_LG023	682.58	682.74	< 2	< 0.5	14.3	< 5	< 5	2.3	< 3	0.2	30.8	58.9	18.74	1.97	0.037	0.53	4.01	8.61	1.27	0.249	0.06	4.12	98.49
IG_BH02_LG024	702.01	702.19	< 2	< 0.5	5.1	21	< 5	1.7	< 3	< 0.2	31.2	75.04	13.86	1.62	0.029	0.25	1.62	4.64	2.93	0.13	0.03	0.47	100.6
IG_BH02_LG025	777.49	777.75	< 2	< 0.5	13.6	24	< 5	1.9	< 3	< 0.2	32	72.74	14.3	1.85	0.031	0.32	1.99	4.97	3.1	0.166	0.05	1.05	100.6
IG_BH02_LG026	904.5	904.74	< 2	< 0.5	13.7	21	< 5	1.9	< 3	< 0.2	29.2	73.11	14.25	1.97	0.027	0.42	1.44	4.7	2.69	0.188	0.05	1.66	100.5

Analyte Symbol	Sc	Be	V	Cr	Co	Ni	Cu	Zn	Cd	S	Ga	Ge	As	Rb	Sr	Y	Zr	Nb	Mo	Ag	In	Sn	Sb	Cs	Ba
Unit Symbol	ppm	ppm	ppm	ppm	ppm	ppm	ppm	ppm	ppm	%	ppm	ppm	ppm	ppm	ppm	ppm	ppm	ppm	ppm	ppm	ppm	ppm	ppm	ppm	ppm
Detection Limit	1	1	5	20	1	1	1	1	0.5	0.001	1	0.5	5	1	2	0.5	1	0.2	2	0.3	0.1	1	0.2	0.1	2
Analysis Method	FUS-ICP	FUS-ICP	FUS-ICP	FUS-MS	FUS-MS	TD-ICP	TD-ICP	TD-ICP	TD-ICP	TD-ICP	FUS-MS	FUS-MS	FUS-MS	FUS-MS	FUS-ICP	FUS-MS	FUS-ICP	FUS-MS	FUS-MS	TD-ICP	FUS-MS	FUS-MS	FUS-MS	FUS-MS	FUS-ICP
IG_BH02_LG001	3	1	25	< 20	4	4	13	66	< 0.5	0.003	19	1	< 5	50	258	4.2	145	4	< 2	< 0.3	< 0.1	1	0.3	2.4	390
IG_BH02_LG002	2	1	14	30	2	4	10	57	< 0.5	0.003	18	1	< 5	91	161	4.9	112	3.6	3	0.3	< 0.1	1	0.6	1.9	555
IG_BH02_LG003	2	1	12	20	2	3	12	46	< 0.5	0.003	19	1	< 5	87	198	5.3	88	3.8	< 2	< 0.3	< 0.1	1	< 0.2	2.6	505
IG_BH02_LG004	2	1	10	20	2	2	7	44	< 0.5	0.003	18	1	< 5	99	181	4.7	85	3.8	< 2	< 0.3	< 0.1	1	< 0.2	3.3	522
IG_BH02_LG005	3	1	26	30	5	4	7	67	< 0.5	0.004	18	1	< 5	52	244	4.3	134	4.2	< 2	< 0.3	< 0.1	1	4	2.3	419
IG_BH02_LG006	2	2	12	20	2	1	12	48	< 0.5	0.002	18	1.1	< 5	88	194	5.2	93	4.3	< 2	< 0.3	< 0.1	1	< 0.2	3.8	466
IG_BH02_LG007	3	1	29	20	5	5	21	39	< 0.5	0.003	20	1	< 5	58	238	5.5	152	4	< 2	0.4	< 0.1	1	< 0.2	1.3	348
IG_BH02_LG008	2	1	10	< 20	2	2	9	39	< 0.5	0.003	18	1.1	< 5	86	182	4.8	79	4.1	< 2	0.3	< 0.1	1	< 0.2	1.8	529
IG_BH02_LG009	2	1	11	40	2	2	8	38	< 0.5	0.002	18	1.1	< 5	86	163	5	86	4.1	2	< 0.3	< 0.1	1	< 0.2	1.5	603
IG_BH02_LG010	3	< 1	24	20	5	4	15	64	< 0.5	0.004	18	0.9	< 5	49	253	3.6	143	3.6	2	0.5	< 0.1	1	< 0.2	1	396
IG_BH02_LG011	2	1	9	40	2	2	7	37	< 0.5	0.003	18	1.1	< 5	105	155	6	74	3.4	< 2	< 0.3	< 0.1	1	< 0.2	2.2	481
IG_BH02_LG012	2	1	12	30	2	2	8	39	< 0.5	0.002	18	1	< 5	81	180	5.3	88	4.1	2	0.3	< 0.1	1	< 0.2	1.7	507
IG_BH02_LG013	2	1	12	30	2	4	7	43	< 0.5	0.014	18	1.1	< 5	90	222	5.2	88	4.3	< 2	< 0.3	< 0.1	1	< 0.2	1.9	565
IG_BH02_LG014	1	1	< 5	< 20	< 1	< 1	2	14	< 0.5	0.001	19	1.8	< 5	126	16	9.4	15	3.5	< 2	< 0.3	< 0.1	< 1	< 0.2	1.3	14
IG_BH02_LG015	39	1	233	750	45	197	71	79	< 0.5	0.067	14	1.4	< 5	104	789	20.2	125	6.4	< 2	< 0.3	< 0.1	1	< 0.2	6.4	655
IG_BH02_LG016	2	1	13	< 20	2	2	6	42	< 0.5	0.003	18	1	< 5	93	192	4.9	91	3.9	< 2	< 0.3	< 0.1	1	< 0.2	2.6	570
IG_BH02_LG017	3	1	23	20	4	2	9	58	< 0.5	0.003	19	0.8	< 5	73	307	5.6	105	4.7	< 2	< 0.3	< 0.1	1	< 0.2	2.9	330
IG_BH02_LG018	2	< 1	10	30	2	2	25	21	< 0.5	0.003	15	0.8	< 5	134	136	3.3	66	2.3	< 2	< 0.3	< 0.1	1	< 0.2	0.7	919
IG_BH02_LG019	2	1	12	20	2	2	8	42	< 0.5	0.003	18	1	< 5	98	193	4.5	89	4.1	< 2	< 0.3	< 0.1	1	< 0.2	2.1	668
IG_BH02_LG020	4	< 1	29	20	5	6	15	48	< 0.5	0.002	16	0.8	< 5	70	236	4.3	119	3.3	< 2	0.3	< 0.1	1	< 0.2	2.3	471
IG_BH02_LG021	20	1	140	420	26	75	43	81	< 0.5	0.004	17	1.8	< 5	37	1226	14.5	109	5.2	< 2	< 0.3	< 0.1	1	0.4	0.3	213
IG_BH02_LG022	2	1	14	20	2	2	9	48	< 0.5	0.002	18	0.9	< 5	83	206	4.4	93	4.1	< 2	< 0.3	< 0.1	1	< 0.2	1.6	561
IG_BH02_LG023	2	1	21	< 20	2	4	37	48	< 0.5	0.003	19	1	< 5	34	310	9	125	7.3	< 2	0.3	< 0.1	1	< 0.2	0.6	495
IG_BH02_LG024	2	1	9	< 20	2	1	8	35	< 0.5	0.003	17	1	< 5	86	153	4	70	3.3	< 2	< 0.3	< 0.1	1	< 0.2	1.9	391
IG_BH02_LG025	2	< 1	14	20	2	2	3	17	< 0.5	0.001	19	1.1	< 5	115	192	4.4	98	4	2	< 0.3	< 0.1	1	< 0.2	0.6	682
IG_BH02_LG026	2	1	14	20	2	3	13	21	< 0.5	0.022	17	0.9	< 5	108	203	4.6	108	3.7	< 2	< 0.3	< 0.1	1	< 0.2	2.8	711

Analyte Symbol	La	Ce	Pr	Nd	Sm	Eu	Gd	Tb	Dy	Ho	Er	Tm	Yb	Lu	Hf	Ta	W	Tl	Pb	Li	Bi	Th	U
Unit Symbol	ppm	ppm	ppm	ppm	ppm	ppm	ppm	ppm	ppm	ppm	ppm	ppm	ppm	ppm	ppm	ppm	ppm	ppm	ppm	ppm	ppm	ppm	ppm
Detection Limit	0.05	0.05	0.01	0.05	0.01	0.005	0.01	0.01	0.01	0.01	0.01	0.005	0.01	0.002	0.1	0.01	0.5	0.05	5	1	0.1	0.05	0.01
Analysis Method	FUS-MS	FUS-MS	FUS-MS	FUS-MS	FUS-MS	FUS-MS	FUS-MS	FUS-MS	FUS-MS	FUS-MS	FUS-MS	FUS-MS	FUS-MS	FUS-MS	FUS-MS	FUS-MS	FUS-MS	FUS-MS	TD-ICP	TD-ICP	FUS-MS	FUS-MS	FUS-MS
IG_BH02_LG001	16.2	31.1	3.08	11.1	1.9	0.614	1.44	0.18	0.84	0.12	0.36	0.05	0.32	0.045	3.6	0.54	1.2	0.37	9	93	0.7	4.41	1.74
IG_BH02_LG002	20.7	36.2	3.58	11.9	1.91	0.494	1.39	0.18	0.88	0.15	0.43	0.056	0.36	0.053	2.8	0.82	< 0.5	0.44	7	69	< 0.1	5.06	1.62
IG_BH02_LG003	16.9	29.3	2.99	10.5	2.08	0.412	1.49	0.2	1.01	0.16	0.44	0.064	0.41	0.06	2.6	0.91	< 0.5	0.4	9	76	< 0.1	6.77	1.4
IG_BH02_LG004	16.4	28.9	3	10.2	1.82	0.431	1.43	0.18	0.88	0.14	0.39	0.057	0.37	0.051	2.6	0.79	3.9	0.41	10	71	< 0.1	6.22	2.21
IG_BH02_LG005	21.7	38.3	3.88	13.8	2.17	0.675	1.62	0.19	0.92	0.14	0.42	0.055	0.34	0.045	3.4	0.61	< 0.5	0.31	< 5	77	0.1	4.73	1.3
IG_BH02_LG006	17.2	30.5	3.13	10.8	1.98	0.463	1.52	0.21	1.01	0.16	0.45	0.059	0.39	0.056	2.8	0.9	0.7	0.39	8	80	< 0.1	6.7	2.85
IG_BH02_LG007	18.4	37.5	3.45	12.5	2.26	0.746	1.75	0.23	1.1	0.18	0.46	0.062	0.43	0.061	3.6	0.53	0.6	0.31	12	89	0.4	4.4	1.91
IG_BH02_LG008	15.1	26.8	2.74	9.74	1.76	0.409	1.39	0.18	0.96	0.15	0.4	0.053	0.34	0.051	2.3	1.07	2.6	0.33	9	62	< 0.1	5.59	1.77
IG_BH02_LG009	16.5	29.5	3.01	10.5	1.91	0.444	1.51	0.19	0.91	0.15	0.42	0.058	0.38	0.055	2.5	1	1.8	0.36	7	44	< 0.1	6.46	1.36
IG_BH02_LG010	20.4	36.7	3.69	12.7	2.07	0.619	1.43	0.19	0.78	0.11	0.29	0.039	0.24	0.036	3.5	0.47	4.4	0.25	< 5	86	< 0.1	4.12	1
IG_BH02_LG011	14.1	25.4	2.62	9.47	1.97	0.401	1.53	0.21	1.05	0.19	0.5	0.071	0.49	0.074	2.5	0.82	< 0.5	0.49	8	56	< 0.1	6.49	1.15
IG_BH02_LG012	16.2	29.2	2.94	10.3	1.94	0.467	1.46	0.21	1.08	0.17	0.44	0.059	0.38	0.058	2.5	0.9	< 0.5	0.32	8	42	< 0.1	6.19	1.8
IG_BH02_LG013	18.1	31	3.15	11.1	1.99	0.408	1.57	0.19	0.93	0.16	0.42	0.061	0.41	0.06	2.7	0.83	2.1	0.39	8	80	< 0.1	7.02	2.45
IG_BH02_LG014	3.31	6.48	0.73	2.71	0.98	0.139	1.22	0.24	1.54	0.29	0.83	0.121	0.82	0.126	1.3	1.14	< 0.5	0.5	18	17	< 0.1	1.97	7.31
IG_BH02_LG015	45.9	101	12.4	49.4	8.86	2.42	6.5	0.78	4.11	0.72	1.96	0.275	1.67	0.248	3.2	0.38	< 0.5	0.47	11	242	< 0.1	5.95	2.12
IG_BH02_LG016	17.6	30.6	3.1	10.4	1.94	0.476	1.49	0.18	0.89	0.16	0.43	0.057	0.39	0.061	2.7	0.86	< 0.5	0.43	8	61	< 0.1	6.21	1.93
IG_BH02_LG017	19.6	34.5	3.41	11.6	1.81	0.478	1.34	0.18	1.03	0.18	0.49	0.073	0.47	0.067	2.8	1.28	< 0.5	0.37	8	71	< 0.1	4.34	2.54
IG_BH02_LG018	10.4	16.9	1.73	5.94	1.09	0.468	0.89	0.12	0.58	0.09	0.23	0.034	0.23	0.031	1.8	0.39	< 0.5	0.55	7	25	< 0.1	3.05	1.37
IG_BH02_LG019	16.8	29.4	2.93	10.1	1.86	0.478	1.27	0.18	0.83	0.14	0.38	0.054	0.32	0.048	2.6	0.9	0.7	0.46	8	65	0.2	5.78	2.71
IG_BH02_LG020	18.2	32.2	3.19	10.9	1.83	0.509	1.28	0.17	0.81	0.14	0.35	0.055	0.37	0.06	3	0.55	< 0.5	0.34	7	58	< 0.1	4.71	1.42
IG_BH02_LG021	37.9	69.7	7.8	30.5	5.21	1.35	3.96	0.49	2.57	0.48	1.4	0.201	1.4	0.218	2.9	0.33	0.5	0.19	20	55	0.1	5.41	2.04
IG_BH02_LG022	17.1	29.9	2.98	10.5	1.77	0.464	1.35	0.18	0.85	0.14	0.36	0.051	0.36	0.059	2.6	0.94	26.1	0.34	8	41	< 0.1	5.48	1.15
IG_BH02_LG023	15.4	30.1	3.08	11.3	2.95	0.937	2.77	0.35	1.7	0.27	0.67	0.088	0.55	0.082	4	1.41	0.6	0.13	< 5	54	< 0.1	6.52	1.19
IG_BH02_LG024	12.7	22.3	2.25	7.8	1.4	0.381	1.12	0.14	0.76	0.13	0.37	0.048	0.28	0.042	2.1	0.69	< 0.5	0.35	11	49	< 0.1	4.47	1.6
IG_BH02_LG025	21	34.4	3.42	11.8	1.84	0.509	1.34	0.17	0.92	0.14	0.36	0.054	0.36	0.054	2.7	0.67	0.7	0.47	< 5	28	< 0.1	4.6	2.34
IG_BH02_LG026	16.8	28.5	2.87	9.86	1.79	0.399	1.45	0.18	0.87	0.14	0.39	0.05	0.33	0.048	3	0.78	0.9	0.47	< 5	58	< 0.1	5.12	1.9

Appendix C: Geophysical Near and Far Density Log Correction

The correction was determined by averaging the difference between each laboratory measurement and the field measurement at the corresponding Position, for the near and far density data sets. Eighteen laboratory core wet density measurements were considered. This correction was applied to the near and far density logs in WellCAD and the updated logs are exported from WellCAD and updated as .LAS files in the NWMO AcQuire database.

Position along borehole	Near Density (ND)	Far Density (FD)	Lab Wet Density	Difference ND-Lab	Difference FD-lab	NDCorrection	FDCorrection
m	g/cm^3	g/cm^3	g/cm^3	g/cm^3	g/cm^3		
240.20	2.76	2.75	2.63	0.13	0.12	1.05	1.05
348.52	2.75	2.78	2.64	0.11	0.14	1.04	1.05
379.60	2.86	2.79	2.66	0.20	0.13	1.07	1.05
382.00	2.77	2.77	2.66	0.11	0.11	1.04	1.04
416.32	2.80	2.76	2.66	0.14	0.10	1.05	1.04
416.55	2.80	2.76	2.66	0.14	0.10	1.05	1.04
455.47	2.82	2.73	2.65	0.17	0.08	1.06	1.03
494.43	2.78	2.77	2.67	0.11	0.10	1.04	1.04
494.62	2.81	2.78	2.67	0.14	0.11	1.05	1.04
503.83	2.81	2.74	2.59	0.22	0.15	1.08	1.06
555.11	2.77	2.73	2.66	0.11	0.07	1.04	1.03
580.81	2.80	2.76	2.67	0.13	0.09	1.05	1.03
582.71	2.78	2.80	2.67	0.11	0.13	1.04	1.05
611.42	2.78	2.79	2.64	0.14	0.15	1.05	1.06
666.09	2.79	2.76	2.65	0.14	0.11	1.05	1.04
771.45	2.75	2.82	2.63	0.12	0.19	1.05	1.07
879.04	2.76	2.81	2.65	0.11	0.16	1.04	1.06
984.47	2.82	2.83	2.63	0.19	0.20	1.07	1.07
					Mean Correction	**1.05**	**1.05**

Appendix D: Structure log integration methodology

Borehole IG_BH02 - Structure type and position verification and the integration activity to define the azimuth of the arbitrary reference line.

Introduction

The orientation of all structures measured during core logging, as described in the WP03 Data Reports, are initially defined based on alpha and beta angles relative to (1) the core axis, and (2) an arbitrary reference line drawn along the length of each core run. Since the core was not oriented, these relative orientation angles (alpha/beta for planes; gamma/delta for lineations on planes), for each logged structure need to be corrected to a true orientation in order to produce the final structural log for IG_BH02.

A final structural log was produced by comparing the core logged structures and the televiewer logged structures. This appendix describes the methodology used to compare the structures from core and televiewer logging to (1) assess the nature of the structure type, (2) determine a correct position of the structure, and (3) identify the angle of each arbitrary reference line traced on each core run relative to low side (reference line correction factor, $\beta_{correction}$).

The process described in this appendix were the steps taken to develop a *final structure log* that included the final assignment of structure positions along borehole, positional discrepancies, structure type (e.g., vein, foliation, etc.), structure dip and dip direction and/or alpha and beta, and structure geological aperture.

Correction and verification Methodology

The following sections describe the steps to *correct* or *verify* individual structures recorded in core logging and televiewer logging activities, which were ultimately used to form the final structural log.

Structure Type and Position Verification

Based on the integration between the two datasets, the structures were classified as being observed in ‘both’ datasets, in ‘core logging only’, or in ‘televiewer only’. When a structure was observed in both datasets, the position and structure type recorded from core logging were used as the final structure position along borehole and final structure type. For structures only seen in the televiewer survey, a positional correction was applied based on the positional offset calculated from the structures observed in both datasets. Positional corrections were applied to these structures in a way as to preserve structure order. Additional detail relating to the positional corrections applied to structures identified from the televiewer surveys is discussed in WP05 Data Report (Golder, 2020c).

At this stage, each individual structure that was common to both data sets was evaluated, and an integrated structure was carried forward to the *final structure log*. The integration of common structures was as follows:

a) Position along borehole of the final structure was based on the position of the core logged structure;
b) Dip and Dip direction of the final structure was based on the orientation of the televiewer logged structure (relative to *low side*);
c) Structure type was assigned, based on the core logging;
d) Other characteristics, such as mineral infilling, etc. was assigned based on core logging.

If a structure was identified only in the televiewer logs, core run photographs acquired during core logging were reviewed to aid in evaluating if this structure was present in the core. If it is determined that this is a real structure and not a drill feature, it was included in the final

structural log, along with its interpreted structure type, dip and dip direction, and corrected position.

If a structure was identified only in core logging, this structure was carried forward to the final structural log, along with its structure type, alpha and beta angles, and position.

Structure Orientation

For each core run logged in WP03, an arbitrary reference line was drawn along the length of the core, where the location is initially unknown. Orientations of all structures identified during core logging were described relative to this reference line (beta angles) in each run. The purpose of this section is to describe the process used to define the *true* location, from the '*low side*' of the borehole, of this reference line (between 0 – 360°) by integrating the oriented televiewer images.

When a structure was observed in both datasets, the alpha and beta angles from the televiewer survey were used as the final structure orientation.

For structures only observed in core logging, a reference line correction factor was applied to the beta angles in order to locate the arbitrary reference line relative to the bottom of the *borehole ('low-side').* The reference line correction factor relies on structures seen in both datasets within the same continuously referenced interval. The correction factor takes an average of the beta angle correction(s), which is the angle from the borehole '*low-side'* (identified from the televiewer survey) to the arbitrary reference from core logging, calculated for each structure ($\beta_{correction} = \beta_{televiewer} - \beta_{core\ logging}$). Figure 1 shows how the beta angle correction relates to the arbitrary reference line and the borehole '*low-side'*.

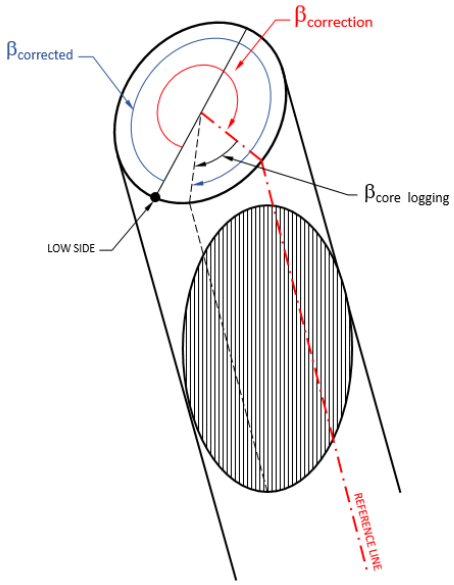


Figure 1: Schematic Showing Beta Angle Correction

$$\beta_{core\ logging} + Reference\ Line\ Correction\ Factor(Average) = \beta_{corrected}$$

$$(if\ \beta_{corrected} > 360°, subtract\ 360°)$$

If no core logged structure within a continuously referenced interval was identified in the televiewer logs, then no reference line correction could be developed and orientation of the structure(s) within that interval was not possible.

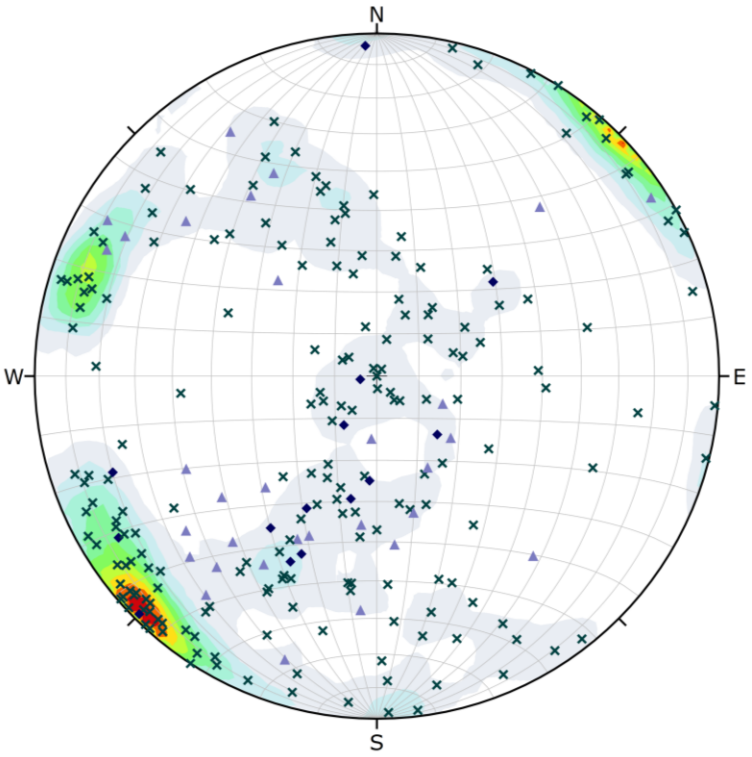
Dip and dip direction of the structures were calculated using the software DIPS© (Version 7), by Rocscience, which processes the data by using stereographic projections based on the alpha and corrected beta measurements and to the borehole deviation survey. The borehole survey file generated from the average of six separate televiewer probe runs using 1 m intervals between survey points was used for the projection of the final structure orientations.

Final Structural Log

The integration of core logged structures and televiewer logged structures resulted in a final structural log. The result of the final structural log includes a table that captures a complete set of attributes of each structure recorded either from core logging, televiewer logging, or a combination of both. Where certain attributes are duplicated between the two logging approaches (i.e., structure type, or position) decisions were made to carry forward the most accurate value to the final structure log. For example, position values and structure type were obtained from the core logging structures.

Appendix E: Stereonets of Fractures by Structural Unit

SU1 (0 – 65.5 m)



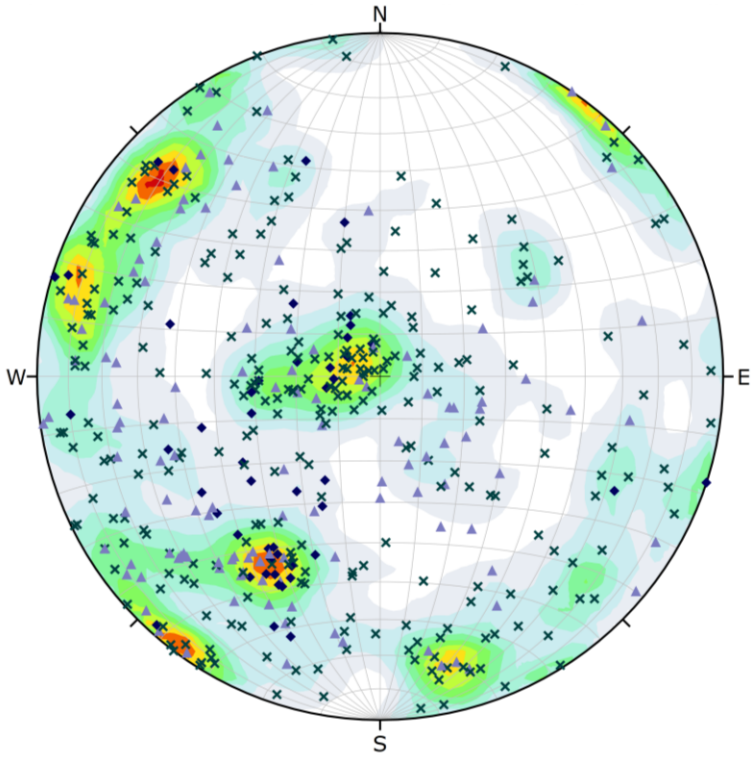
Symbol	STR_TYPE	Quantity
◆	FLT	14
×	JN	201
▲	VN	31

Color	Density Concentrations
	0.00 - 1.00
	1.00 - 2.00
	2.00 - 3.00
	3.00 - 4.00
	4.00 - 5.00
	5.00 - 6.00
	6.00 - 7.00
	7.00 - 8.00
	8.00 - 9.00
	9.00 - 10.00

Contour Data	Pole Vectors
Maximum Density	9.63%
Contour Distribution	Fisher
Counting Circle Size	1.0%

Plot Mode	Pole Vectors
Vector Count (Weighted)	481 (246 Entries)
Terzaghi Weighting	Minimum Bias Angle 15°
Hemisphere	Lower
Projection	Equal Area

SU2 (65.5 – 291 m)



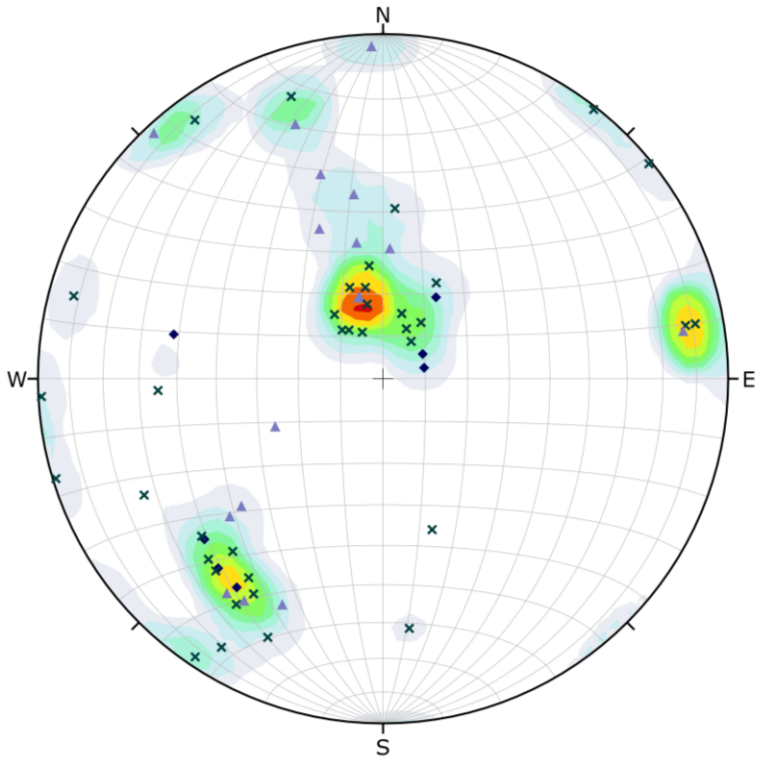
Symbol	STR_TYPE	Quantity
◆	FLT	48
×	JN	296
▲	VN	126

Color	Density Concentrations
	0.00 - 0.45
	0.45 - 0.90
	0.90 - 1.35
	1.35 - 1.80
	1.80 - 2.25
	2.25 - 2.70
	2.70 - 3.15
	3.15 - 3.60
	3.60 - 4.05
	4.05 - 4.50

Contour Data	Pole Vectors
Maximum Density	4.22%
Contour Distribution	Fisher
Counting Circle Size	1.0%

Plot Mode	Pole Vectors
Vector Count (Weighted)	865 (470 Entries)
Terzaghi Weighting	Minimum Bias Angle 15°
Hemisphere	Lower
Projection	Equal Area

SU3 (291 – 370.5 m)



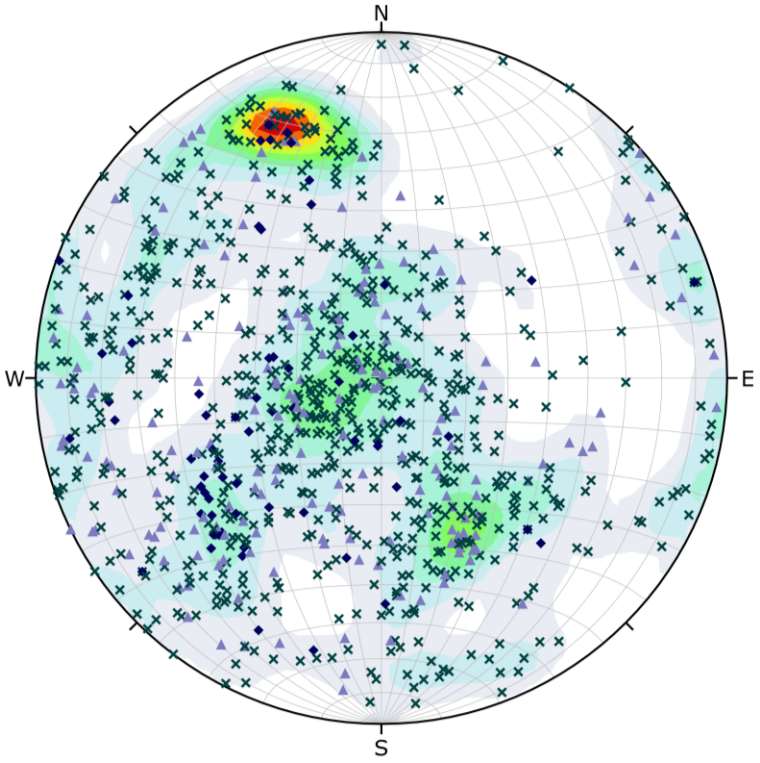
Symbol	STR_TYPE	Quantity
◆	FLT	7
×	JN	38
▲	VN	20

Color	Density Concentrations
	0.00 - 1.30
	1.30 - 2.60
	2.60 - 3.90
	3.90 - 5.20
	5.20 - 6.50
	6.50 - 7.80
	7.80 - 9.10
	9.10 - 10.40
	10.40 - 11.70
	11.70 - 13.00

Contour Data	Pole Vectors
Maximum Density	12.08%
Contour Distribution	Fisher
Counting Circle Size	1.0%

Plot Mode	Pole Vectors
Vector Count (Weighted)	115 (65 Entries)
Terzaghi Weighting	Minimum Bias Angle 15°
Hemisphere	Lower
Projection	Equal Area

SU4 (370.5 – 683 m)



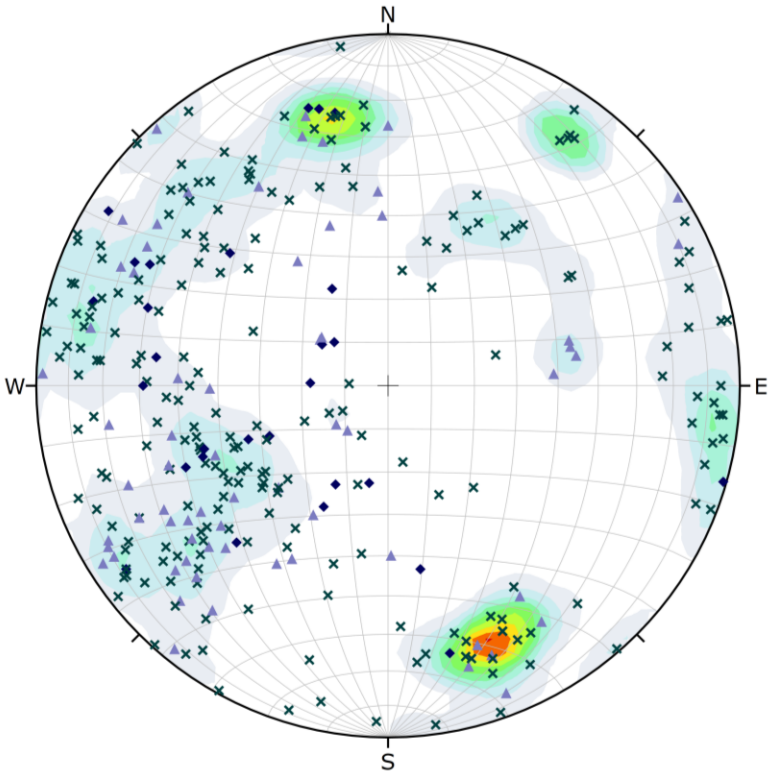
Symbol	STR_TYPE	Quantity
◆	FLT	66
×	JN	709
▲	VN	199

Color	Density Concentrations
	0.00 - 0.55
	0.55 - 1.10
	1.10 - 1.65
	1.65 - 2.20
	2.20 - 2.75
	2.75 - 3.30
	3.30 - 3.85
	3.85 - 4.40
	4.40 - 4.95
	4.95 - 5.50

Contour Data	Pole Vectors
Maximum Density	5.27%
Contour Distribution	Fisher
Counting Circle Size	1.0%

Plot Mode	Pole Vectors
Vector Count (Weighted)	1644 (974 Entries)
Terzaghi Weighting	Minimum Bias Angle 15°
Hemisphere	Lower
Projection	Equal Area

SU5 (683 – 1000.41 m)



Symbol	STR_TYPE	Quantity
◆	FLT	28
×	JN	230
▲	VN	66

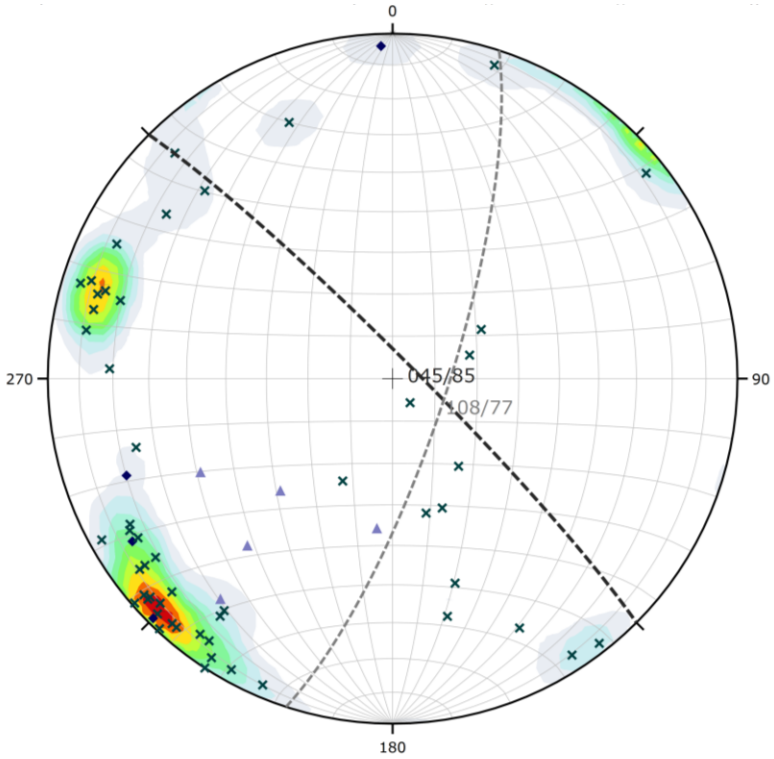
Color	Density Concentrations
	0.00 - 0.90
	0.90 - 1.80
	1.80 - 2.70
	2.70 - 3.60
	3.60 - 4.50
	4.50 - 5.40
	5.40 - 6.30
	6.30 - 7.20
	7.20 - 8.10
	8.10 - 9.00

Contour Data	Pole Vectors
Maximum Density	8.16%
Contour Distribution	Fisher
Counting Circle Size	1.0%

Plot Mode	Pole Vectors
Vector Count (Weighted)	644 (324 Entries)
Terzaghi Weighting	Minimum Bias Angle 15°
Hemisphere	Lower
Projection	Equal Area

Appendix F: Stereonets of IG_BH02 High Fracture Frequency Intervals (HFFI)

IG_BH02 HFFI_1 (19.11 – 34.38 m):



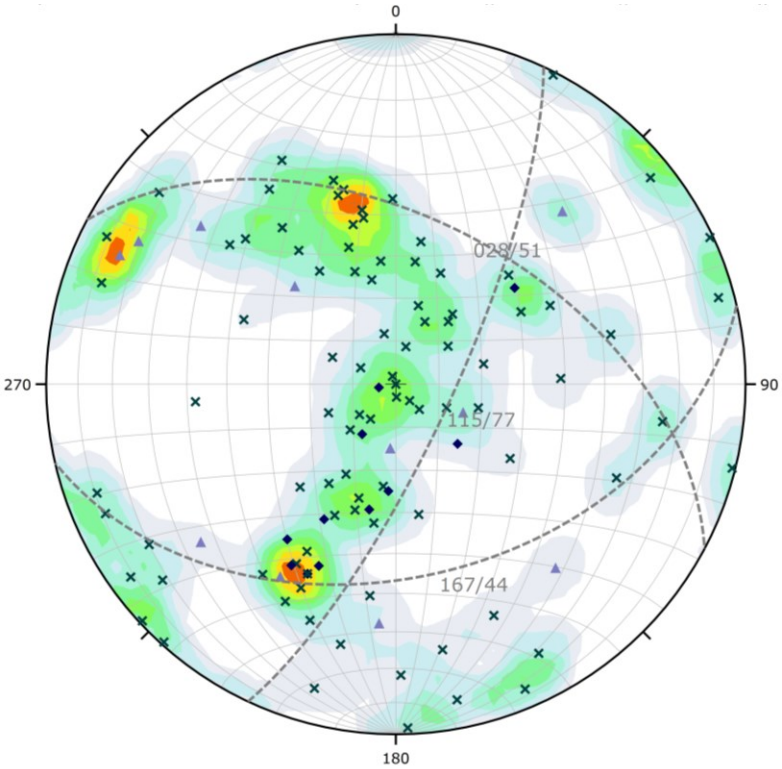
Symbol	STR_TYPE	Quantity
◆	FLT	4
×	JN	55
▲	VN	5

Color	Density Concentrations
	0.00 - 1.90
	1.90 - 3.80
	3.80 - 5.70
	5.70 - 7.60
	7.60 - 9.50
	9.50 - 11.40
	11.40 - 13.30
	13.30 - 15.20
	15.20 - 17.10
	17.10 - 19.00

Contour Data	Pole Vectors
Maximum Density	18.04%
Contour Distribution	Fisher
Counting Circle Size	1.0%

Plot Mode	Pole Vectors
Vector Count (Weighted)	144 (64 Entries)
Terzaghi Weighting	Minimum Bias Angle 15°
Hemisphere	Lower
Projection	Equal Area

IG_BH02 HFFI_2 (47.50 – 68.27 m):



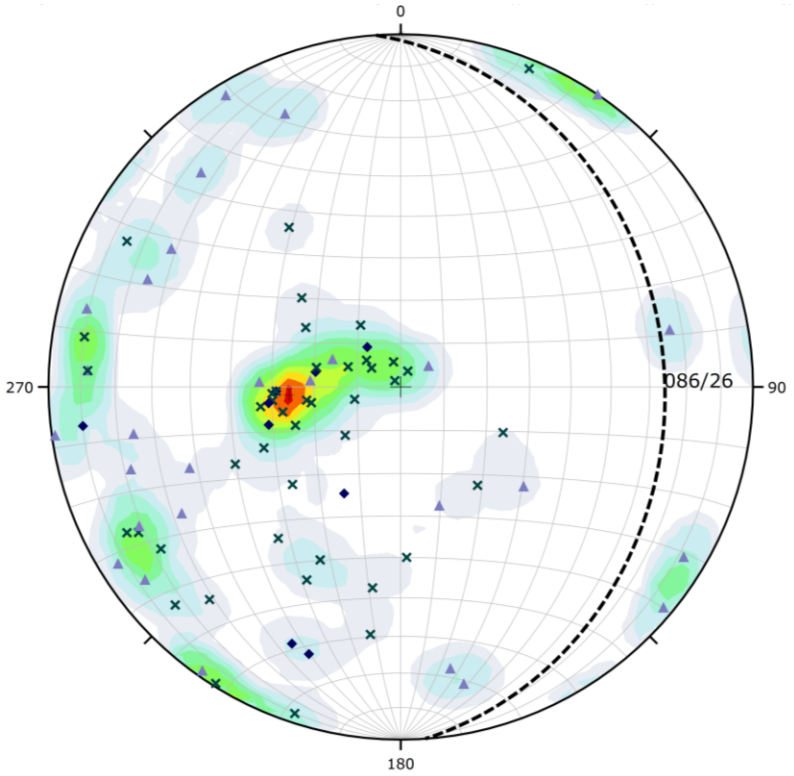
Symbol	STR_TYPE	Quantity
◆	FLT	11
×	JN	94
▲	VN	11

Color	Density Concentrations
	0.00 - 0.60
	0.60 - 1.20
	1.20 - 1.80
	1.80 - 2.40
	2.40 - 3.00
	3.00 - 3.60
	3.60 - 4.20
	4.20 - 4.80
	4.80 - 5.40
	5.40 - 6.00

Contour Data	Pole Vectors
Maximum Density	5.39%
Contour Distribution	Fisher
Counting Circle Size	1.0%

Plot Mode	Pole Vectors
Vector Count (Weighted)	201 (116 Entries)
Terzaghi Weighting	Minimum Bias Angle 15°
Hemisphere	Lower
Projection	Equal Area

IG_BH02 HFFI_3 (272.84 – 289.33 m):



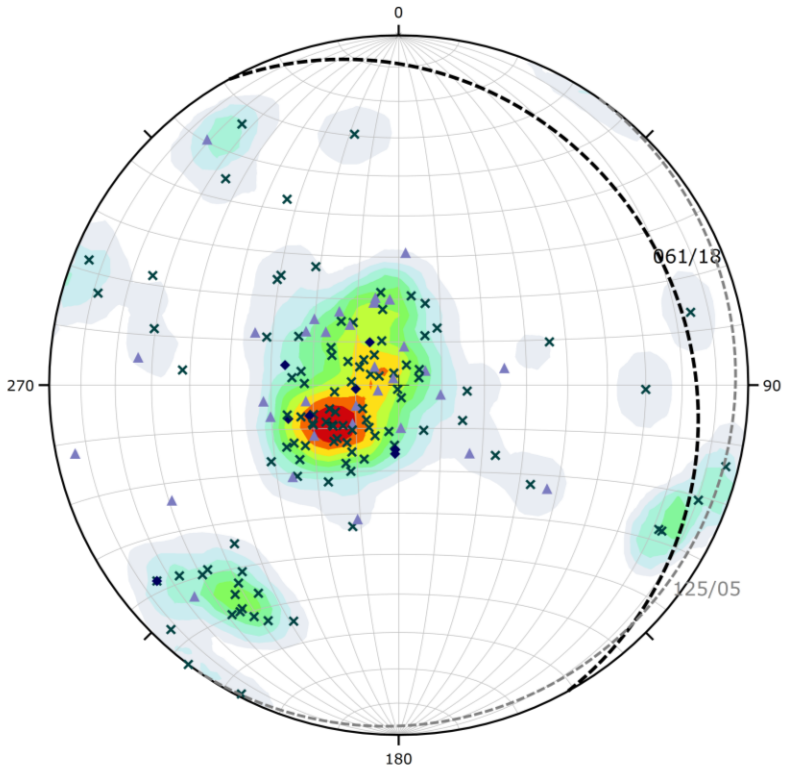
Symbol	STR_TYPE	Quantity
◆	FLT	9
×	JN	47
▲	VN	28

Color	Density Concentrations
	0.00 - 1.00
	1.00 - 2.00
	2.00 - 3.00
	3.00 - 4.00
	4.00 - 5.00
	5.00 - 6.00
	6.00 - 7.00
	7.00 - 8.00
	8.00 - 9.00
	9.00 - 10.00

Contour Data	Pole Vectors
Maximum Density	9.34%
Contour Distribution	Fisher
Counting Circle Size	1.0%

Plot Mode	Pole Vectors
Vector Count (Weighted)	136 (84 Entries)
Terzaghi Weighting	Minimum Bias Angle 15°
Hemisphere	Lower
Projection	Equal Area

IG_BH02 HFFI_4 (369.78 – 386.62 m):



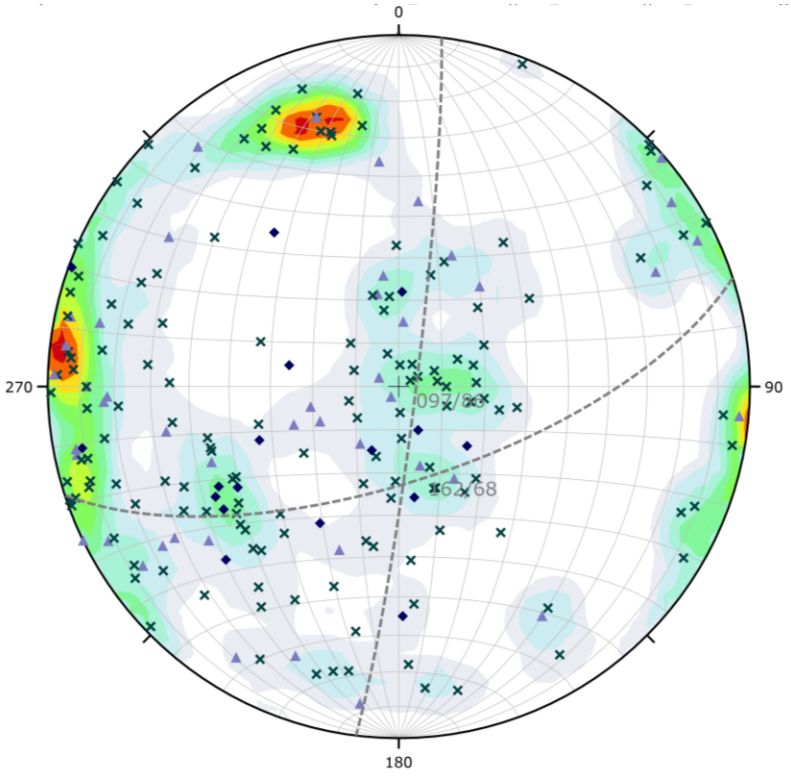
Symbol	STR_TYPE	Quantity
◆	FLT	8
×	JN	105
▲	VN	35

Color	Density Concentrations
	0.00 - 1.00
	1.00 - 2.00
	2.00 - 3.00
	3.00 - 4.00
	4.00 - 5.00
	5.00 - 6.00
	6.00 - 7.00
	7.00 - 8.00
	8.00 - 9.00
	9.00 - 10.00

Contour Data	Pole Vectors
Maximum Density	9.97%
Contour Distribution	Fisher
Counting Circle Size	1.0%

Plot Mode	Pole Vectors
Vector Count (Weighted)	208 (148 Entries)
Terzaghi Weighting	Minimum Bias Angle 15°
Hemisphere	Lower
Projection	Equal Area

IG_BH02 HFFI_5 (662.81 – 686.19 m):



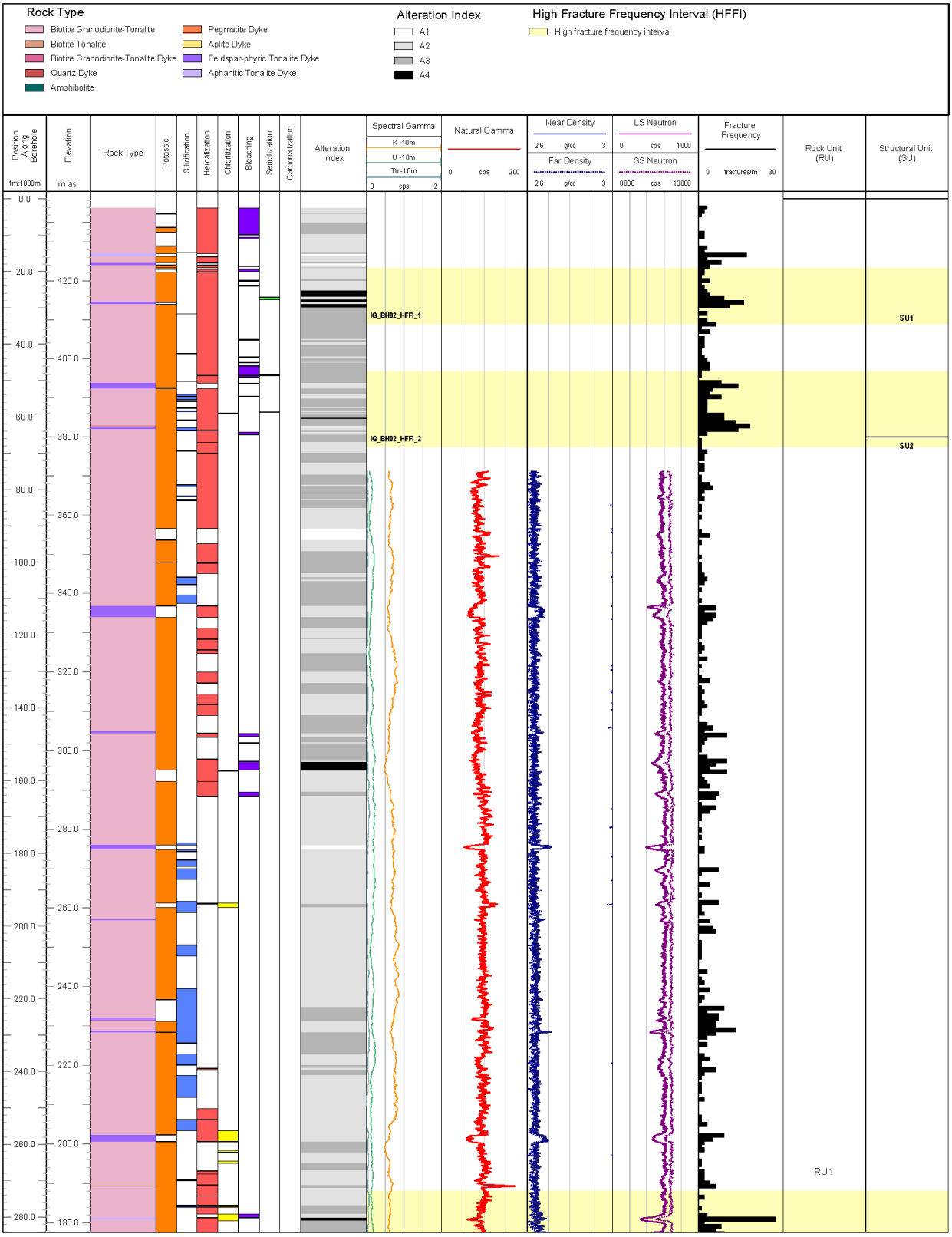
Symbol	STR_TYPE	Quantity
◆	FLT	18
×	JN	151
▲	VN	46

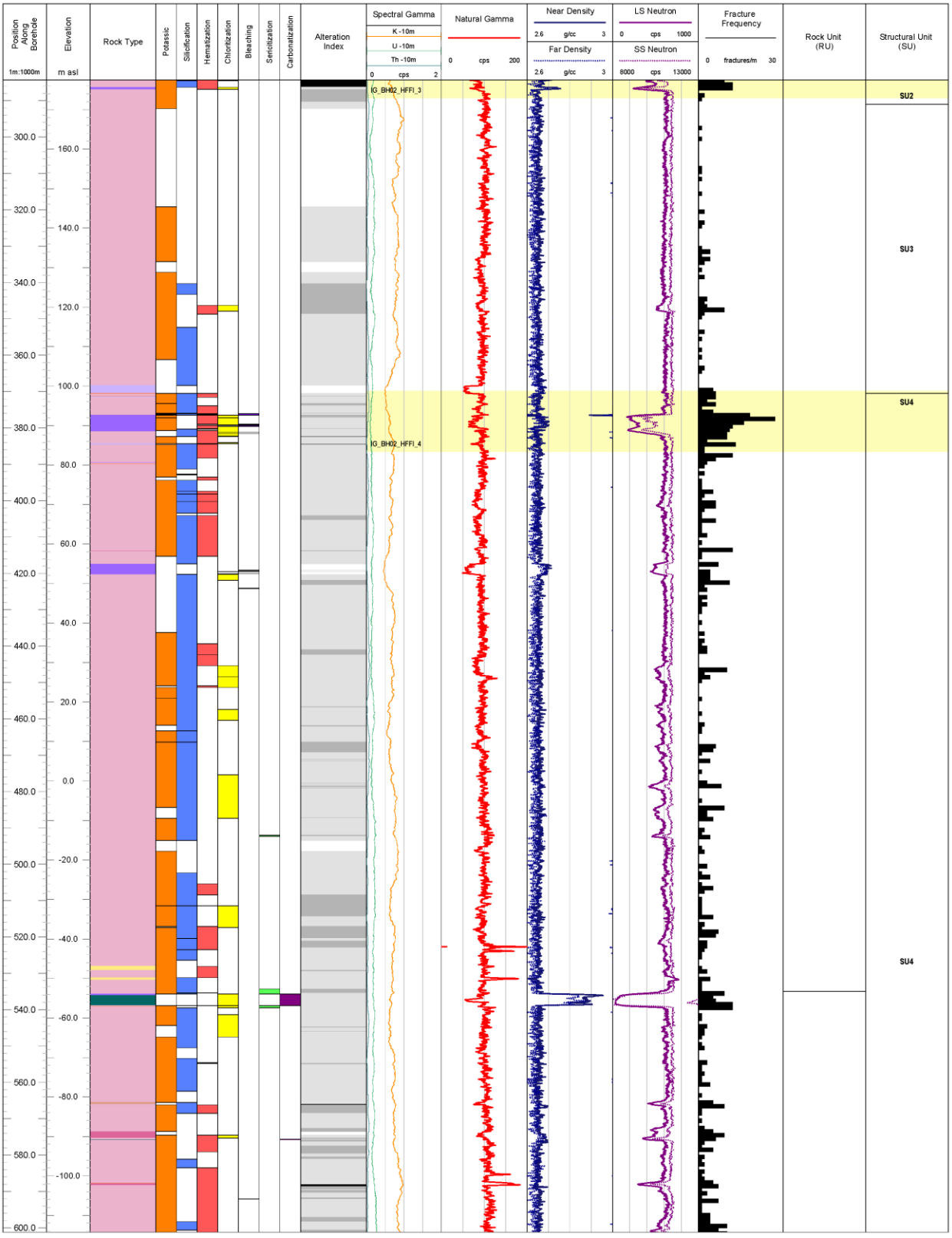
Color	Density Concentrations
	0.00 - 0.65
	0.65 - 1.30
	1.30 - 1.95
	1.95 - 2.60
	2.60 - 3.25
	3.25 - 3.90
	3.90 - 4.55
	4.55 - 5.20
	5.20 - 5.85
	5.85 - 6.50

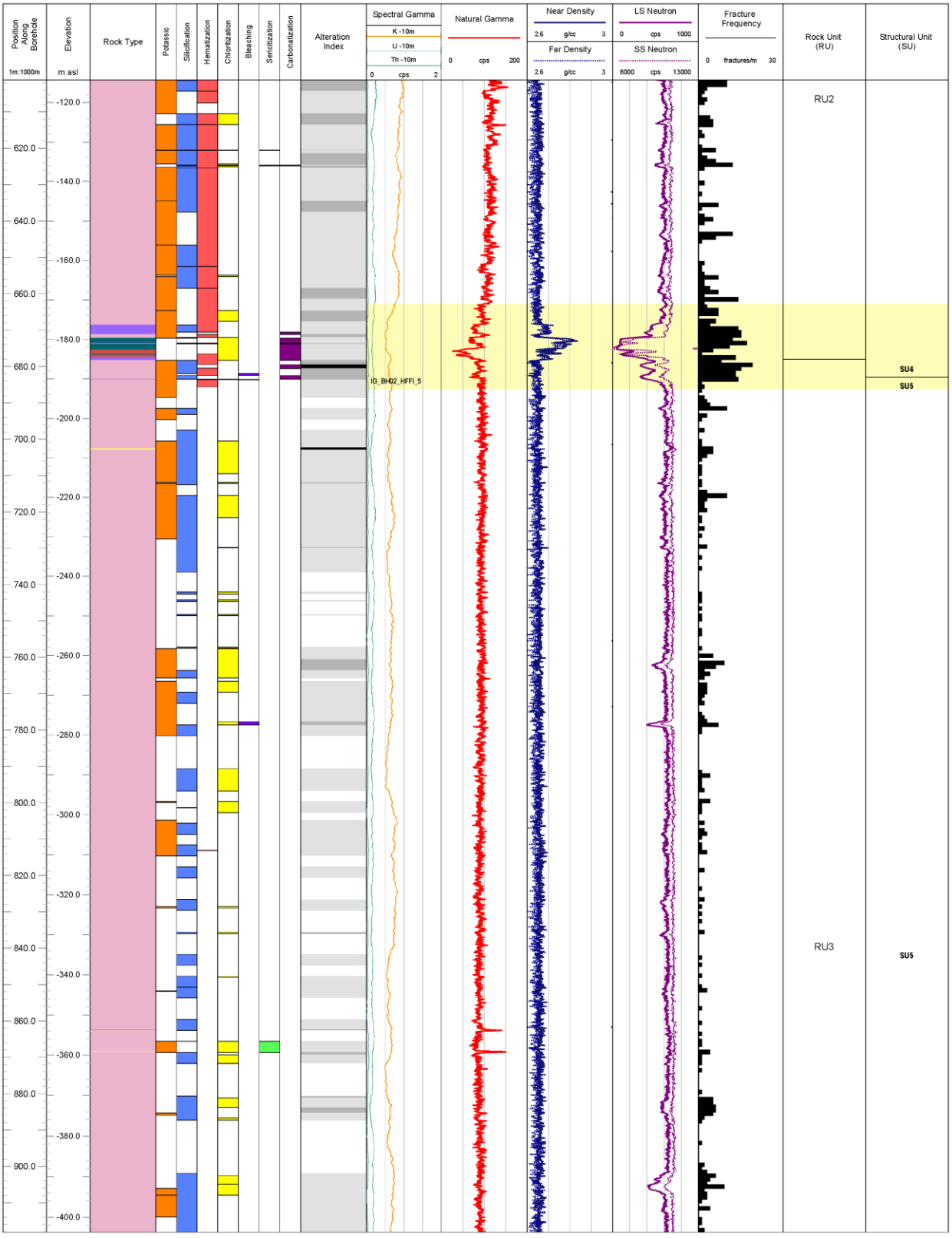
Contour Data	Pole Vectors
Maximum Density	6.18%
Contour Distribution	Fisher
Counting Circle Size	1.0%

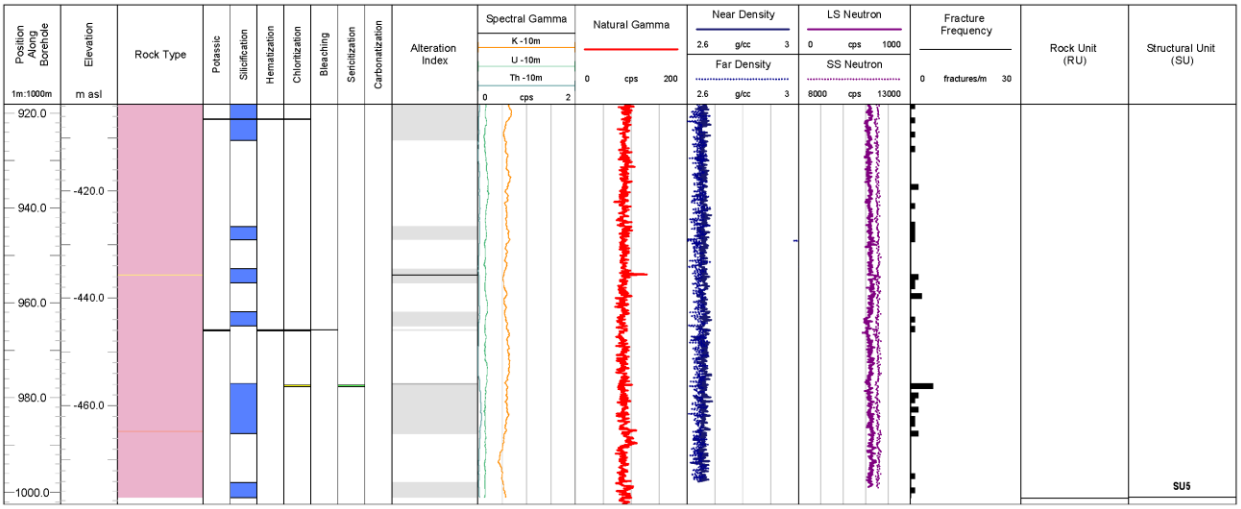
Plot Mode	Pole Vectors
Vector Count (Weighted)	386 (215 Entries)
Terzaghi Weighting	Minimum Bias Angle 15°
Hemisphere	Lower
Projection	Equal Area

Appendix G: Summary of borehole logs at 1:1,000 scale


Rock Type
Biotite Granodiorite-Tonalite
Biotite Tonalite
Biotite Granodiorite-Tonalite Dyke
Quartz Dyke
Amphibolite
Pegmatite Dyke
Aplite Dyke
Feldspar-phyric Tonalite Dyke
Aphanitic Tonalite Dyke
Alteration Index
A1
A2
A3
A4
High Fracture Frequency Interval (HFFI)
High fracture frequency interval
Position Along Borehole
1m:1000m
Elevation
m asl
Rock Type
Potassic
Silicification
Hematization
Chloritization
Bleaching
Sericitization
Carbonatization
Alteration Index
Spectral Gamma
K -10m
U -10m
Th -10m
0 cps 2
Natural Gamma
0 cps 200
Near Density
2.6 g/cc 3
Far Density
2.6 g/cc 3
LS Neutron
0 cps 1000
SS Neutron
8000 cps 13000
Fracture Frequency
0 fractures/m 30
Rock Unit (RU)
Structural Unit (SU)
IG_BH02_HFFI_1
IG_BH02_HFFI_2
SU1
SU2
RU1
0.0
20.0
40.0
60.0
80.0
100.0
120.0
140.0
160.0
180.0
200.0
220.0
240.0
260.0
280.0
300.0
320.0
340.0
360.0
380.0
400.0
420.0
180.0
200.0
220.0
240.0
260.0
280.0


Position Along Borehole
1m:1000m
Elevation
m asl
Rock Type
Potassic
Silicification
Hematization
Chloritization
Bleaching
Sericitization
Carbonatization
Alteration Index
Spectral Gamma
K -10m
U -10m
Th -10m
0 cps 2
Natural Gamma
0 cps 200
Near Density
2.6 g/cc 3
Far Density
2.6 g/cc 3
LS Neutron
0 cps 1000
SS Neutron
8000 cps 13000
Fracture Frequency
0 fractures/m 30
Rock Unit (RU)
Structural Unit (SU)
IG_BH02_HFFI_3
IG_BH02_HFFI_4
SU2
SU3
SU4
SU4
300.0
320.0
340.0
360.0
380.0
400.0
420.0
440.0
460.0
480.0
500.0
520.0
540.0
560.0
580.0
600.0
160.0
140.0
120.0
100.0
80.0
60.0
40.0
20.0
0.0
-20.0
-40.0
-60.0
-80.0
-100.0


Position Along Borehole
1m:1000m
Elevation
m asl
Rock Type
Potassic
Silicification
Hematization
Chloritization
Bleaching
Sericitization
Carbonatization
Alteration Index
Spectral Gamma
K -10m
U -10m
Th -10m
0 cps 2
Natural Gamma
0 cps 200
Near Density
2.6 g/cc 3
Far Density
2.6 g/cc 3
LS Neutron
0 cps 1000
SS Neutron
8000 cps 13000
Fracture Frequency
0 fractures/m 30
Rock Unit (RU)
Structural Unit (SU)
RU2
RU3
SU4
SU5
IG_BH02_HFFI_5
620.0
640.0
660.0
680.0
700.0
720.0
740.0
760.0
780.0
800.0
820.0
840.0
860.0
880.0
900.0
-120.0
-140.0
-160.0
-180.0
-200.0
-220.0
-240.0
-260.0
-280.0
-300.0
-320.0
-340.0
-360.0
-380.0
-400.0


Position Along Borehole
1m:1000m
Elevation
m asl
Rock Type
Potassic
Silicification
Hematization
Chloritization
Bleaching
Sericitization
Carbonatization
Alteration Index
Spectral Gamma
K -10m
U -10m
Th -10m
0 cps 2
Natural Gamma
0 cps 200
Near Density
2.6 g/cc 3
Far Density
2.6 g/cc 3
LS Neutron
0 cps 1000
SS Neutron
8000 cps 13000
Fracture Frequency
0 fractures/m 30
Rock Unit (RU)
Structural Unit (SU)
920.0
940.0
960.0
980.0
1000.0
-420.0
-440.0
-460.0
SU5